

1 SEARCH FOR PRODUCTION OF A HIGGS BOSON AND A SINGLE TOP
2 QUARK IN MULTILEPTON FINAL STATES IN pp COLLISIONS AT $\sqrt{s} = 13$
3 TeV.

4 by

5 Jose Andres Monroy Montañez

A DISSERTATION

7 Presented to the Faculty of

8 The Graduate College at the University of Nebraska

In Partial Fulfilment of Requirements

10 For the Degree of Doctor of Philosophy

11 Major: Physics and Astronomy

12 Under the Supervision of Kenneth Bloom and Aaron Dominguez

13 Lincoln, Nebraska

14 July, 2018

15 SEARCH FOR PRODUCTION OF A HIGGS BOSON AND A SINGLE TOP
16 QUARK IN MULTILEPTON FINAL STATES IN pp COLLISIONS AT $\sqrt{s} = 13$
17 TeV.

18 Jose Andres Monroy Montañez, Ph.D.

19 University of Nebraska, 2018

20 Adviser: Kenneth Bloom and Aaron Dominguez

²¹ Table of Contents

²²	Table of Contents	iii
²³	List of Figures	vii
²⁴	List of Tables	xi
²⁵	1 Theoretical approach	1
²⁶	1.1 Introduction	1
²⁷	1.2 Standard model of particle physics	2
²⁸	1.2.1 Fermions	4
²⁹	1.2.1.1 Leptons	5
³⁰	1.2.1.2 Quarks	7
³¹	1.2.2 Fundamental interactions	11
³²	1.2.3 Gauge invariance.	15
³³	1.2.4 Gauge bosons	17
³⁴	1.3 Electroweak unification and the Higgs mechanism	18
³⁵	1.3.1 Spontaneous symmetry breaking (SSB)	26
³⁶	1.3.2 Higgs mechanism	30
³⁷	1.3.3 Masses of the gauge bosons	33
³⁸	1.3.4 Masses of the fermions	34

39	1.3.5	The Higgs field	35
40	1.3.6	Production of Higgs bosons at LHC	36
41	1.3.7	Higgs boson decay channels	40
42	1.4	Experimental status of the anomalous Higgs-fermion coupling	42
43	1.5	Associated production of a Higgs boson and a single top quark	44
44	1.6	CP-mixing in tH processes	49
45	2	The CMS experiment at the LHC	54
46	2.1	Introduction	54
47	2.2	The LHC	55
48	2.3	The CMS experiment	65
49	2.3.1	CMS coordinate system	68
50	2.3.2	Tracking system	70
51	2.3.3	Silicon strip tracker	73
52	2.3.4	Electromagnetic calorimeter	74
53	2.3.5	Hadronic calorimeter	76
54	2.3.6	Superconducting solenoid magnet	77
55	2.3.7	Muon system	79
56	2.3.8	CMS trigger system	80
57	2.3.9	CMS computing	81
58	3	Event generation, simulation and reconstruction	86
59	3.1	Event generation	87
60	3.2	Monte Carlo Event Generators.	91
61	3.3	CMS detector simulation.	92
62	3.4	Event reconstruction.	94
63	3.4.1	Particle-Flow Algorithm.	94

64	3.4.1.1	Missing transverse energy.	109
65	3.4.2	Event reconstruction examples	110
66	5	Statistical methods	113
67	5.1	Multivariate analysis	113
68	5.1.1	Decision trees	117
69	5.1.2	Boosted decision trees (BDT)	119
70	5.1.3	Overtraining	122
71	5.1.4	Variable ranking	122
72	5.1.5	BDT output example	123
73	5.2	Statistical inference	124
74	5.2.1	Nuisance parameters	124
75	5.2.2	Maximum likelihood estimation method	125
76	5.3	Upper limits	127
77	5.4	Asymptotic limits	131
78	6	Search for production of a Higgs boson and a single top quark in multilepton final states in pp collisions at $\sqrt{s} = 13$ TeV	133
80	6.1	Introduction	133
81	6.2	<i>tHq</i> signature	136
82	6.3	Background processes	138
83	6.4	Data and MC Samples	140
84	6.4.1	Full 2016 data set	140
85	6.4.2	Triggers	141
86	6.4.3	Signal modeling and MC samples	144
87	6.5	Object Identification	148
88	6.5.1	Lepton reconstruction and identification	148

89	6.5.2 Lepton selection efficiency	155
90	6.5.3 Jets and b -jet tagging	158
91	6.5.4 Missing Energy MET	159
92	6.6 Event selection	160
93	6.7 Background predictions	161
94	6.8 Signal discrimination	163
95	6.8.1 Classifiers response	168
96	6.9 Additional discriminating variables	168
97	A Datasets and triggers	172
98	Bibliography	174
99	References	177

¹⁰⁰ List of Figures

101	1.1	Standard Model of particle physics.	3
102	1.2	Transformations between quarks	11
103	1.3	Fundamental interactions in nature.	12
104	1.4	SM interactions diagrams	13
105	1.5	Neutral current processes	19
106	1.6	Spontaneous symmetry breaking mechanism	27
107	1.7	SSB Potential form	28
108	1.8	Potential for complex scalar field	29
109	1.9	SSB mechanism for complex scalar field	30
110	1.10	Proton-Proton collision	36
111	1.11	Proton PDFs	37
112	1.12	Higgs boson production mechanism Feynman diagrams	38
113	1.13	Higgs boson production cross section and decay branching ratios	39
114	1.14	κ_t - κ_V plot of the coupling modifiers. ATLAS and CMS combination.	42
115	1.15	Higgs boson production in association with a top quark	45
116	1.16	Cross section for tHq process as a function of κ_t	48
117	1.17	Cross section for tHW process as a function of κ_{Htt}	48
118	1.18	NLO cross section for tX_0 and $t\bar{t}X_0$.	52

119	1.19 NLO cross section for $tWX_0, t\bar{t}X_0$	53
120	2.1 CERN accelerator complex	55
121	2.2 LHC protons source. First acceleration stage.	56
122	2.3 The LINAC2 accelerating system at CERN.	57
123	2.4 LHC layout and RF cavities module.	58
124	2.5 LHC dipole magnet.	60
125	2.6 Integrated luminosity delivered by LHC and recorded by CMS during 2016	62
126	2.7 LHC interaction points	63
127	2.8 Multiple pp collision bunch crossing at CMS.	65
128	2.9 Layout of the CMS detector	66
129	2.10 CMS detector transverse slice	67
130	2.11 CMS detector coordinate system	69
131	2.12 CMS tracking system schematic view.	70
132	2.13 CMS pixel detector	71
133	2.14 SST Schematic view.	73
134	2.15 CMS ECAL schematic view	75
135	2.16 CMS HCAL schematic view	77
136	2.17 CMS solenoid magnet	78
137	2.18 CMS Muon system schematic view	79
138	2.19 CMS Level-1 trigger architecture	81
139	2.20 WLCG structure	82
140	2.21 Data flow from CMS detector through hardware Tiers	84
141	3.1 Event generation process.	87
142	3.2 Particle flow algorithm.	95
143	3.3 Stable cones identification	103

144	3.4	Jet reconstruction.	105
145	3.5	Jet energy corrections.	106
146	3.6	Secondary vertex in a b-hadron decay.	108
147	3.7	HIG-13-004 Event 1 reconstruction.	110
148	3.8	$e\mu$ event reconstruction.	111
149	3.9	Recorded event reconstruction.	112
150	5.1	Scatter plots-MVA event classification.	115
151	5.2	Scalar test statistical.	116
152	5.3	Decision tree.	117
153	5.4	Decision tree output example.	120
154	5.5	BDT output example.	123
155	5.6	t_r p.d.f. assuming each H_0 and H_1	128
156	5.7	Illustration of the CL_s limit.	130
157	5.8	Example of Brazilian flag plot	131
158	6.1	Analysis strategy workflow	136
159	6.2	tHq event signature	137
160	6.3	$t\bar{t}$ and $t\bar{t}W$ events signature	140
161	6.4	Trigger efficiency for the same-sign $\mu\mu$ category	142
162	6.5	Trigger efficiency for the $e\mu$ category	143
163	6.6	Trigger efficiency for the ee category	144
164	6.7	Trigger efficiency for the $3l$ category	145
165	6.8	Tight vs loose lepton selection efficiencies in the $2lss$ channel.	156
166	6.9	Tight vs loose lepton selection efficiencies in the $3l$ channel.	157
167	6.10	Input variables to the BDT for signal discrimination normalized.	163
168	6.11	Input variables to the BDT for signal discrimination not normalized.	165

169	6.12 BDT input variables. Discrimination against $t\bar{t}$	166
170	6.13 BDT input variables. Discrimination against $t\bar{t}V$	167
171	6.14 Correlation matrices for the BDT input variables.	168
172	6.15 MVA classifiers performance.	169
173	6.16 Additional discriminating variables distributions.	170

¹⁷⁴ List of Tables

175	1.1	Fermions of the SM.	4
176	1.2	Fermion masses.	5
177	1.3	Lepton properties.	7
178	1.4	Quark properties.	8
179	1.5	Fermion weak isospin and weak hypercharge multiplets.	9
180	1.6	Fundamental interactions features.	14
181	1.7	SM gauge bosons.	18
182	1.8	Higgs boson properties.	36
183	1.9	Predicted branching ratios for a SM Higgs boson with $m_H = 125 \text{ GeV}/c^2$	41
184	1.10	Predicted SM cross sections for tH production at $\sqrt{s} = 13 \text{ TeV}$	46
185	1.11	Predicted enhancement of the tHq and tHW cross sections at LHC	49
186	6.1	Trigger efficiency scale factors and associated uncertainties.	143
187	6.2	Signal samples and their cross section and branching fraction.	145
188	6.3	κ_V and κ_t combinations.	146
189	6.4	List of background samples used in this analysis (CMSSW 80X).	147
190	6.5	Leading-order $t\bar{t}W$ and $t\bar{t}Z$ samples used in the signal BDT training.	147
191	6.6	Effective areas, for electrons and muons.	152
192	6.7	Requirements on each of the three muon selections.	154

193	6.8 Criteria for each of the three electron selections.	155
194	6.9 MVA input discriminating variables	164
195	6.10 TMVA input variables ranking for BDTA_GRAD method	169
196	6.11 TMVA configuration used in the BDT training.	170
197	6.12 ROC-integral for all the testing cases.	171
198	A.1 Full 2016 dataset.	172
199	A.2 HLT	173
200	A.3 Signal samples and their cross section and branching fraction.	174
201	A.4 κ_V and κ_t combinations.	175
202	A.5 List of background samples used in this analysis (CMSSW 80X).	176
203	A.6 Leading-order $t\bar{t}W$ and $t\bar{t}Z$ samples used in the signal BDT training. . .	176

²⁰⁴ **Chapter 1**

²⁰⁵ **Theoretical approach**

²⁰⁶ **1.1 Introduction**

²⁰⁷ The physical description of the universe is a challenge that physicists have faced by
²⁰⁸ making theories that refine existing principles and proposing new ones in an attempt
²⁰⁹ to embrace emerging facts and phenomena.

²¹⁰ At the end of 1940s Julian Schwinger [1] and Richard P. Feynman [2], based on
²¹¹ the work of Sin-Itiro Tomonaga [3], developed an electromagnetic theory consistent
²¹² with special relativity and quantum mechanics that describes how matter and light
²¹³ interact; the so-called *quantum electrodynamics* (QED) was born.

²¹⁴ QED has become the blueprint for developing theories that describe the universe.
²¹⁵ It was the first example of a quantum field theory (QFT), which is the theoretical
²¹⁶ framework for building quantum mechanical models that describes particles and their
²¹⁷ interactions. QFT is composed of a set of mathematical tools that combines classical
²¹⁸ fields, special relativity and quantum mechanics, while keeping the quantum point
²¹⁹ particles and locality ideas.

²²⁰ This chapter gives an overview of the standard model of particle physics, starting

221 with a description of the particles and their interactions, followed by a description of
 222 the electroweak interaction, the Higgs boson and the associated production of Higgs
 223 boson and a single top quark (tH). The description contained in this chapter is based
 224 on References [4–6].

225 1.2 Standard model of particle physics

226 The *standard model of particle physics (SM)* describes particle physics at the funda-
 227 mental level in terms of a collection of interacting particles and fields. The full picture
 228 of the SM is composed of three fields¹ whose excitations are interpreted as particles
 229 called mediators or force-carriers, a set of fields whose excitations are interpreted as
 230 elementary particles interacting through the exchange of those mediators, and a field
 231 that gives the mass to elementary particles. Figure 1.1 shows a scheme of the SM
 232 particles’ organization. In addition, for each of the particles in the scheme there exists
 233 an antiparticle with the same mass and opposite quantum numbers. The existence of
 234 antiparticles is a prediction of the relativistic quantum mechanics from the solution
 235 of the Dirac equation for which a negative energy solution is also possible. In some
 236 cases a particle is its own anti-particle, like photon or Higgs boson.

237 The mathematical formulation of the SM is based on group theory and the use of
 238 Noether’s theorem [8] which states that for a physical system modeled by a Lagrangian
 239 that is invariant under a group of transformations a conservation law is expected. For
 240 instance, a system described by a time-independent Lagrangian is invariant (symmet-
 241 ric) under time changes (transformations) with the total energy conservation law as
 242 the expected conservation law. In QED, the charge operator (Q) is the generator of

¹ The formal and complete treatment of the SM is out of the scope of this document, however a plenty of textbooks describing it at several levels are available in the literature. The treatment in References [5, 6] is quite comprehensive and detailed. Note that gravitational field is not included in the standard model formulation

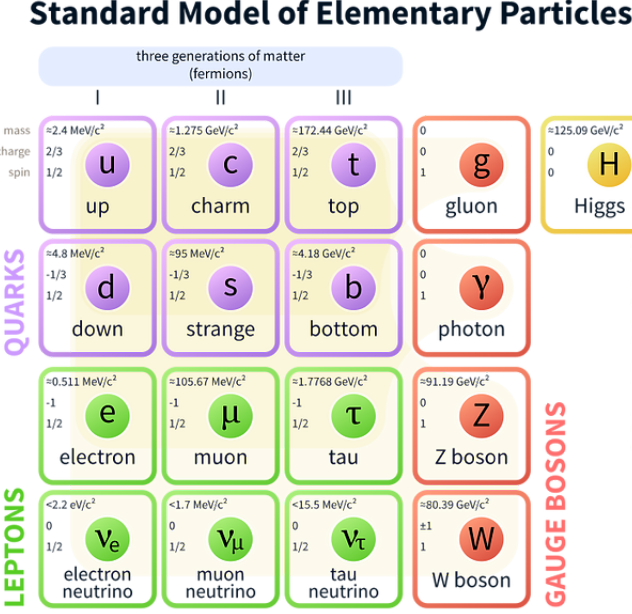


Figure 1.1: Schematic representation of the Standard Model of particle physics. The SM is a theoretical model intended to describe three of the four fundamental forces of the universe in terms of a set of particles and their interactions. [7].

243 the $U(1)$ symmetry which according to the Noether's theorem means that there is a
 244 conserved quantity; this conserved quantity is the electric charge and thus the law
 245 conservation of electric charge is established.

246 In the SM, the symmetry group $SU(3)_C \otimes SU(2)_L \otimes U(1)_Y$ describes three of the
 247 four fundamental interactions in nature (see Section 1.2.2): strong interaction (SI),
 248 weak interaction (WI) and electromagnetic interactions (EI) in terms of symmetries
 249 associated to physical quantities:

- 250 • Strong: $SU(3)_C$ associated to color charge
- 251 • Weak: $SU(2)_L$ associated to weak isospin and chirality
- 252 • Electromagnetic: $U(1)_Y$ associated to weak hypercharge and electric charge
- 253 It will be shown that the electromagnetic and weak interactions are combined in

254 the so-called electroweak interaction where chirality, hypercharge, weak isospin and
 255 electric charge are the central concepts.

256 **1.2.1 Fermions**

257 The basic constituents of the ordinary matter at the lowest level, which form the set
 258 of elementary particles in the SM formulation, are quarks and leptons. All of them
 259 have spin 1/2, therefore they are classified as fermions since they obey Fermi-Dirac
 260 statistics. There are six *flavors* of quarks and three of leptons organized in three
 261 generations, or families, as shown in Table 1.1.

		Generation		
Type		1st	2nd	3rd
Leptons	Charged	Electron (e)	Moun(μ)	Tau (τ)
	Neutral	Electron neutrino (ν_e)	Muon neutrino (ν_μ)	Tau neutrino (ν_τ)
Quarks	Up-type	Up (u)	Charm (c)	Top (t)
	Down-type	Down (d)	Strange (s)	Bottom (b)

Table 1.1: Fermions of the SM. There are six flavors of quarks and three of leptons, organized in three generations, or families, composed of two pairs of closely related particles. The close relationship is motivated by the fact that each pair of particles is a member of an $SU(2)_L$ doublet that has an associated invariance under isospin transformations. WI between leptons is limited to the members of the same generation; WI between quarks is not limited but greatly favored, to same generation members.

262

263 There is a mass hierarchy between generations (see Table 1.2), where the higher
 264 generation particles decays to the lower one, which can explain why the ordinary
 265 matter is made of particles from the first generation. In the SM, neutrinos are modeled
 266 as massless particles so they are not subject to this mass hierarchy; however, today it
 267 is known that neutrinos are massive so the hierarchy could be restated. The reason
 268 behind this mass hierarchy is one of the most important open questions in particle
 269 physics, and it becomes more puzzling when noticing that the mass difference between

270 first and second generation fermions is small compared to the mass difference with
 271 respect to the third generation.

Lepton	Mass (MeV/c ²)	Quark	Mass (MeV/c ²)
e	0.51	u	2.2
μ	105.65	c	1.28×10^3
τ	1776.86	t	173.1×10^3
ν_e	Unknown	d	4.7
ν_μ	Unknown	s	96
τ_μ	Unknown	b	4.18×10^3

Table 1.2: Fermion masses [9]. Generations differ by mass in a way that has been interpreted as a mass hierarchy. Approximate values with no uncertainties are used, for comparison purpose.

272

273 Usually, the second and third generation fermions are produced in high energy
 274 processes, like the ones recreated in particle accelerators.

275 **1.2.1.1 Leptons**

276 A lepton is an elementary particle that is not subject to the SI. As seen in Table 1.1,
 277 there are two types of leptons, the charged ones (electron, muon and tau) and the
 278 neutral ones (the three neutrinos). The electric charge (Q) is the property that gives
 279 leptons the ability to participate in the EI. From the classical point of view, Q plays
 280 a central role determining, among others, the strength of the electric field through
 281 which the electromagnetic force is exerted. It is clear that neutrinos are not affected
 282 by EI because they don't carry electric charge.

283 Another feature of the leptons that is fundamental in the mathematical description
 284 of the SM is the chirality, which is closely related to spin and helicity. Helicity
 285 defines the handedness of a particle by relating its spin and momentum such that
 286 if they are parallel then the particle is right-handed; if spin and momentum are

287 antiparallel the particle is said to be left-handed. The study of parity conservation
 288 (or violation) in β -decay has shown that only left-handed electrons/neutrinos or right-
 289 handed positrons/anti-neutrinos are created [10]; the inclusion of that feature in the
 290 theory was achieved by using projection operators for helicity, however, helicity is
 291 frame dependent for massive particles which makes it not Lorentz invariant and then
 292 another related attribute has to be used: *chirality*.

293 Chirality is a purely quantum attribute which makes it not so easy to describe in
 294 graphical terms but it defines how the wave function of a particle transforms under
 295 certain rotations. As with helicity, there are two chiral states, left-handed chiral (L)
 296 and right-handed chiral (R). In the highly relativistic limit where $E \approx p \gg m$ helicity
 297 and chirality converge, becoming exactly the same for massless particles.

298 In the following, when referring to left-handed (right-handed) it will mean left-
 299 handed chiral (right-handed chiral). The fundamental fact about chirality is that
 300 while EI and SI are not sensitive to chirality, in WI left-handed and right-handed
 301 fermions are treated asymmetrically, such that only left-handed fermions and right-
 302 handed anti-fermions are allowed to couple to WI mediators, which is a violation of
 303 parity. The way to translate this statement in a formal mathematical formulation is
 304 based on the isospin symmetry group $SU(2)_L$.

305 Each generation of leptons is seen as a weak isospin doublet.² The left-handed
 306 charged lepton and its associated left-handed neutrino are arranged in doublets of
 307 weak isospin $T=1/2$ while their right-handed partners are singlets:

$$\begin{pmatrix} \nu_l \\ l \end{pmatrix}_L, l_R := \begin{pmatrix} \nu_e \\ e \end{pmatrix}_L, \begin{pmatrix} \nu_\mu \\ \mu \end{pmatrix}_L, \begin{pmatrix} \nu_\tau \\ \tau \end{pmatrix}_L, e_R, \mu_R, \tau_R, \nu_{eR}, \nu_{\mu R}, \nu_{\tau R} \quad (1.1)$$

308 The isospin third component refers to the eigenvalues of the weak isospin operator

² The weak isospin is an analogy of the isospin symmetry in strong interaction where neutron and proton are affected equally by strong force but differ in their charge.

309 which for doublets is $T_3 = \pm 1/2$, while for singlets it is $T_3 = 0$. The physical meaning
 310 of this doublet-singlet arrangement falls in that the WI couples the two particles in
 311 the doublet by exchanging the interaction mediator while the singlet member is not
 312 involved in WI. The main properties of the leptons are summarized in Table 1.3.

313 Although all three flavor neutrinos have been observed, their masses remain un-
 314 known and only some estimations have been made [11]. The main reason is that
 315 the flavor eigenstates are not the same as the mass eigenstates which implies that
 316 when a neutrino is created its mass state is a linear combination of the three mass
 317 eigenstates and experiments can only probe the squared difference of the masses. The
 318 Pontecorvo-Maki-Nakagawa-Sakata (PMNS) mixing matrix encodes the relationship
 319 between flavor and mass eigenstates.

Lepton	$Q(e)$	T_3	L_e	L_μ	L_τ	Lifetime (s)
Electron (e)	-1	-1/2	1	0	0	Stable
Electron neutrino(ν_e)	0	1/2	1	0	0	Unknown
Muon (μ)	-1	-1/2	0	1	0	2.19×10^{-6}
Muon neutrino (ν_μ)	0	1/2	0	1	0	Unknown
Tau (τ)	-1	-1/2	0	0	1	290.3×10^{-15}
Tau neutrino (ν_τ)	0	1/2	0	0	1	Unknown

Table 1.3: Lepton properties [9]. Q: electric charge, T_3 : weak isospin. Only left-handed leptons and right-handed anti-leptons participate in the WI. Anti-particles with inverted T_3 , Q and lepton number complete the leptons set but are not listed. Right-handed leptons and left-handed anti-leptons, neither listed, form weak isospin singlets with $T_3 = 0$ and do not take part in the weak interaction.

320

321 1.2.1.2 Quarks

322 Quarks are the basic constituents of protons and neutrons. The way quarks join to
 323 form bound states, called *hadrons*, is through the SI. Quarks are affected by all the
 324 fundamental interactions which means that they carry all the four types of charges:
 325 color, electric charge, weak isospin and mass.

Flavor	$Q(e)$	I_3	T_3	B	C	S	T	B'	Y	Color
Up (u)	2/3	1/2	1/2	1/3	0	0	0	0	1/3	r,b,g
Charm (c)	2/3	0	1/2	1/3	1	0	0	0	4/3	r,b,g
Top(t)	2/3	0	1/2	1/3	0	0	1	0	4/3	r,b,g
Down(d)	-1/3	-1/2	-1/2	1/3	0	0	0	0	1/3	r,b,g
Strange(s)	-1/3	0	-1/2	1/3	0	-1	0	0	-2/3	r,b,g
Bottom(b)	-1/3	0	-1/2	1/3	0	0	0	-1	-2/3	r,b,g

Table 1.4: Quark properties [9]. Q: electric charge, I_3 : isospin, T_3 : weak isospin, B: baryon number, C: charmness, S: strangeness, T: topness, B' : bottomness, Y: hypercharge. Anti-quarks posses the same mass and spin as quarks but all charges (color, flavor numbers) have opposite sign.

326

327 Table 1.4 summarizes the features of quarks, among which the most remarkable
 328 is their fractional electric charge. Note that fractional charge is not a problem, given
 329 that quarks are not found isolated, but serves to explain how composed particles are
 330 formed out of two or more valence quarks³.

331 Color charge is responsible for the SI between quarks and is the symmetry ($SU(3)_C$)
 332 that defines the formalism to describe SI. There are three colors: red (r), blue (b)
 333 and green (g) and their corresponding three anti-colors; thus each quark carries one
 334 color unit while anti-quarks carries one anti-color unit. As explained in Section 1.2.2,
 335 quarks are not allowed to be isolated due to the color confinement effect, hence, their
 336 features have been studied indirectly by observing their bound states created when

- 337 • one quark with a color charge is attracted by an anti-quark with the correspond-
 338 ing anti-color charge forming a colorless particle called a *meson*.

 339 • three quarks (anti-quarks) with different color (anti-color) charges are attracted
 340 among them forming a colorless particle called a *baryon (anti-baryon)*.

³ Hadrons can contain an indefinite number of virtual quarks and gluons, known as the quark and gluon sea, but only the valence quarks determine hadrons' quantum numbers.

341 In practice, when a quark is left alone isolated a process called *hadronization* occurs
 342 where the quark emits gluons (see Section 1.2.4) which eventually will generate new
 343 quark-antiquark pairs and so on; those quarks will recombine to form hadrons that
 344 will decay into leptons. This proliferation of particles looks like a *jet* coming from
 345 the isolated quark. More details about the hadronization process and jet structure
 346 will be given in chapter3.

347 In the first version of the quark model (1964), M. Gell-Mann [12] and G. Zweig
 348 [13, 14] developed a consistent way to classify hadrons according to their properties.
 349 Only three quarks (u, d, s) were involved in a scheme in which all baryons have baryon
 350 number $B=1$ and therefore quarks have $B=1/3$; non-baryons have $B=0$. Baryon
 351 number is conserved in SI and EI which means that single quarks cannot be created
 352 but in pairs $q - \bar{q}$.

353 The scheme organizes baryons in a two-dimensional space (I_3 - Y); Y (hyper-
 354 charge) and I_3 (isospin) are quantum numbers related by the Gell-Mann-Nishijima
 355 formula [15, 16]:

$$Q = I_3 + \frac{Y}{2} \quad (1.2)$$

356 where $Y = B + S + C + T + B'$ are the quantum numbers listed in Table 1.4.

357 There are six quark flavors organized in three generations (see Table 1.1) fol-
 358 lowing a mass hierarchy which, again, implies that higher generations decay to first
 359 generation quarks.

	Quarks			T_3	Y_W	Leptons			T_3	Y_W
Doublets	$(\frac{u}{d'})_L$	$(\frac{c}{s'})_L$	$(\frac{t}{b'})_L$	$(\frac{1/2}{-1/2})$	$1/3$	$(\nu_e)_L$	$(\nu_\mu)_L$	$(\nu_\tau)_L$	$(\frac{1/2}{-1/2})$	-1
Singlets	u_R	c_R	t_R	0	$4/3$	ν_{eR}	$\nu_{\mu R}$	$\nu_{\tau R}$		
	d'_R	s'_R	b'_R	0	$-2/3$	e_R	μ_R	τ_R	0	-2

Table 1.5: Fermion weak isospin and weak hypercharge multiplets. Weak hypercharge is calculated through the Gell-Mann-Nishijima formula 1.2 but using the weak isospin and charge for quarks.

360

361 Isospin doublets of quarks are also defined (see Table 1.5), and same as for neutrinos,
 362 the WI eigenstates are not the same as the mass eigenstates which means that
 363 members of different quark generations are connected by the WI mediator; thus, up-
 364 type quarks are coupled not to down-type quarks (the mass eigenstates) directly but
 365 to a superposition of down-type quarks (q'_d ; *the weak eigenstates*) via WI according
 366 to:

367

$$\begin{aligned} q'_d &= V_{CKM} q_d \\ \begin{pmatrix} d' \\ s' \\ b' \end{pmatrix} &= \begin{pmatrix} V_{ud} & V_{us} & V_{ub} \\ V_{cd} & V_{cs} & V_{cb} \\ V_{td} & V_{ts} & V_{tb} \end{pmatrix} \begin{pmatrix} d \\ s \\ b \end{pmatrix} \end{aligned} \quad (1.3)$$

368 where V_{CKM} is known as Cabibbo-Kobayashi-Maskawa (CKM) mixing matrix [17,18]
 369 given by

$$\begin{pmatrix} |V_{ud}| & |V_{us}| & |V_{ub}| \\ |V_{cd}| & |V_{cs}| & |V_{cb}| \\ |V_{td}| & |V_{ts}| & |V_{tb}| \end{pmatrix} = \begin{pmatrix} 0.97427 \pm 0.00015 & 0.22534 \pm 0.00065 & 0.00351^{+0.00015}_{-0.00014} \\ 0.22520 \pm 0.00065 & 0.97344 \pm 0.00016 & 0.0412^{+0.0011}_{-0.0005} \\ 0.00867^{+0.00029}_{-0.00031} & 0.0404^{+0.0011}_{-0.0005} & 0.999146^{+0.000021}_{-0.000046} \end{pmatrix}. \quad (1.4)$$

370 The weak decays of quarks are represented in the diagram of Figure 1.2; again
 371 the CKM matrix plays a central role since it contains the probabilities for the differ-
 372 ent quark decay channels, in particular, note that quark decays are greatly favored
 373 between generation members.

374 CKM matrix is a 3×3 unitary matrix parametrized by three mixing angles and
 375 the *CP-mixing phase*; the latter is the parameter responsible for the Charge-Parity

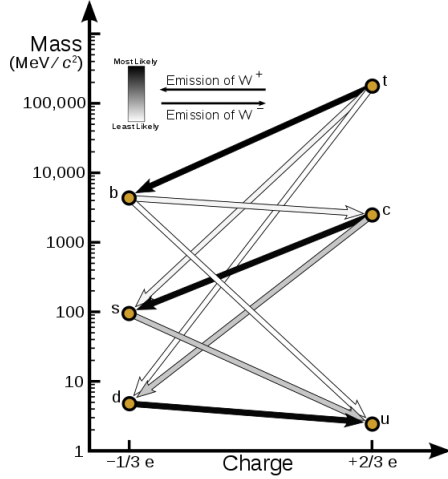


Figure 1.2: Transformations between quarks through the exchange of a WI. Higher generations quarks decay to first generation quarks by emitting a W boson. The arrow color indicates the likelihood of the transition according to the grey scale in the top left side which represent the CKM matrix parameters [19].

376 symmetry violation (CP-violation) in the SM. The fact that the top quark decays
 377 almost all the time to a bottom quark is exploited in this thesis when making the
 378 selection of the signal events by requiring the presence of a jet tagged as a jet coming
 379 from a b quark in the final state.

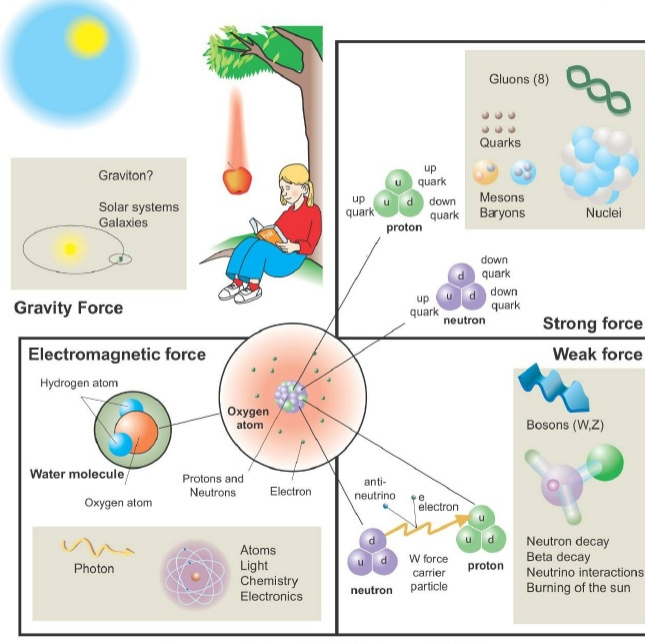
380 1.2.2 Fundamental interactions

381 Even though there are many manifestations of force in nature, like the ones repre-
 382 sented in Figure 1.3, we can classify all of them in four fundamental interactions:

- 383 • *Electromagnetic interaction (EI)* affects particles that are *electrically charged*,
 384 like electrons and protons. Figure 1.4a. shows a graphical representation, known
 385 as *Feynman diagram*, of electron-electron scattering.
- 386 • *Strong interaction (SI)* described by Quantum Chromodynamics (QCD). Hadrons
 387 like the proton and the neutron have internal structure given that they are com-

Fundamental interactions.

Illustration: Typoform



Summer School KPI 15 August 2009

Figure 1.3: Fundamental interactions in nature. Despite the many manifestations of forces in nature, we can track all of them back to one of the fundamental interactions. The most common forces are gravity and electromagnetic given that all of us are subject and experience them in everyday life.

388 posed of two or more valence quarks⁴. Quarks have fractional electric charge
 389 which means that they are subject to electromagnetic interaction and in the case
 390 of the proton they should break apart due to electrostatic repulsion; however,
 391 quarks are held together inside the hadrons against their electrostatic repulsion
 392 by the *Strong Force* through the exchange of *gluons*. The analog to the electric
 393 charge is the *color charge*. Electrons and photons are elementary particles as
 394 quarks but they don't carry color charge, therefore they are not subject to SI. A
 395 Feynman diagram for gluon exchange between quarks is shown in Figure 1.4b.

- 396 • *Weak interaction (WI)* described by the weak theory (WT), is responsible, for
 397 instance, for the radioactive decay in atoms and the deuterium production

⁴ Particles made of four and five quarks are exotic states not so common.

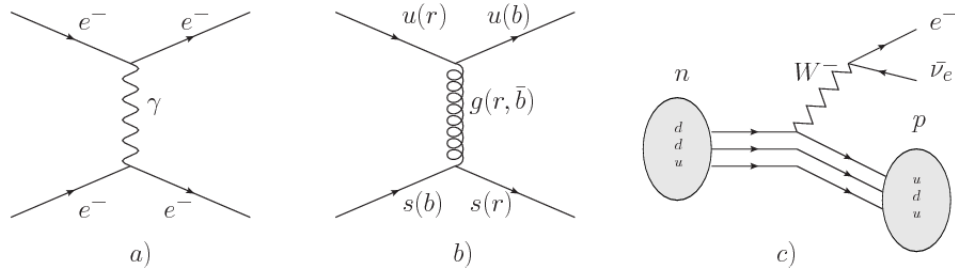


Figure 1.4: Feynman diagrams representing the interactions in SM; a) EI: e - e scattering; b) SI: gluon exchange between quarks ; c) WI: β -decay

within the sun. Quarks and leptons are the particles affected by the weak interaction; they possess a property called *flavor charge* (see 1.2.1) which can be changed by emitting or absorbing one weak force mediator. There are three mediators of the *weak force* known as Z boson in the case of electrically neutral flavor changes and W^\pm bosons in the case of electrically charged flavor changes. The *weak isospin* is the WI analog to electric charge in EI, and color charge in SI, and defines how quarks and leptons are affected by the weak force. Figure 1.4c. shows the Feynman diagram of β -decay where a neutron (n) is transformed in a proton (p) by emitting a W^- particle.

- *Gravitational interaction (GI)* described by General Theory of Relativity (GR). It is responsible for the structure of galaxies and black holes as well as the expansion of the universe. As a classical theory, in the sense that it can be formulated without even appeal to the concept of quantization, it implies that the space-time is a continuum and predictions can be made without limitation to the precision of the measurement tools. The latter represents a direct contradiction of the quantum mechanics principles. Gravity is deterministic while quantum mechanics is probabilistic; despite that, efforts to develop a quantum theory of gravity have predicted the *graviton* as mediator of the gravitational

416 force⁵.

Interaction	Acts on	Relative strength	Range (m)	Mediators
Electromagnetic (QED)	Electrically charged particles	10^{-2}	Infinite	Photon
Strong (QCD)	Quarks and gluons	1	10^{-15}	Gluon
Weak (WI)	Leptons and quarks	10^{-6}	10^{-18}	W^\pm, Z
Gravitational (GI)	Massive particles	10^{-39}	Infinite	Graviton

Table 1.6: Fundamental interactions features [20].

417

418 Table 1.6 summarizes the main features of the fundamental interactions. The
 419 strength of the interactions is represented by the coupling constants which depend
 420 on the energy scale at which the interaction is evaluated, therefore, it is the relative
 421 strength of the fundamental forces that reveals the meaning of strong and weak; in
 422 a context where the relative strength of the SI is 1, the EI is about hundred times
 423 weaker and WI is about million times weaker than the SI. A good description on how
 424 the relative strength and range of the fundamental interactions are calculated can
 425 be found in References [20, 21]. In the everyday life, only EI and GI are explicitly
 426 experienced due to the range of these interactions; i.e., at the human scale distances
 427 only EI and GI have appreciable effects, in contrast to SI which at distances greater
 428 than 10^{-15} m become negligible. Is it important to clarify that the weakness of the
 429 WI is attributed to the fact that its mediators are highly massive which affects the
 430 propagators of the interaction, as a result, the effect of the coupling constant is
 431 reduced.

⁵ Actually a wide variety of theories have been developed in an attempt to describe gravity; some famous examples are string theory and supergravity.

432 **1.2.3 Gauge invariance.**

433 QED was built successfully on the basis of the classical electrodynamics theory (CED)
 434 of Maxwell and Lorentz, following theoretical and experimental requirements imposed
 435 by

- 436 • Lorentz invariance: independence on the reference frame.
- 437 • Locality: interacting fields are evaluated at the same space-time point to avoid
 438 action at a distance.
- 439 • Renormalizability: physical predictions are finite and well defined.
- 440 • Particle spectrum, symmetries and conservation laws already known must emerge
 441 from the theory.
- 442 • Local gauge invariance.

443 The gauge invariance requirement reflects the fact that the fundamental fields
 444 cannot be directly measured but associated fields which are the observables. Electric
 445 (**E**) and magnetic (**B**) fields in CED are associated with the electric scalar potential
 446 V and the vector potential **A**. In particular, **E** can be obtained by measuring the
 447 change in the space of the scalar potential (ΔV); however, two scalar potentials
 448 differing by a constant f correspond to the same electric field. The same happens
 449 in the case of the vector potential **A**; thus, different configurations of the associated
 450 fields result in the same set of values of the observables. The freedom in choosing one
 451 particular configuration is known as *gauge freedom*; the transformation law connecting
 452 two configurations is known as *gauge transformation* and the fact that the observables
 453 are not affected by a gauge transformation is called *gauge invariance*.

454 When the gauge transformation:

$$\begin{aligned} \mathbf{A} &\rightarrow \mathbf{A} - \Delta f \\ V &\rightarrow V - \frac{\partial f}{\partial t} \end{aligned} \tag{1.5}$$

455 is applied to Maxwell equations, they are still satisfied and the fields remain invariant.
 456 Thus, CED is invariant under gauge transformations and is called a *gauge theory*.
 457 The set of all gauge transformations form the *symmetry group* of the theory, which
 458 according to the group theory, has a set of *group generators*. The number of group
 459 generators determine the number of *gauge fields* of the theory.

460 As mentioned in the first lines of Section 1.2, QED has one symmetry group ($U(1)$)
 461 with one group generator (the Q operator) and one gauge field (the electromagnetic
 462 field A^μ). In CED there is not a clear definition, beyond the historical convention,
 463 of which fields are the fundamental and which are the associated, but in QED the
 464 fundamental field is A^μ . When a gauge theory is quantized, the gauge fields are
 465 quantized and their quanta are called *gauge bosons*. The word boson characterizes
 466 particles with integer spin which obey Bose-Einstein statistics.

467 As will be detailed in Section 1.3, interactions between particles in a system can
 468 be obtained by considering first the Lagrangian density of free particles in the sys-
 469 tem, which of course is incomplete because the interaction terms have been left out,
 470 and demanding global phase transformation invariance. Global phase transforma-
 471 tion means that a gauge transformation is performed identically to every point
 472 in the space⁶ and the Lagrangian remains invariant. Then, the global transforma-
 473 tion is promoted to a local phase transformation (this time the gauge transformation
 474 depends on the position in space) and again invariance is required.

⁶ Here space corresponds to the 4-dimensional space i.e. space-time.

475 Due to the space dependence of the local transformation, the Lagrangian density is
 476 not invariant anymore. In order to reinstate the gauge invariance, the gauge covariant
 477 derivative is introduced in the Lagrangian and with it the gauge field responsible for
 478 the interaction between particles in the system. The new Lagrangian density is gauge
 479 invariant, includes the interaction terms needed to account for the interactions and
 480 provides a way to explain the interaction between particles through the exchange of
 481 the gauge boson.

482 This recipe was used to build QED and the theories that aim to explain the
 483 fundamental interactions.

484 1.2.4 Gauge bosons

485 The importance of the gauge bosons comes from the fact that they are the force
 486 mediators or force carriers. The features of the gauge bosons reflect those of the fields
 487 they represent and they are extracted from the Lagrangian density used to describe
 488 the interactions. In Section 1.3, it will be shown how the gauge bosons of the EI and
 489 WI emerge from the electroweak Lagrangian. The SI gauge bosons features are also
 490 extracted from the SI Lagrangian but it is not detailed in this document. The main
 491 features of the SM gauge bosons will be briefly presented below and summarized in
 492 Table 1.7.

- 493 • **Photon.** EI occurs when the photon couples to (is exchanged between) parti-
 494 cles carrying electric charge; however, The photon itself does not carry electric
 495 charge, therefore, there is no coupling between photons. Given that the photon
 496 is massless the EI is of infinite range, i.e., electrically charged particles interact
 497 even if they are located far away one from each other; this also implies that
 498 photons always move with the speed of light.

- 499 • **Gluon.** SI is mediated by gluons which just as photons are massless. They
 500 carry one unit of color charge and one unit of anticolor charge, hence, gluons
 501 can couple to other gluons. As a result, the range of the SI is not infinite
 502 but very short due to the attraction between gluons, giving rise to the *color*
 503 *confinement* which explains why color charged particles cannot be isolated but
 504 live within composite particles, like quarks inside protons.
- 505 • **W, Z.** W^\pm and Z, are massive which explains their short-range. Given that
 506 the WI is the only interaction that can change the flavor of the interacting
 507 particles, the W boson is the responsible for the nuclear transmutation where
 508 a neutron is converted into a proton or vice versa with the involvement of an
 509 electron and a neutrino (see Figure 1.4c). The Z boson is the responsible for the
 510 neutral weak processes like neutrino elastic scattering where no electric charge
 511 but momentum transference is involved. WI gauge bosons carry isospin charge
 512 which makes interaction between them possible.

Interaction	Mediator	Electric charge (e)	Color charge	Weak Isospin	mass (GeV/c ²)
Electromagnetic	Photon (γ)	0	No	0	0
Strong	Gluon (g)	0	Yes -octet	No	0
Weak	W^\pm	± 1	No	± 1	80.385 ± 0.015
	Z	0	No	0	91.188 ± 0.002

Table 1.7: SM gauge bosons main features [9].

513

514 1.3 Electroweak unification and the Higgs 515 mechanism

516 Physicists dream of building a theory that contains all the interactions in one single
 517 interaction, i.e., showing that at some scale in energy all the four fundamental inter-

actions are unified and only one interaction emerges in a *Theory of everything*. The first sign of the feasibility of such unification came from success in the construction of the CED. Einstein spent years trying to reach that full unification, which by 1920 only involved electromagnetism and gravity, with no success; however, a new partial unification was achieved in the 1960's, when S.Glashow [22], A.Salam [23] and S.Weinberg [24] independently proposed that electromagnetic and weak interactions are two manifestations of a more general interaction called *electroweak interaction* (EWI). EWI was developed by following the useful prescription provided by QED and the gauge invariance principles.

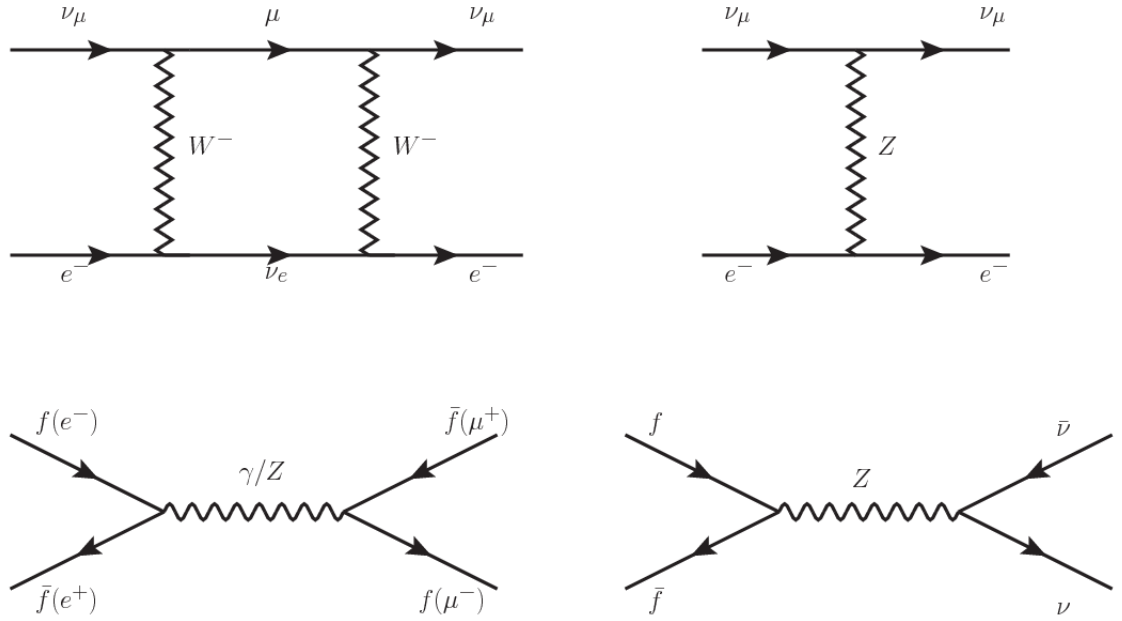


Figure 1.5: Top: $\nu_\mu - e^-$ scattering going through charged currents (left) and neutral currents (right). Bottom: neutral current processes for charged fermions (left) and involving neutrinos (right). While neutral current processes involving only charged fermions can proceed through EI or WI, those involving neutrinos can only proceed via WI.

The *classic* weak theory developed by Fermi, did not have the concept of the W boson but instead it was treated as a point interaction with the dimensionful constant G_F associated with it. It works really well at low energies very far off the W mass

shell. When going up in energy, the theory of weak interactions involving the W boson is capable of explaining the β -decay and in general the processes mediated by W^\pm bosons. However, there were some processes like the $\nu_\mu - e$ scattering which would require the exchange of two W bosons (see Figure 1.5 top diagrams) giving rise to divergent loop integrals and then non-finite predictions. The EWI theory, by including neutral currents involving fermions via the exchange of a neutral bosons Z, overcomes those divergences and the predictions become realistic.

Neutral weak interaction vertices conserve flavor in the same way as the electromagnetic vertices do, but additionally, the Z boson can couple to neutrinos which implies that processes involving charged fermions can proceed through EI or WI but processes involving neutrinos can proceed only through WI.

The prescription to build a gauge theory of the WI consists of proposing a free field Lagrangian density that includes the particles involved; next, by requesting invariance under global phase transformations first and generalizing to local phase transformations invariance later, the conserved currents are identified and interactions are generated by introducing gauge fields. Given that the goal is to include the EI and WI in a single theory, the group symmetry considered should be a combination of $SU(2)_L$ and $U(1)_{em}$, however the latter cannot be used directly because the EI treats left and right-handed particles indistinctly in contrast to the former. Fortunately, the weak hypercharge, which is a combination of the weak isospin and the electric charge (Eqn. 1.2) is suitable to be used since it is conserved by the EI and WI. Thus, the symmetry group to be considered is

$$G \equiv SU(2)_L \otimes U(1)_Y \quad (1.6)$$

The following treatment applies to any of the fermion generations, but for sim-

553 plicity the first generation of leptons will be considered [5, 6, 25, 26].

554 Given the first generation of leptons

$$\psi_1 = \begin{pmatrix} \nu_e \\ e^- \end{pmatrix}_L, \quad \psi_2 = \nu_{eR}, \quad \psi_3 = e_R^- \quad (1.7)$$

555 the charged fermionic currents are given by

$$J_\mu \equiv J_\mu^+ = \bar{\nu}_{eL} \gamma_\mu e_L, \quad J_\mu^\dagger \equiv J_\mu^- = \bar{e}_L \gamma_\mu \nu_{eL} \quad (1.8)$$

556 and the free Lagrangian is given by

$$\mathcal{L}_0 = \sum_{j=1}^3 i\bar{\psi}_j(x) \gamma^\mu \partial_\mu \psi_j(x). \quad (1.9)$$

557 Mass terms are included directly in the QED free Lagrangians since they preserve
 558 the invariance under the symmetry transformations involved which treat left and right
 559 handed particles similarly, however mass terms of the form

$$m_W^2 W_\mu^\dagger(x) W^\mu(x) + \frac{1}{2} m_Z^2 Z_\mu(x) Z^\mu(x) - m_e \bar{\psi}_e(x) \psi_e(x) \quad (1.10)$$

560 which represent the mass of W^\pm , Z and electrons, are not invariant under G trans-
 561 formations, therefore the gauge fields described by the EWI are in principle massless.

562 Experiments have shown that the EWI gauge fields are not massless [27–30];
 563 however, they have to acquire mass through a mechanism compatible with the gauge
 564 invariance; that mechanism is known as the *Higgs mechanism* and will be considered
 565 later in this Section. The global transformations in the combined symmetry group G
 566 can be written as

$$\begin{aligned}
\psi_1(x) &\xrightarrow{G} \psi'_1(x) \equiv U_Y U_L \psi_1(x), \\
\psi_2(x) &\xrightarrow{G} \psi'_2(x) \equiv U_Y \psi_2(x), \\
\psi_3(x) &\xrightarrow{G} \psi'_3(x) \equiv U_Y \psi_3(x)
\end{aligned} \tag{1.11}$$

567 where U_L represent the $SU(2)_L$ transformation acting only on the weak isospin dou-
 568 blet and U_Y represent the $U(1)_Y$ transformation acting on all the weak isospin mul-
 569 tiplets. Explicitly

$$U_L \equiv \exp\left(i \frac{\sigma_i}{2} \alpha^i\right), \quad U_Y \equiv \exp(i y_i \beta) \quad (i = 1, 2, 3) \tag{1.12}$$

570 with σ_i the Pauli matrices and y_i the weak hypercharges. In order to promote the
 571 transformations from global to local while keeping the invariance, it is required that
 572 $\alpha^i = \alpha^i(x)$, $\beta = \beta(x)$ and the replacement of the ordinary derivatives by the covariant
 573 derivatives

$$\begin{aligned}
D_\mu \psi_1(x) &\equiv \left[\partial_\mu + ig\sigma_i W_\mu^i(x)/2 + ig'y_1 B_\mu(x) \right] \psi_1(x) \\
D_\mu \psi_2(x) &\equiv \left[\partial_\mu + ig'y_2 B_\mu(x) \right] \psi_2(x) \\
D_\mu \psi_3(x) &\equiv \left[\partial_\mu + ig'y_3 B_\mu(x) \right] \psi_3(x)
\end{aligned} \tag{1.13}$$

574 introducing in this way four gauge fields, $W_\mu^i(x)$ and $B_\mu(x)$, in the process. The
 575 covariant derivatives (Eqn. 1.13) are required to transform in the same way as fermion
 576 fields $\psi_i(x)$ themselves, therefore, the gauge fields transform as:

$$\begin{aligned} B_\mu(x) &\xrightarrow{G} B'_\mu(x) \equiv B_\mu(x) - \frac{1}{g'} \partial_\mu \beta(x) \\ W_\mu^i(x) &\xrightarrow{G} W_\mu^{i\prime}(x) \equiv W_\mu^i(x) - \frac{i}{g} \partial_\mu \alpha_i(x) - \varepsilon_{ijk} \alpha_i(x) W_\mu^j(x). \end{aligned} \quad (1.14)$$

577 The G invariant version of the Lagrangian density 1.9 can be written as

$$\mathcal{L}_0 = \sum_{j=1}^3 i \bar{\psi}_j(x) \gamma^\mu D_\mu \psi_j(x) \quad (1.15)$$

578 where free massless fermion and gauge fields and fermion-gauge boson interactions
 579 are included. The EWI Lagrangian density must additionally include kinetic terms
 580 for the gauge fields (\mathcal{L}_G) which are built from the field strengths, according to

$$B_{\mu\nu}(x) \equiv \partial_\mu B_\nu - \partial_\nu B_\mu \quad (1.16)$$

$$W_{\mu\nu}^i(x) \equiv \partial_\mu W_\nu^i(x) - \partial_\nu W_\mu^i(x) - g \varepsilon^{ijk} W_\mu^j W_\nu^k \quad (1.17)$$

581 the last term in Eqn. 1.17 is added in order to hold the gauge invariance; therefore,

$$\mathcal{L}_G = -\frac{1}{4} B_{\mu\nu}(x) B^{\mu\nu}(x) - \frac{1}{4} W_{\mu\nu}^i(x) W_i^{\mu\nu}(x) \quad (1.18)$$

582 which contains not only the free gauge fields contributions, but also the gauge fields
 583 self-interactions and interactions among them.

584 The three weak isospin conserved currents resulting from the $SU(2)_L$ symmetry
 585 are given by

$$J_\mu^i(x) = \frac{1}{2} \bar{\psi}_1(x) \gamma_\mu \sigma^i \psi_1(x) \quad (1.19)$$

586 while the weak hypercharge conserved current resulting from the $U(1)_Y$ symmetry is
 587 given by

$$J_\mu^Y = \sum_{j=1}^3 \bar{\psi}_j(x) \gamma_\mu y_j \psi_j(x) \quad (1.20)$$

588 In order to evaluate the electroweak interactions modeled by an isos triplet field
 589 W_μ^i that couples to isospin currents J_μ^i with strength g and additionally the singlet
 590 field B_μ which couples to the weak hypercharge current J_μ^Y with strength $g'/2$. The
 591 interaction Lagrangian density to be considered is

$$\mathcal{L}_I = -g J^{i\mu}(x) W_\mu^i(x) - \frac{g'}{2} J^{Y\mu}(x) B_\mu(x) \quad (1.21)$$

592 Note that the weak isospin currents are not the same as the charged fermionic cur-
 593 rents that were used to describe the WI (Eqn. 1.8), since the weak isospin eigenstates
 594 are not the same as the mass eigenstates, but they are closely related

$$J_\mu = \frac{1}{2}(J_\mu^1 + iJ_\mu^2), \quad J_\mu^\dagger = \frac{1}{2}(J_\mu^1 - iJ_\mu^2). \quad (1.22)$$

595 The same happens with the gauge fields W_μ^i which are related to the mass eigen-
 596 states W^\pm by

$$W_\mu^+ = \frac{1}{\sqrt{2}}(W_\mu^1 - iW_\mu^2), \quad W_\mu^- = \frac{1}{\sqrt{2}}(W_\mu^1 + iW_\mu^2). \quad (1.23)$$

597 The fact that there are three weak isospin conserved currents is an indication that
 598 in addition to the charged fermionic currents, which couple charged to neutral leptons,
 599 there should be a neutral fermionic current that does not involve electric charge
 600 exchange; therefore, it couples neutral fermions or fermions of the same electric charge.
 601 The third weak isospin current contains a term that is similar to the electromagnetic

602 current (j_μ^{em}), indicating that there is a relation between them and resembling the
 603 Gell-Mann-Nishijima formula 1.2 adapted to electroweak interactions

$$Q = T_3 + \frac{Y_W}{2}. \quad (1.24)$$

604 Just as Q generates the $U(1)_{em}$ symmetry, the weak hypercharge generates the
 605 $U(1)_Y$ symmetry as said before. It is possible to write the relationship in terms of
 606 the currents as

$$j_\mu^{em} = J_\mu^3 + \frac{1}{2} J_\mu^Y. \quad (1.25)$$

607 The neutral gauge fields W_μ^3 and B_μ cannot be directly identified with the Z
 608 and the photon fields since the photon interacts similarly with left and right-handed
 609 fermions; however, they are related through a linear combination given by

$$\begin{aligned} A_\mu &= B_\mu \cos \theta_W + W_\mu^3 \sin \theta_W \\ Z_\mu &= -B_\mu \sin \theta_W + W_\mu^3 \cos \theta_W \end{aligned} \quad (1.26)$$

where θ_W is known as the *Weinberg angle*. The interaction Lagrangian is now given by

$$\begin{aligned} \mathcal{L}_I = -\frac{g}{\sqrt{2}}(J^\mu W_\mu^+ + J^{\mu\dagger} W_\mu^-) - &\left(g \sin \theta_W J_\mu^3 + g' \cos \theta_W \frac{J_\mu^Y}{2}\right) A^\mu \\ &- \left(g \cos \theta_W J_\mu^3 - g' \sin \theta_W \frac{J_\mu^Y}{2}\right) Z^\mu \end{aligned} \quad (1.27)$$

610 the first term is the weak charged current interaction, while the second term is the

611 electromagnetic interaction under the condition

$$g \sin \theta_W = g' \cos \theta_W = e, \quad \frac{g'}{g} = \tan \theta_W \quad (1.28)$$

612 contained in the Eqn.1.25; the third term is the neutral weak current.

613

614 Note that the neutral fields transformation given by the Eqn. 1.26 can be written
 615 in terms of the coupling constants g and g' as:

$$A_\mu = \frac{g' W_\mu^3 + g B_\mu}{\sqrt{g^2 + g'^2}}, \quad Z_\mu = \frac{g W_\mu^3 - g' B_\mu}{\sqrt{g^2 + g'^2}}. \quad (1.29)$$

616 So far, the Lagrangian density describing the non-massive EWI is:

$$\mathcal{L}_{nmEWI} = \mathcal{L}_0 + \mathcal{L}_G \quad (1.30)$$

617 where fermion and gauge fields have been considered massless because their regular
 618 mass terms are manifestly non invariant under G transformations; therefore, masses
 619 have to be generated in a gauge invariant way. The mechanism by which this goal is
 620 achieved is known as the *Higgs mechanism* and is closely connected to the concept of
 621 *spontaneous symmetry breaking*.

622 1.3.1 Spontaneous symmetry breaking (SSB)

623 Figure 1.6 left shows a steel nail (top) which is subject to an external force; the form
 624 of the potential energy is also shown (bottom).

625 Before reaching the critical force value, the system has rotational symmetry with
 626 respect to the nail axis; however, after the critical force value is reached the nail buck-

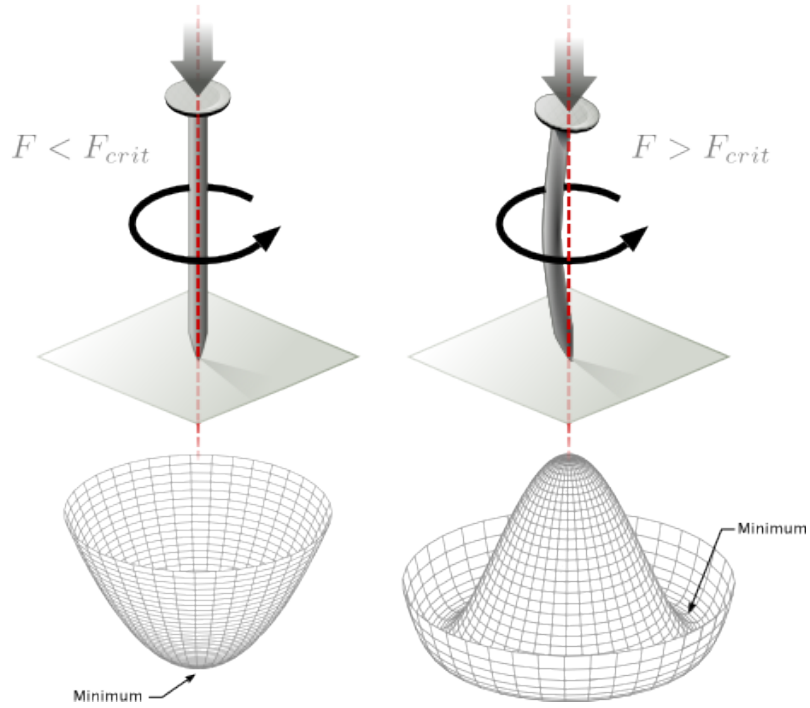


Figure 1.6: Spontaneous symmetry breaking mechanism. The steel nail, subject to an external force (top left), has rotational symmetry with respect to its axis. When the external force overcomes a critical value the nail buckles (top right) choosing a minimal energy state (ground state) and thus *breaking spontaneously the rotational symmetry*. The potential energy (bottom) changes but holds the rotational symmetry; however, an infinite number of asymmetric ground states are generated and circularly distributed in the bottom of the potential [31].

627 les (top right). The form of the potential energy (bottom right) changes appearing a
 628 set of infinity minima but preserving its rotational symmetry. Right before the nail
 629 buckles there is no indication of the direction the nail will bend because any of the
 630 directions are equivalent, but once the nail bends, choosing a direction, an arbitrary
 631 minimal energy state (ground state) is selected and it does not share the system's
 632 rotational symmetry. This mechanism for reaching an asymmetric ground state is
 633 known as *spontaneous symmetry breaking*.

634 The lesson from this analysis is that the way to introduce the SSB mechanism
 635 into a system is by adding the appropriate potential to it.

636 Figure 1.7 shows a plot of the potential $V(\phi)$ in the case of a scalar field ϕ

$$V(\phi) = \mu^2 \phi^\dagger \phi + \lambda (\phi^\dagger \phi)^2 \quad (1.31)$$

637 If $\mu^2 > 0$ the potential has only one minimum at $\phi = 0$ and describes a scalar field
 638 with mass μ . If $\mu^2 < 0$ the potential has a local maximum at $\phi = 0$ and two minima
 639 at $\phi = \pm\sqrt{-\mu^2/\lambda}$ which enables the SSB mechanism to work.

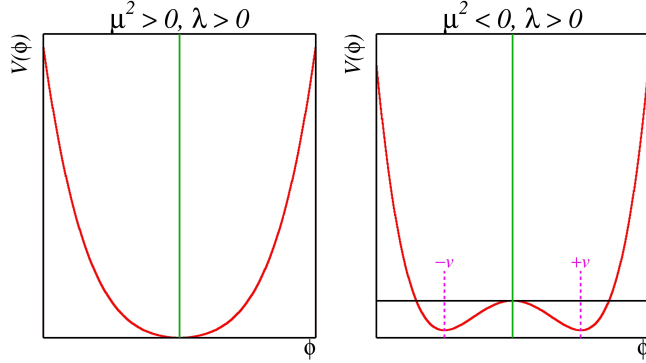


Figure 1.7: Shape of the potential $V(\phi)$ for $\lambda > 0$ and: $\mu^2 > 0$ (left) and $\mu^2 < 0$ (right). The case $\mu^2 < 0$ corresponds to the potential suitable for introducing the SSB mechanism by choosing one of the two ground states which are connected via reflection symmetry. [31].

640 In the case of a complex scalar field $\phi(x)$

$$\phi(x) = \frac{1}{\sqrt{2}}(\phi_1 + i\phi_2) \quad (1.32)$$

641 the Lagrangian (invariant under global $U(1)$ transformations) is given by

$$\mathcal{L} = (\partial_\mu \phi)^\dagger (\partial^\mu \phi) - V(\phi), \quad V(\phi) = \mu^2 \phi^\dagger \phi + \lambda (\phi^\dagger \phi)^2 \quad (1.33)$$

642 where an appropriate potential has been added in order to introduce the SSB.

643 As seen in Figure 1.8, the potential has now an infinite number of minima circularly
 644 distributed along the ξ -direction which makes possible the occurrence of the SSB by
 645 choosing an arbitrary ground state; for instance, $\xi = 0$, i.e. $\phi_1 = v, \phi_2 = 0$

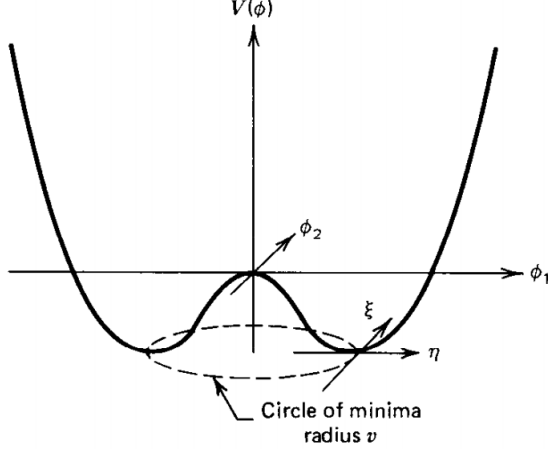


Figure 1.8: Potential for complex scalar field. There is a circle of minima of radius v along the ξ -direction [6].

$$\phi_0 = \frac{v}{\sqrt{2}} \exp(i\xi) \xrightarrow{\text{SSB}} \phi_0 = \frac{v}{\sqrt{2}} \quad (1.34)$$

646 As usual, excitations over the ground state are studied by making an expansion
647 about it; thus, the excitations can be parametrized as:

$$\phi(x) = \frac{1}{\sqrt{2}}(v + \eta(x) + i\xi(x)) \quad (1.35)$$

648 which when substituted into Eqn. 1.33 produces a Lagrangian in terms of the new
649 fields η and ξ

$$\mathcal{L}' = \frac{1}{2}(\partial_\mu \xi)^2 + \frac{1}{2}(\partial_\mu \eta)^2 + \mu^2 \eta^2 - V(\phi_0) - \lambda v \eta (\eta^2 + \xi^2) - \frac{\lambda}{4}(\eta^2 + \xi^2)^2 \quad (1.36)$$

650 where the last two terms represent the interactions and self-interaction between the
651 two fields η and ξ . The particular feature of the SSB mechanism is revealed when
652 looking to the first three terms of \mathcal{L}' . Before the SSB, only the massless ϕ field is

653 present in the system; after the SSB there are two fields of which the η -field has
 654 acquired mass $m_\eta = \sqrt{-2\mu^2}$ while the ξ -field is still massless (see Figure 1.9).

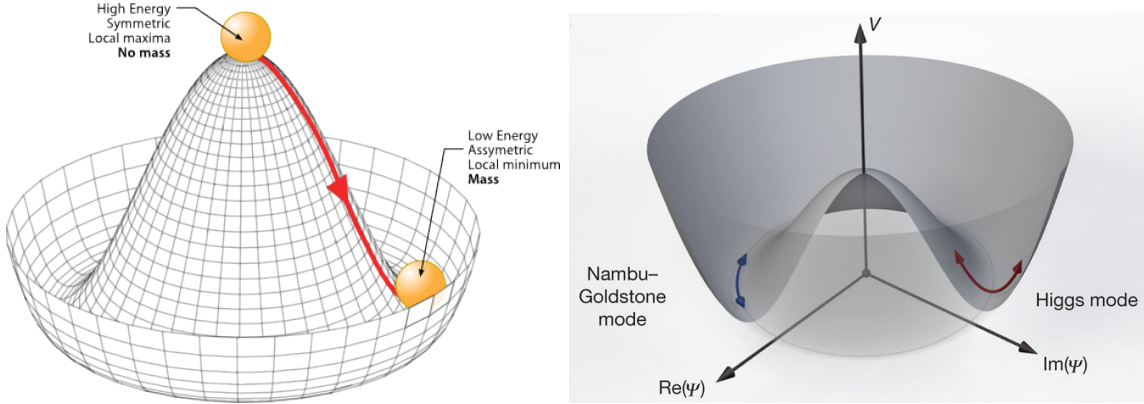


Figure 1.9: SSB mechanism for a complex scalar field [31, 32].

655 Thus, the SSB mechanism serves as a method to generate mass but as a side ef-
 656 fect a massless field is introduced in the system. This fact is known as the Goldstone
 657 theorem and states that a massless scalar field appears in the system for each con-
 658 tinuous symmetry spontaneously broken. Another version of the Goldstone theorem
 659 states that “if a Lagrangian is invariant under a continuous symmetry group G , but
 660 the vacuum is only invariant under a subgroup $H \subset G$, then there must exist as many
 661 massless spin-0 particles (Nambu-Goldstone bosons) as broken generators.” [26] The
 662 Nambu-Goldstone boson can be understood considering that the potential in the ξ -
 663 direction is flat so excitations in that direction are not energy consuming and thus
 664 represent a massless state.

665 1.3.2 Higgs mechanism

666 When the SSB mechanism is introduced in the formulation of the EWI in an attempt
 667 to generate the mass of the so far massless gauge bosons and fermions, an interesting
 668 effect is revealed. In order to keep the G symmetry group invariance and generate

669 the mass of the EW gauge bosons, a G invariant Lagrangian density (\mathcal{L}_S) has to be
 670 added to the non massive EWI Lagrangian (Eqn. 1.30)

$$\mathcal{L}_S = (D_\mu \phi)^\dagger (D^\mu \phi) - \mu^2 \phi^\dagger \phi - \lambda (\phi^\dagger \phi)^2, \quad \lambda > 0, \mu^2 < 0 \quad (1.37)$$

$$D_\mu \phi = \left(i\partial_\mu - g \frac{\sigma_i}{2} W_\mu^i - g' \frac{Y}{2} B_\mu \right) \phi \quad (1.38)$$

671 ϕ has to be an isospin doublet of complex scalar fields so it preserves the G invariance;
 672 thus ϕ can be defined as:

$$\phi = \begin{pmatrix} \phi^+ \\ \phi^0 \end{pmatrix} \equiv \frac{1}{\sqrt{2}} \begin{pmatrix} \phi_1 + i\phi_2 \\ \phi_3 + i\phi_4 \end{pmatrix}. \quad (1.39)$$

673 The minima of the potential are defined by

$$\phi^\dagger \phi = \frac{1}{2} (\phi_1^2 + \phi_2^2 + \phi_3^2 + \phi_4^2) = -\frac{\mu^2}{2\lambda}. \quad (1.40)$$

674 The choice of the ground state is critical. By choosing a ground state, invariant
 675 under $U(1)_{em}$ gauge symmetry, the photon will remain massless and the W^\pm and Z
 676 bosons masses will be generated which is exactly what is needed. In that sense, the
 677 best choice corresponds to a weak isospin doublet with $T_3 = -1/2$, $Y_W = 1$ and $Q = 0$
 678 which defines a ground state with $\phi_1 = \phi_2 = \phi_4$ and $\phi_3 = v$:

$$\phi_0 \equiv \frac{1}{\sqrt{2}} \begin{pmatrix} 0 \\ v \end{pmatrix}, \quad v^2 \equiv -\frac{\mu^2}{\lambda}. \quad (1.41)$$

679 where the vacuum expectation value v is fixed by the Fermi coupling G_F according
 680 to $v = (\sqrt{2}G_F)^{1/2} \approx 246$ GeV.

681 The G symmetry has been broken and three Nambu-Goldstone bosons will appear.

682 The next step is to expand ϕ about the chosen ground state as:

$$\phi(x) = \frac{1}{\sqrt{2}} \exp\left(\frac{i}{v} \sigma_i \theta^i(x)\right) \begin{pmatrix} 0 \\ v + H(x) \end{pmatrix} \approx \frac{1}{\sqrt{2}} \begin{pmatrix} \theta_1(x) + i\theta_2(x) \\ v + H(x) - i\theta_3(x) \end{pmatrix} \quad (1.42)$$

683 to describe fluctuations from the ground state ϕ_0 . The fields $\theta_i(x)$ represent the
 684 Nambu-Goldstone bosons while $H(x)$ is known as *Higgs field*. The fundamental fea-
 685 ture of the parametrization used is that the dependence on the $\theta_i(x)$ fields is factored
 686 out in a global phase that can be eliminated by taking the physical *unitary gauge*
 687 $\theta_i(x) = 0$. Therefore the expansion about the ground state is given by:

$$\phi(x) \frac{1}{\sqrt{2}} \begin{pmatrix} 0 \\ v + H(x) \end{pmatrix} \quad (1.43)$$

688 which when substituted into \mathcal{L}_S (Eqn. 1.37) results in a Lagrangian containing the
 689 now massive three gauge bosons W^\pm, Z , one massless gauge boson (photon) and
 690 the new Higgs field (H). The three degrees of freedom corresponding to the Nambu-
 691 Goldstone bosons are now integrated into the massive gauge bosons as their lon-
 692 gitudinal polarizations which were not available when they were massless particles.
 693 The effect by which vector boson fields acquire mass after an spontaneous symmetry
 694 breaking, but without an explicit gauge invariance breaking is known as the *Higgs*
 695 *mechanism*.

696 The mechanism was proposed by three independent groups: F.Englert and R.Brout
 697 in August 1964 [33], P.Higgs in October 1964 [34] and G.Guralnik, C.Hagen and
 698 T.Kibble in November 1964 [35]; however, its importance was not realized until
 699 S.Glashow [22], A.Salam [23] and S.Weinberg [24], independently, proposed that elec-
 700 tromagnetic and weak interactions are two manifestations of a more general interac-
 701 tion called *electroweak interaction* in 1967.

702 **1.3.3 Masses of the gauge bosons**

703 The masses of the gauge bosons are extracted by evaluating the kinetic part of La-
 704 grangian \mathcal{L}_S in the ground state (known also as the vacuum expectation value), i.e.,

$$\left| \left(\partial_\mu - ig \frac{\sigma_i}{2} W_\mu^i - i \frac{g'}{2} B_\mu \right) \phi_0 \right|^2 = \left(\frac{1}{2} v g \right)^2 W_\mu^+ W^{-\mu} + \frac{1}{8} v^2 (W_\mu^3, B_\mu) \begin{pmatrix} g^2 & -gg' \\ -gg' & g'^2 \end{pmatrix} \begin{pmatrix} W^{3\mu} \\ B^\mu \end{pmatrix} \quad (1.44)$$

705 comparing with the typical mass term for a charged boson $M_W^2 W^+ W^-$

$$M_W = \frac{1}{2} v g. \quad (1.45)$$

The second term in the right side of the Eqn.1.44 comprises the masses of the neutral bosons, but it needs to be written in terms of the gauge fields Z_μ and A_μ in order to be compared to the typical mass terms for neutral bosons, therefore using Eqn. 1.29

$$\begin{aligned} \frac{1}{8} v^2 [g^2 (W_\mu^3)^2 - 2gg' W_\mu^3 B^\mu + g'^2 B_\mu^2] &= \frac{1}{8} v^2 [g W_\mu^3 - g' B_\mu]^2 + 0[g' W_\mu^3 + g B_\mu]^2 \quad (1.46) \\ &= \frac{1}{8} v^2 [\sqrt{g^2 + g'^2} Z_\mu]^2 + 0[\sqrt{g^2 + g'^2} A_\mu]^2 \end{aligned}$$

706 and then

$$M_Z = \frac{1}{2} v \sqrt{g^2 + g'^2}, \quad M_A = 0 \quad (1.47)$$

707 **1.3.4 Masses of the fermions**

708 The lepton mass terms can be generated by introducing a gauge invariant Lagrangian
 709 term describing the Yukawa coupling between the lepton field and the Higgs field

$$\mathcal{L}_{Yl} = -G_l \left[(\bar{\nu}_l, \bar{l})_L \begin{pmatrix} \phi^+ \\ \phi^0 \end{pmatrix} l_R + \bar{l}_R (\phi^-, \bar{\phi}^0) \begin{pmatrix} \nu_l \\ l \end{pmatrix} \right], \quad l = e, \mu, \tau. \quad (1.48)$$

710 After the SSB and replacing the usual field expansion about the ground state
 711 (Eqn.1.41) into \mathcal{L}_{Yl} , the mass term arises

$$\mathcal{L}_{Yl} = -m_l (\bar{l}_L l_R + \bar{l}_R l_L) - \frac{m_l}{v} (\bar{l}_L l_R + \bar{l}_R l_L) H = -m_l \bar{l} l \left(1 + \frac{H}{v} \right) \quad (1.49)$$

712

$$m_l = \frac{G_l}{\sqrt{2}} v \quad (1.50)$$

713 where the additional term represents the lepton-Higgs interaction. The quark masses
 714 are generated in a similar way as lepton masses but for the upper member of the
 715 quark doublet a different Higgs doublet is needed:

$$\phi_c = -i\sigma_2 \phi^* = \begin{pmatrix} -\bar{\phi}^0 \\ \phi^- \end{pmatrix}. \quad (1.51)$$

716 Additionally, given that the quark isospin doublets are not constructed in terms
 717 of the mass eigenstates but in terms of the flavor eigenstates, as shown in Table 1.5,
 718 the coupling parameters will be related to the CKM matrix elements; thus, the quark
 719 Lagrangian is given by:

$$\mathcal{L}_{Yq} = -G_d^{i,j} (\bar{u}_i, \bar{d}'_i)_L \begin{pmatrix} \phi^+ \\ \phi^0 \end{pmatrix} d_{jR} - G_u^{i,j} (\bar{u}_i, \bar{d}'_i)_L \begin{pmatrix} -\bar{\phi}^0 \\ \phi^- \end{pmatrix} u_{jR} + h.c. \quad (1.52)$$

720 with $i, j = 1, 2, 3$. After SSB and expansion about the ground state, the diagonal form

721 of \mathcal{L}_{Yq} is:

$$\mathcal{L}_{Yq} = -m_d^i \bar{d}_i d_i \left(1 + \frac{H}{v}\right) - m_u^i \bar{u}_i u_i \left(1 + \frac{H}{v}\right) \quad (1.53)$$

722 Fermion masses depend on arbitrary couplings G_l and $G_{u,d}$ and are not predicted
723 by the theory.

724 **1.3.5 The Higgs field**

725 After the characterization of the fermions and gauge bosons as well as their interac-
726 tions, it is necessary to characterize the Higgs field itself. The Lagrangian \mathcal{L}_S in Eqn.
727 1.37 written in terms of the gauge bosons is given by

$$\mathcal{L}_S = \frac{1}{4} \lambda v^4 + \mathcal{L}_H + \mathcal{L}_{HV} \quad (1.54)$$

728

$$\mathcal{L}_H = \frac{1}{2} \partial_\mu H \partial^\mu H - \frac{1}{2} m_H^2 H^2 - \frac{1}{2v} m_H^2 H^3 - \frac{1}{8v^2} m_H^2 H^4 \quad (1.55)$$

729

$$\mathcal{L}_{HV} = m_H^2 W_\mu^+ W^{\mu-} \left(1 + \frac{2}{v} H + \frac{2}{v^2} H^2\right) + \frac{1}{2} m_Z^2 Z_\mu Z^\mu \left(1 + \frac{2}{v} H + \frac{2}{v^2} H^2\right) \quad (1.56)$$

730 The mass of the Higgs boson is deduced as usual from the mass term in the Lagrangian
731 resulting in:

$$m_H = \sqrt{-2\mu^2} = \sqrt{2\lambda}v \quad (1.57)$$

732 however, it is not predicted by the theory either. The experimental measurement of
733 the Higgs boson mass have been performed by the *Compact Muon Solenoid (CMS)*
734 experiment and the *A Toroidal LHC Appartus (ATLAS)* experiments at the *Large
735 Hadron Collider (LHC)*, [36–38], and is presented in Table 1.8.

Property	Value
Electric charge	0
Color charge	0
Spin	0
Weak isospin	-1/2
Weak hypercharge	1
Parity	1
Mass (GeV/c ²)	125.09±0.21 (stat.)±0.11 (syst.)

Table 1.8: Higgs boson properties. Higgs mass is not predicted by the theory and the value here corresponds to the experimental measurement.

737 1.3.6 Production of Higgs bosons at LHC

738 At the LHC, Higgs bosons are produced as a result of the collision of two counter-
739 rotating protons beams. A detailed description of the LHC machine will be presented
in chapter 2.

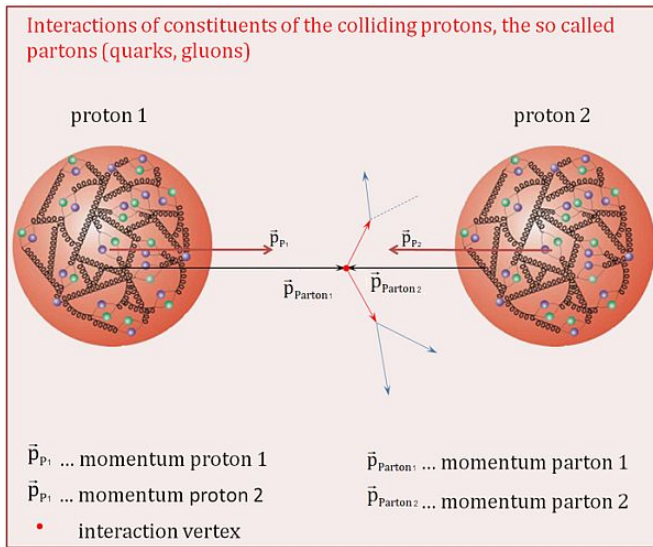


Figure 1.10: Proton-proton collision. Protons are composed of 3 valence quarks, a sea of quarks and gluons; therefore in a proton-proton collision, quarks and gluons are those who collide. [39].

740

741 Protons are composed of quarks and these quarks are bound by gluons; however,
742 what is commonly called the quark content of the proton makes reference to the
743 valence quarks. In fact, a proton is not just a rigid entity with three balls in it all
744 tied up with springs, but the gluons exchanged by the valence quarks tend to split

745 spontaneously into quark-antiquark pairs or more gluons, creating *sea of quarks and*
 746 *gluons* as represented in Figure 1.10.

747 In a proton-proton (pp) collision, the proton's constituents, quarks and gluons, are
 748 those that collide. The pp cross section depends on the momentum of the colliding
 749 particles, reason for which it is needed to know how the momentum is distributed
 750 inside the proton. Quarks and gluons are known as partons, hence, the functions
 751 that describe how the proton momentum is distributed among partons inside it are
 752 called *parton distribution functions (PDFs)*; PDFs are determined from experimental
 753 data obtained in experiments where the internal structure of hadrons is tested, and
 754 depend on the momentum transfer Q and the fraction of momentum x carried by an
 755 specific parton. Figure 1.11 shows the proton PDFs ($xf(x, Q^2)$) for two values of Q .

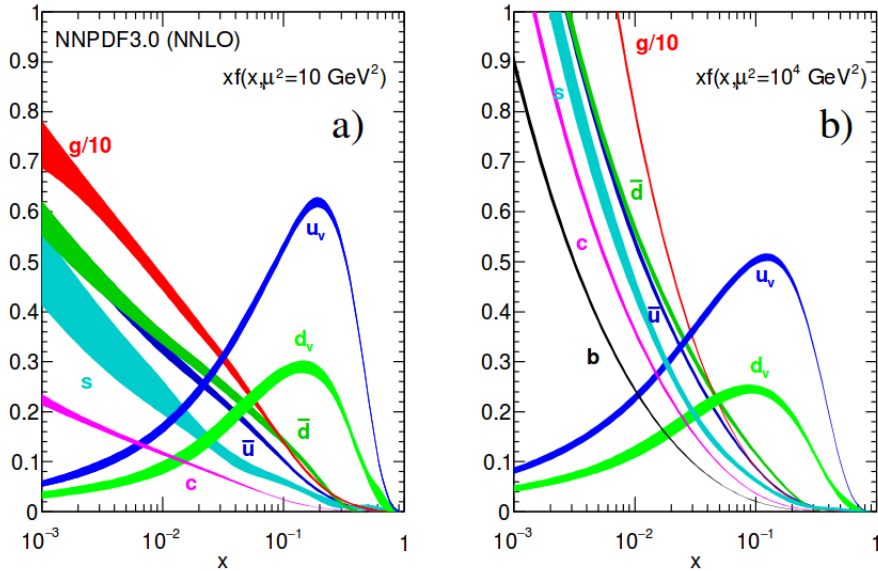


Figure 1.11: Proton PDFs for two values of Q^2 : left. $\mu^2 = Q^2 = 10 \text{ GeV}^2$, right. $\mu^2 = Q^2 = 10^4 \text{ GeV}^2$. u_v and d_v correspond to the u and d valence quarks, $s, c, b, \bar{u}, \bar{d}$ correspond to sea quarks, and g corresponds to gluons. Note that gluons carry a high fraction of the proton's momentum. [9]

756 In physics, a common approach to study complex systems consists of starting
 757 with a simpler version of them, for which a well known description is available, and

adding an additional *perturbation* which represents a small deviation from the known behavior. If the perturbation is small enough, the physical quantities associated with the perturbed system are expressed as a series of corrections to those of the simpler system. The perturbation series corresponds to an expansion in power series of a small parameter, therefore, the more terms are considered in the series (the higher order in the perturbation series), the more precise is the description of the complex system. If the perturbation does not get progressively smaller, the strategy cannot be applied and new methods have to be employed.

High energy systems, like the Higgs production at LHC explored in this thesis, usually can be treated perturbatively with the expansion made in terms of the coupling constants. The overview presented here will be oriented specifically to the Higgs boson production mechanisms in pp collisions at LHC.

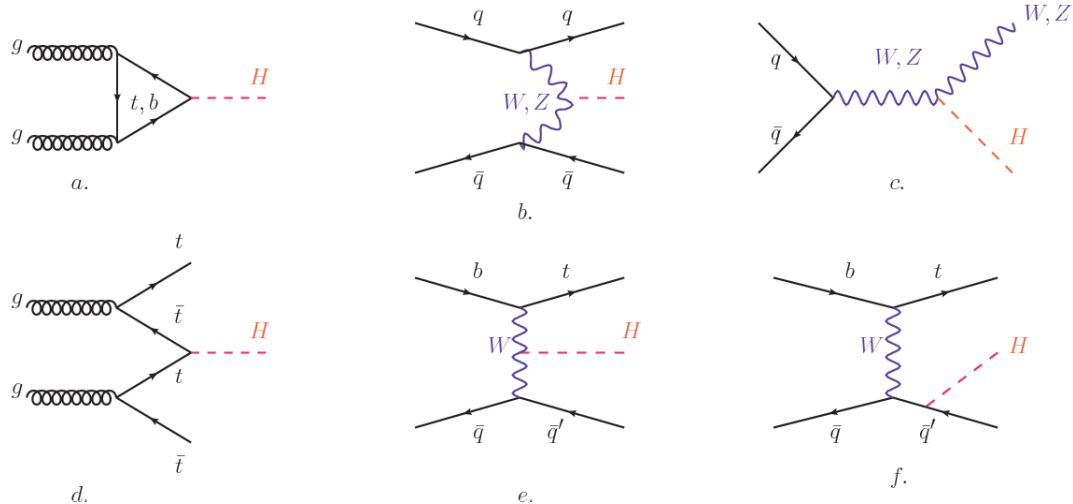


Figure 1.12: Main Higgs boson production mechanism Feynman diagrams. a. gluon-gluon fusion, b. vector boson fusion (VBF), c. Higgs-strahlung, d. Associated production with a top or bottom quark pair, e-f. associated production with a single top quark.

Figure 1.12 shows the Feynman diagrams for the leading order (first order) Higgs production processes at LHC; note that in these diagrams the incoming particles are not the protons themselves but the partons from the protons that actually participate

in the interaction, hence, theorists typically calculate the cross section for the parton interaction, and then convolute that cross section with the information from the PDFs to get a production cross section that is actually measured in experiments. The cross section for Higgs production as a function of the center of mass-energy (\sqrt{s}) for pp collisions is showed in Figure 1.13 left. The tags NLO (next to leading order), NNLO (next to next to leading order) and N3LO (next to next to next to leading order) make reference to the order at which the perturbation series have been considered while the tags QCD and EW correspond to the strong and electroweak coupling constants respectively.

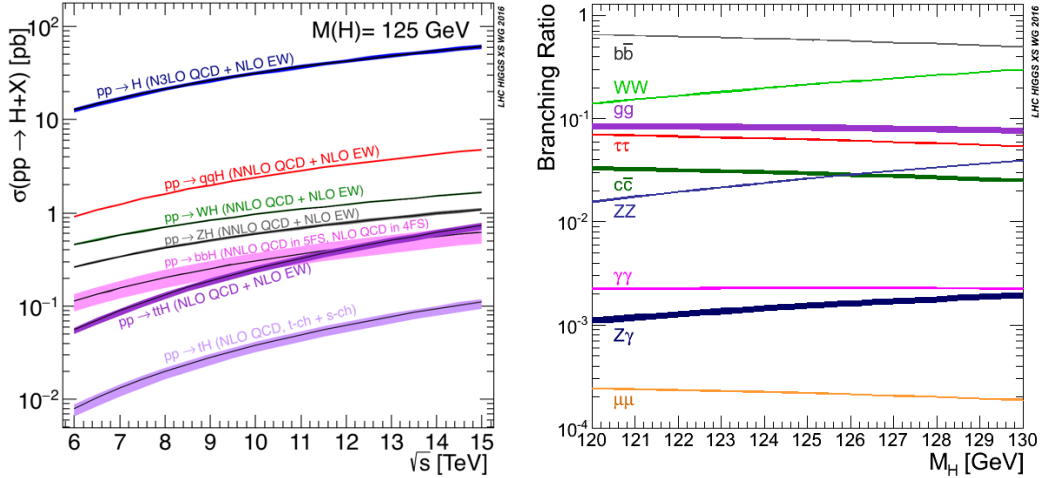


Figure 1.13: Higgs boson production cross sections (left) and decay branching ratios (right) for the main mechanisms. The VBF is indicated as qqH [40].

The main production mechanism is the gluon fusion (Figure 1.12a and $pp \rightarrow H$ in Figure 1.13) given that gluons carry the highest fraction of momentum of the protons in pp colliders (as shown in Figure ??). Since the Higgs boson does not couple to gluons, the mechanism proceeds through the exchange of a virtual top-quark loop. Note that in this process the Higgs boson is produced alone, turning out to be problematic for some Higgs decays, because such absence of anything produced in

788 association with the Higgs represent a trouble for triggering, however, this mechanism
 789 is experimentally clean when combined with the two-photon or the four-lepton decay
 790 channels (see Section 1.3.7).

791 Vector boson fusion (Figure 1.12b and $pp \rightarrow qqH$ in Figure 1.13) has the second
 792 largest production cross section. The scattering of two fermions is mediated by a weak
 793 gauge boson which later emits a Higgs boson. In the final state, the two fermions tend
 794 to be located in the central region of the detector; this kind of features are generally
 795 used as a signature when analyzing the datasets provided by the experiments⁷.

796 In the Higgs-strahlung mechanism (Figure 1.12c and $pp \rightarrow WH, pp \rightarrow ZH$ in
 797 Figure 1.13) two fermions annihilate to form a weak gauge boson. If the initial
 798 fermions have enough energy, the emergent boson might emit a Higgs boson.

799 The associated production with a top or bottom quark pair and the associated
 800 production with a single top quark (Figure 1.12d-f and $pp \rightarrow bbH, pp \rightarrow t\bar{t}H, pp \rightarrow tH$
 801 in Figure 1.13) have a smaller cross section than the main three mechanisms above,
 802 but they provide a good opportunity to test the Higgs-top coupling. The analysis
 803 reported in this thesis is developed using these production mechanisms. A detailed
 804 description of the tH mechanism will be given in Section 1.5.

805 1.3.7 Higgs boson decay channels

806 When a particle can decay through several modes, also known as channels, the prob-
 807 ability of decaying through a given channel is quantified by the *branching ratio (BR)*
 808 of the decay channel; thus, the BR is defined as the ratio of number of decays go-
 809 ing through that given channel to the total number of decays. In regard to the
 810 Higgs boson decay, the BR can be predicted with accuracy once the Higgs mass is
 811 known [41, 42]. In Figure 1.13 right, a plot of the BR as a function of the Higgs mass

⁷ More details about how to identify events of interest in this analysis will be given in chapter 6.

812 is presented; the largest predicted BR corresponds to the $b\bar{b}$ pair decay channel (see
 813 Table 1.9) given that it is the heaviest particle pair whose on-shell⁸ production is
 814 kinematically allowed in the decay.

Decay channel	Branching ratio	Rel. uncertainty
$H \rightarrow b\bar{b}$	5.84×10^{-1}	+3.2% – 3.3%
$H \rightarrow W^+W^-$	2.14×10^{-1}	+4.3% – 4.2%
$H \rightarrow \tau^+\tau^-$	6.27×10^{-2}	+5.7% – 5.7%
$H \rightarrow ZZ$	2.62×10^{-2}	+4.3% – 4.1%
$H \rightarrow \gamma\gamma$	2.27×10^{-3}	+5.0% – 4.9%
$H \rightarrow Z\gamma$	1.53×10^{-3}	+9.0% – 8.9%
$H \rightarrow \mu^+\mu^-$	2.18×10^{-4}	+6.0% – 5.9%

Table 1.9: Predicted branching ratios and the relative uncertainty for some decay channels of a SM Higgs boson with $m_H = 125\text{GeV}/c^2$ [9]; the uncertainties are driven by theoretical uncertainties for the different Higgs boson partial widths and by parametric uncertainties associated to the strong coupling and the masses of the quarks which are the input parameters. Further details on these calculations can be found in Reference [43]

815

816 Decays to other lepton and quark pairs, like electron, strange, up, and down
 817 quark pairs not listed in the table, are also possible but their likelihood is too small
 818 to measure since they are very lightweight, hence, their interaction with the Higgs
 819 boson is very weak. On other hand, the decay to top quark pairs is heavily suppressed
 820 due to the top quark mass ($\approx 173\text{ GeV}/c^2$).

821 Decays to gluons proceed indirectly through a virtual top quark loop while the
 822 decays to photons proceed through a virtual W boson loop, therefore, their branching
 823 ratio is smaller compared to direct interaction decays. Same is true for the decay to
 824 a photon and a Z boson.

⁸ In general, on-shell or real particles are those which satisfy the energy-momentum relation ($E^2 - |\vec{p}|^2 c^2 = m^2 c^4$); off-shell or virtual particles does not satisfy it which is possible under the uncertainty principle of quantum mechanics. Usually, virtual particles correspond to internal propagators in Feynman diagrams.

825 In the case of decays to pairs of W and Z bosons, the decay proceed with one of
 826 the bosons being on-shell and the other being off-shell. The likelihood of the process
 827 diminish depending on how far off-shell are the virtual particles involved, hence, the
 828 branching ratio for W boson pairs is bigger than for Z boson pairs since Z boson mass
 829 is bigger than W boson mass.

830 Note that the decay to a pair of virtual top quarks is possible, but the probability
 831 is way too small.

832 **1.4 Experimental status of the anomalous
 833 Higgs-fermion coupling**

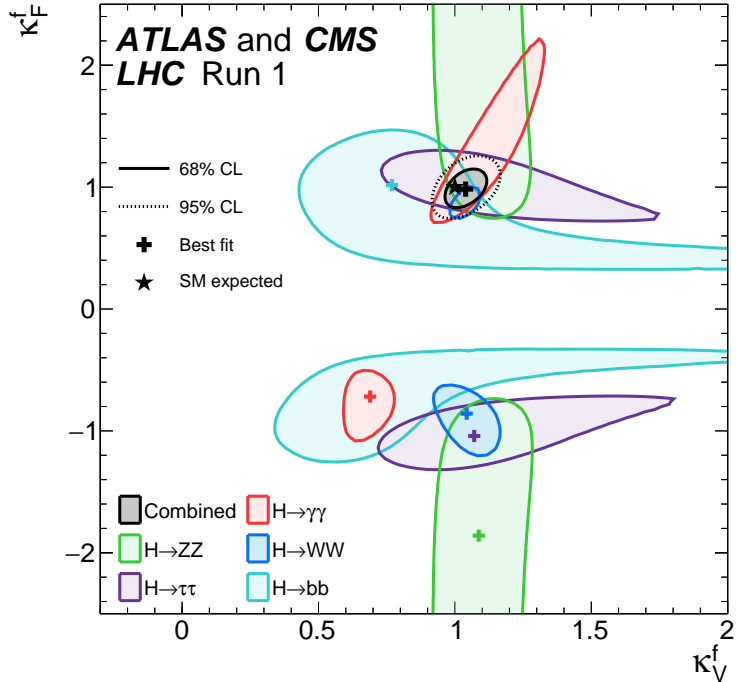


Figure 1.14: Combination of the ATLAS and CMS fits for coupling modifiers $\kappa_t - \kappa_V$; also shown the individual decay channels combination and their global combination. No assumptions have been made on the sign of the coupling modifiers [44].

834 ATLAS and CMS have performed analyses of the anomalous Higgs-fermion cou-
 835 pling by making likelihood scans for the two coupling modifiers, κ_f and κ_V , under
 836 the assumption that $\kappa_Z = \kappa_W \equiv \kappa_V$ and $\kappa_t = \kappa_\tau = \kappa_b \equiv \kappa_f$. Figure 1.14 shows the
 837 result of the combination of ATLAS and CMS fits; also the individual decay channels
 838 combination and the global combination results are shown. Note that from this plot
 839 there is limited information on the sign of the coupling since the only information
 840 available about the sign of the coupling comes from decays rather than production.

841 While all the channels are compatible for positive values of the modifiers, for
 842 negative values of κ_f there is no compatibility. The best fit for individual channels
 843 is compatible with negative values of κ_f except for the $H \rightarrow bb$ channel. The best
 844 fit for the combination yields $\kappa_f \geq 0$, in contrast to the yields from the individual
 845 channels; the reason of this yield resides in the $H \rightarrow \gamma\gamma$ coupling. $H \rightarrow \gamma\gamma$ decay
 846 proceeds through a loop of either top quarks or W bosons, hence, this channel is
 847 sensitive to κ_t thanks to the interference of these two amplitude contributions; under
 848 the assumption that no beyond SM particles take part in the loops, a flipped sign
 849 of κ_t will increase the $H \rightarrow \gamma\gamma$ branching fraction by a factor of ~ 2.4 which is not
 850 supported by measurements; thus, this large asymmetry between the positive and
 851 negative coupling ratios in the $H \rightarrow \gamma\gamma$ channel drives the yield of the global fit and
 852 would mean that the anomalous H-t coupling is excluded as stated in Reference [44],
 853 but there is a caveat, this exclusion holds only if no new particles contribute to the
 854 loop in the main diagram for that decay.

855 Although the $H \rightarrow bb$ channel is expected to be the most sensitive channel and
 856 its best fit value of κ_t is positive, and then the global fit yield is still supported,
 857 the contributions from all the other decay channels, small compared to the $H \rightarrow bb$,
 858 indicate that the anomalous H-t coupling cannot be excluded completely, motivating
 859 to look at tH processes which can help with both, the limited information on the sign

860 of the H-t coupling and the access to information from the Higgs boson production
 861 rather than from its decays.

862 It will be shown in Section 1.5 that the same interference effect enhance the
 863 tH production rate and could reveal evidence of direct production of heavy new par-
 864 ticles as predicted in composite and little Higgs models [45], or new physics related
 865 to Higgs boson mediated flavor changing neutral currents [46] as well as probes the
 866 CP-violating phase of the H-t coupling [47, 48].

867 **1.5 Associated production of a Higgs boson and a 868 single top quark**

869 The production of Higgs boson in association with a top quark has been extensively
 870 studied [47, 49–52]. While measurements of the main Higgs production mechanisms
 871 rates are sensitive to the strength of the Higgs coupling to W boson or top quark,
 872 they are not sensitive to the relative sign between the two couplings. In this thesis,
 873 the Higgs boson production mechanism explored is the associated production with a
 874 single top quark (tH) which offers sensitivity to the relative sign of the Higgs couplings
 875 to W boson and to top quark. The description given here is based on Reference [51]

A process where two incoming particles interact and produce a final state with two particles can proceed in three called channels (see, for instance, Figure 1.15 omitting the red line). The t-channel represents processes where an intermediate particle is emitted by one of the incoming particles and absorbed by the other. The s-channel represents processes where the two incoming particles merge into an intermediate particle which eventually will split into the particles in the final state. The third channel, u-channel, is similar to the t-channel but the two outgoing particles interchange their

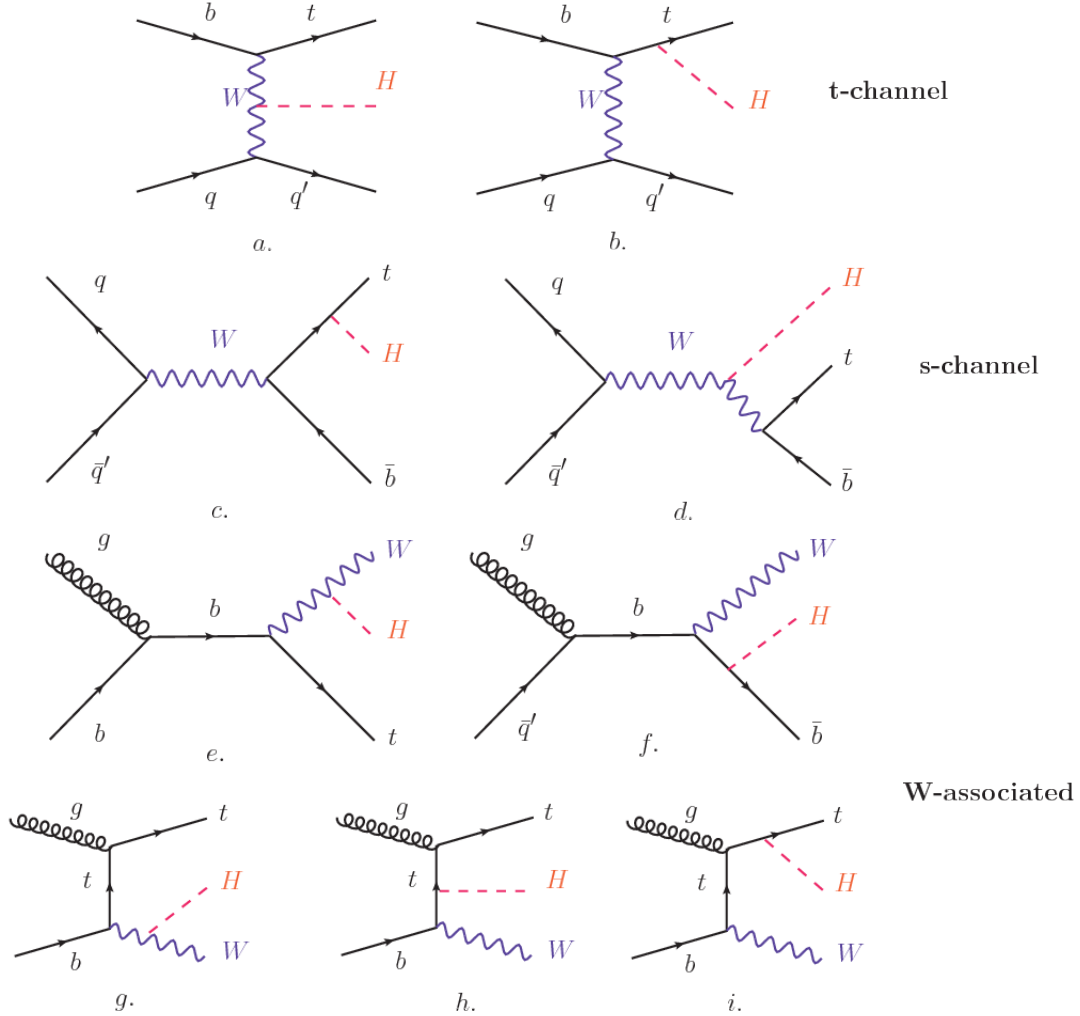


Figure 1.15: Associated Higgs boson production with a top quark mechanism Feynman diagrams. a.,b. t-channel (tHq), c.,d. s-channel (tHb), e-i. W-associated.

roles. These three channels are connected to the so-called Mandelstam variables

$$s = (p_1 + p_2)^2 = (p'_1 + p'_2)^2 \rightarrow \text{square of the center mass-energy.} \quad (1.58)$$

$$t = (p_1 - p'_1)^2 = (p'_2 - p_2)^2 \rightarrow \text{square of the four-momentum transfer.} \quad (1.59)$$

$$u = (p_1 - p'_2)^2 = (p'_1 - p_2)^2 \rightarrow \text{square of the crossed four-momentum transfer.} \quad (1.60)$$

$$s + t + u = m_1^2 + m_2^2 + m'_1^2 + m'_2^2 \quad (1.61)$$

which relate the momentum, energy and the angles of the incoming and outgoing particles in an scattering process of two particles to two particles. The importance of the Mandelstam variables reside in that they form a minimum set of variables needed to describe the kinematics of this scattering process; they are Lorentz invariant which makes them very useful when doing calculations.

The tH production, where Higgs boson can be radiated either from the top quark or from the W boson, is represented by the leading order Feynman diagrams in Figure 1.15. The cross section for the tH process is calculated, as usual, summing over the contributions from the different Feynman diagrams; therefore it depends on the interference between the contributions. In the SM, the interference for t-channel (tHq process) and W-associated (tHW process) production is destructive [49] resulting in the small cross sections presented in Table 1.10.

tH production channel	Cross section (fb)
t-channel ($pp \rightarrow tHq$)	$70.79^{+2.99}_{-4.80}$
W-associated ($pp \rightarrow tHW$)	$15.61^{+0.83}_{-1.04}$
s-channel($pp \rightarrow tHb$)	$2.87^{+0.09}_{-0.08}$

Table 1.10: Predicted SM cross sections for tH production at $\sqrt{s} = 13$ TeV [53, 54].

888

The s-channel contribution can be neglected. It will be shown that a deviation from the SM destructive interference would result in an enhancement of the tH cross section compared to that in SM, which could be used to get information about the sign of the Higgs-top coupling [51, 52]. In order to describe tH production processes, Feynman diagram 1.15b will be considered; there, the W boson is radiated by a quark in the proton and eventually it will interact with the b quark. In the high energy regime, the effective W approximation [55] is used to describe the process as the

896 emission of an approximately on-shell W and its hard scattering with the b quark;
 897 i.e. $Wb \rightarrow th$. The scattering amplitude for the process is given by

$$\mathcal{A} = \frac{g}{\sqrt{2}} \left[(\kappa_t - \kappa_V) \frac{m_t \sqrt{s}}{m_W v} A \left(\frac{t}{s}, \varphi; \xi_t, \xi_b \right) + \left(\kappa_V \frac{2m_W s}{v t} + (2\kappa_t - \kappa_V) \frac{m_t^2}{m_W v} \right) B \left(\frac{t}{s}, \varphi; \xi_t, \xi_b \right) \right], \quad (1.62)$$

898 where $\kappa_V \equiv g_{HVV}/g_{HVV}^{SM}$ and $\kappa_t \equiv g_{Ht}/g_{Ht}^{SM} = y_t/y_t^{SM}$ are scaling factors that quantify
 899 possible deviations of the couplings from the SM values, Higgs-Vector boson (H-
 900 W) and Higgs-top (H-t) respectively, from the SM couplings; $s = (p_W + p_b)^2$, $t =$
 901 $(p_W - p_H)^2$, φ is the Higgs azimuthal angle around the z axis taken parallel to the
 902 direction of motion of the incoming W; A and B are functions describing the weak
 903 interaction in terms of the chiral states (ξ_t, ξ_b) of the quarks b and t . Terms that
 904 vanish in the high energy limit have been neglected as well as the Higgs and b quark
 905 masses⁹.

906 The scattering amplitude grows with energy like \sqrt{s} for $\kappa_V \neq \kappa_t$, in contrast to
 907 the SM ($\kappa_t = \kappa_V = 1$), where the first term in 1.62 cancels out and the amplitude
 908 is constant for large s ; therefore, a deviation from the SM predictions represents an
 909 enhancement in the tHq cross section. In particular, for a SM H-W coupling and a
 910 H-t coupling of inverted sign with respect to the SM ($\kappa_V = -\kappa_t = 1$) the tHq cross
 911 section is enhanced by a factor greater 10 as seen in the Figure 1.16 taken from
 912 Reference [51]; Reference [56] has reported similar enhancement results.

913 A similar analysis is valid for the W-associated channel but, in that case, the in-
 914 terference is more complicated since there are more than two contributions and an ad-
 915 ditional interference with the production of Higgs boson and a top pair process($t\bar{t}H$).
 916 The calculations are made using the so-called Diagram Removal (DR) technique where

⁹ A detailed explanation of the structure and approximations used to derive \mathcal{A} can be found in Reference [51]

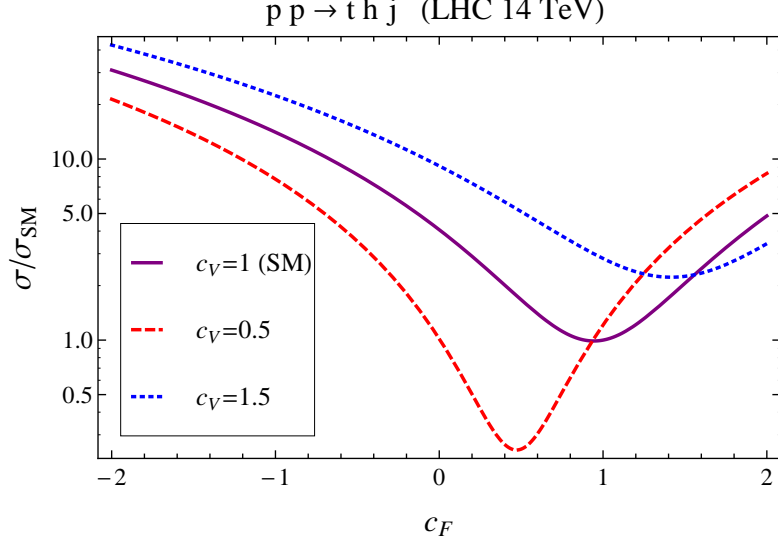


Figure 1.16: Cross section for tHq process as a function of κ_t , normalized to the SM, for three values of κ_V . In the plot c_f refers to the Higgs-fermion coupling which is dominated by the H-t coupling and represented here by κ_t . Solid, dashed and dotted lines correspond to $c_V \rightarrow \kappa_V = 1, 0.5, 1.5$ respectively. Note that for the SM ($\kappa_V = \kappa_t = 1$), the destructive effect of the interference is maximal.

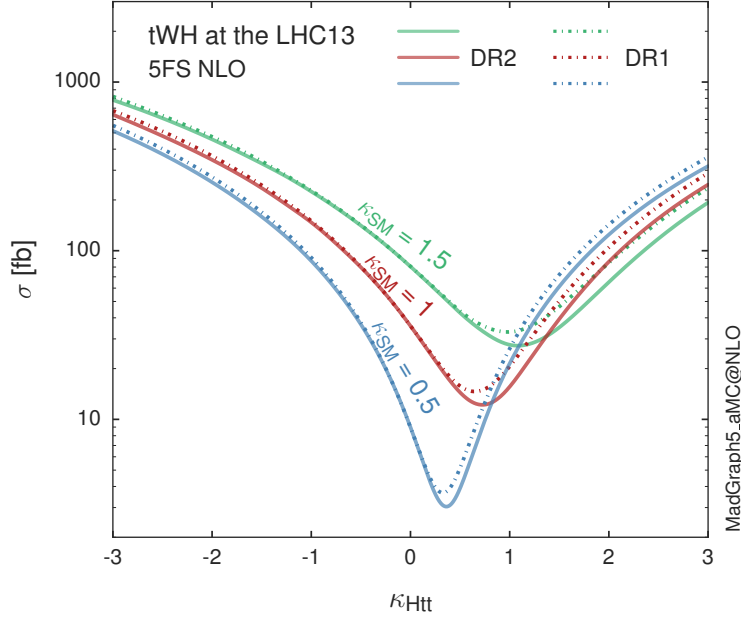


Figure 1.17: Cross section for tHW process as a function of κ_{Htt} , for three values of κ_{SM} at $\sqrt{s} = 13$ TeV. $\kappa_{Htt}^2 = \sigma_{Htt}/\sigma_{Htt}^{SM}$ is a simple re-scaling of the SM Higgs interactions.

interfering diagrams are removed (or added) from the calculations in order to evaluate the impact of the removed contributions. DR1 was defined to neglect $t\bar{t}H$ interference while DR2 was defined to take $t\bar{t}H$ interference into account [48]. As shown in Figure 1.17, the tHW cross section is enhanced from about 15 fb (SM: $\kappa_{Htt} = 1$) to about 150 fb ($\kappa_{Htt} = -1$). Differences between curves for DR1 and DR2 help to gauge the impact of the interference with $t\bar{t}H$. Results of the calculations of the tHq and tHW cross sections at $\sqrt{s} = 13$ TeV can be found in Reference [57] and a summary of the results is presented in Table 1.11.

	\sqrt{s} TeV	$\kappa_t = 1$	$\kappa_t = -1$
$\sigma^{LO}(tHq)(fb)$ [51]	8	≈ 17.4	≈ 252.7
	14	≈ 80.4	≈ 1042
$\sigma^{NLO}(tHq)(fb)$ [51]	8	$18.28^{+0.42}_{-0.38}$	$233.8^{+4.6}_{-0.0}$
	14	$88.2^{+1.7}_{-0.0}$	$982.8^{+28}_{-0.0}$
$\sigma^{LO}(tHq)(fb)$ [56]	14	≈ 71.8	≈ 893
$\sigma^{LO}(tHW)(fb)$ [56]	14	≈ 16.0	≈ 139
$\sigma^{NLO}(tHq)(fb)$ [57]	8	$18.69^{+8.62\%}_{-17.13\%}$	-
	13	$74.25^{+7.48\%}_{-15.35\%}$	$848^{+7.37\%}_{-13.70\%}$
	14	$90.10^{+7.34\%}_{-15.13\%}$	$1011^{+7.24\%}_{-13.39\%}$
$\sigma^{LO}(tHW)(fb)$ [48]	13	$15.77^{+15.91\%}_{-15.76\%}$	-
$\sigma^{NLO}DR1(tHW)(fb)$ [48]	13	$21.72^{+6.52\%}_{-5.24\%}$	≈ 150
$\sigma^{NLO}DR2(tHW)(fb)$ [48]	13	$16.28^{+7.34\%}_{-15.13\%}$	≈ 150

Table 1.11: Predicted enhancement of the tHq and tHW cross sections at LHC for $\kappa_V = 1$ and $\kappa_t = \pm 1$ at LO and NLO; the cross section enhancement of more than a factor of 10 is due to the flipping in the sign of the H-t coupling with respect to the SM one.

925

926 1.6 CP-mixing in tH processes

927 In addition to the sensitivity to sign of the H-t coupling, the tHq and tHW processes
928 have been proposed as a tool to investigate the possibility of a H-t coupling that does

929 not conserve CP [47, 48, 58].

930 In this thesis, the sensitivity of tH processes to CP-mixing is also studied on the
 931 basis of References [47, 48] using the effective field theory framework where a generic
 932 particle (X_0) of spin-0 and a general CP violating interaction with the top quark
 933 (Htt coupling), can couple to scalar and pseudo-scalar fermionic densities. The H-W
 934 interaction is assumed to be SM-like. The Lagrangian modeling the H-t interaction
 935 is given by

$$\mathcal{L}_0^t = -\bar{\psi}_t (c_\alpha \kappa_{Htt} g_{Htt} + i s_\alpha \kappa_{Att} g_{Att} \gamma_5) \psi_t X_0, \quad (1.63)$$

936 where α is the CP-mixing phase, $c_\alpha \equiv \cos \alpha$ and $s_\alpha \equiv \sin \alpha$, κ_{Htt} and κ_{Att} are real
 937 dimensionless re-scaling parameters¹⁰ used to parametrize the magnitude of the CP-
 938 violating and CP-conserving parts of the amplitude. The model defines $g_{Htt} =$
 939 $g_{Att} = m_t/v = y_t/\sqrt{2}$ with $v \sim 246$ GeV the Higgs vacuum expectation value. In
 940 this parametrization, three special cases can be recovered

941 • CP-even coupling $\rightarrow \alpha = 0^\circ$

942 • CP-odd coupling $\rightarrow \alpha = 90^\circ$

943 • SM coupling $\rightarrow \alpha = 0^\circ$ and $\kappa_{Htt} = 1$

944 The loop induced X_0 coupling to gluons can also be described in terms of the
 945 parametrization above, according to

$$\mathcal{L}_0^g = -\frac{1}{4} \left(c_\alpha \kappa_{Hgg} g_{Hgg} G_{\mu\nu}^a G^{a,\mu\nu} + s_\alpha \kappa_{Agg} g_{Agg} G_{\mu\nu}^a \tilde{G}^{a,\mu\nu} \right) X_0. \quad (1.64)$$

946 where $g_{Hgg} = -\alpha_s/3\pi v$ and $g_{Agg} = \alpha_s/2\pi v$ and $G_{\mu\nu}$ is the gluon field strength tensors.

947 Under the assumption that the top quark dominates the gluon-fusion process at LHC

¹⁰ analog to κ_t and κ_V

948 energies, $\kappa_{Hgg} \rightarrow \kappa_{Htt}$ and $\kappa_{Agg} \rightarrow \kappa_{Att}$, so that the ratio between the gluon-gluon
 949 fusion cross section for X_0 and for the SM Higgs prediction can be written as

$$\frac{\sigma_{NLO}^{gg \rightarrow X_0}}{\sigma_{NLO,SM}^{gg \rightarrow H}} = c_\alpha^2 \kappa_{Htt}^2 + s_\alpha^2 \left(\kappa_{Att} \frac{g_{Agg}}{g_{Hgg}} \right)^2. \quad (1.65)$$

950 If the re-scaling parameters are set to

$$\kappa_{Htt} = 1, \quad \kappa_{Att} = \left| \frac{g_{Hgg}}{g_{Agg}} \right| = \frac{2}{3}. \quad (1.66)$$

951 the gluon-fusion SM cross section is reproduced for every value of the CP-mixing
 952 angle α ; therefore, by imposing that condition to the Lagrangian density 1.63, the
 953 CP-mixing angle is not constrained by current data. Figure 1.18 shows the NLO cross
 954 sections for t-channel tX_0 (blue) and $t\bar{t}X_0$ (red) associated production processes as a
 955 function of the CP-mixing angle α . X_0 is a generic spin-0 particle with top quark
 956 CP-violating coupling. Re-scaling factors κ_{Htt} and κ_{Att} have been set to reproduce
 957 the SM gluon-fusion cross sections.

958 It is interesting to notice that the tX_0 cross section is enhanced, by a factor of
 959 about 10, when a continuous rotation in the scalar-pseudoscalar plane is applied; this
 960 enhancement is similar to the enhancement produced when the H-t coupling is flipped
 961 in sign with respect to the SM ($y_t = -y_{t,SM}$ in the plot), as showed in Section 1.5. In
 962 contrast, the degeneracy in the $t\bar{t}X_0$ cross section is still present given that it depends
 963 quadratically on the H-t coupling, but more interesting is to notice that $t\bar{t}X_0$ cross
 964 section is exceeded by tX_0 cross section after $\alpha \sim 60^\circ$.

965 A similar parametrization can be used to investigate the tHW process sensitivity
 966 to CP-violating H-t coupling. As said in 1.5, the interference in the W-associated
 967 channel is more complicated because there are more than two contributions and also
 968 there is interference with the $t\bar{t}H$ production process.

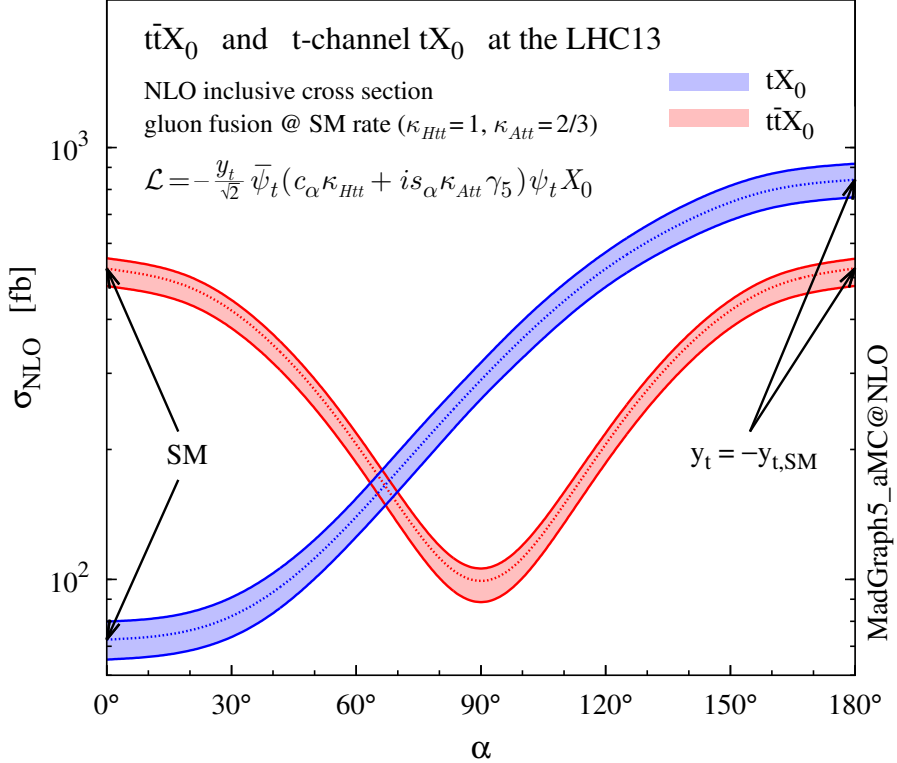


Figure 1.18: NLO cross sections for t-channel tX_0 (blue) and $t\bar{t}X_0$ (red) associated production processes as a function of the CP-mixing angle α . X_0 is a generic spin-0 particle with top quark CP-violating coupling [47].

969 Figure 1.19 shows the NLO cross sections for t-channel tX_0 (blue), $t\bar{t}X_0$ (red)
970 associated production and for the combined $tWX_0+t\bar{t}X_0+interference$ (orange) as
971 a function of the CP-mixing angle. It is clear that the effect of the interference in the
972 combined case is the lifting of the degeneracy present in the $t\bar{t}X_0$ production. The
973 constructive interference enhances the cross section from about 500 fb at SM ($\alpha = 0$)
974 to about 600 fb ($\alpha = 180^\circ \rightarrow y_t = -y_{t,SM}$).

975 An analysis combining tHq and tHW processes will be made in this thesis taking
976 advantage of the sensitivity improvement.

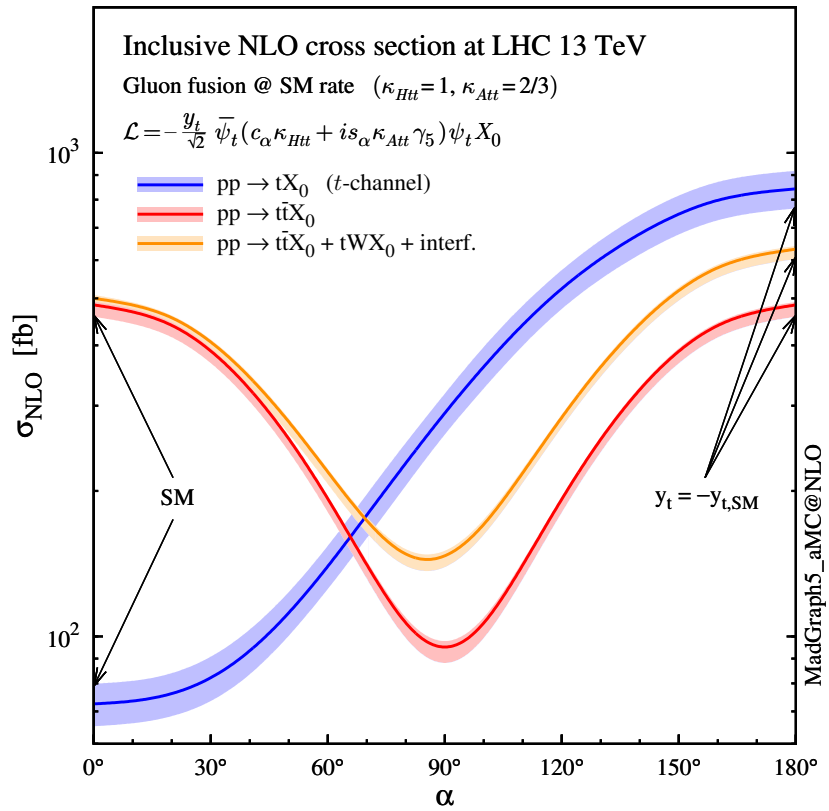


Figure 1.19: NLO cross sections for t-channel tX_0 (blue), $t\bar{t}X_0$ (red) associated production processes and combined $tWX_0 + t\bar{t}X_0$ (including interference) production as a function of the CP-mixing angle α [47].

₉₇₇ **Chapter 2**

₉₇₈ **The CMS experiment at the LHC**

₉₇₉ **2.1 Introduction**

₉₈₀ Located on the Swiss-French border, the European Council for Nuclear Research
₉₈₁ (CERN) is the largest scientific organization leading particle physics research. About
₉₈₂ 13000 people in a broad range of roles including users, students, scientists, engineers,
₉₈₃ among others, contribute to the data taking and analysis, with the goal of unveiling
₉₈₄ the secrets of nature and revealing the fundamental structure of the universe. CERN
₉₈₅ is also the home of the Large Hadron Collider (LHC), the largest particle accelerator
₉₈₆ around the world, where protons (or heavy ions) traveling close to the speed of light,
₉₈₇ are made to collide. These collisions open a window to investigate how particles (and
₉₈₈ their constituents if they are composite) interact with each other, providing clues
₉₈₉ about the laws of nature. This chapter presents an overview of the LHC structure
₉₉₀ and operation. A detailed description of the CMS detector is offered, given that the
₉₉₁ data used in this thesis have been taken with this detector.

992 2.2 The LHC

993 With 27 km of circumference, the LHC is currently the most powerful circular accelerator
 994 in the world. It is installed in the same tunnel where the Large Electron-Positron
 995 (LEP) collider was located, taking advantage of the existing infrastructure. The LHC
 996 is part of the CERN's accelerator complex composed of several successive accelerat-
 997 ing stages before the particles are injected into the LHC ring where they reach their
 998 maximum energy (see Figure 2.1).

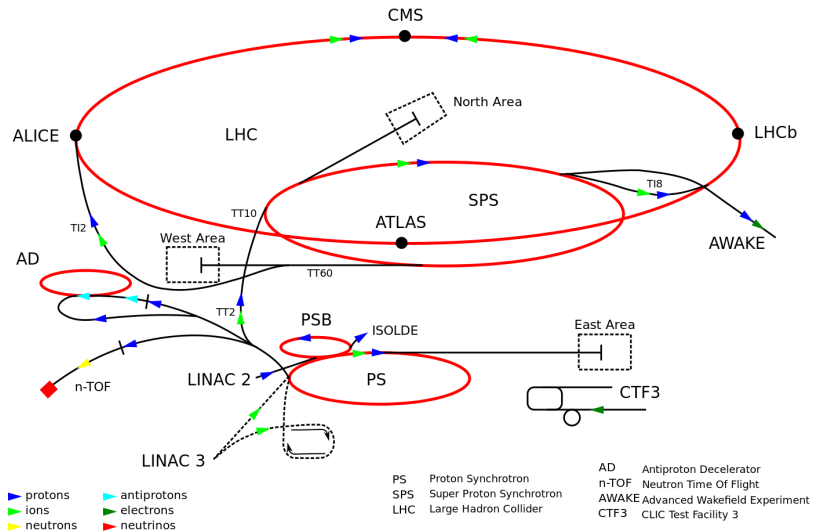


Figure 2.1: CERN accelerator complex. Blue arrows show the path followed by protons along the acceleration process [61].

999 The LHC runs in three collision modes depending on the particles being acceler-
 1000 ated

1001 • Proton-Proton collisions (pp) for multiple physics experiments.

1002 • Lead-Lead collisions ($Pb-Pb$) for heavy ion experiments.

1003 • Proton-Lead collisions ($p-Pb$) for quark-gluon plasma experiments.

1004 In this thesis only pp collisions will be considered.

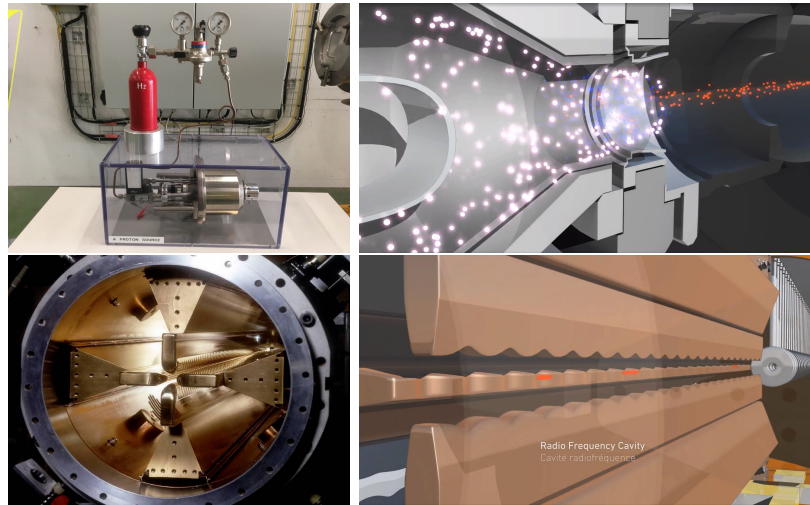


Figure 2.2: LHC protons source and the first acceleration stage. Top: the bottle contains hydrogen gas which is injected into the metal cylinder (white dots) to be broken down into electrons (blue dots) and protons (red dots); Bottom: the obtained protons are directed towards the radio frequency quadrupole which perform the first acceleration, focus the beam and create the bunches of protons. Left images are real pictures while right images are drawings [65, 66].

1005 Collection of protons starts with hydrogen atoms taken from a bottle, containing
 1006 hydrogen gas, and injecting them in a metal cylinder; hydrogen atoms are broken
 1007 down into electrons and protons by an intense electric field (see Figure 2.2 top).
 1008 The resulting protons leave the metal cylinder towards a radio frequency quadrupole
 1009 (RFQ) that focus the beam, accelerates the protons and creates the packets of protons
 1010 called bunches. In the RFQ, an electric field is generated by a RF wave at a frequency
 1011 that matches the resonance frequency of the cavity where the electrodes are contained.
 1012 The beam of protons traveling on the RFQ axis experiences an alternating electric
 1013 field gradient that generates the focusing forces.

1014 In order to accelerate the protons, a longitudinal time-varying electric field com-
 1015 ponent is added to the system; it is done by giving the electrodes a sine-like profile as
 1016 shown in Figure 2.2 bottom. By matching the speed and phase of the protons with
 1017 the longitudinal electric field the bunching is performed; protons synchronized with

1018 the RFQ (synchronous protons) do not feel an accelerating force, but those protons in
 1019 the beam that have more (or less) energy than the synchronous proton (asynchronous
 1020 protons) will feel a decelerating (accelerating) force; therefore, asynchronous protons
 1021 will oscillate around the synchronous ones forming bunches of protons [63]. From the
 1022 RFQ protons emerge with energy 750 keV in bunches of about 1.15×10^{11} protons [64].

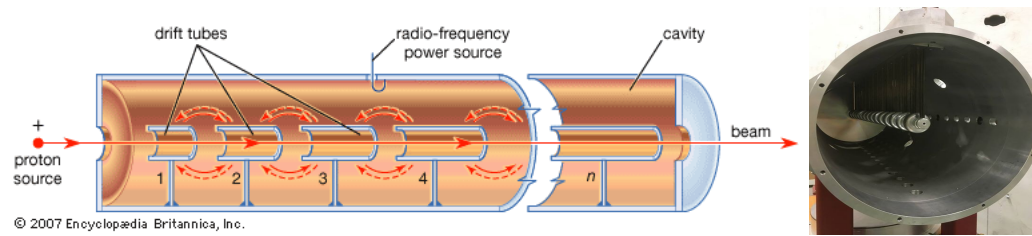


Figure 2.3: Left: drawing of the LINAC2 accelerating system at CERN. Electric fields generated by radio frequency (RF) create acceleration and deceleration zones inside the cavity; deceleration zones are blocked by drift tubes where quadrupole magnets focus the proton beam. Right: picture of a real RF cavity [67].

1023 Proton bunches coming from the RFQ go to the linear accelerator 2 (LINAC2)
 1024 where they are accelerated to reach 50 MeV energy. In the LINAC2 stage, acceleration
 1025 is performed using electric fields generated by radio frequency which create zones
 1026 of acceleration and deceleration as shown in Figure 2.3. In the deceleration zones,
 1027 the electric field is blocked using drift tubes where protons are free to drift while
 1028 quadrupole magnets focus the beam.

1029 The beam coming from LINAC2 is injected into the proton synchrotron booster
 1030 (PSB) to reach 1.4 GeV in energy. The next acceleration is provided at the proton
 1031 synchrotron (PS) up to 26 GeV, followed by the injection into the super proton
 1032 synchrotron (SPS) where protons are accelerated to 450 GeV. Finally, protons are
 1033 injected into the LHC where they are accelerated to the target energy of 6.5 TeV.

1034 PSB, PS, SPS and LHC accelerate protons using the same RF acceleration tech-
 1035 nique described before.

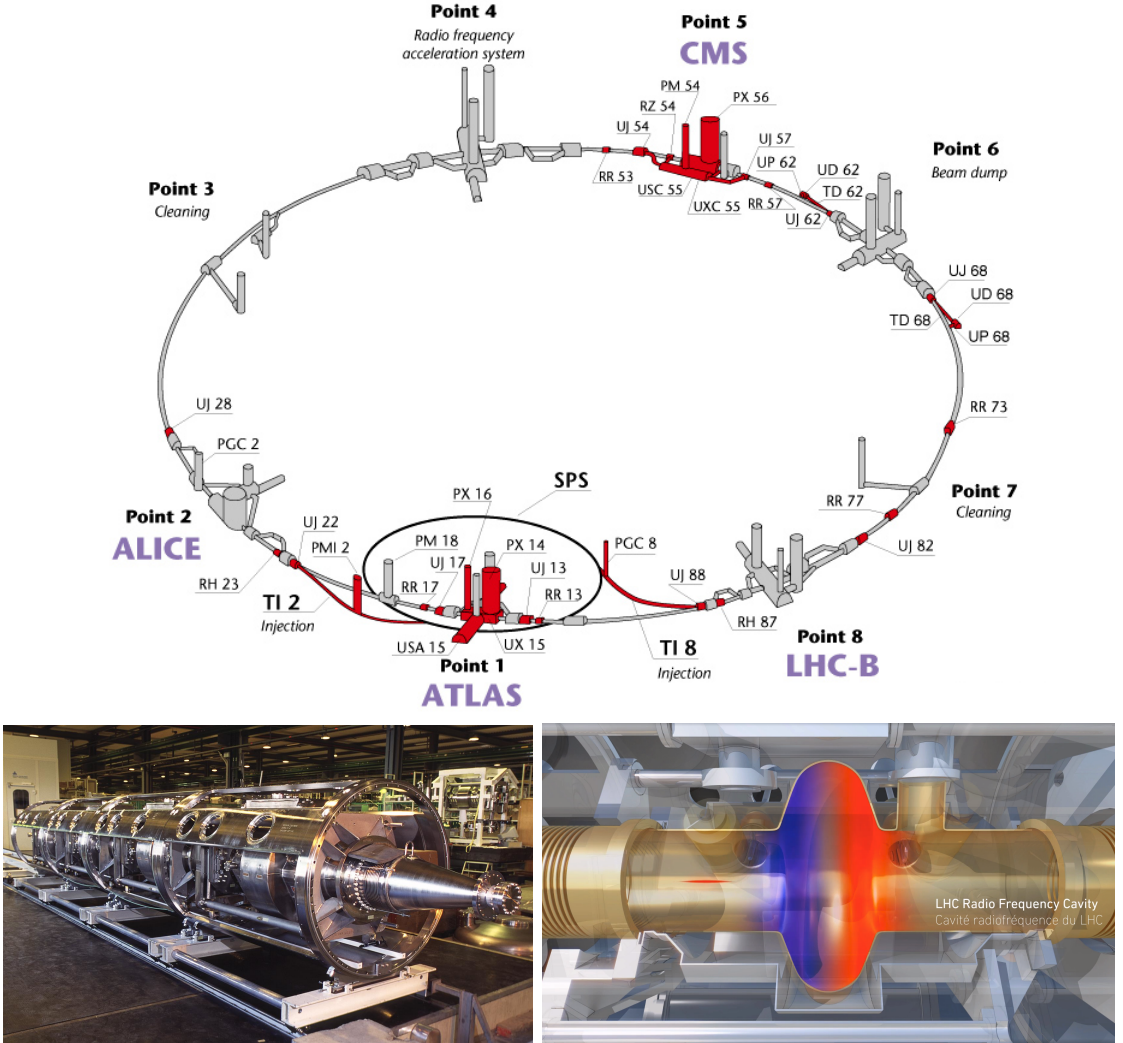


Figure 2.4: Top: LHC layout. The red zones indicate the infrastructure additions to the LEP installations, built to accommodate the ATLAS and CMS experiments which exceed the size of the former experiments located there [62]. Bottom: LHC RF cavities. A module (left picture) accommodates 4 cavities, each like the one in the right drawing, that accelerate protons and preserve the bunch structure of the beam. The color gradient pattern represents the strength of the electric field inside the cavity; red zone corresponds to the maximum of the oscillation electric field while the blue zone corresponds to the minimum. [66, 68]

1036 The LHC has a system of 16 RF cavities located in the so-called point 4, as
 1037 shown in Figure 2.4 top, tuned at a frequency of 400 MHz. The bottom side of
 1038 Figure 2.4 shows a picture of a RF module composed of 4 RF cavities working in a
 1039 superconducting state at 4.5 K; also, a representation of the accelerating electric field

that accelerates the protons in the bunch is shown. The maximum of the oscillating electric field (red region) picks the proton bunches at the entrance of the cavity and keeps accelerating them through the whole cavity. The protons are carefully timed so that in addition to the acceleration effect the bunch structure of the beam is preserved.

While protons are accelerated in one section of the LHC ring, where the RF cavities are located, in the rest of their path they have to be kept in the curved trajectory defined by the LHC ring. Technically, LHC is not a perfect circle; RF, injection, beam dumping, beam cleaning and sections before and after the experimental points where protons collide are all straight sections. In total, there are 8 arcs 2.45 km long each and 8 straight sections 545 m long each. In order to curve the proton's trajectory in the arc sections, superconducting dipole magnets are used.

Inside the LHC ring, there are two proton beams traveling in opposite directions in two separated beam pipes; the beam pipes are kept at ultra-high vacuum ($\sim 10^{-9}$ Pa) to ensure that there are no particles that interact with the proton beams. The superconducting dipole magnets used in LHC are made of a NbTi alloy, capable of transporting currents of about 12000 A when cooled at a temperature below 2K using liquid helium (see Figure 2.5).

Protons in the arc sections of LHC feel a centripetal force exerted by the dipole magnets; the magnitude of magnetic field needed to keep the protons in the LHC curved trayectomy can be found assuming that protons travel at $v \approx c$, using the standard values for proton mass and charge and the LHC radius, as

$$F_m = \frac{mv^2}{r} = qBv \rightarrow B = 8.33T \quad (2.1)$$

which is about 100000 times the Earth's magnetic field. A representation of the

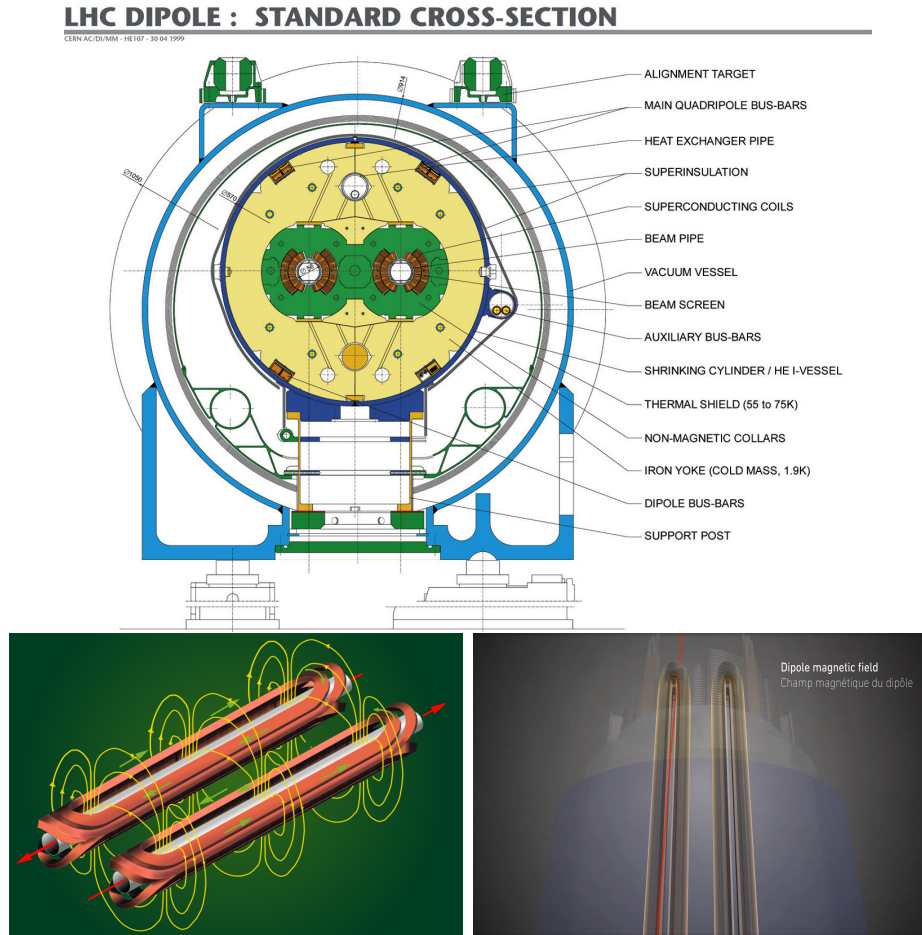


Figure 2.5: Top: LHC dipole magnet transverse view; cooling, shielding and mechanical support are indicated. Bottom left: Magnetic field generated by the dipole magnets; note that the direction of the field inside one beam pipe is opposite with respect to the other beam pipe which guarantee that both proton beams are curved in the same direction towards the center of the ring. The effect of the dipole magnetic field on the proton beam is represented on the bottom right side [66, 69, 70].

1063 magnetic field generated by the dipole magnets is shown on the bottom left side of
 1064 Figure 2.5. The bending effect of the magnetic field on the proton beam is shown on
 1065 the bottom right side of Figure 2.5. Note that the dipole magnets are not curved;
 1066 the arc section of the LHC ring is composed of straight dipole magnets of about 15
 1067 m. In total there are 1232 dipole magnets along the LHC ring.
 1068 In addition to the bending of the beam trajectory, the beam has to be focused. The

1069 focusing is performed by quadrupole magnets installed in a different straight section;
 1070 in total 858 quadrupole magnets are installed along the LHC ring. Other effects like
 1071 electromagnetic interaction among bunches, interaction with electron clouds from the
 1072 beam pipe, the gravitational force on the protons, differences in energy among protons
 1073 in the same bunch, among others, are corrected using sextupole and other magnetic
 1074 multipoles.

1075 The two proton beams inside the LHC ring are made of bunches with a cylindrical
 1076 shape of about 7.5 cm long and about 1 mm in diameter; when bunches are close to the
 1077 interaction point (IP), the beam is focused up to a diameter of about 16 μm in order
 1078 to maximize the probability of collisions between protons. The number of collisions
 1079 per second is proportional to the cross section of the bunches with the *luminosity* (L)
 1080 as the proportionality factor, thus, the luminosity can be calculated using

$$L = fn \frac{N_1 N_2}{4\pi\sigma_x\sigma_y} \quad (2.2)$$

1081 where f is the revolution frequency, n is the number of bunches per beam, N_1 and N_2
 1082 are the numbers of protons per bunch, σ_x and σ_y are the gaussian transverse sizes of
 1083 the bunches. With the expected parameters, the LHC expected luminosity is about

$$f = \frac{v}{2\pi r_{LHC}} \approx \frac{3 \times 10^8 \text{ m/s}}{27 \text{ km}} \approx 11.1 \text{ kHz},$$

$$n = 2808$$

$$N_1 = N_2 \sim 1.5 \times 10^{11}$$

$$\sigma_x = \sigma_y = 16 \mu\text{m}$$

1084

$$L = 1.28 \times 10^{34} \text{ cm}^{-2} \text{ s}^{-1} = 1.28 \times 10^{-5} \text{ fb}^{-1} \text{ s}^{-1} \quad (2.3)$$

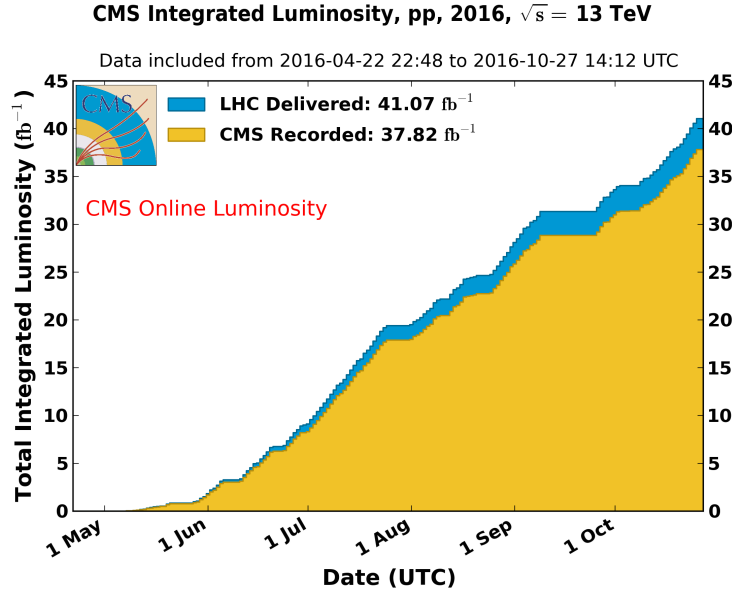


Figure 2.6: Integrated luminosity delivered by LHC and recorded by CMS during 2016. The difference between the delivered and the recorded luminosity is due to fails and issues occurred during the data taking in the CMS experiment [71].

1085 Luminosity is a fundamental aspect of LHC given that the bigger luminosity the
 1086 bigger number of collisions, which means that for processes with a very small cross
 1087 section the number of expected occurrences is increased and so the chances of being
 1088 detected. The integrated luminosity, collected by the CMS experiment during 2016
 1089 is shown in Figure 2.6; the data analyzed in this thesis corresponds to an integrated
 1090 luminosity of 35.9 fb^{-1} at a center of mass-energy $\sqrt{s} = 13 \text{ TeV}$.

1091 One way to increase L is increasing the number of bunches in the beam. Cur-
 1092 rently, the separation between two consecutive bunches in the beam is 7.5 m which
 1093 corresponds to a time separation of 25 ns. In the full LHC ring the allowed number
 1094 of bunches is $n = 27\text{km}/7.5\text{m} = 3600$; however, there are some gaps in the bunch pat-
 1095 tern intended for preparing the dumping and injection of the beam, thus, the proton
 1096 beams are composed of 2808 bunches.

1097 Once the proton beams reach the desired energy, they are brought to cross each

1098 other producing pp collisions. The bunch crossing happens in precise places where
 1099 the four LHC experiments are located, as seen in the top of Figure 2.7. In 2008 pp
 1100 collisions of $\sqrt{s} = 7$ TeV were performed; the energy was increased to 8 TeV in 2012
 1101 and to 13 TeV in 2015.

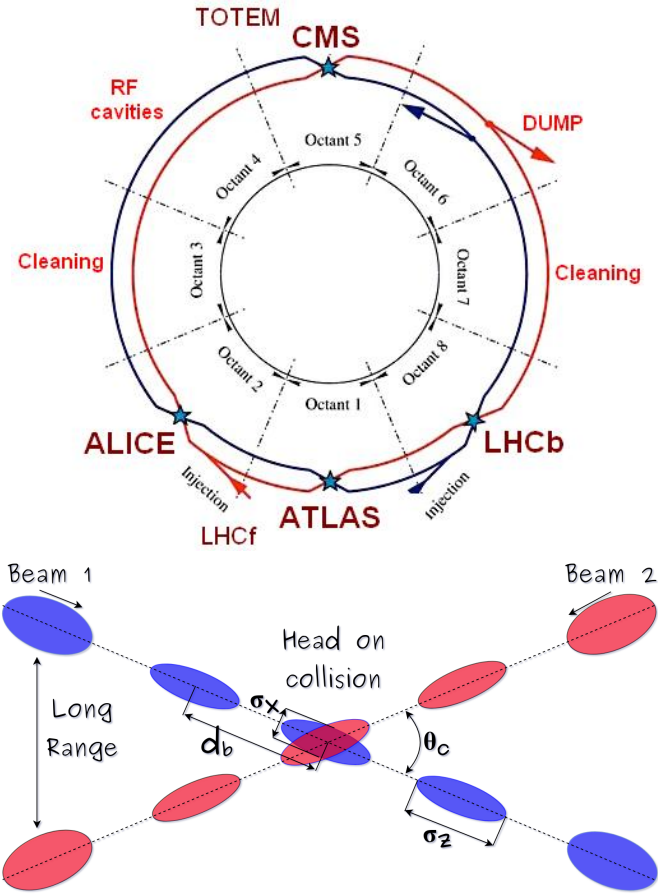


Figure 2.7: Top: LHC interaction points. Bunch crossing occurs where the LHC experiments are located [72]. Sections indicated as cleaning are dedicated to collimate the beam in order to protect the LHC ring from collisions with protons in very spreaded bunches. Bottom: bunch crossing scheme. Since the bunch crossing is not perfectly head-on, the luminosity is reduced in a factor of 17%; adapted from Reference [86].

1102 The CMS and ATLAS experiments are multi-purpose experiments, hence, they
 1103 are enabled to explore physics in any of the LHC collision modes. LHCb experiment
 1104 is optimized to explore bottom quark physics, while ALICE is optimized for heavy

1105 ion collisions searches; TOTEM and LHCf are dedicated to forward physics studies;
 1106 MoEDAL (not indicated in the Figure) is intended for monopole or massive pseudo
 1107 stable particles searches.

1108 At the IP there are two interesting details that need to be addressed. The first
 1109 one is that the bunch crossing does not occur head-on but at a small crossing angle θ_c
 1110 (280 μ rad in CMS and ATLAS) as shown in the bottom side of Figure 2.7, affecting
 1111 the overlapping between bunches; the consequence is a reduction of about 17% in
 1112 the luminosity (represented by a factor not included in eqn. 2.2). The second one
 1113 is the occurrence of multiple pp collisions in the same bunch crossing; this effect is
 1114 called *pileup* (PU). A fairly simple estimation of the PU follows from estimating the
 1115 probability of collision between two protons, one from each of the bunches in the
 1116 course of collision; it depends roughly on the ratio of proton size and the cross section
 1117 of the bunch in the IP, i.e.,

$$P(pp\text{-}collision) \sim \frac{d_{proton}^2}{\sigma_x \sigma_y} = \frac{(1\text{fm})^2}{(16\mu\text{m})^2} \sim 4 \times 10^{-21} \quad (2.4)$$

1118 however, there are $N = 1.15 \times 10^{11}$ protons in a bunch, thus the estimated number of
 1119 collisions in a bunch crossing is

$$PU = N^2 * P(pp\text{-}collision) \sim 50pp \text{ collision per bunch crossing}, \quad (2.5)$$

1120 about 20 of which are inelastic. A multiple pp collision event in a bunch crossing at
 1121 CMS is shown in Figure 2.8.

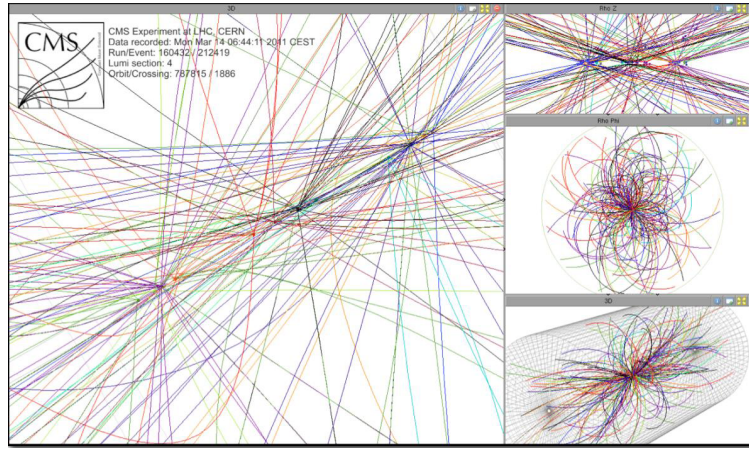


Figure 2.8: Multiple pp collision bunch crossing at CMS. [73].

1122 2.3 The CMS experiment

1123 CMS is a general-purpose detector designed to conduct research in a wide range
 1124 of physics from the standard model to new physics like extra dimensions and dark
 1125 matter. Located at Point 5 in the LHC layout as shown in Figure 2.4, CMS is
 1126 composed of several detection systems distributed in a cylindrical structure; in total,
 1127 CMS weights about 12500 tons in a very compact 21.6 m long and 14.6 m diameter
 1128 cylinder. It was built in 15 separate sections at the ground level and lowered to the
 1129 cavern individually to be assembled. A complete and detailed description of the CMS
 1130 detector and its components is given in Reference [74] on which this section is based.
 1131 Figure 2.9 shows the layout of the CMS detector. The detection system is composed
 1132 of (from the innermost to the outermost)

- 1133 • Pixel detector.
- 1134 • Silicon strip tracker.
- 1135 • Preshower detector.
- 1136 • Electromagnetic calorimeter.

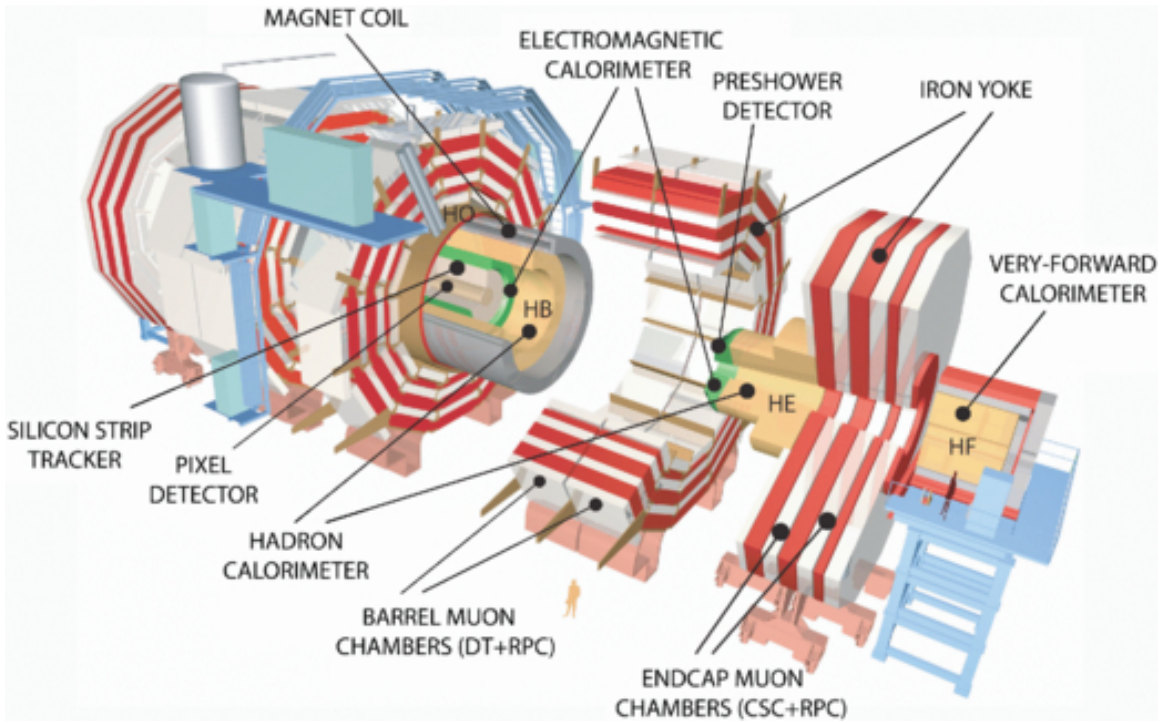


Figure 2.9: Layout of the CMS detector. The several subdetectors are indicated. The central region of the detector is referred as the barrel section while the endcaps are referred as the forward sections. [75].

1137 • Hadronic calorimeter.

1138 • Muon chambers (barrel and endcap)

1139 The central region of the detector is commonly referred as the barrel section while
 1140 the endcaps are referred as the forward sections of the detector; thus, each subdetector
 1141 is composed of a barrel section and a forward section.

1142 When a pp collision happens inside the CMS detector, many different particles are
 1143 produced, but only some of them live long enough to be detected; they are electrons,
 1144 photons, pions, kaons, protons, neutrons and muons; neutrinos are not detected by
 1145 the CMS detector. Thus, the CMS detector was designed to detect those particles and
 1146 measure their properties. Figure 2.10 shows a transverse slice of the CMS detector.
 1147 The silicon tracker (pixel detector + strip tracker) is capable to register the track of

the charged particles traversing it, while calorimeters (electromagnetic and hadronic) measure the energy of the particles that are absorbed by their materials. Considering the detectable particles, mentioned above, emerging from the IP, a basic description of the detection process is as follows.

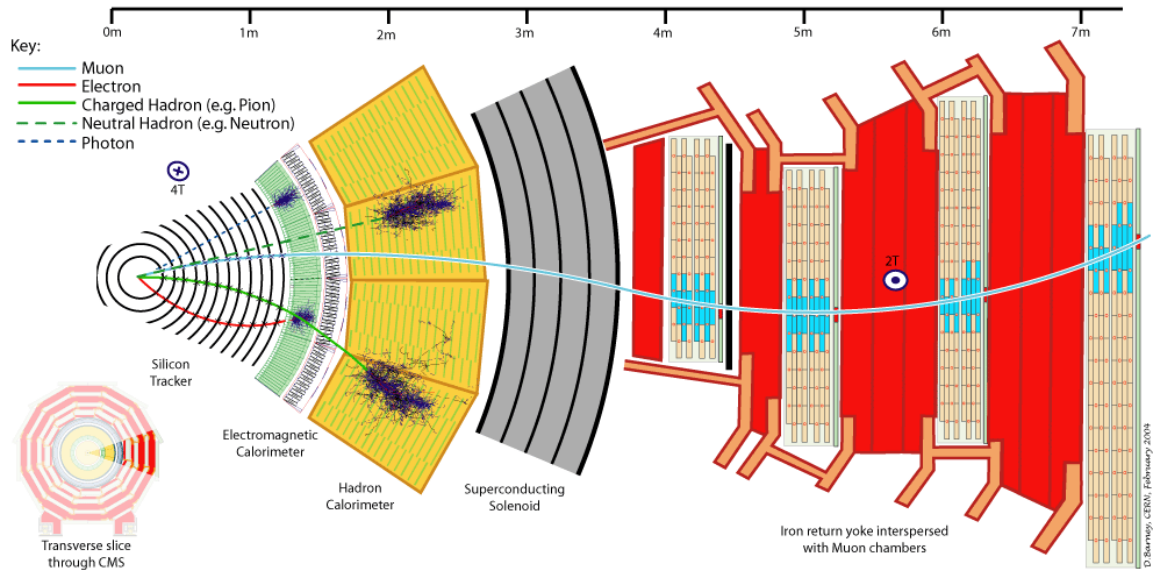


Figure 2.10: CMS detector transverse slice [76].

A muon emerging from the IP, will create a track on the silicon tracker and on the muon chambers. The design of the CMS detector is driven by the requirements on the identification, momentum resolution and unambiguous charge determination of the muons; therefore, a large bending power is provided by the solenoid magnet made of superconducting cable capable of generating a 3.8 T magnetic field. The muon track is bent twice since the magnetic field inside the solenoid is directed along the z -direction but outside its direction is reversed. Muons interact very weakly with the calorimeters, therefore, it is not absorbed but escape away from the detector.

An electron emerging from the IP will create a track along the tracker which will be bent due to the presence of the magnetic field, later, it will be absorbed in the electromagnetic calorimeter where its energy is measured.

1163 A photon will not leave a track because it is neutral, but it will be absorbed in
 1164 the electromagnetic calorimeter.

1165 A neutral hadron, like the neutron, will not leave a track either but it will lose a
 1166 small amount of its energy during its passage through the electromagnetic calorimeter
 1167 and then it will be absorbed in the hadron calorimeter depositing the rest of its energy.

1168 A charged hadron, like the proton or π^\pm , will leave a curved track on the silicon
 1169 tracker, some of its energy in the electromagnetic calorimeter and finally will be
 1170 absorbed in the hadronic calorimeter.

1171 A more detailed description of each detection system will be presented in the
 1172 following sections.

1173 2.3.1 CMS coordinate system

1174 The coordinate system used by CMS is centered on the geometrical center of the
 1175 detector which is the nominal IP as shown in Figure 2.11¹. The z -axis is parallel
 1176 to the beam direction, while the Y -axis pointing vertically upward, and the X -axis
 1177 pointing radially inward toward the center of the LHC.

1178 In addition to the common cartesian and cylindrical coordinate systems, two co-
 1179 ordinates are of particular utility in particle physics: rapidity (y) and pseudorapidity
 1180 (η), defined in connection to the polar angle θ , energy and longitudinal momentum
 1181 component (momentum along the z -axis) according to

$$y = \frac{1}{2} \ln \frac{E + p_z}{E - p_z} \quad \eta = -\ln \left(\tan \frac{\theta}{2} \right) \quad (2.6)$$

1182 Rapidity is related to the angle between the XY -plane and the direction in which
 1183 the products of a collision are emitted; it has the nice property that the difference

¹ Not all the pp interaction occur at the nominal IP because of the bunch lenght, therefore, each pp collision has its own IP location

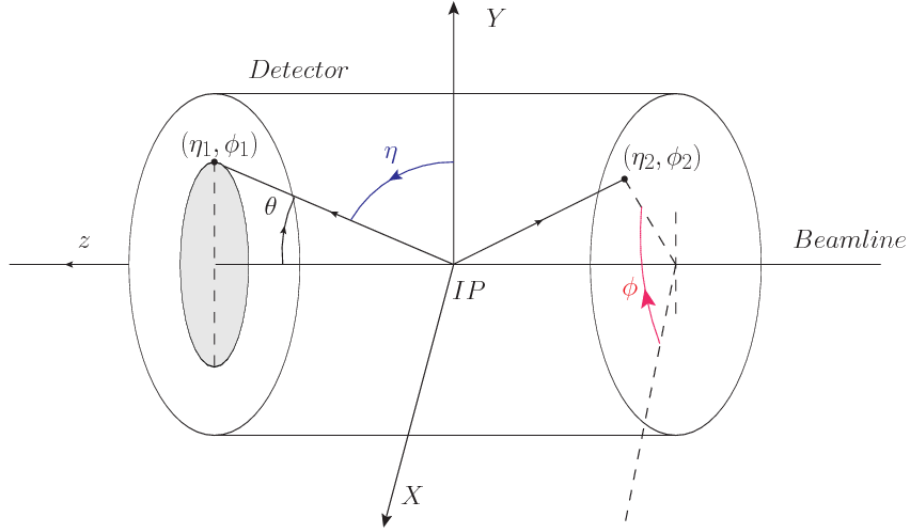


Figure 2.11: CMS detector coordinate system.

1184 between the rapidities of two particles is invariant with respect to Lorentz boosts
 1185 along the z -axis, hence, data analysis becomes more simple when based on rapid-
 1186 ity; however, it is not simple to measure the rapidity of highly relativistic particles,
 1187 as those produced after pp collisions. Under the highly relativistic motion approxi-
 1188 mation, y can be rewritten in terms of the polar angle, concluding that rapidity is
 1189 approximately equal to the pseudorapidity defined above, i.e., $y \approx \eta$. Note that η
 1190 is easier to measure than y given the direct relationship between the former and the
 1191 polar angle.

1192 The angular distance between two objects in the detector (ΔR) is commonly used
 1193 to judge the isolation of those object; it is defined in terms of their coordinates (η_1, ϕ_1) ,
 1194 (η_2, ϕ_2) as

$$\Delta R = \sqrt{(\Delta\eta)^2 - (\Delta\phi)^2} \quad (2.7)$$

1195 2.3.2 Tracking system

1196 The CMS tracking system is designed to provide a precise measurement of the trajectories (*track*) followed by the charged particles created after the pp collisions; also, the
 1197 precise reconstruction of the primary and secondary origins of the tracks (*vertices*) is
 1198 expected in an environment where, each 25 ns, the bunch crossing produces about 20
 1199 inelastic collisions and about 1000 particles.
 1200

1201 Physics requirements guiding the tracking system performance include the precise characterization of events involving gauge bosons, W and Z, and their leptonic
 1202 decays for which an efficient isolated lepton and photon reconstruction is of capital
 1203 importance, given that isolation is required to suppress background events to a level
 1204 that allows observations of interesting processes like Higgs boson decays or beyond
 1205 SM events.

1207 The ability to identify and reconstruct b -jets and B-hadrons within these jets is also
 1208 a fundamental requirement, achieved through the ability to reconstruct accurately
 1209 displaced vertices, given that b -jets are part of the signature of top quark physics, like
 1210 the one treated in this thesis.

1211 An schematic view of the CMS tracking system is shown in Figure 2.12

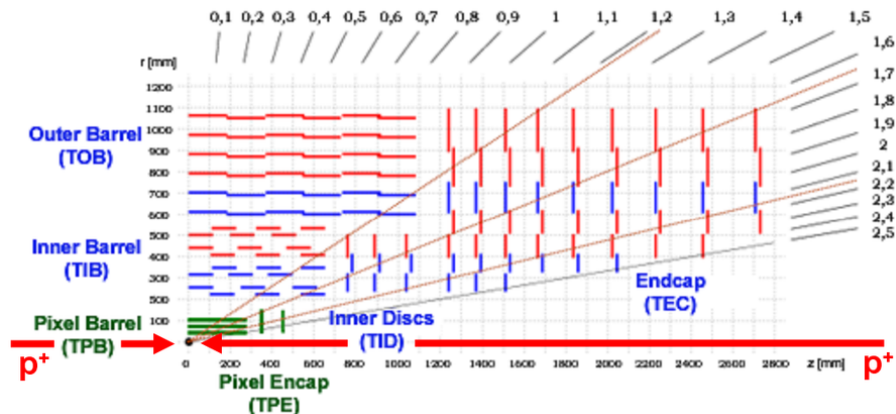


Figure 2.12: CMS tracking system schematic view [78].

1212 In order to satisfy these performance requirements, the tracking system uses two
 1213 different detector subsystems arranged in concentric cylindrical volumes, the pixel
 1214 detector and the silicon strip tracker; the pixel detector is located in the high particle
 1215 density region ($r < 20\text{cm}$) while the silicon strip tracker is located in the medium and
 1216 lower particle density regions $20\text{cm} < r < 116\text{cm}$.

1217 **Pixel detector**

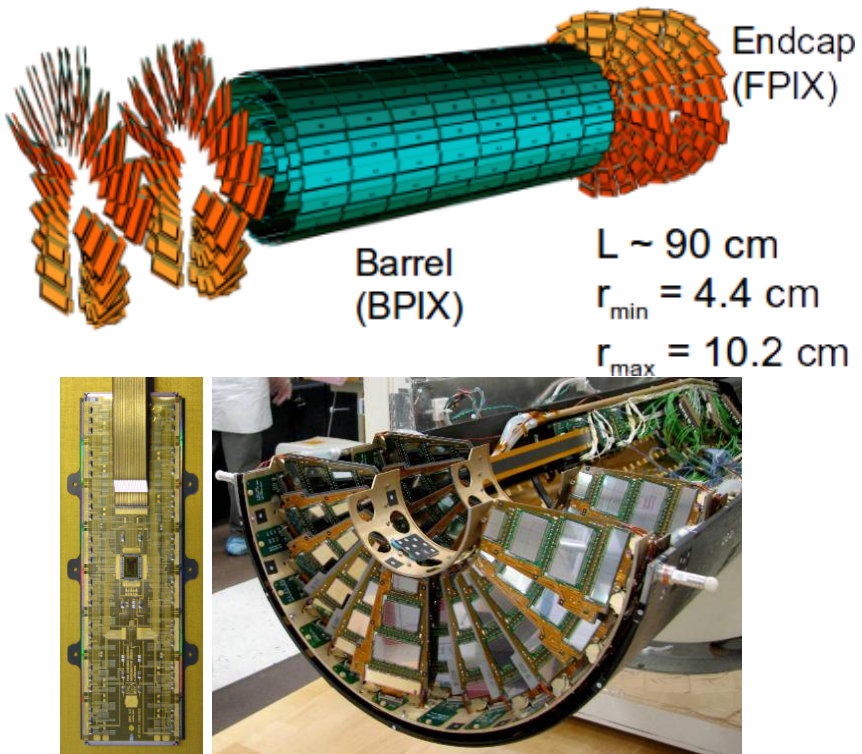


Figure 2.13: CMS pixel detector. Top: schematic view; Bottom: pictures of a barrel(BPIX) module(left) and forward modules(right) [74].

1218 The pixel detector was replaced during the 2016-2017 extended year-end technical
 1219 stop, due to the increasingly challenging operating conditions like the higher particle
 1220 flux and more radiation harsh environment, among others. The new one is responding
 1221 as expected, reinforcing its crucial role in the successful way to fulfill the new LHC

physics objectives after the discovery of the Higgs boson. Since the data sets used in this thesis were produced using the previous version of the pixel detector, it will be the subject of the description in this section. The last chapter of this thesis is dedicated to describe my contribution to the *Forward Pixel Phase 1 upgrade*.

The pixel detector was composed of 1440 silicon pixel detector modules organized in three-barrel layers in the central region (BPix) and two disks in the forward region (FPix) as shown in the top side of Figure 2.13; it was designed to record efficiently and with high precision, up to $20\mu\text{m}$ in the XY -plane and $20\mu\text{m}$ in the z -direction, the first three space-points (*hits*) nearest to the IP region in the range $|\eta| \leq 2.5$. The first barrel layer was located at a radius of 44 mm from the beamline, while the third layer was located at a radius of 102 mm, closer to the strip tracker inner barrel layer (see Section 2.3.3) in order to reduce the rate of fake tracks. The high granularity of the detector is represented in its about 66 Mpixels, each of size $100 \times 150\mu\text{m}^2$. The transverse momentum resolution of tracks can be measured with a resolution of 1-2% for muons of $p_T = 100$ GeV.

A charged particle passing through the pixel sensors produce ionization in them, giving energy for electrons to be removed from the silicon atoms, hence, creating electron-hole pairs. The collection of charges in the pixels generates an electrical signal that is read out by an electronic readout chip (ROC); each pixel has its own electronics which amplifies the signal. Combining the signal from the pixels activated by a traversing particle in the several layers of the detector allows one to reconstruct the particle's trajectory in 3D.

Commonly, the charge produced by traversing of a particle is collected by and shared among several pixels; by interpolating between pixels, the spatial resolution is improved. In the barrel section the charge sharing in the $r\phi$ -plane is due to the Lorentz effect. In the forward pixels the charge sharing is enhanced by arranging the

1248 blades in the turbine-like layout as shown in Figure 2.13 bottom left.

1249 2.3.3 Silicon strip tracker

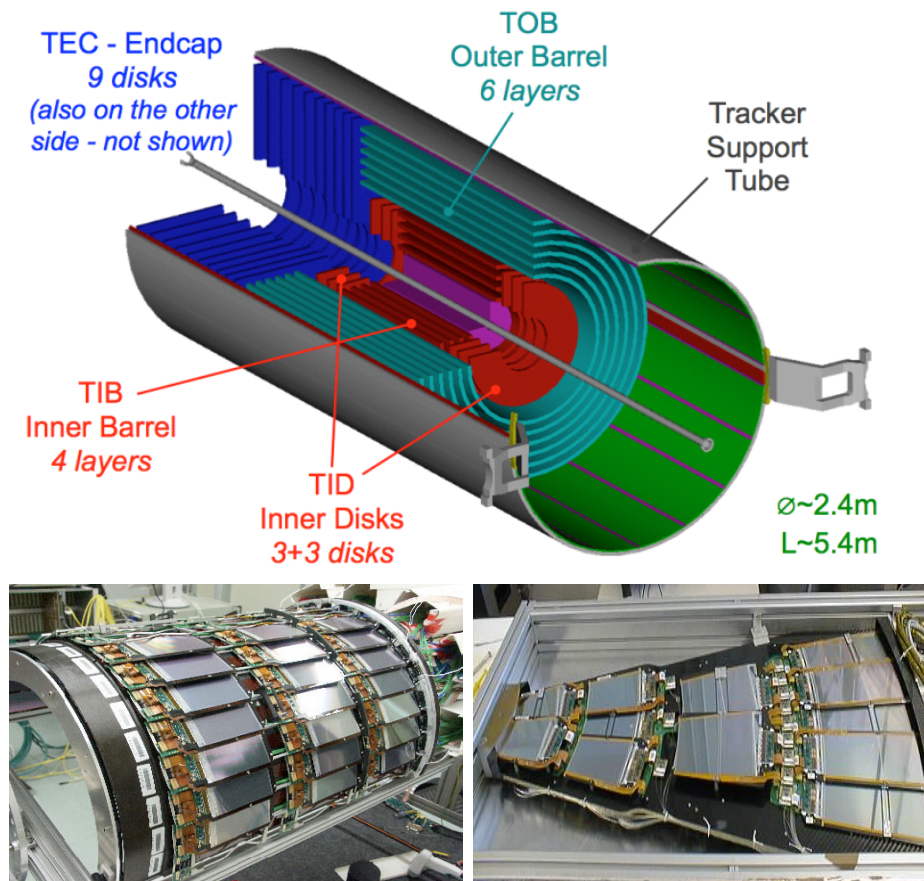


Figure 2.14: Top: CMS Silicon Strip Tracker (SST) schematic view. The SST is composed of the tracker inner barrel (TIB), the tracker inner disks (TID), the tracker outer barrel (TOB) and the tracker endcaps (TEC). Each part is made of silicon strip modules; the modules in blue represent two modules mounted back-to-back and rotated in the plane of the module by a stereo angle of 120 mrad in order to provide a 3-D reconstruction of the hit positions. Bottom: pictures of the TIB (left) and TEC (right) modules [80–82].

1250 The silicon strip tracker (SST) is the second stage in the CMS tracking system.

1251 The top side of Figure 2.14 shows a schematic of the SST. The inner tracker region is

1252 composed of the tracker inner barrel (TIB) and the tracker inner disks (TID) covering

1253 the region $r < 55$ cm and $|z| < 118$ cm. The TIB is composed of 4 layers while the TID

1254 is composed of 3 disks at each end. The silicon sensors in the inner tracker are 320
 1255 μm thick, providing a resolution of about 13-38 μm in the $r\phi$ position measurement.

1256 The modules indicated in blue in the schematic view of Figure 2.14 are two mod-
 1257 ules mounted back-to-back and rotated in the plane of the module by a *stereo* angle
 1258 of 100 mrad; the hits from these two modules, known as *stereo hits*, are combined to
 1259 provide a measurement of the second coordinate (z in the barrel and r on the disks)
 1260 allowing the reconstruction of hit positions in 3-D.

1261 The outer tracker region is composed of the tracker outer barrel (TOB) and the
 1262 tracker endcaps (TEC). The six layers of the TOB offer coverage in the region $r > 55$
 1263 cm and $|z| < 118$ cm, while the 9 disks of the TEC cover the region $124 < |z| < 282$
 1264 cm. The resolution offered by the outer tracker is about 13-38 μm in the $r\phi$ position
 1265 measurement. The inner four TEC disks use silicon sensors 320 μm thick; those in
 1266 the TOB and the outer three TEC disks use silicon sensors of 500 μm thickness. The
 1267 silicon strips run parallel to the z -axis and the distance between strips varies from 80
 1268 μm in the inner TIB layers to 183 μm in the inner TOB layers; in the endcaps the
 1269 wedge-shaped sensors with radial strips, whose pitch range between 81 μm at small
 1270 radii and 205 μm at large radii.

1271 The whole SST has 15148 silicon modules, 9.3 million silicon strips and cover a
 1272 total active area of about 198 m^2 .

1273 2.3.4 Electromagnetic calorimeter

1274 The CMS electromagnetic calorimeter (ECAL) is designed to measure the energy of
 1275 electrons and photons. It is composed of 75848 lead tungstate crystals which have a
 1276 short radiation length (0.89 cm) and fast response, since 80% of the light is emitted
 1277 within 25 ns; however, they are combined with Avalanche photodiodes (APDs) as

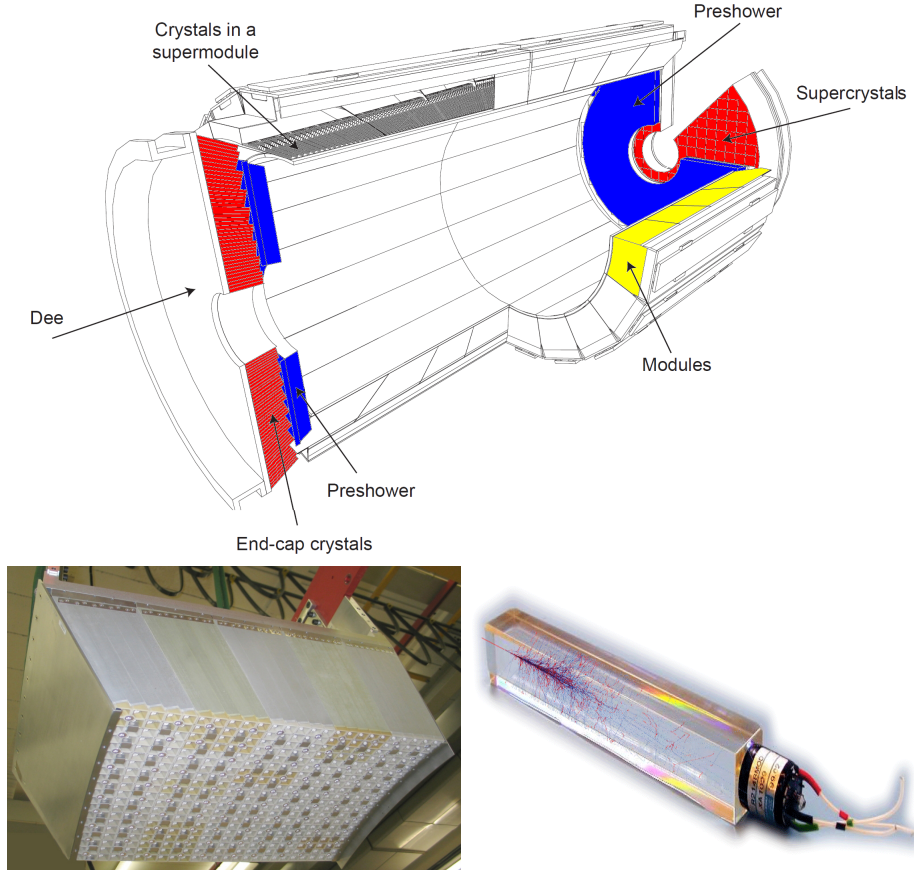


Figure 2.15: Top: CMS ECAL schematic view. Bottom: Module equipped with the crystals (left); ECAL crystal(right) with an artistic representation of an electromagnetic shower [74].

1278 photodetectors given that crystals themselves have a low light yield ($30\gamma/\text{MeV}$). A
 1279 schematic view of the ECAL is shown in Figure 2.15.

1280 Energy is measured when electrons and photons are absorbed by the crystals
 1281 which generates an electromagnetic *shower*, as seen in bottom right picture of the
 1282 Figure 2.15; the shower is seen as a *cluster* of energy which depending on the amount
 1283 of energy deposited can involve several crystals. The ECAL barrel (EB) covers the
 1284 region $|\eta| < 1.479$, using crystals of depth of 23 cm and $2.2 \times 2.2 \text{ cm}^2$ transverse
 1285 section; the ECAL endcap (EE) covers the region $1.479 < |\eta| < 3.0$ using crystals of
 1286 depth 22 cm and transverse section of $2.86 \times 2.86 \text{ cm}^2$; the photodetectors used are

vacuum phototriodes (VPTs). Each EE is divided in two structures called *Dees*.

The preshower detector (ES) is installed in front of the EE and covers the region $1.653 < |\eta| < 2.6$. The ES provides a precise measurement of the position of electromagnetic showers, which allows to distinguish electrons and photon signals from π^0 decay signals. The ES is composed of a layer of lead radiators followed by a layer of silicon strip sensors. The lead radiators initiate electromagnetic showers when reached by photons and electrons, then, the strip sensors measure the deposited energy and the transverse shower profiles. The full ES thickness is 20 cm.

2.3.5 Hadronic calorimeter

Hadrons are not absorbed by the ECAL² but by the hadron calorimeter (HCAL), which is made of a combination of alternating brass absorber layers and silicon photomultiplier(SiPM) layers; therefore, particles passing through the scintillator material produce showers, as in the ECAL, as a result of the inelastic scattering of the hadrons with the detector material. Since the particles are not absorbed in the scintillator, their energy is sampled; therefore the total energy is not measured but estimated from the energy clusters, which reduces the resolution of the detector. Brass was chosen as the absorber material due to its short interaction length ($\lambda_I = 16.42\text{cm}$) and its non-magnetivity. Figure 2.16 shows a schematic view of the CMS HCAL.

The HCAL is divided into four sections; the Hadron Barrel (HB), the Hadron Outer (HO), the Hadron Endcap (HE) and the Hadron Forward (HF) sections. The HB covers the region $0 < |\eta| < 1.4$, while the HE covers the region $1.3 < |\eta| < 3.0$. The HF, made of quartz fiber scintillator and steel as absorption material, covers the forward region $3.0 < |\eta| < 5.2$. Both the HB and HF are located inside the solenoid. The HO is placed outside the magnet as an additional layer of scintillators with the

² Most hadrons are not absorbed, but few low-energy ones might be.

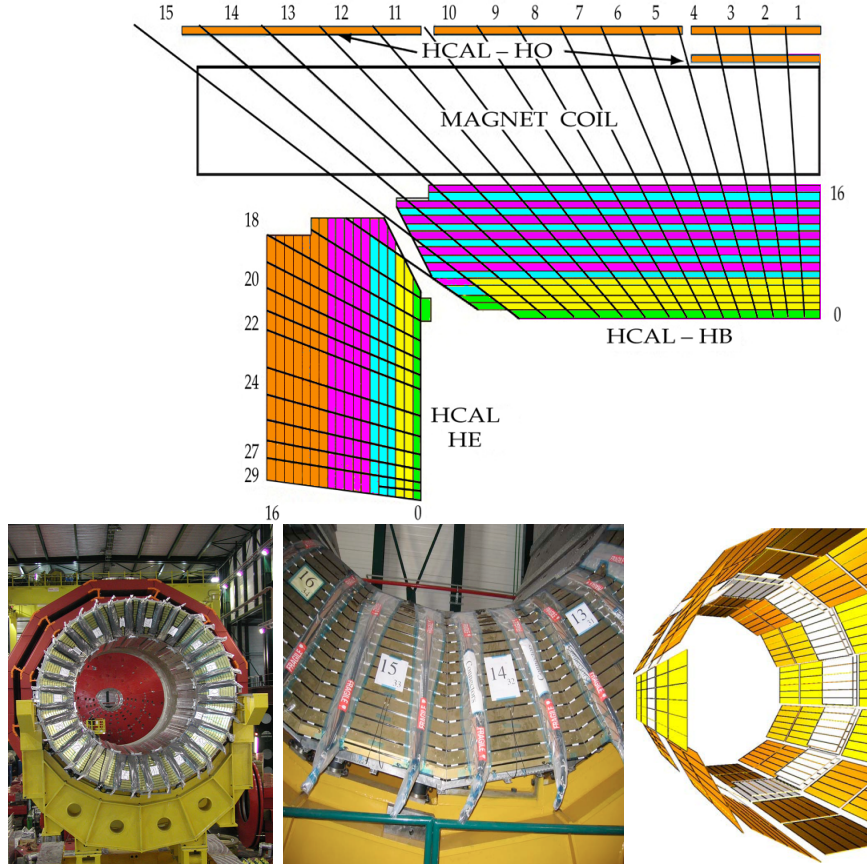


Figure 2.16: Top: CMS HCAL schematic view, the colors indicate the layers that are grouped into the same readout channels. Bottom: picture of a section of the HB; the absorber material is the golden region and scintillators are placed in between the absorber material (left and center). Schematic view of the HO (right). [83,84]

1311 purpose of measure the energy tails of particles passing through the HB and the
 1312 magnet (see Figure 2.16 top and bottom right).

1313 **2.3.6 Superconducting solenoid magnet**

1314 The superconducting magnet installed in the CMS detector is designed to provide
 1315 an intense and highly uniform magnetic field in the central part of the detector.
 1316 In fact, the tracking system takes advantage of the bending power of the magnetic
 1317 field to measure with precision the momentum of the particles that traverse it; the

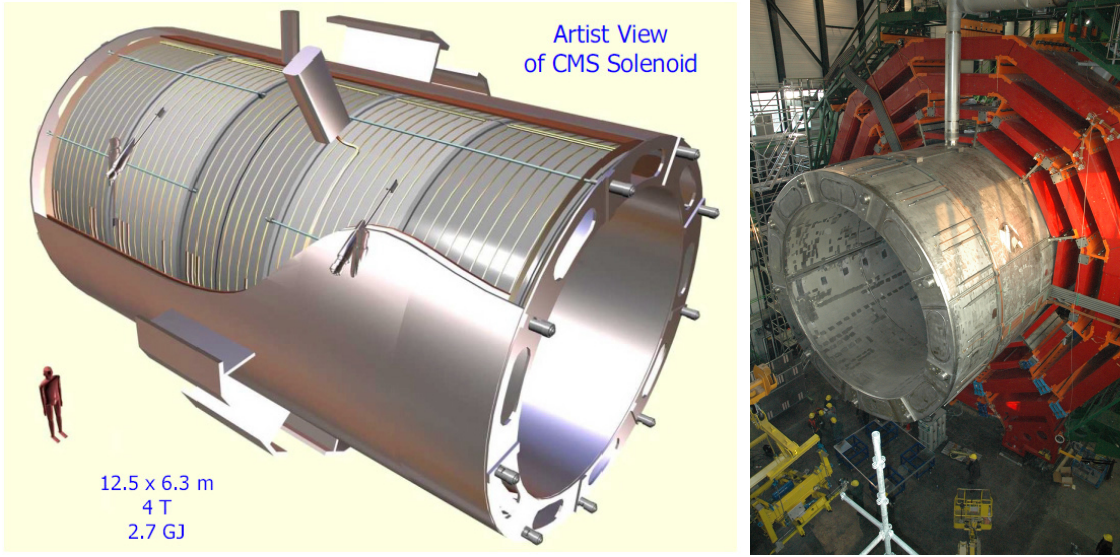


Figure 2.17: Artistic representation of the CMS solenoid magnet(left). The magnet is supported on an iron yoke (right) which also serves as the house of the muon detector and as mechanical support for the whole CMS detector [77].

1318 unambiguous determination of the sign for high momentum muons was a driving
 1319 principle during the design of the magnet. The magnet has a diameter of 6.3 m, a
 1320 length of 12.5 m and a cold mass of 220 t; the generated magnetic field reaches a
 1321 strength of 3.8T. Since it is made of Ni-Tb superconducting cable it has to operate at
 1322 a temperature of 4.7 K by using a helium cryogenic system; the current circulating in
 1323 the cables reaches 18800 A under normal running conditions. The left side of Figure
 1324 2.17 shows an artistic view of the CMS magnet, while the right side shows a transverse
 1325 view of the cold mass where the winding structure is visible.

1326 The yoke (see Figure 2.17), composed of 5 barrel wheels and 6 endcap disks made
 1327 of iron, serves not only as the media for magnetic flux return but also provides housing
 1328 for the muon detector system and structural stability to the full detector.

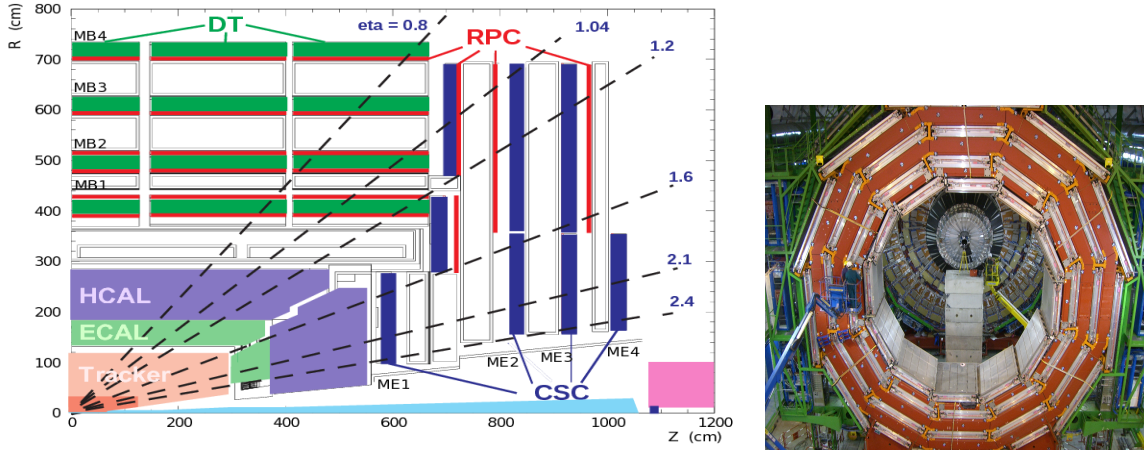


Figure 2.18: Left: CMS muon system schematic view; Right: one of the yoke rings with the muon DTs and RPCs installed; in the back it is possible to see the muon endcap [85].

1329 2.3.7 Muon system

1330 Muons are the only charged particles able to pass through all the CMS detector due
 1331 to their low ionization energy loss; thus, muons can be separated easily from the
 1332 high amount of particles produced in a pp collision. Also, muons are expected to be
 1333 produced in the decay of several new particles; therefore, good detection of muons
 1334 was one of the leading principles when designing the CMS detector.

1335 The CMS muon detection system (muon spectrometer) is embedded in the return
 1336 yoke as seen in Figure 2.18. It is composed of three different detector types, the drift
 1337 tube chambers (DT), cathode strip chambers (CSC), and resistive plate chambers
 1338 (RPC); DT are located in the central region $\eta < 1.2$ arranged in four layers of drift
 1339 chambers filled with an Ar/CO₂ gas mixture.

1340 The muon endcaps are made of CSCs covering the region $\eta < 2.4$ and filled with
 1341 a mixture of Ar/CO₂/CF₄. The reason behind using a different detector type lies on
 1342 the different conditions in the forward region like the higher muon rate and higher
 1343 residual magnetic field compared to the central region.

1344 The third type of detector used in the muon system is a set of four disks of RPCs

1345 working in avalanche mode. The RPCs provide good spatial and time resolutions. The
 1346 track of high- p_T muon candidates is built combining information from the tracking
 1347 system and the signal from up to six RPCs and four DT chambers.

1348 The muon tracks are reconstructed from the hits in the several layers of the muon
 1349 system.

1350 2.3.8 CMS trigger system

1351 CMS expects pp collisions every 25 ns, i.e., an interaction rate of 40 MHz for which
 1352 it is not possible to store the recorded data in full. In order to handle this high event
 1353 rate data, an online event selection, known as triggering, is performed; triggering
 1354 reduces the event rate to 100 Hz for storage and further offline analysis.

1355 The trigger system starts with a reduction of the event rate to 100 kHz in the
 1356 so-called *the level 1 trigger* (L1). L1 is based on dedicated programmable hardware
 1357 like Field Programmable Gate Arrays (FPGAs) and Application Specific Integrated
 1358 Circuits (ASICs), partly located in the detector itself; another portion is located in
 1359 the CMS underground cavern. Hit pattern information from the muon chambers
 1360 and the energy deposits in the calorimeter are used to decide if an event is accepted
 1361 or rejected, according to selection requirements previously defined, which reflect the
 1362 interesting physics processes. Figure 2.19 shows the L1 trigger architecture.

1363 The second stage in the trigger system is called *the high-level trigger* (HLT); events
 1364 accepted by L1 are passed to HLT in order to make an initial reconstruction of them.
 1365 HLT is software based and runs on a dedicated server farm, using selection algorithms
 1366 and high-level object definitions; the event rate at HLT is reduced to 100 Hz. The
 1367 first HLT stage takes information from the muon detectors and the calorimeters to
 1368 make the initial object reconstruction; in the next HLT stage, information from the

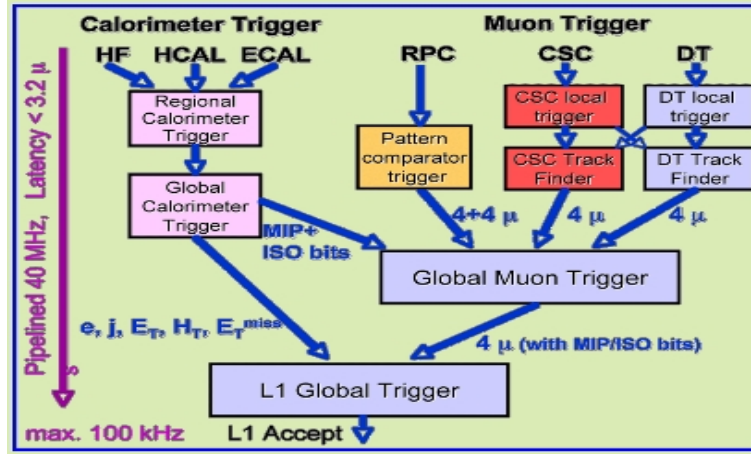


Figure 2.19: CMS Level-1 trigger architecture [86].

pixel and strip detectors is used to do first fast tracking and then full tracking online.
 This initial object reconstruction is used in further steps of the trigger system.

Events and preliminary reconstructed physics objects from HLT are sent to be fully reconstructed at the CERN computing center known also as Tier-0 facility. Again, the pixel detector information provides high-quality seeds for the track reconstruction algorithm offline, primary vertex reconstruction, electron and photon identification, muon reconstruction, τ identification, and b-tagging. After full reconstruction, data sets are made available for offline analyses.

2.3.9 CMS computing

Data coming from the experiment have to be stored and made available for further analysis; in order to cope with all the tasks implied in the offline data processing, like transfer, simulation, reconstruction and reprocessing, among others, a large computing power is required. The CMS computing system is based on the distributed architecture concept, where users of the system and physical computer centers are distributed worldwide and interconnected by high-speed networks.

The worldwide LHC computing grid (WLCG) is the mechanism used to provide

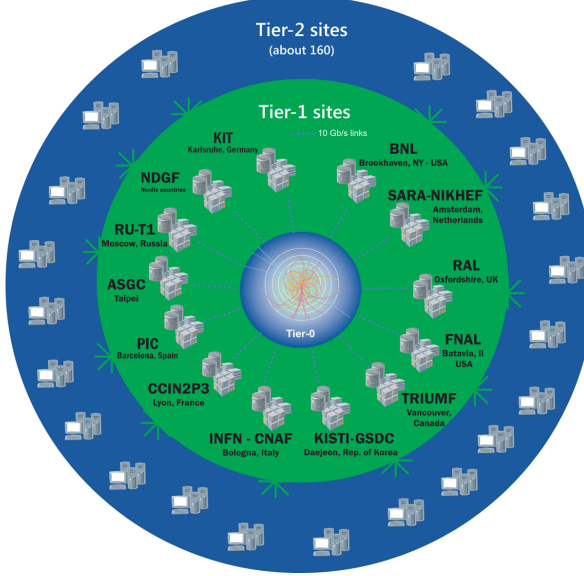


Figure 2.20: WLCG structure. The primary computer centers (Tier-0) are located at CERN (data center) and at the Wigner datacenter in Budapest. Tier-1 is composed of 13 centers and Tier-2 is composed of about 160 centers. [87].

1385 that distributed environment. WLCG is a tiered structure connecting computing
 1386 centers around the world, which provides the necessary storage and computing facil-
 1387 ities. The primary computing centers of the WLCG are located at the CERN and
 1388 the Wigner datacenter in Budapest and are known as Tier-0 as shown in Figure 2.20.
 1389 The main responsibilities for each tier level are [87]

- 1390 • **Tier-0:** initial reconstruction of recorded events and storage of the resulting
 1391 datasets, the distribution of raw data to the Tier-1 centers.
- 1392 • **Tier-1:** provide storage capacity, support for the Grid, safe-keeping of a pro-
 1393 portional share of raw and reconstructed data, large-scale reprocessing and safe-
 1394 keeping of corresponding output, generation of simulated events, distribution
 1395 of data to Tier 2s, safe-keeping of a share of simulated data produced at these
 1396 Tier 2s.
- 1397 • **Tier-2:** store sufficient data and provide adequate computing power for spe-

1398 cific analysis tasks and proportional share of simulated event production and
1399 reconstruction.

1400 Aside from the general computing strategy to manage the huge amount of data
1401 produced by experiments, CMS uses a software framework to perform a variety of
1402 processing, selection and analysis tasks. The central concept of the CMS data model
1403 referred to as *event data model* (EDM) is the *Event*; therefore, an event is the unit
1404 that contains the information from a single bunch crossing, any data derived from
1405 that information like the reconstructed objects, and the details of the derivation.

1406 Events are passed as the input to the *physics modules* that obtain information
1407 from them and create new information; for instance, *event data producers* add new
1408 data into the events, *analyzers* produce an information summary from an event set,
1409 *filters* perform selection and triggering.

1410 CMS uses several event formats with different levels of detail and precision

1411 • **Raw format:** events in this format contain the full recorded information from
1412 the detector as well as trigger decision and other metadata. An extended version
1413 of raw data is used to store information from the CMS Monte Carlo simulation
1414 tools (see Chapter 3). Raw data are stored permanently, occupying about
1415 2MB/event

1416 • **RECO format:** events in this format correspond to raw data that have been
1417 submitted to reconstruction algorithms like primary and secondary vertex re-
1418 construction, particle ID, and track finding. RECO events contain physics ob-
1419 jects and all the information used to reconstruct them; average size is about 0.5
1420 MB/event.

- 1421 • **AOD format:** Analysis Object Data (AOD) is the data format used in the
 1422 physics analyses given that it contains the parameters describing the high-level
 1423 physics objects in addition to enough information to allow a kinematic refitting if
 1424 needed. AOD events are filtered versions of the RECO events to which skimming
 1425 or other filtering have been applied, hence AOD events are subsets of RECO
 1426 events. Requires about 100 kB/event.
- 1427 • **Non-event data** are data needed to interpret and reconstruct events. Some
 1428 of the non-event data used by CMS contains information about the detector
 1429 contraction and condition data like calibrations, alignment, and detector status.

1430 Figure 2.21 shows the data flow scheme between CMS detector and tiers.

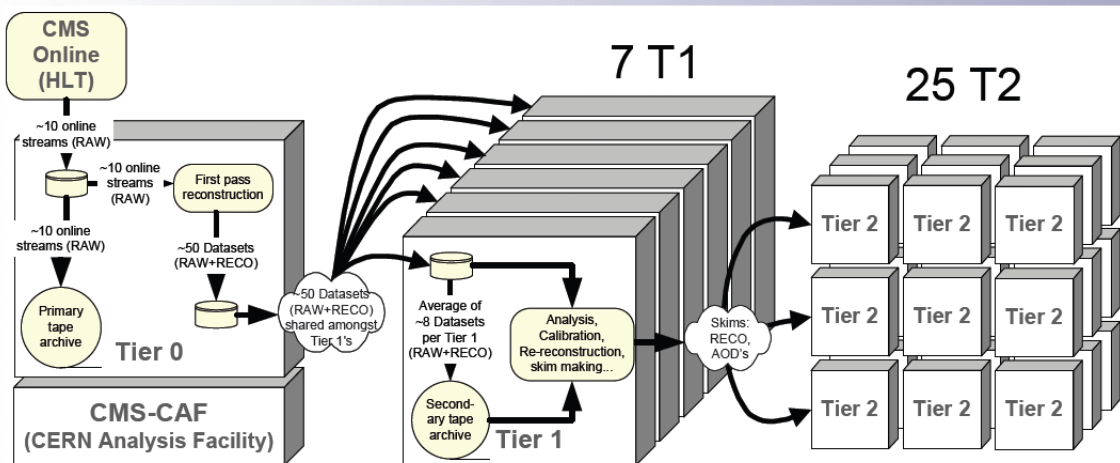


Figure 2.21: Data flow from CMS detector through tiers.

1431 The whole collection of software built as a framework is referred to as *CMSSW*. This
 1432 framework provides the services needed by the simulation, calibration and alignment,
 1433 and reconstruction modules that process event data, so that physicists can perform
 1434 analysis. The CMSSW event processing model is composed of one executable, called
 1435 `cmsRun`, and several plug-in modules which contains all the tools (calibration, recon-

1436 struction algorithms) needed to process an event. The same executable is used for
1437 both detector data and Monte Carlo simulations [88].

¹⁴³⁸ **Chapter 3**

¹⁴³⁹ **Event generation, simulation and**
¹⁴⁴⁰ **reconstruction**

¹⁴⁴¹ The process of analyzing data recorded by the CMS experiment involves several stages
¹⁴⁴² where the data are processed in order to interpret the information provided by all
¹⁴⁴³ the detection systems; in those stages, the particles produced after the pp collision
¹⁴⁴⁴ are identified by reconstructing their trajectories and measuring their features. In
¹⁴⁴⁵ addition, the SM provides a set of predictions that have to be compared with the
¹⁴⁴⁶ experimental results; however, in most of the cases, theoretical predictions are not
¹⁴⁴⁷ directly comparable to experimental results due to the diverse source of uncertainties
¹⁴⁴⁸ introduced by the experimental setup and theoretical approximations, among others.

¹⁴⁴⁹

¹⁴⁵⁰ The strategy to face these conditions consists in using statistical methods imple-
¹⁴⁵¹ mented in computational algorithms to produce numerical results that can be con-
¹⁴⁵² trasted with the experimental results. These computational algorithms are commonly
¹⁴⁵³ known as Monte Carlo (MC) methods and, in the case of particle physics, they are
¹⁴⁵⁴ designed to apply the SM rules and produce predictions about the physical observ-

ables measured in the experiments. Since particle physics is governed by quantum mechanics principles, predictions are not allowed from single events; therefore, a high number of events are *generated* and predictions are produced in the form of statistical distributions for the observables. Effects of the detector presence are included in the predictions by introducing simulations of the detector itself.

1460

1461 This chapter presents a description of the event generation strategy and the tools
 1462 used to perform the detector simulation and physics objects reconstruction. A com-
 1463 prehensive review of event generators for LHC physics can be found in Reference [89]
 1464 on which this chapter is based.

1465 3.1 Event generation

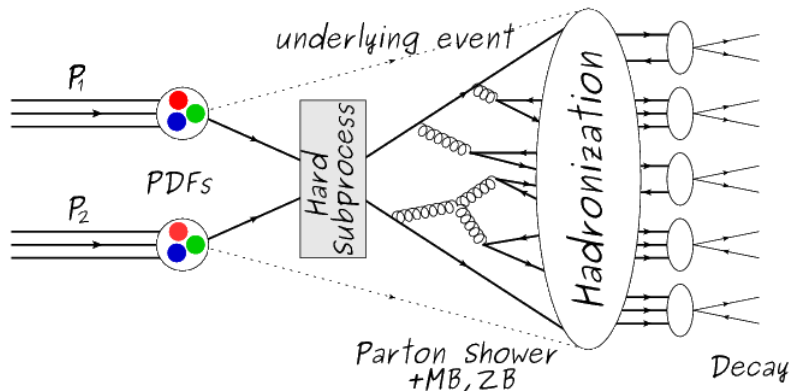


Figure 3.1: Event generation process. The actual interaction is generated in the hard subprocess. The parton shower describes the evolution of the partons from the hard subprocess. Modified from Reference [90].

1466 The event generation is intended to create events that mimic the behavior of ac-
 1467 tual events produced in collisions; they obey a sequence of steps from the particles
 1468 collision hard process to the decay process into the final state. Figure 3.1 shows a
 1469 schematic view of the event generation process; the fact that the full process can be

1470 treated as several independent steps is motivated by the QCD factorization theorem.

1471

1472 Generation starts by taking into account the PDFs of the incoming particles.

1473 Event generators offer the option to chose from several PDF sets depending on the

1474 particular process under simulation¹; in the following, pp collisions will be consid-

1475 ered. The *hard subprocess* describes the actual interaction between partons from the

1476 incoming protons; it is represented by the matrix element connecting the initial and

1477 final states of the interaction. Normally, the matrix element can be written as a sum

1478 over Feynman diagrams and consider interferences between terms in the summation.

1479 During the generation of the hard subprocess, the production cross section is calcu-

1480 lated.

1481

1482 The order to which the cross section is calculated depends on the order of the Feyn-

1483 man diagrams involved in the calculation; therefore, radiative corrections are included

1484 by considering a higher order Feynman diagrams where QCD radiation dominates.

1485 Currently, cross sections calculated to LO do not offer a satisfactory description of the

1486 processes, i.e., the results are only reliable for the shape of distributions; therefore,

1487 NLO calculations have to be performed with the implication that the computing time

1488 needed is highly increased.

1489

1490 The final parton content of the hard subprocess is subjected to the *parton shower*

1491 which generates the gluon radiation. Parton shower evolves the partons, i.e., glouns

1492 split into quark-antiquark pairs and quarks with enough energy radiate gluons giv-

1493 ing rise to further parton multiplication, following the DGLAP (Dokshitzer-Gribov-

1494 Lipatov-Altarelli-Parisi) equations. Showering continues until the energy scale is low

¹ Tool in Reference [91] allows to plot different PDF sets under customizable conditions.

1495 enough to reach the non-perturbative limit.

1496

1497 In the simulation of LHC processes that involve b quarks, like the single top quark
 1498 or Higgs associated production, it is needed to consider that the b quark is heavier
 1499 than the proton; hence, the QCD interaction description is made in two different
 1500 schemes [95]

1501 • four-flavor (4F) scheme. b quarks appear only in the final state because they
 1502 are heavier than the proton and therefore they can be produced only from the
 1503 splitting of a gluon into pairs or singly in association with a t quark in high
 1504 energy-scale interactions; furthermore, during the simulation, the b -PDFs are set
 1505 to zero. Calculations in this scheme are more complicated due to the presence
 1506 of the second b quark but the full kinematics is considered already at LO and
 1507 therefore the accuracy of the description is better.

1508 • five-flavor (5F) scheme. b quarks are considered massless, therefore they can
 1509 appear in both initial and final states since they can now be part of the proton;
 1510 thus, during the simulation b -PDFs are not set to zero. In this scheme, calcu-
 1511 lations are simpler than in the 4F scheme and possible logarithmic divergences
 1512 are absorbed by the PDFs through the DGLAP evolution.

1513 In this thesis, the tHq events are generated using the 4F scheme in order to reduce
 1514 uncertainties, while the tHW events are generated using the 5F scheme to eliminate
 1515 LO interference with $t\bar{t}H$ process [48].

1516

1517 Partons involved in the pp collision are the focus of the simulation, however, the
 1518 rest of the partons inside the incoming protons are also affected because the remnants
 1519 are colored objects; also, multiple parton interactions can occur. The hadronization

1520 of the remnants and multiple parton interactions are known as *underlying event* and
 1521 it has to be included in the simulation. In addition, multiple pp collisions in the same
 1522 bunch crossing (pile-up mentioned in 2.2) occurs, actually in two forms

- 1523 • *in-time PU* which refers to multiple pp collision in the bunch crossing but that
 1524 are not considered as primary vertices.
- 1525 • *Out-of-time PU* which refers to overlapping pp collisions from consecutive bunch
 1526 crossings; this can occur due to the time-delays in the detection systems where
 1527 information from one bunch crossing is assigned to the next or previous one.

1528 While the underlying event effects are included in generation using generator-
 1529 specific tools, PU effects are added to the generation by overlaying Minimum-bias
 1530 (MB) and Zero-bias (ZB) events to the generated events. MB events are inelastic
 1531 events selected by using a loose trigger with as little bias as possible, therefore ac-
 1532 cepting a large fraction of the overall inelastic event; ZB events correspond to random
 1533 events recorded by the detector when collisions are likely. MB models in-time PU
 1534 and ZB models out-of-time PU.

1535

1536 The next step in the generation process is called *hadronization*. Since particles
 1537 with a net color charge are not allowed to exits isolated, they have to recombine
 1538 to form bound states. This is precisely the process by which the partons resulting
 1539 from the parton shower arrange themselves as color singlets to form hadrons. At
 1540 this step, the energy-scale is low and the strong coupling constant is large, there-
 1541 fore hadronization process is non-perturbative and the evolution of the partons is
 1542 described using phenomenological models. Most of the baryons and mesons produced
 1543 in the hadronization are unstable and hence they will decay in the detector.

1544

1545 The last step in the generation process corresponds to the decay of the unstable
 1546 particles generated during hadronization; it is also simulated in the hadronization
 1547 step, based on the known branching ratios.

1548 **3.2 Monte Carlo Event Generators.**

1549 The event generation described in the previous section has been implemented in
 1550 several software packages for which a brief description is given.

- 1551 • **PYTHIA 8.** It is a program designed to perform the generation of high energy
 physics events which describes the collisions between particles such as electrons
 and protons. Several theories and models are implemented in it, in order to
 describe physical aspects like hard and soft interaction, parton distributions,
 initial and final-state parton showers, multiple parton interactions, beam rem-
 nants, hadronization² and particle decay. Thanks to extensive testing, several
 optimized parametrizations, known as *tunings*, have been defined in order to
 improve the description of actual collisions to a high degree of precision; for
 analysis at $\sqrt{s} = 13$ TeV, the underline event CUETP8M1 tune is employed [97].
 The calculation of the matrix element is performed at LO which is not enough
 for the current required level of precision; therefore, pythia is often used for
 parton shower, hadronization and decays, while other event generators are used
 to generate the matrix element at NLO.

- 1564 • **MadGraph5_aMC@NLO.** MadGraph is a matrix element generator which
 calculates the amplitudes for all contributing Feynman diagrams of a given pro-
 cess but does not provide a parton shower while MC@NLO incorporates NLO

² based in the Lund string model [96]

1567 QCD matrix elements consistently into a parton shower framework; thus, Mad-
 1568 Graph5_aMC@NLO, as a merger of the two event generators MadGraph5 and
 1569 aMC@NLO, is an event generator capable to calculate tree-level and NLO cross
 1570 sections and perform the matching of those with the parton shower. It is one of
 1571 the most frequently used matrix element generators; however, it has the partic-
 1572 ular feature of the presence of negative event weights which reduce the number
 1573 of events used to reproduce the properties of the objects generated [98].

1574

1575 • **POWHEG.** It is an NLO matrix element generator where the hardest emis-
 1576 sion of color charged particles is generated in such a way that the negative event
 1577 weights issue of MadGraph5_aMC@NLO is overcome; however, the method re-
 1578 quires an interface with p_T -ordered parton shower or a parton shower generator
 1579 where this highest emission can be vetoed in order to avoid double counting of
 1580 this highest-energetic emission. PYTHIA is a commonly matched to POWHEG
 1581 event generator [100].

1582 Events resulting from the whole generation process are known as MC events.

1583 3.3 CMS detector simulation.

1584 After generation, MC events contain the physics of the collisions but they are not
 1585 ready to be compared to the events recorded by the experiment since these recorded
 1586 events correspond to the response of the detection systems to the interaction with
 1587 the particles traversing them. The simulation of the CMS detector has to be applied
 1588 on top of the event generation; it is simulated with a MC toolkit for the simulation
 1589 of particles passing through matter called Geant4 which is also able to simulate the

1590 electronic signals that would be measured by all detectors inside CMS.

1591

1592 The simulation takes the generated particles contained in the MC events as input,
1593 makes them pass through the simulated geometry, and models physics processes that
1594 particles experience during their passage through matter. The full set of results from
1595 particle-matter interactions corresponds to the simulated hit which contains informa-
1596 tion about the energy loss, momentum and position. Particles of the input event are
1597 called *primary*, while the particles originating from GEANT4-modeled interactions of
1598 a primary particle with matter are called a *secondary*. Simulated hits are the input
1599 of subsequent modules that emulate the response of the detector readout system and
1600 triggers. The output from the emulated detection systems and triggers is known as
1601 digitization [101, 102].

1602

1603 The modeling of the CMS detector corresponds to the accurate modeling of the
1604 interaction among particles, the detector material, and the magnetic field. This
1605 simulation procedure includes the following standard steps

1606 • Modeling of the Interaction Region.

1607 • Modeling of the particle passage through the hierarchy of volumes that compose
1608 CMS detector and of the accompanying physics processes.

1609 • Modeling of the effect of multiple interactions per beam crossing and/or the
1610 effect of events overlay (Pile-Up simulation).

1611 • Modeling of the detector's electronics response, signal shape, noise, calibration
1612 constants (digitization).

1613 In addition to the full simulation, i.e., a detailed detector simulation, a faster sim-
 1614 ulation (FastSim) have been developed, that may be used where much larger statistics
 1615 are required. In FastSim, detector material effects are parametrized and included in
 1616 the hits; those hits are used as input of the same higher-level algorithms³ used to an-
 1617 alyze the recorded events. In this way, comparisons between fast and full simulations
 1618 can be performed [104].

1619

1620 After the full detector simulation, the output events can be directly compared
 1621 to events actually recorded in the CMS detector. The collection of MC events that
 1622 reproduces the expected physics for a given process is known as MC sample.

1623 **3.4 Event reconstruction.**

1624 The CMS experiment use the *particle-flow event reconstruction algorithm (PF)* to do
 1625 the reconstruction of particles produced in pp collisions. Next sections will present
 1626 a basic description of the *Elements* used by PF (tracker tracks, energy clusters, and
 1627 muon tracks), based in the References [105, 106] where more detailed descriptions can
 1628 be found.

1629 **3.4.1 Particle-Flow Algorithm.**

1630 Each of the several sub detection systems of the CMS detector is dedicated to identify
 1631 an specific type of particles, i.e., photons and electrons are absorbed by the ECAL
 1632 and their reconstruction is based on ECAL information; hadrons are reconstructed
 1633 from clusters in the HCAL while muons are reconstructed from hits in the muon

³ track fitting, calorimeter clustering, b tagging, electron identification, jet reconstruction and calibration, trigger algorithms which will be considered in the next sections

1634 chambers. PF is designed to correlate signals from all the detector layers (tracks and
 1635 energy clusters) in order to reconstruct and identify each final state particle and its
 1636 properties as sketched in Figure 3.2.

1637

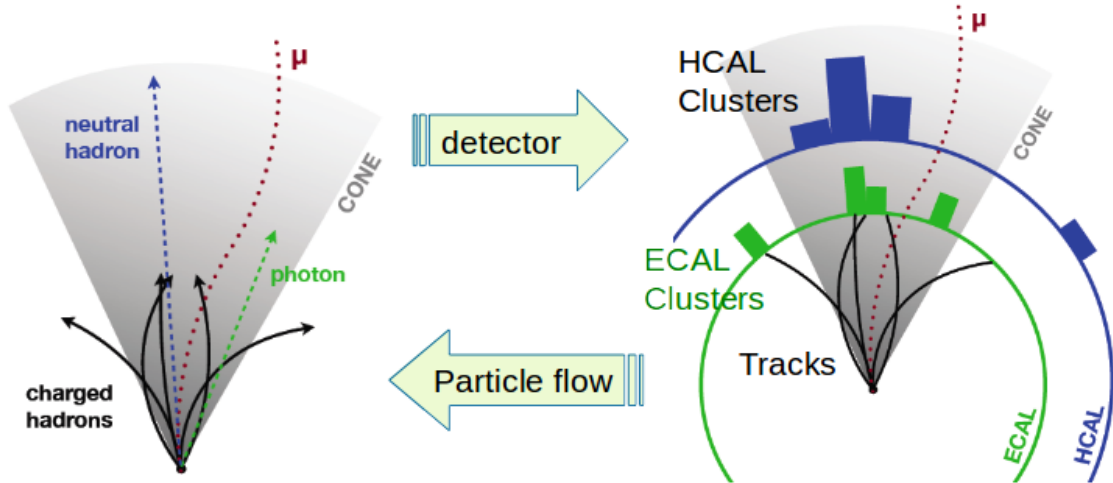


Figure 3.2: Particle flow algorithm. Information from the several CMS detection systems is provided as input to the algorithm which then combine it to identify and reconstruct all the particles in the final state and their properties. Reconstruction of simulated events is also performed by providing information from MC samples, detector and trigger simulation [107].

1638 For instance, a charged hadron is identified by a geometrical connection, known
 1639 as *link*, between one or more calorimeter clusters and a track in the tracker, provided
 1640 there are no hits in the muon system; combining several measurements allows a better
 1641 determination of the energy and charge sign of the charged hadron.

1642 Charged-particle track reconstruction.

1643 The strategy used by PF in order to reconstruct tracks is called *Iterative Tracking*
 1644 which occurs in four steps

- 1645 • Seed generation where initial track candidates are found by looking for a combi-
 1646 nation of hits in the pixel detector, strip tracker, and muon chambers. In total

1647 ten iterations are performed, each one with a different seeding requirement.
 1648 Seeds are used to estimate the trajectory parameters and uncertainties at the
 1649 time of the full track reconstruction. Seeds are also considered track candidates.

- 1650 • Track finding using a tracking software known as Combinatorial Track Finder
 1651 (CTF) [108]. The seed trajectories are extrapolated along the expected flight
 1652 path of a charged particle, in agreement to the trajectory parameters obtained
 1653 in the first step, in an attempt to find additional hits that can be assigned to
 1654 the track candidates.
- 1655 • Track-fitting where the found tracks are passed as input to a module which
 1656 provides the best estimate of the parameters of each trajectory.
- 1657 • Track selection where track candidates are submitted to a selection which dis-
 1658 cards those that fail a set of defined quality criteria.

1659 Iterations differ in the seeding configuration and the final track selection as elab-
 1660 orated in References [105, 106]. In the first iteration, high p_T tracks and tracks pro-
 1661 duced near to the interaction region are identified and those hits are masked thereby
 1662 reducing the combinatorial complexity. Next, iterations search for more complicated
 1663 tracks, like low p_T tracks and tracks from b hadron decays, which tend to be displaced
 1664 from the interaction region.

1665 **Vertex reconstruction.**

1666 During the track reconstruction, an extrapolation toward to the calorimeters is per-
 1667 formed in order to match energy deposits; that extrapolation is performed also toward
 1668 the beamline in order to find the origin of the track known as *vertex*. The vertex re-
 1669 construction is performed by selecting from the available reconstructed tracks, those

1670 that are consistent with being originated in the interaction region where pp collisions
 1671 are produced. The selection involves a requirement on the number of tracker (pixel
 1672 and strip) hits and the goodness of the track fit.

1673

1674 Selected tracks are clustered using a *deterministic annealing algorithm (DA)*⁴. A
 1675 set of candidate vertices and their associated tracks, resulting from the DA, are then
 1676 fitted with an *adaptive vertex fitter (AVF)* to produce the best estimate of the vertices
 1677 locations.

1678

1679 The p_T of the tracks associated to a reconstructed vertex is added, squared and
 1680 used to organize the vertices; the vertex with the highest squared sum is designated
 1681 as the *primary vertex (PV)* while the rest are designated as PU vertices.

1682 Calorimeter clustering.

1683 After traversing the CMS tracker system, electrons, photons and hadrons deposit their
 1684 energy in the ECAL and HCAL cells. The PF clustering algorithm aims to provide
 1685 a high detection efficiency even for low-energy particles and an efficient distinction
 1686 between close energy deposits. The clustering runs independently in the ECAL barrel
 1687 and endcaps, HCAL barrel and endcaps, and the two preshower layers, following two
 1688 steps

- 1689 • cells with an energy larger than a given seed threshold and larger than the energy
 1690 of the neighboring cells are identified as cluster seeds. The neighbor cells are
 1691 those that either share a side with the cluster seed candidate, or the eight closest
 1692 cells including cells that only share a corner with the seed candidate.

⁴ DA algorithm and AVF are described in detail in References [110,111]

1693 • cells with at least a corner in common with a cell already in the cluster seed
 1694 and with an energy above a cell threshold are grouped into topological clusters.

1695 Clusters formed in this way are known as *particle-flow clusters*. With this cluster-
 1696 ing strategy, it is possible to detect and measure the energy and direction of photons
 1697 and neutral hadrons as well as differentiate these neutral particles from the charged
 1698 hadron energy deposits. In cases involving charged hadrons for which the track pa-
 1699 rameters are not determined accurately, for instance, low-quality and high- p_T tracks,
 1700 clustering helps in the energy measurements.

1701 **Electron track reconstruction.**

1702 Although the charged-particle track reconstruction described above works for elec-
 1703 trons, they lose a significant fraction of their energy via bremsstrahlung photon radi-
 1704 ation before reaching the ECAL; thus, the reconstruction performance depends on the
 1705 ability to measure also the radiated energy. The reconstruction strategy, in this case,
 1706 requires information from the tracking system and from the ECAL. Bremsstrahlung
 1707 photons are emitted at similar η values to that of the electron but at different values
 1708 of ϕ ; therefore, the radiated energy can be recovered by grouping ECAL clusters in a
 1709 η window over a range of ϕ around the electron direction. The group is called ECAL
 1710 supercluster.

1711 Electron candidates from the track-seeding and ECAL super clustering are merged
 1712 into a single collection which is submitted to a full electron tracking fit with a
 1713 Gaussian-sum filter (GSF) [109]. The electron track and its associated ECAL su-
 1714 percluster form a *particle-flow electron*.

1715 **Muon track reconstruction.**

1716 Given that the CMS detector is equipped with a muon spectrometer capable to iden-
 1717 tify and measure the momentum of the muons traversing it, the muon reconstruction
 1718 is not specific to PF; therefore, three different muon types are defined

- 1719 • *Standalone muon.* A clustering on the DTs or CSCs hits is performed to form
 1720 track segments; those segments are used as seeds for the reconstruction in the
 1721 muon spectrometer. All DTs, CSCs, and RPCs hits along the muon trajectory
 1722 are combined and fitted to form the full track. The fitting output is called a
 1723 *standalone-muon track*.
- 1724 • *Tracker muon.* Each track in the inner tracker with p_T larger than 0.5 GeV and
 1725 a total momentum p larger than 2.5 GeV is extrapolated to the muon system.
 1726 A *tracker muon track* corresponds to a extrapolated track that matches at least
 1727 one muon segment.
- 1728 • *Global muon.* When tracks in the inner tracker (inner tracks) and standalone-
 1729 muon tracks are matched and turn out being compatibles, their hits are com-
 1730 bined and fitted to form a *global-muon track*.

1731 Global muons sharing the same inner track with tracker muons are merged into
 1732 a single candidate. PF muon identification uses the muon energy deposits in ECAL,
 1733 HCAL, and HO associated with the muon track to improve the muon identification.

1734 **Particle identification and reconstruction.**

1735 PF elements are connected by a linker algorithm that tests the connection between any
 1736 pair of elements; if they are found to be linked, a geometrical distance that quantifies
 1737 the quality of the link is assigned. Two elements may be linked indirectly through

1738 common elements. Linked elements form *PF blocks* and each PF block may contain
 1739 elements originating in one or more particles. Links can be established between
 1740 tracks, between calorimeter clusters, and between tracks and calorimeter clusters.
 1741 The identification and reconstruction start with a PF block and proceed as follows

1742 • Muons. An *isolated global muon* is identified by evaluating the presence of
 1743 inner track and energy deposits close to the global muon track in the (η, ϕ)
 1744 plane, i.e., in a particular point of the global muon track, inner tracks and
 1745 energy deposits are sought within a radius of $\Delta R = 0.3$ (see eqn. 2.7) from the
 1746 muon track; if they exit and the p_T of the found track added to the E_T of the
 1747 found energy deposit does not exceed 10% of the muon p_T then the global muon
 1748 is an isolated global muon. This isolation condition is stringent enough to reject
 1749 hadrons misidentified as muons.

1750 *Non-isolated global muons* are identified using additional selection requirements
 1751 on the number of track segments in the muon system and energy deposits along
 1752 the muon track. Muons inside jets are identified with more stringent criteria
 1753 in isolation and momentum as described in Reference [112]. The PF elements
 1754 associated with an identified muon are masked from the PF block.

1755 • Electrons are identified and reconstructed as described above plus some addi-
 1756 tional requirements on fourteen variables like the amount of energy radiated,
 1757 the distance between the extrapolated track position at the ECAL and the po-
 1758 sition of the associated ECAL supercluster, among others, which are combined
 1759 in an specialized multivariate analysis strategy that improves the electron iden-
 1760 tification. Tracks and clusters used to identify and reconstruct electrons are
 1761 masked in the PF block.

- 1762 ● Isolated photons are identified from ECAL superclusters with E_T larger than 10
 1763 GeV, for which the energy deposited at a distance of 0.15, from the supercluster
 1764 position on the (η,ϕ) plane, does not exceed 10% of the supercluster energy;
 1765 note that this is an isolation requirement. In addition, there must not be links
 1766 to tracks. Clusters involved in the identification and reconstruction are masked
 1767 in the PF block.

- 1768 ● Bremsstrahlung photons and prompt photons tend to convert to electron-positron
 1769 pairs inside the tracker, therefore, a dedicated finder algorithm is used to link
 1770 tracks that seem to originate from a photon conversion; in case those two tracks
 1771 are compatible with the direction of a bremsstrahlung photon, they are also
 1772 linked to the original electron track. Photon conversion tracks are also masked
 1773 in the PF block.

- 1774 ● The remaining elements in the PF block are used to identify hadrons. In the
 1775 region $|\eta| \leq 2.5$, neutral hadrons are identified with HCAL clusters not linked
 1776 to any track while photons from neutral pion decays are identified with ECAL
 1777 clusters without links to tracks. In the region $|\eta| > 2.5$ ECAL clusters linked to
 1778 HCAL clusters are identified with a charged or neutral hadron shower; ECAL
 1779 clusters with no links are identified with photons. HCAL clusters not used yet,
 1780 are linked to one or more unlinked tracks and to an unlinked ECAL in order to
 1781 reconstruct charged-hadrons or a combination of photons and neutral hadrons
 1782 according to certain conditions on the calibrated calorimetric energy.

- 1783 ● Charged-particle tracks may be liked together when they converge to a *sec-
 1784 ondary vertex (SV)* displaced from the IP where the PV and PU vertices are
 1785 reconstructed; at least three tracks are needed in that case, of which at most

1786 one has to be an incoming track with hits in tracker region between a PV and
 1787 the SV.

1788 The linker algorithm, as well as the whole PF algorithm, has been validated and
 1789 commissioned; results from that validation are presented in the Reference [105].

1790 **Jet reconstruction.**

1791 Quarks and gluons may be produced in the pp collisions, therefore, their hadronization
 1792 will be seen in the detector as a shower of hadrons and their decay products in the
 1793 form of a *jet*. Two classes of clustering algorithms have been developed based in
 1794 their jet definition [113]:

- 1795 • Iterative cone algorithms (IC). Jets are defined in terms of circles of fixed radius
 1796 R in the $\eta\text{-}\phi$ plane, known as *stable cones*, for which the sum of the momenta
 1797 of all the particles within the cone points in the same direction as the center
 1798 of the circle. The seed of the iteration is the hardest non-isolated particle in
 1799 the event, then, the resulting momentum direction is assigned as the new cone
 1800 direction and a new iteration starts; iteration process stops when the cone is
 1801 found to be stable.
- 1802 • Sequential recombination algorithms. The distance between non-isolated par-
 1803 ticles is calculated; if that distance is below a threshold, these particles are
 1804 recombined into a new object. The sequence is repeated until the separation
 1805 between the recombined object and any other particle is above certain thresh-
 1806 old; the recombined object is called a jet and the algorithm starts again with
 1807 the remaining particles.

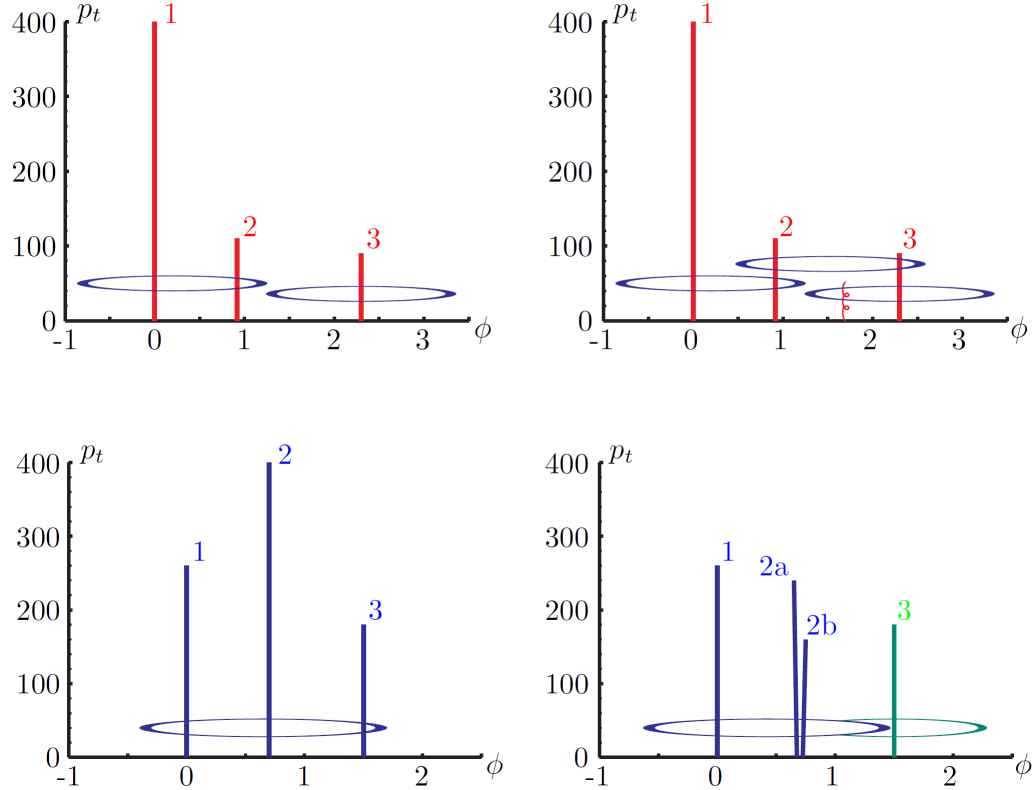


Figure 3.3: Stable cones identification using IC algorithms [113].

1808 Two conditions are of particular importance for the clustering algorithms, *infrared*
 1809 *and collinear (IRC) safety*. In order to explain the concept of infrared (IR) safety,
 1810 consider an event with three hard particles as shown in the top left side of Figure 3.3,
 1811 two stable cones are found and then two jets are identified; if a soft gluon is added, as
 1812 shown in the top right side of Figure 3.3, three stable cones are found and the three
 1813 hard particles are now clustered into a single jet. If the addition of soft particles
 1814 change the outcome of the clustering, then it is said that the algorithm is IR unsafe.
 1815 Soft radiation is highly likely in perturbative QCD, which dominates the physics of
 1816 the jets, and then IR unsafe effect leads to divergences [113].

1817 The concept of collinear safety can also be explained considering a three hard
 1818 particles event, as shown in the bottom left side of Figure 3.3, where one stable cone
 1819 containing all three particles is found and one jet is identified; if the hardest particle

1820 is split into two collinear particles (2a and 2b) in the bottom right side of Figure 3.3,
 1821 then the clustering results in a different jet identification and the algorithm is said
 1822 to be collinear unsafe. The collinear unsafe effect leads to divergences in jet cross
 1823 section calculations [114].

1824 It has been determined that IC algorithms are IRC unsafe, and therefore, they
 1825 have to be replaced by algorithms that not only provide the finite perturbative results
 1826 from theoretical computations, but also that are not highly dependent on underlying
 1827 event and pileup effects which leads to significant corrections [113].

1828 The sequential recombination algorithms arise as the IRC safe alternative used by
 1829 the CMS experiment; in particular the anti- k_t algorithm which is a generalization of
 1830 the previously existing k_t [115] and Cambridge/Aachen [116] jet clustering algorithms.

1831 The anti- k_t algorithm is used to perform the jet reconstruction by clustering those
 1832 PF particles within a cone (see Figure 3.4); previously, isolated electrons, isolated
 1833 muons, and charged particles associated with other interaction vertices are excluded
 1834 from the clustering.

1835 The anti- k_t algorithm proceeds in a sequential recombination of PF particles; the
 1836 distance between particles i and j (d_{ij}) and the distance between particles and the
 1837 beam are defined as

$$d_{ij} = \min \left(\frac{1}{k_{ti}^2}, \frac{1}{k_{tj}^2} \right) \frac{\Delta_{ij}^2}{R^2}$$

$$d_{iB} = \frac{1}{k_{ti}^2} \quad (3.1)$$

1838 where $\Delta_{ij}^2 = (y_i - y_j)^2 + (\phi_i - \phi_j)^2$, k_{ti} , y_i and ϕ_i are the transverse momentum, ra-
 1839 pidity and azimuth of particle i respectively and R is the called jet radius. For all
 1840 the remaining PF particles, after removing the isolated ones, d_{ij} and d_{iB} are calcu-

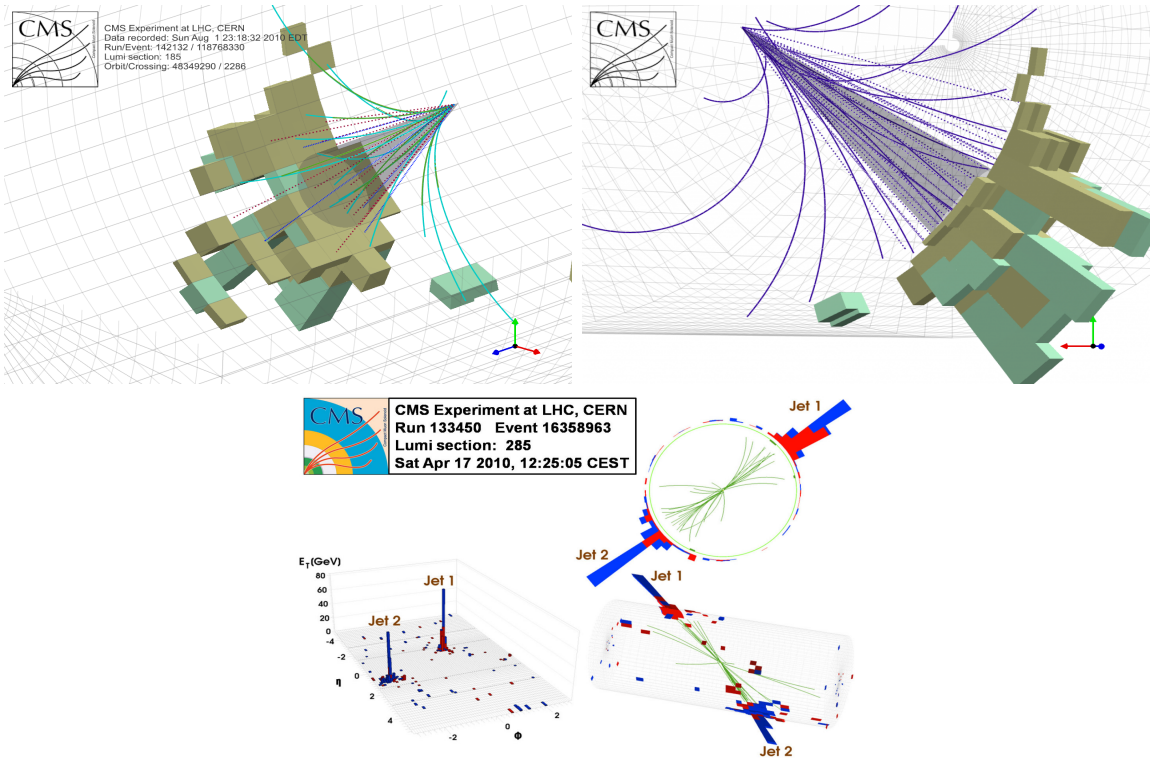


Figure 3.4: Jet reconstruction performed by the anti- k_t algorithm. Top: Two different views of a CMS recorded event are presented. Continuous lines correspond to tracks left by charged particles in the tracker while dotted lines are the imaginary paths followed by neutral particles. The green cubes represent the ECAL cells while the blue ones represent the HCAL cells; in both cases, the height of the cube represent the amount of energy deposited in the cells [117]. Bottom: Reconstruction of a recorded event with two jets [118].

lated⁵ and the smallest is identified; if it is a d_{ij} , particles i and j are replaced with a new object whose momentum is the vectorial sum of the combined particles. If the smallest distance is a d_{iB} the clustering process ends, the object i (which at this stage should be a combination of several PF particles) is declared as a *Particle-flow-jet* (PF jet) and all the associated PF particles are removed from the detector. The clustering process is repeated until no PF particles remain. R is a free parameter that can be adjusted according to the specific analysis conditions; usually, two values are used, $R=0.4$ and $R=0.5$, giving the name to the so-called AK4-jet and AK5-jet respectively.

⁵ Notice that this is a combinatorial calculation.

1849 An advantage of the anti- k_t algorithm over other clustering algorithms is the reg-
 1850 ularity of the boundaries of the resulting jets. For all known IRC safe algorithms,
 1851 soft radiation can introduce irregularities in the boundaries of the final jets; however,
 1852 anti- k_t algorithm is soft-resilient, meaning that jets shape is not affected by soft radi-
 1853 ation, which is a valuable property considering that knowing the typical shape of jets
 1854 makes experimental calibration of jets more simple. In addition, that soft-resilience
 1855 is expected to simplify certain theoretical calculations and reduce the momentum-
 1856 resolution loss caused by underlying-event (UE) and pileup contamination [114].

1857 The effect of the UE and pileup contamination over a jet identification, can be
 1858 seen as if soft events are added to the jet; for instance, if a soft event representing UE
 1859 or pileup is added to an event for which a set of jets J have been identified, and the
 1860 clustering is rerun on that new extended event, the outcome will be different in two
 1861 aspects: jets will contain some additional soft energy and the distribution of particles
 1862 in jets may have change; that effect is called *back-reaction*. The back-reaction effect in
 1863 the anti- k_t algorithm is suppressed not by the amount of momentum added to the jet
 1864 but by the jet transverse momentum $p_{T,J}$, which means that this strong suppression
 1865 leads to a smaller correction due to EU and pileup effect [114].

1866 Jet energy Corrections

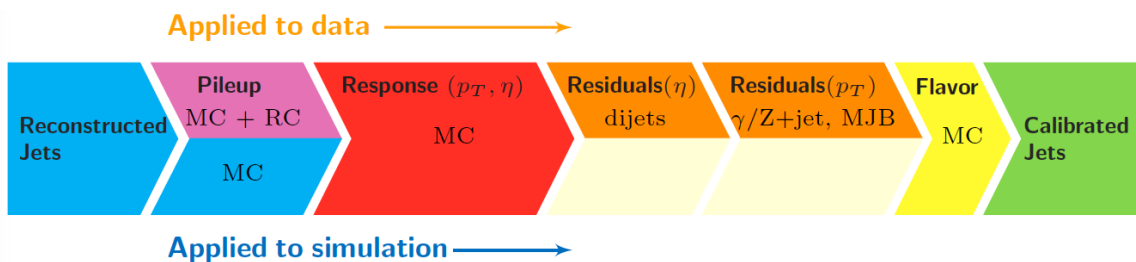


Figure 3.5: Jet energy correction diagram. Correction levels are applied sequentially in the indicated fixed order [120].

1867 Even though jets can be reconstructed efficiently, there are some effects that are
 1868 not included in the reconstruction and that lead to discrepancies between the re-
 1869 constructed results and the predicted results; in order to overcome these discrep-
 1870 ancies, a factorized model has been designed in the form of jet energy corrections
 1871 (JEC) [119, 120] applied sequentially as shown in the diagram of Figure 3.5.

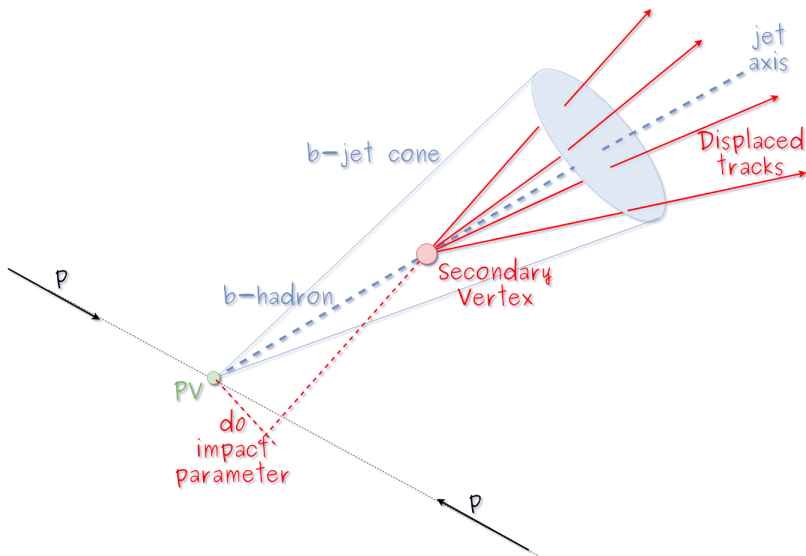
1872 At each level, the jet four-momentum is multiplied by a scaling factor based on
 1873 jet properties, i.e., η , flavor, etc.

- 1874 • Level 1 correction removes the energy coming from pile-up. The scale factor is
 1875 determined using a MC sample of QCD dijet (2 jets) events with and without
 1876 pileup overlay; it is parametrized in terms of the offset energy density ρ , jet
 1877 area A, jet η and jet p_T . Different corrections are applied to data and MC due
 1878 to the detector simulation.
- 1879 • MC-truth correction accounts for differences between the reconstructed jet en-
 1880 ergy and the MC particle-level energy. The correction is determined on a QCD
 1881 dijet MC sample and is parametrized in terms of the jet p_T and η .
- 1882 • Residuals correct remaining small differences within jet response in data and
 1883 MC. The Residuals η -dependent correction compares jets of similar p_T in the
 1884 barrel reference region. The Residuals p_T -dependent correct the jet absolute
 1885 scale (JES vs p_T).
- 1886 • Jet-flavor corrections are derived in the same way as MC-truth corrections but
 1887 using QCD pure flavor samples.

1888 ***b*-tagging of jets.**

1889 A particular feature of the hadrons containing bottom quarks (*b*-hadrons) is that
 1890 their lifetime is long enough to travel some distance before decaying, but it is not as
 1891 long as those of light quark hadrons; therefore, when looking at the hadrons produced
 1892 in $p\bar{p}$ collisions, *b*-hadrons decay typically inside the tracker rather than reaching the
 1893 calorimeters as some light-hadrons do. As a result, a *b*-hadron decay gives rise to a
 1894 displaced vertex (secondary vertex) with respect to the primary vertex as shown in
 1895 Figure 3.6; the SV displacement is in the order of a few millimeters. A jet resulting
 1896 from the decay of a *b*-hadron is called *b* jet; other jets are called light jets.

1897

**Figure 3.6:** Secondary vertex in a *b*-hadron decay.

1898 Several methods to identify *b*-jets (*b*-tagging) have been developed; the method
 1899 used in this thesis is known as *Combined Secondary Vertex* algorithm in its second
 1900 version (CSVv2) [121]. By using information of the impact parameter, the recon-
 1901 structed secondary vertices, and the jet kinematics as input in a multivariate analysis
 1902 that combines the discrimination power of each variable in one global discrimina-

1903 tor variable, three working points (references): loose, medium and tight, are defined
 1904 which quantify the probabilities of mistag jets from light quarks as jets from b quarks;
 1905 10, 1 and 0.1 % respectively. Although the mistagging probability decreases with the
 1906 working point strength, the efficiency to correctly tag b -jets also decreases as 83, 69
 1907 and 49 % for the respective working point; therefore, a balance needs to be achieved
 1908 according to the specific requirements of the analysis.

1909 **3.4.1.1 Missing transverse energy.**

1910 The fact that proton bunches carry momentum along the z -axis implies that for each
 1911 event it is expected that the momentum in the transverse plane is balanced. Imbal-
 1912 ances are quantified by the missing transverse energy (MET) and are attributed to
 1913 several sources including particles escaping undetected through the beam pipe, neu-
 1914 trinos produced in weak interactions processes which do not interact with the detector
 1915 and thus escaping without leaving a sign, or even undiscovered particles predicted by
 1916 models beyond the SM.

1917

1918 The PF algorithm assigns the negative sum of the momenta of all reconstructed
 1919 PF particles to the *particle-flow MET* according to

$$\vec{E}_T = - \sum_i \vec{p}_{T,i} \quad (3.2)$$

1920 JEC are propagated to the calculation of the \vec{E}_T as described in the Reference [122].

1921

1922 3.4.2 Event reconstruction examples

1923 Figures 3.7-3.9 show the results of the reconstruction performed on 3 recorded events.

1924 Descriptions are taken directly from the source.

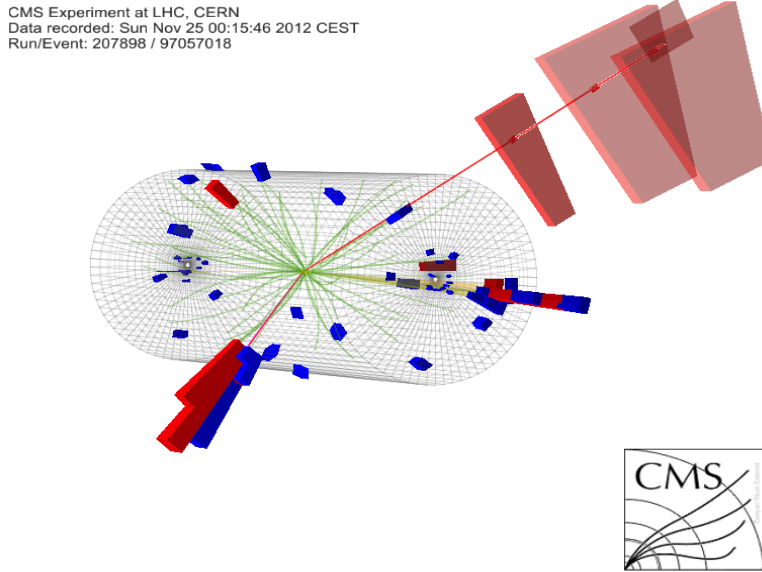


Figure 3.7: HIG-13-004 Event 1 reconstruction results; “HIG-13-004 Event 1: Event recorded with the CMS detector in 2012 at a proton-proton center-of-mass energy of 8 TeV. The event shows characteristics expected from the decay of the SM Higgs boson to a pair of τ leptons. Such an event is characterized by the production of two forward-going jets, seen here in opposite endcaps. One of the τ decays to a muon (red lines on the right) and neutrinos, while the other τ decays into a charged hadron and a neutrino.” [123].

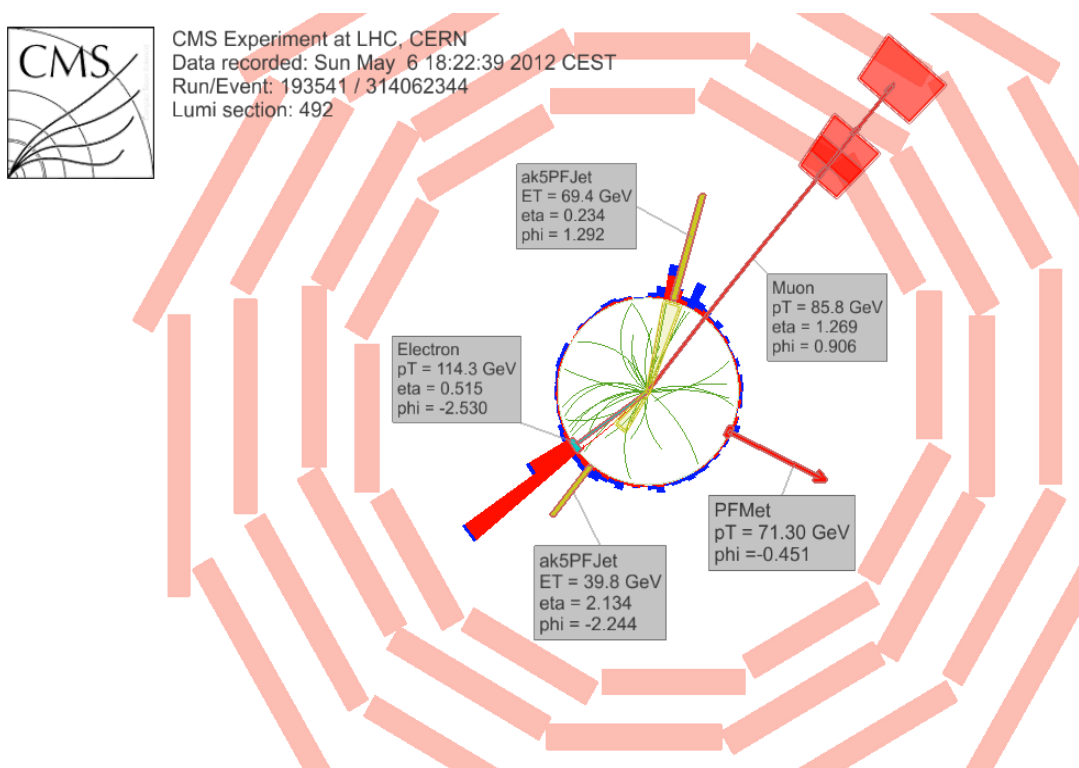


Figure 3.8: $e\mu$ event reconstruction results; “An $e\mu$ event candidate selected in 8 TeV data, as seen from the direction of the proton beams. The kinematics of the main objects used in the event selection are highlighted: two isolated leptons and two particle-flow jets. The reconstructed missing transverse energy is also displayed for reference” [124].

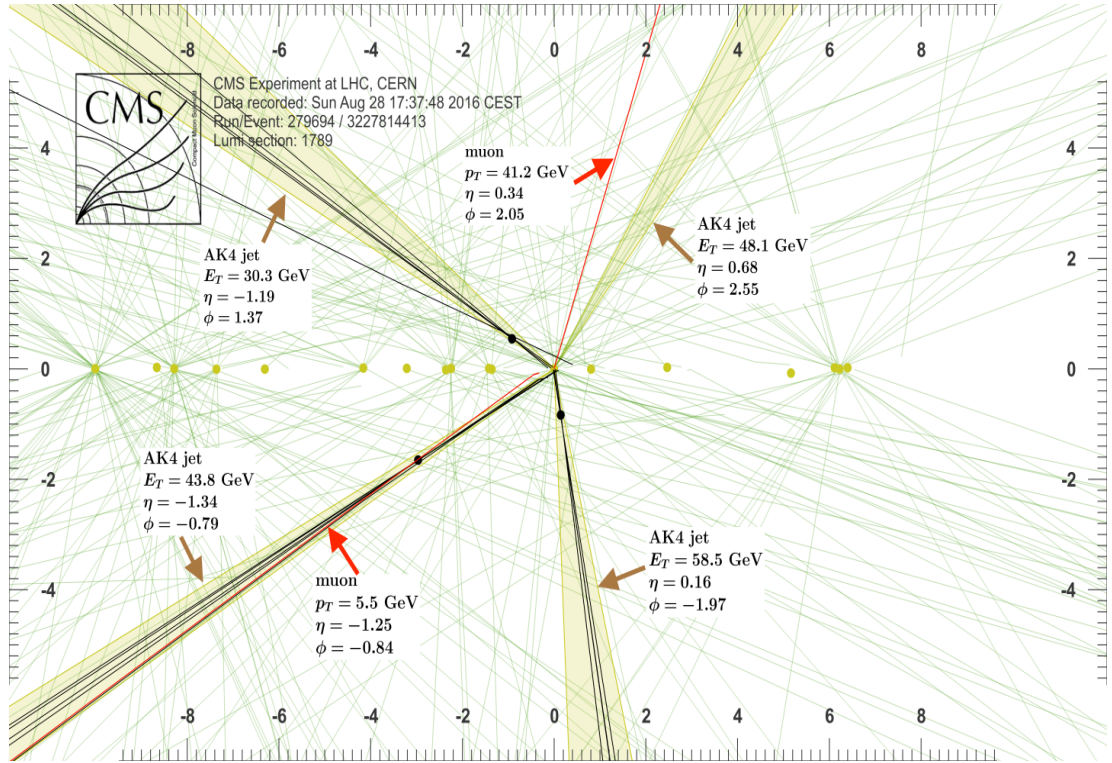


Figure 3.9: Recorded event reconstruction results; “Recorded event (ρ - z projection) with three jets with $p_T > 30$ GeV with one displaced muon track in 2016 data collected at 13 TeV. Each of the three jets has a displaced reconstructed vertex. The jet with $p_T(j) = 43.8$ GeV, $\eta(j) = -1.34$, $\phi(j) = -0.79$ contains muon with $p_T(\mu) = 5.5$ GeV, $\eta(\mu) = -1.25$, $\phi(\mu) = -0.84$. Event contains reconstructed isolated muon with $p_T(\mu) = 41.2$ GeV, $\eta(\mu) = 0.34$, $\phi(\mu) = 2.05$ and MET with $p_T = 72.5$ GeV, $\phi = -0.32$. Jet candidates for a b -jet from top quark leptonic and hadronic decays are tagged by CSVv2T algorithm. One of the other two jets is tagged by CharmT algorithm. Tracks with $p_T > 0.5$ GeV are shown. The number of reconstructed primary vertices is 18. Reconstructed $m_T(W)$ is 101.8 GeV. Beam spot position correction is applied. Reconstructed primary vertices are shown in yellow color, while reconstructed displaced vertices and associated tracks are presented in black color. Dimensions are given in cm” [125].

₁₉₂₅ **Chapter 5**

₁₉₂₆ **Statistical methods**

₁₉₂₇ In the course of analyzing the data sets provided by the CMS experiment and used in
₁₉₂₈ this thesis, several statistical tools have been employed; in this chapter, a description
₁₉₂₉ of these tools will be presented, starting with the general statement of the multivariate
₁₉₃₀ analysis methods, followed by the particularities of the Boosted Decision Trees (BDT)
₁₉₃₁ method and its application to the classification problem. Statistical inference methods
₁₉₃₂ used will also be presented. This chapter is based mainly on References [126–128].

₁₉₃₃ **5.1 Multivariate analysis**

₁₉₃₄ Multivariate data analysis (MVA) makes use of the statistical techniques developed
₁₉₃₅ to analyze more than one variable at once, taking into account all the correlations
₁₉₃₆ among variables. MVA is employed in a variety of fields like consumer and market
₁₉₃₇ researches, quality control and process optimization. Using MVA it is possible to
₁₉₃₈ identify the dominant patterns in a data sample, like groups, outliers and trends, and
₁₉₃₉ determine to which group a set of values belong; in the particle physics context, MVA
₁₉₄₀ methods are used to perform the selection of certain type of events from a large data

1941 set, e.g., a raw data input.

1942 Processes with small cross section, such as the tHq process, are hard to detect
 1943 in the presence of the processes with larger cross sections; therefore, only a small
 1944 fraction of the data contains events of interest (signal), the major part is signal-like
 1945 events, which mimic signal characteristics but belong to different process, so they are
 1946 a background to the process of interest. This implies that it is not possible to say
 1947 with certainty that a given event is a signal or a background and statistical methods
 1948 should be involved. In that sense, the challenge can be formulated as one where a
 1949 set of events have to be classified according to certain special features; these features
 1950 correspond to the measurements of several parameters like energy or momentum,
 1951 organized in a set of *input variables*. The measurements for each event can be written
 1952 in a vector $\mathbf{x} = (x_1, \dots, x_n)$ for which

1953 • $f(\mathbf{x}|s)$ is the probability density (*likelihood function*) that \mathbf{x} is the set of mea-
 1954 sured values given that the event is a signal event (signal hypothesis).

1955 • $f(\mathbf{x}|b)$ is the probability density (*likelihood function*) that \mathbf{x} is the set of mea-
 1956 sured values given that the event is a background event (background hypothe-
 1957 sis).

1958 Figure 5.1 shows three ways to perform a classification of events for which mea-
 1959 surements of two properties, i.e., two input variables x_1 and x_2 , have been performed;
 1960 blue circles represent signal events while red triangles represent background events.
 1961 The classification on the left is *cut-based* requiring $x_1 < c_1$ and $x_2 < c_2$; usually the cut
 1962 values (c_1 and c_2) are chosen according to some knowledge about the event process.
 1963 In the middle plot, the classification is performed using a linear function of the input
 1964 variables, hence the boundary is a line, while in the right plot the the relationship
 1965 between input variables is not linear thus the boundary is not linear either.

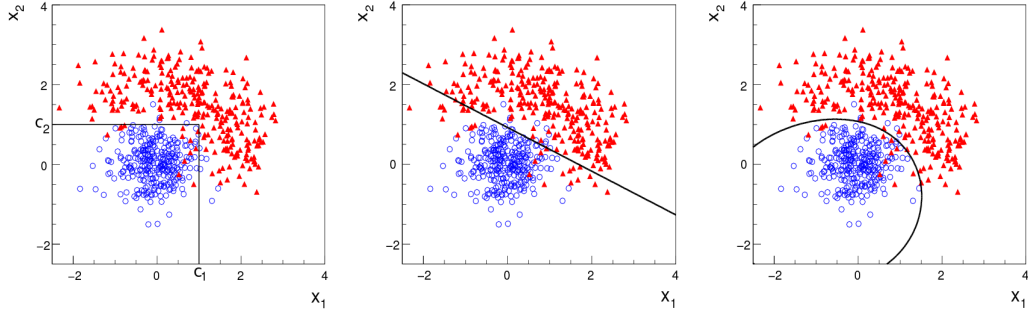


Figure 5.1: Scatter plots-MVA event classification. Distribution of two input variables x_1 and x_2 measured for a set of events; blue circles represent signal events and red triangles represent background events. The classification is based on cuts (left), linear boundary (center), and nonlinear boundary (right) [126]

1966 In general, the boundary can be parametrized in terms of the input variables such
 1967 that the cut is set on the parametrization instead of on the variables, i.e., $y(\mathbf{x}) = y_{cut}$
 1968 with y_{cut} being a constant; thus, the acceptance or rejection of an event is based on
 1969 which side of the boundary the event is located. If $y(\mathbf{x})$, usually called *test statistic*,
 1970 has functional form, it can be used to determine the probability distribution functions
 1971 $p(y|s)$ and $p(y|b)$ and then perform a scalar test statistic with a single cut on the scalar
 1972 variable y .

1973 Figure 5.2 illustrates what would be the probability distribution functions under
 1974 the signal and background hypotheses for a scalar test statistic with a cut on the
 1975 classifier y . Note that the tails of the distributions indicate that some signal events
 1976 fall on the rejection region and some background events fall on the acceptance region;
 1977 therefore, it is convenient to define the *efficiency* with which events of a given type
 1978 are accepted. The signal and background efficiencies are given by

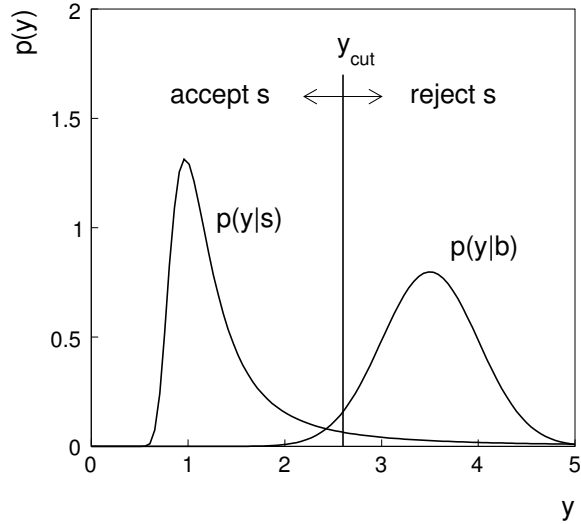


Figure 5.2: Distributions of the scalar test statistic $y(\mathbf{x})$ under the signal and background hypotheses. [126]

$$\varepsilon_s = P(\text{accept event}|s) = \int_A f(\mathbf{x}|s) d\mathbf{x} = \int_{-\infty}^{y_{cut}} p(y|s) dy , \quad (5.1)$$

$$\varepsilon_b = P(\text{accept event}|b) = \int_A f(\mathbf{x}|b) d\mathbf{x} = \int_{-\infty}^{y_{cut}} p(y|b) dy , \quad (5.2)$$

1979 where A is the acceptance region. If the background hypothesis is the *null hypothesis*
 1980 (H_0), the signal hypothesis would be *alternative hypothesis* (H_1); in this context, the
 1981 background efficiency corresponds to the significance level of the test (α) and describes
 1982 the misidentification probability, while the signal efficiency corresponds to the power
 1983 of the test ($1-\beta$) and describes the probability of rejecting the background hypothesis
 1984 if the signal hypothesis is true. What is sought in an analysis is to maximize the
 1985 power of the test relative to the significance level, i.e., set a selection with the largest
 1986 possible selection efficiency and the smallest possible misidentification probability.

1987 **5.1.1 Decision trees**

1988 For this thesis, the implementation of the MVA strategy, described above, is per-
 1989 formed through decision trees by using the TMVA software package [127] included in
 1990 the the ROOT analysis framework [129]. In a simple picture, a decision tree classifies
 1991 events according to their input variables values by setting a cut on each input variable
 1992 and checking which events are on which side of the cut, just as proposed in the MVA
 1993 strategy, but in addition, as a machine learning algorithm, decision trees offer the
 1994 possibility to be trained and then perform the classification efficiently.

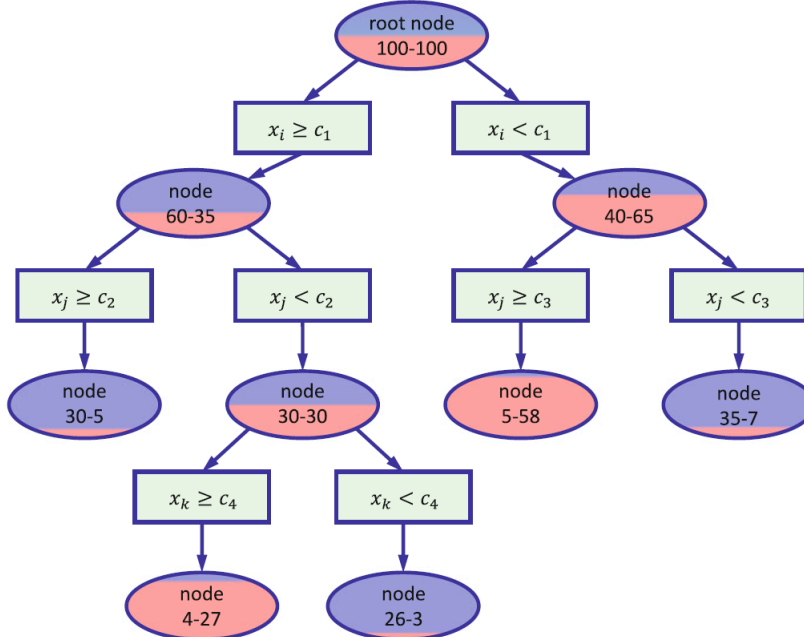


Figure 5.3: Example of a decision tree. Each node is fed with a MC sample mixing signal and background events (left-right numbers); nodes colors represent the relative number of signal/background events [128].

1995 The training or growing of a decision tree is the process where the rules for clas-
 1996 sifying events are defined; this process is represented in Figure 5.3 and consists of
 1997 several steps:

- 1998 • take MC samples of signal and background events and split them into two parts

1999 each; first parts will be used in the decision tree training, while the second parts
 2000 will be used for testing the final classifier obtained from the training. Each event
 2001 has associated a set of input variables $\mathbf{x} = (x_1, \dots, x_n)$ which serve to distinguish
 2002 between signal and background events. The training sample is taken in at the
 2003 root *node*.

- 2004 • pick one variable, say x_i
- 2005 • pick one value of x_i , each event has its own value of x_i , and split the training
 2006 sample into two subsamples B_1 and B_2 ; B_1 contains events for which $x_i < c_1$
 2007 while B_2 contains the rest of the training events;
- 2008 • scan all possible values of x_i and find the splitting value that provides the *best*
 2009 classification¹, i.e., B_1 is mostly made of signal events while B_2 is mostly made
 2010 of background events.
- 2011 • It is possible that variables other than the picked one produce a better classi-
 2012 fication, hence, all the variables have to be evaluated. Pick the next variable,
 2013 say x_j , and repeat the scan over its possible values.
- 2014 • At the end, all the variables and their values will have been scanned, the *best*
 2015 variable and splitting value will have been identified, say x_1, c_1 , and there will
 2016 be two nodes fed with the subsamples B_1 and B_2 .

2017 Nodes are further split by repeating the decision process until a given number of
 2018 final nodes is obtained, nodes are largely dominated by either signal or background
 2019 events, or nodes have too few events to continue. Final nodes are called *leaves* and
 2020 they are classified as signal or background leaves according to the class of the majority
 2021 of events in them. Each *branch* in the tree corresponds to a sequence of cuts.

¹ Quality of the classification will be treated in the next paragraph.

2022 The quality of the classification at each node is evaluated through a separation
 2023 criteria; there are several of them but the *Gini Index* (G) is the one used in the
 2024 decision trees trained for the analysis in this thesis. G is written in terms of the
 2025 purity (P), i.e., the fraction of signal events in the samples after the separation is
 2026 made; it is given by

$$G = P(1 - P) \quad (5.3)$$

2027 note that $P=0.5$ at the root node while $G=0$ for pure leaves. For a node A split into
 2028 two nodes B_1 and B_2 the G gain is

$$\Delta G = G(A) - G(B_1) - G(B_2) \quad (5.4)$$

2029 the *best* classification corresponds to that for which the gain of G is maximized; hence,
 2030 the scanning over all the variables in an event and their values is of great importance.

2031 In order to provide a numerical output for the classification, events in a sig-
 2032 nal(background) leaf are assigned an score of 1(-1) each, defining in this way the
 2033 decision tree *classifier/weak learner* as

$$f(\mathbf{x}) = \begin{cases} 1 & \mathbf{x} \text{ in signal region,} \\ -1 & \mathbf{x} \text{ in background region.} \end{cases}$$

2034 Figure 5.4 shows an example of the classification of a sample of events, containing
 2035 two variables, performed by a decision tree.

2036 5.1.2 Boosted decision trees (BDT).

2037 Event misclassification occurs when a training event ends up in the wrong leaf, i.e., a
 2038 signal event ends up in a background leaf or a background event ends up in a signal

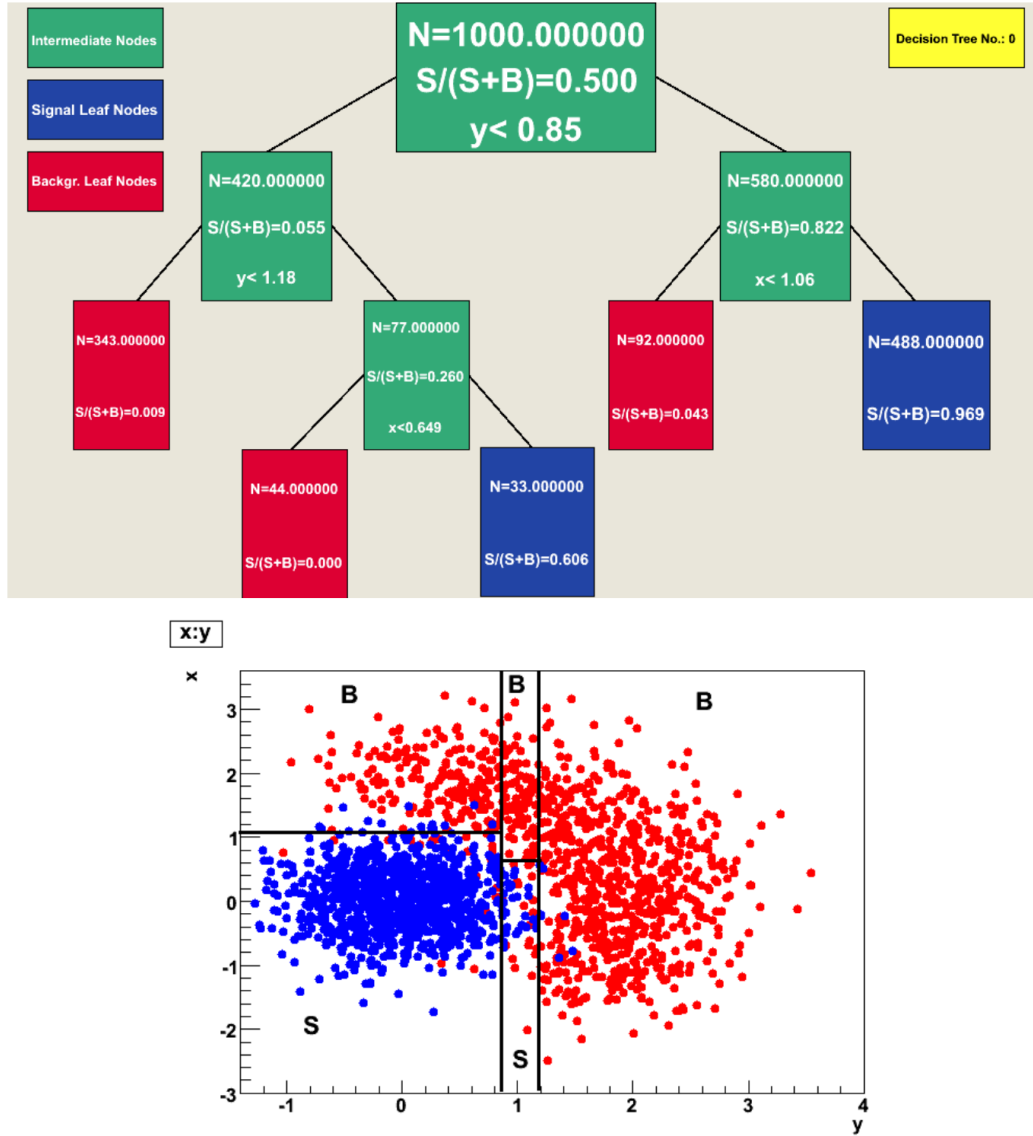


Figure 5.4: Example of a decision tree output. Each leaf, blue for signal events and red for background events, is represented by a region in the variables phase space [130].

leaf. A way to correct it is to assign a weight to the misclassified events and train a second tree using the reweighted events; the event reweighting is performed by a boosting algorithm in such a way that when used in the training of a new decision tree the *boosted events* get correctly classified. The process is repeated iteratively adding a new tree to the forest and creating a set of classifiers, which are combined

2044 to create the next classifier; the final classifier offers more stability² and has a smaller
 2045 misclassification rate than any individual ones. The resulting tree collection is known
 2046 as a *boosted decision tree (BDT)*.

2047 Thus, purity of the sample is generalized to

$$P = \frac{\sum_s w_s}{\sum_s w_s + \sum_b w_b} \quad (5.5)$$

2048 where w_s and w_b are the weights of the signal and background events respectively;
 2049 the Gini index is also generalized

$$G = \left(\sum_i^n w_i \right) P(1 - P) \quad (5.6)$$

2050 with n the number of events in the node. The final score of an event, after pass-
 2051 ing through the forest, is calculated as the renormalized sum of all the individual
 2052 (possibly weighted) scores; thus, high(low) score implies that the event is most likely
 2053 signal(background).

2054 The boosting procedure, implemented in the *Gradient boosting* algorithm used in
 2055 this thesis, produces a classifier $F(\mathbf{x})$ which is the weighted sum of the individual
 2056 classifiers obtained after each iteration, i.e.,

$$F(\mathbf{x}) = \sum_{m=1}^M \beta_m f(\mathbf{x}; a_m) \quad (5.7)$$

2057 where M is the number of trees in the forest. The *loss function* $L(F, y)$ represents the
 2058 deviation between the classifier $F(\mathbf{x})$ response and the true value y obtained from the
 2059 training sample (1 for signal events and -1 for background event), according to

² Decision trees suffer from sensitivity to statistical fluctuations in the training sample which may lead to very different results with a small change in the training samples.

$$L(F, y) = \ln(1 + e^{-2F(\mathbf{x})y}) \quad (5.8)$$

thus, the reweighting is employed to ensure the minimization of the loss function; a more detailed description of the minimization procedure can be found in Reference [131]. The final classifier output is later used as a final discrimination variable, labeled as *BDT output/response*.

5.1.3 Overtraining

Decision trees offer the possibility to have as many nodes as wished in order to reduce the misclassification to zero (in theory); however, when a classifier is too much adjusted to a particular training sample, the classifier's response to a slightly different sample may leads to a completely different classification results; this effect is known as *overtraining*.

An alternative to reduce the overtraining in BDTs consists in pruning the tree by removing statistically insignificant nodes after the tree growing is completed but this option is not available for BDTs with gradient boosting in the TMVA-toolkit, therefore, the overtraining has to be reduced by tuning the algorithm, number of nodes, minimum number of events in the leaves, etc. The overtraining can be evaluated by comparing the responses of the classifier when running over the training and test samples.

5.1.4 Variable ranking

BDTs have a couple of particular advantages related to the input variables; on one side, they are relatively insensitive to the number of input variables used in the vector \mathbf{x} . The ranking of the BDT input variables is determined by counting the number of

times a variable is used to split decision tree nodes; in addition, the separation gain-squared achieved in the splitting and the number of events in the node are accounted by applying a weighting to that number. Thus, those variables with small or no power to separate signal and background events are rarely chosen to split the nodes, i.e., are effectively ignored.

On the other side, variables correlations play an important role for some MVA methods like the Fisher discriminant algorithm in which the first step consist of performing a linear transformation to a phase space where the correlations between variables are removed; in the case of BDT algorithm, correlations do not affect the performance.

5.1.5 BDT output example.

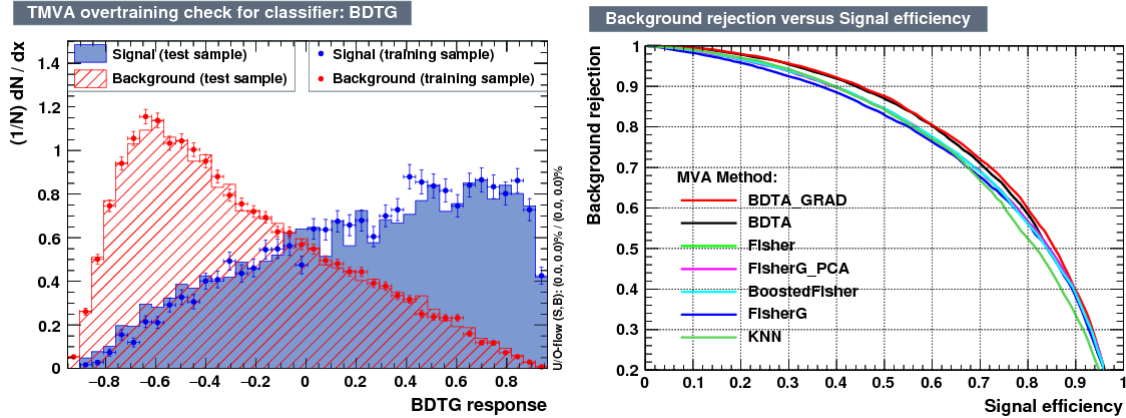


Figure 5.5: Left: Output distributions for the gradient boosted decision tree (BDTG) classifier using a sample of signal ($pp \rightarrow tHq$) and background ($pp \rightarrow t\bar{t}$) events. Right: Background rejection vs signal efficiency (ROC curves) for various MVA classifiers running over the same sample used to produce the plot on the left.

Left side of figure 5.5 shows the BDT output distributions for signal ($pp \rightarrow tHq$) and background ($pp \rightarrow t\bar{t}$) events; this plot is the equivalent to the one showed in Figure 5.2. A forest with 800 trees, maximum depth per tree = 3, and gradient

2095 boosting have been used as training parameters. The BDTG classifier offers a good
 2096 separation power; while there is a small overtraining in the signal distribution, the
 2097 background distribution seems to be well predicted which might indicate that the
 2098 sample is composed of more background than signal events.

2099 Right side of figure 5.5 shows the background rejection vs signal efficiency curves
 2100 for several combinations of MVA classifiers-boosting algorithms; these curves are
 2101 known as ROC curves and give an indication of the performance of the classifier. The
 2102 best performance is achieved with the BDTG classifier (BDTA_GRAD).

2103 5.2 Statistical inference.

2104 Once events are classified, the next step consists in finding the parameters that define
 2105 the likelihood functions $f(\mathbf{x}|s), f(\mathbf{x}|b)$ for signal and background events respectively.
 2106 In general, likelihood functions depend not only on the measurements but also on
 2107 parameters (θ_m) that define their shapes; the process of estimating these *unknown*
 2108 *parameters* and their uncertainties from the experimental data is called *inference*.

2109 The statistical inference tools used in this analysis are implemented in the RooFit
 2110 toolkit [132] and COMBINE package [133] included in the CMSSW software frame-
 2111 work.

2112 5.2.1 Nuisance parameters.

2113 The unknown parameter vector $\boldsymbol{\theta}$ is made of two types of parameters: on one side,
 2114 those parameters that provide information about the physical observables of interest
 2115 for the experiment or *parameters of interest*. On the other side, the *nuisance parame-
 2116 ters* that are not of direct interest for the experiment but that need to be included in
 2117 the analysis in order to achieve a satisfactory description of the data; they represent

2118 effects of the detector response like the finite resolutions of the detection systems,
 2119 miscalibrations, and in general any source of uncertainty introduced in the analysis.

2120 Nuisance parameters can be estimated from experimental data; for instance, data
 2121 samples from a test beam are usually employed for calibration purposes. In cases
 2122 where experimental samples are not available, the estimation of nuisance parameters
 2123 makes use of dedicated simulation programs to provide the required samples.

2124 The estimation of the unknown parameters involves certain deviation from their
 2125 true values, hence, the measurement of the nuisance parameter is written in terms
 2126 of an estimated value, also called central value, $\hat{\theta}$ and its uncertainty $\delta\theta$ using the
 2127 notation

$$\theta = \hat{\theta} \pm \delta\theta \quad (5.9)$$

2128 where the interval $[\hat{\theta} - \delta\theta, \hat{\theta} + \delta\theta]$ is called *confidence interval*; it is usually interpreted,
 2129 in the limit of infinite number of experiments, as the interval where the true value
 2130 of the unknown parameter θ is contained with a probability of 0.6827 (if no other
 2131 convention is stated); this interval represents the area under a Gaussian distribution
 2132 in the interval $\pm 1\sigma$.

2133 The uncertainties associated to nuisance parameters produce *systematic uncer-*
 2134 *tainties* in the final measurement, while the uncertainties related only to fluctuations
 2135 in data and that affect the determination of parameters of interest produce *statistical*
 2136 *uncertainties*.

2137 5.2.2 Maximum likelihood estimation method

2138 The estimation of the unknown parameters that are in best agreement with the ob-
 2139 served data is performed through a function of the data sample that return the

2140 estimate of those parameters; that function is called an *estimator*. Estimators are
 2141 usually constructed using mathematical expressions encoded in algorithms.

2142 In this thesis, the estimator used is the likelihood function $f(\mathbf{x}|\boldsymbol{\theta})$ ³ which depends
 2143 on a set of measured variables \mathbf{x} and a set of unknown parameters $\boldsymbol{\theta}$. The likelihood
 2144 function for N events in a sample is the combination of all the individual likelihoods
 2145 functions, i.e.,

$$L(\boldsymbol{\theta}) = \prod_{i=1}^N f(\mathbf{x}^i|\boldsymbol{\theta}) = \prod_{i=1}^N f(x_1^i, \dots, x_n^i; \theta_1, \dots, \theta_m) \quad (5.10)$$

2146 and the estimation method used is the *Maximum Likelihood Estimation* method
 2147 (MLE); it is based on the combined likelihood function defined by eqn. 5.10 and
 2148 the procedure seeks for the parameter set that corresponds to the maximum value of
 2149 the combined likelihood function, i.e., the *maximum likelihood estimator* of the un-
 2150 known parameter vector $\boldsymbol{\theta}$ is the function that produces the vector of *best estimators*
 2151 $\hat{\boldsymbol{\theta}}$ for which the likelihood function $L(\boldsymbol{\theta})$ evaluated at the measured \mathbf{x} is maximum.

2152 Usually, the logarithm of the likelihood function is used in numerical algorithm
 2153 implementations in order to avoid underflow the numerical precision of the computers
 2154 due to the product of low likelihoods. In addition, it is common to minimize the
 2155 negative logarithm of the likelihood function, therefore, the negative log-likelihood
 2156 function is

$$F(\boldsymbol{\theta}) = -\ln L(\boldsymbol{\theta}) = -\sum_{i=1}^N f(\mathbf{x}^i|\boldsymbol{\theta}). \quad (5.11)$$

2157 The minimization process is performed by the software MINUIT [134] imple-
 2158 mented in the ROOT analysis framework. In case of data samples with large number
 2159 of measurements, the computational resources necessary to calculate the likelihood
 2160 function are too big; therefore, the parameter estimation is performed using binned

³ analogue to the likely functions described in previous sections

2161 distributions of the variables of interest for which the *binned likelihood function* is
 2162 given by

$$L(\mathbf{x}|r, \boldsymbol{\theta}) = \prod_{i=1} \frac{(r \cdot s_i(\boldsymbol{\theta}) + b_i(\boldsymbol{\theta}))^{n_i}}{n_i!} e^{-r \cdot s_i(\boldsymbol{\theta}) - b_i(\boldsymbol{\theta})} \prod_{j=1} \frac{1}{\sqrt{2\pi}\sigma_{\theta_j}^2} e^{-(\theta_j - \theta_{0,j})^2/2\sigma_{\theta_j}^2}, \quad (5.12)$$

2163 with s_i and b_i the expected number of signal and background yields for the bin i , n_i
 2164 is the observed number of events in the bin i and $r = \sigma/\sigma_{SM}$ is the signal strength.
 2165 Note that the number of entries per bin follows a Poisson distribution. The effect
 2166 of the nuisance parameters have been included in the likelihood function through
 2167 the multiplication by a Gaussian distribution that models the nuisance. The three
 2168 parameters, r , s_i and b_i are jointly fitted to estimate the value of r .

2169 5.3 Upper limits

2170 In this analysis, two hypotheses are considered; the background only hypothesis
 2171 ($H_0(b)$) and the signal plus background hypothesis ($H_1(s+b)$), i.e., the sample of
 2172 events is composed of background only events ($r=0$) or it is a mixture of signal plus
 2173 background events ($r=1$). The exclusion of one hypothesis against the other means
 2174 that the observed data sample better agrees with H_0 or rather with H_1 . In order
 2175 to discriminate these hypotheses, a test statistic is constructed on the basis of the
 2176 likelihood function evaluated for each of the hypothesis.

2177 The *Neyman-Pearson* lemma [135] states that the test statistic that provide the
 2178 maximum power for H_1 for a given significance level (background misidentification
 2179 probability α), is given by the ratio of the likelihood functions $L(\mathbf{x}|H_1)$ and $L(\mathbf{x}|H_0)$;
 2180 however, in order to use that definition it is necessary to know the true likelihood
 2181 functions, which in practice is not always possible. Approximate functions obtained

2182 by numerical methods, like the BDT method described above, have to be used, so
 2183 that the *profile likelihood* test statistic is defined by

$$\lambda(\mathbf{r}) = \frac{L(\mathbf{x}|r, \hat{\boldsymbol{\theta}}(r))}{L(\mathbf{x}|\hat{r}, \hat{\boldsymbol{\theta}})}, \quad (5.13)$$

2184 where, \hat{r} and $\hat{\boldsymbol{\theta}}$ maximize the likelihood function, and $\hat{\boldsymbol{\theta}}$ maximize the likelihood
 2185 function for a given value of the signal strength modifier r . In practice, the test
 2186 statistic t_r

$$t_r = -2\ln\lambda(r) \quad (5.14)$$

2187 is used to evaluate the presence of signal in the sample, since the minimum of t_r at
 2188 $r = \hat{r}$ suggest the presence of signal with signal strength \hat{r} . The uncertainty interval
 2189 for r is determined by the values of r for which $t_r = 1$.

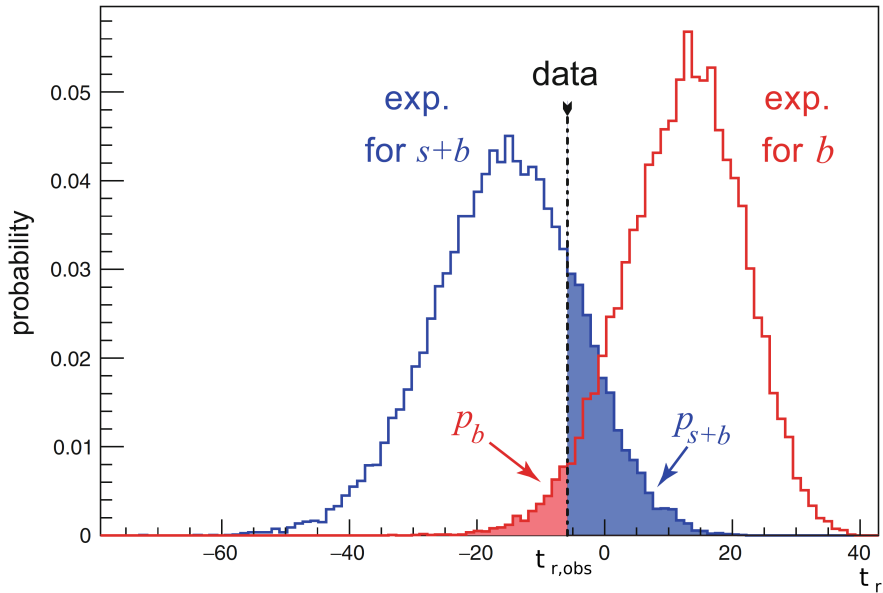


Figure 5.6: t_r p.d.f. from MC pseudo experiments assuming H_0 (red) and H_1 (blue). The black dashed line shows the value of the test statistic as measured from data. Adapted from Reference [128].

2190 The expected probability density function (p.d.f) $f(t_r|r, \boldsymbol{\theta})$ of the test statistic t_r

2191 can be obtained numerically by generating MC pseudo-experiments assuming each
 2192 $H_0(b)$ and $H_1(s+b)$ as shown in Figure 5.6. The probability that t_r takes a value
 2193 equal or greater than the observed value ($t_{r,obs}$) when a signal with a signal modifier r
 2194 is present in the data sample, is called *p-value* of the observation; it can be calculated
 2195 using

$$p_r = \int_{t_{r,obs}}^{\infty} f(t'_r|r, \boldsymbol{\theta}) dt'_r, \quad (5.15)$$

2196 thus, $p_r < 0.05$ means that, for that particular value of r , H_1 could be excluded at
 2197 95% Confidence Level (CL). The corresponding background-only p-value is given by

$$1 - p_b = \int_{t_{r,obs}}^{\infty} f(t'_r|0, \boldsymbol{\theta}) dt'_r, \quad (5.16)$$

2198 If the t_r p.d.f. for both hypotheses are well separated, as shown in the top side
 2199 of Figure 5.7, the experiment is sensitive to the presence of signal in the sample. If
 2200 the signal presence is small, both p.d.f. will be largely overlapped (bottom of Figure
 2201 ??) and either the signal hypothesis could be rejected with not enough justification
 2202 because experiment is not sensitive to the signal or a fluctuation of the background
 2203 could be misinterpreted as presence of signal with the corresponding rejection of
 2204 the background-only hypothesis. These issues are corrected by using the modified
 2205 p-value [136]

$$p'_r = \frac{p_r}{1 - p_b} \equiv CL_s. \quad (5.17)$$

2206 If H_1 is true, then p_b is small, $CL_s \simeq p_r$ and H_0 is rejected; if there is large
 2207 overlap and an statistical fluctuation cause that p_b is large, then both numerator and
 2208 denominator in Eqn. 5.17 become small but CL_s would allow the rejection of H_1

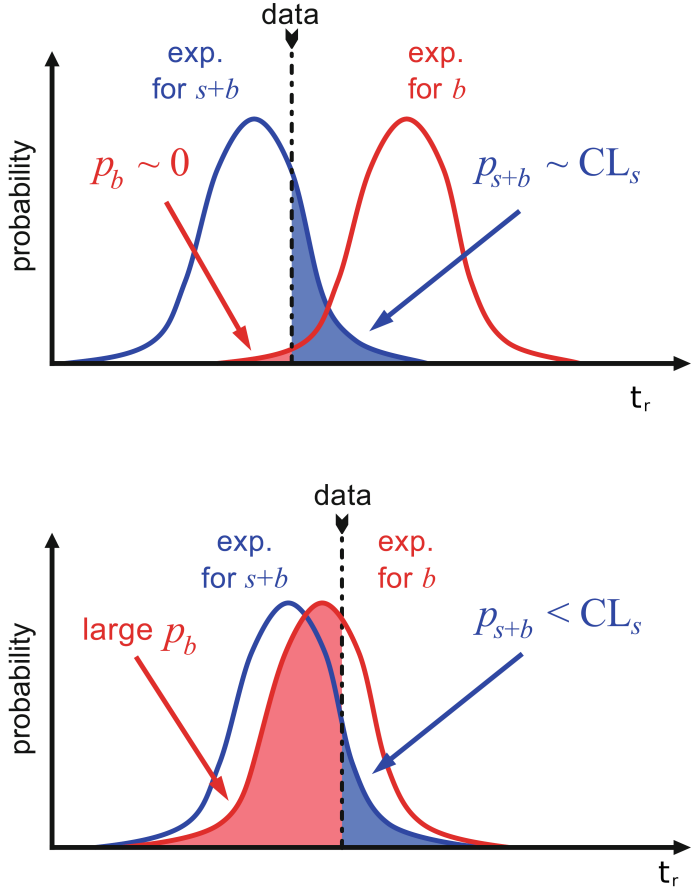


Figure 5.7: CL_s limit illustration. When the test statistic p.d.f. for the two hypotheses H_0 and H_1 are well separated (top) and when they are largely overlapped (bottom). Adapted from Reference [128].

2209 even if there is poor sensitivity to signal.

2210 The upper limit of the parameter of interest r^{up} is determined by excluding the
2211 range of values of r for which $CL_s(r, \theta)$ is lower than the confidence level desired,
2212 normally 90% or 95%, e.g., scanning over r and finding the value for which $p_r'^{up} =$
2213 0.05. The expected upper limit can be calculated using pseudo-experiments based on
2214 the background-only hypothesis and obtaining a distribution for r_{ps}^{up} ; the median of
2215 that distribution corresponds to the expected upper limit, while the $\pm 1\sigma$ and $\pm 2\sigma$
2216 deviations correspond to the values of the distribution that defines the 68% and 95%

of the area under the distribution centered in the median. It is usual to present all the information about the expected and observed limits in the so-called *Brazilian-flag plot* as the one showed in Figure 5.8.

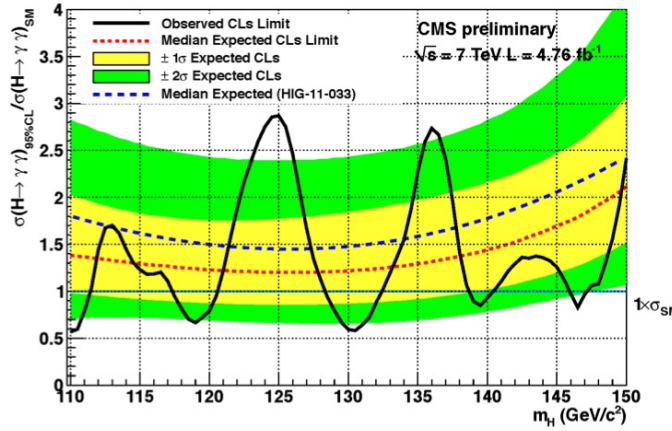


Figure 5.8: Brazilian flag plot of CMS experiment limits for Higgs boson decaying to photons [137].

5.4 Asymptotic limits

As said before, the complexity of the likelihood functions, the construction of test statistics, and the calculation of the limits and their uncertainties is not always manageable and requires extensive computational resources; in order to overcome those issues, asymptotic approximations for likelihood-based test statistics, like the ones described in previous sections, have been developed [138, 139] using Wilks' theorem. Asymptotic approximations replace the construction of the test statistics p.d.f.s using MC pseudo-experiments, with the approximate calculation of the test statistics p.d.f.s by employing the so-called *Asimov dataset*.

The Asimov dataset is defined as the dataset that produce the true values of the nuisance parameters when it is used to evaluate the estimators for all the parameters;

2231 it is obtained by setting the values of the variables in the dataset to their expected
2232 values [139].

2233 Limits calculated by using the asymptotic approximation and the Asimov dataset
2234 are known as *asymptotic limits*.

²²³⁵ **Chapter 6**

²²³⁶ **Search for production of a Higgs**

²²³⁷ **boson and a single top quark in**

²²³⁸ **multilepton final states in pp**

²²³⁹ **collisions at $\sqrt{s} = 13$ TeV**

²²⁴⁰ **6.1 Introduction**

²²⁴¹ The Higgs boson discovery, supported on experimental observations and theoretical
²²⁴² predictions made about the SM, gives the clue of the way in that elementary particles
²²⁴³ acquire mass through the Higgs mechanism; therefore, knowing the Higgs mass, the
²²⁴⁴ Higgs-vector boson and Higgs-fermion couplings can be determined. In order to test
²²⁴⁵ the Higgs-top coupling, several measurements have been performed, as stated in the
²²⁴⁶ chapter 1, but they are limited in sensitivity to measure the square of the coupling.
²²⁴⁷ The production of a Higgs boson in association with a single top quark (tH) not
²²⁴⁸ only offers access to the sign of the coupling, but also, to the CP phase of the Higgs

2249 couplings.

2250 This chapter presents the search for the associated production of a Higgs boson
 2251 and a single top quark (tHq) events, focusing on leptonic signatures provided by the
 2252 Higgs decay modes to WW , ZZ , and $\tau\tau$; the 13 TeV dataset produced in 2016, which
 2253 corresponds to an integrated luminosity of 35.9fb^{-1} , is used.

2254 As shown in Section 1.5, the SM cross section of tHq process is driven by a
 2255 destructive interference between two contributions (see Figure 1.15), where the Higgs
 2256 couples to either the W boson or the top quark; however, if the sign of the Higgs-
 2257 top coupling is flipped with respect to the SM prediction, a large enhancement of
 2258 the cross section occurs, making this analysis sensitive to such deviation. A second
 2259 process, where the Higgs boson and top quark are accompanied by a W boson (tHW)
 2260 has similar behavior, albeit with a weaker interference pattern and lower contribution
 2261 to the cross section, therefore, a combination of both processes would increase the
 2262 sensitivity to the sign of the coupling; in this analysis both contributions are combined
 2263 and referred as tH channel. A third contribution comes from $t\bar{t}H$ process. The purpose
 2264 of this analysis is to investigate the exclusion of the presence of the $tH + t\bar{t}H$ processes
 2265 under the assumption of the anomalous Higgs-top coupling modifier ($\kappa_t = -1$). The
 2266 analysis exploits signatures with two leptons of the same sign ($\cancel{2}lss$) channel and three
 2267 leptons ($\cancel{3}l$) channel in the final state.

2268 Constraints on the sign of the Higgs-top coupling (y_t) have been derived from the
 2269 decay rate of Higgs boson to photon pairs [50] and from the cross section for associated
 2270 production of Higgs and Z bosons via gluon fusion [141], with recent results disfavoring
 2271 negative signs of the coupling [44, 59, 142], although the negative sign coupling have
 2272 not been completely excluded.

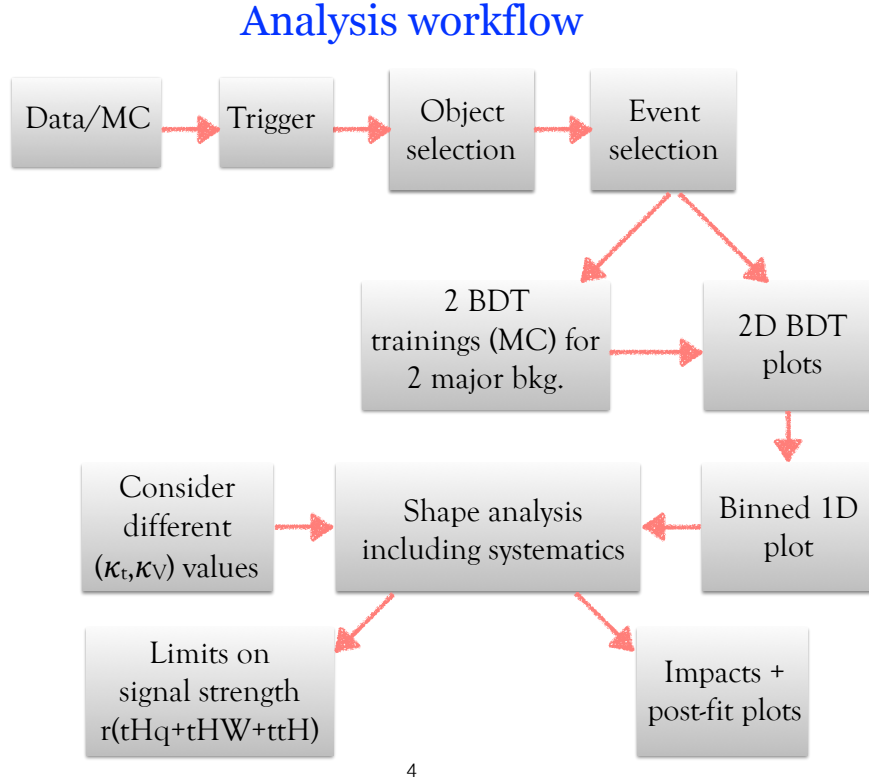
2273 The analysis presented here, expands previous analyses performed at 8 TeV [143,
 2274 144] and searches for associated production of $t\bar{t}$ pair and a Higgs boson in the multi-

lepton final state channel [145]; it also complements searches in other decay channels targeting $H \rightarrow b\bar{b}$ [146].

The first sections present the characteristic tHq signature as well as the expected backgrounds. The MC samples, data sets, and the physics object definitions are then defined. Following, the background predictions, the signal extraction, and the statistical treatment of the selected events as well as the systematic uncertainties are described. The final section present the results for the exclusion limits as a function of the ratio of κ_t and the dimensionless modifier of the Higgs-vector boson coupling κ_V .

The analysis is designed to efficiently identify and select prompt leptons from on-shell W and Z boson decays and to reject non-prompt leptons from b quark decays and spurious lepton signatures from hadronic jets. Events are then selected in the $2lss$ and $3l$ channels, and are required to contain hadronic jets, some of which must be consistent with b quark hadronization. Finally, the signal yield is extracted by simultaneously fitting the output of two dedicated multivariate discriminants, trained to separate the tHq signal from the two dominant backgrounds, in all categories. The fit result is then used to set an upper limit on the combined $t\bar{t}H + tH$ production cross section, as a function of the relative coupling strengths of Higgs-top quark and Higgs-Vector boson. Figure 6.1 shows an schematic overview of the analysis strategy workflow.

With respect to the 8 TeV analysis, the object selections have been adjusted for the updated LHC running conditions at 13 TeV, the lepton identification has been improved, and more powerful multivariate analysis techniques are used for the signal extraction.



4

Figure 6.1: A schematic overview of the analysis workflow. Based on sets of optimized physics object definitions and selection criteria, signal and background events in a data sample are discriminated. The discrimination is performed by a BDT, previously trained using MC samples of the dominant backgrounds, using discriminant variables based on the b -jet multiplicity, the activity in the forward region of the detector, and the kinematic properties of leptons. The CL_s limits on the combined $t\bar{t}H + tH$ production cross section, as a function of the relative coupling strengths are calculated.

2299 6.2 tHq signature

2300 In order to select events of tHq process, its features are translated into a set of
 2301 selection rules; Figure 6.2 shows the Feynman diagram and an schematic view of the
 2302 tHq process from the pp collision to the final state configuration. A single top quark
 2303 is produced accompanied by a light quark, denoted as q ; this light quark is produced
 2304 predominantly in the forward region of the detector. The Higgs boson can be either
 2305 emitted by the exchanged W boson or directly by the singly produced top quark.

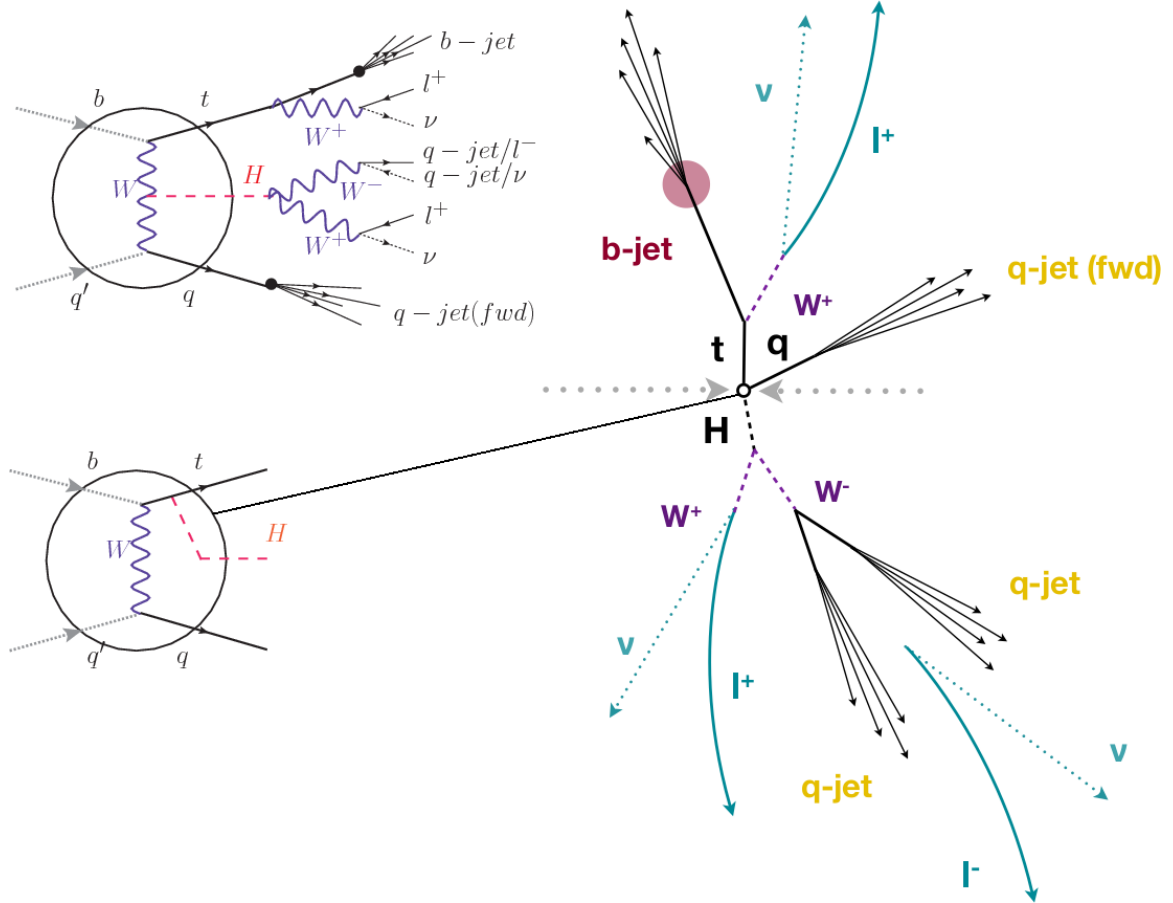


Figure 6.2: tHq event signature. Left: Feynman diagram including the whole evolution up to the final state for the case of the Higgs boson emitted by the W boson (top); Feynman diagram for the case where the Higgs boson is emitted by the top quark. Right: Schematic view as it would be seen in the detector; the circle in the Feynman diagrams on the left corresponds to the circle in the center of the schematic view as indicated by the line connecting them. In the $2lss$ channel, one of the W bosons from the Higgs boson decays to two light-quark jets while in the $3l$ channel both W bosons decay to leptons.

2306 Due to their high masses/short lifetimes, top quark and Higgs boson decay after
 2307 their production within the detector. The Higgs boson is required to decay into a W
 2308 boson pair¹. The top quark almost always decays into a bottom quark and a W boson,
 2309 as encoded in the CMK matrix. The W bosons are required to decay hadronically
 2310 in the $2lss$ channel case and leptonically in the $3l$ channel case, while τ leptons are

¹ ZZ and $\tau\tau$ decays are also included in the analysis but they are not separately reconstructed

2311 not reconstructed separately and only their leptonic decays into either electrons or
 2312 muons are considered in this analysis.

2313 In summary, the signal process is characterized by a the final state with

2314 • one light-flavored forward jet,

2315 • one central b-jet,

2316 • $2lss$ channel → two leptons of the same sign, two neutrinos and two light (often
 2317 soft) jets,

2318 • $3l$ channel → three leptons, three neutrinos and no central light-flavored jets,

2319 The presence of neutrinos is inferred from the presence of MET. The analysis has
 2320 been made public by CMS as a Physics Analysis Summary [147] combining the result
 2321 for the three lepton and two lepton same-sign channels. Currently, an effort to turn
 2322 the analysis into a paper is ongoing.

2323 6.3 Background processes

2324 The background processes are those that can mimic the signal signature or at least
 2325 can be reconstructed as that as a result of certain circumstances. The backgrounds
 2326 can be classified as

2327 • irreducible backgrounds: where genuine prompt leptons are produced in on-
 2328 shell W and Z boson decays; they can be reliably estimated directly from MC
 2329 simulated events, using higher-order cross sections or data control regions for
 2330 the overall normalization.

2331 • reducible backgrounds: where at least one of the leptons is *non-prompt*, i.e.,
 2332 produced within a hadronic jet; genuine leptons from heavy flavor decays and
 2333 misreconstructed jets, also known as *mis-ID leptons* or *fake leptons*, are consid-
 2334 ered non-prompt leptons. These non-prompt leptons leave tracks and hits in
 2335 the detection systems as would a prompt lepton, but correlating those hits with
 2336 nearby jets could be a way of removing them. The misassignment of electron
 2337 charge in processes like $t\bar{t}$ or Drell-Yan, represent an additional source of back-
 2338 ground, but it is relevant only for the $2lss$ channel. Reducible backgrounds are
 2339 not well predicted by simulation, hence, they are estimated using data-driven
 2340 methods.

2341 The main sources of background events for tHq process are $t\bar{t}$ process and $t\bar{t} +$
 2342 X ($X = W, Z, \gamma$) processes, the latter regarded together as $t\bar{t}V$ process. Figure 6.3
 2343 shows the signature for $t\bar{t}$ and $t\bar{t}W$ processes.

2344 The largest contribution to irreducible backgrounds comes from $t\bar{t}W$ and $t\bar{t}Z$ processes
 2345 for which the number of (b -)jets ((b -)jet multiplicity) is higher than that of the sig-
 2346 nal events, while for other contributing background events, WZ , ZZ , and rare SM
 2347 processes like $W^\pm W^\pm qq$, $t\bar{t}t\bar{t}$, tZq , tZW , WWW , WWZ , WZZ , ZZZ , the (b -)jet
 2348 multiplicity is lower compared to that of the signal events. None of the irreducible
 2349 backgrounds present activity in the forward region of the detector.

2350 On the side of the reducible backgrounds, the largest contribution comes from the
 2351 $t\bar{t}$ events which have a very similar signature to the signal events but does no present
 2352 activity in the forward region of the detector either; A particular feature of the $t\bar{t}$
 2353 events is their charge-symmetry, which is also a difference with respect to the signal
 2354 events.

2355 The charge misidentification plays an important role in the the $2lss$ channel since

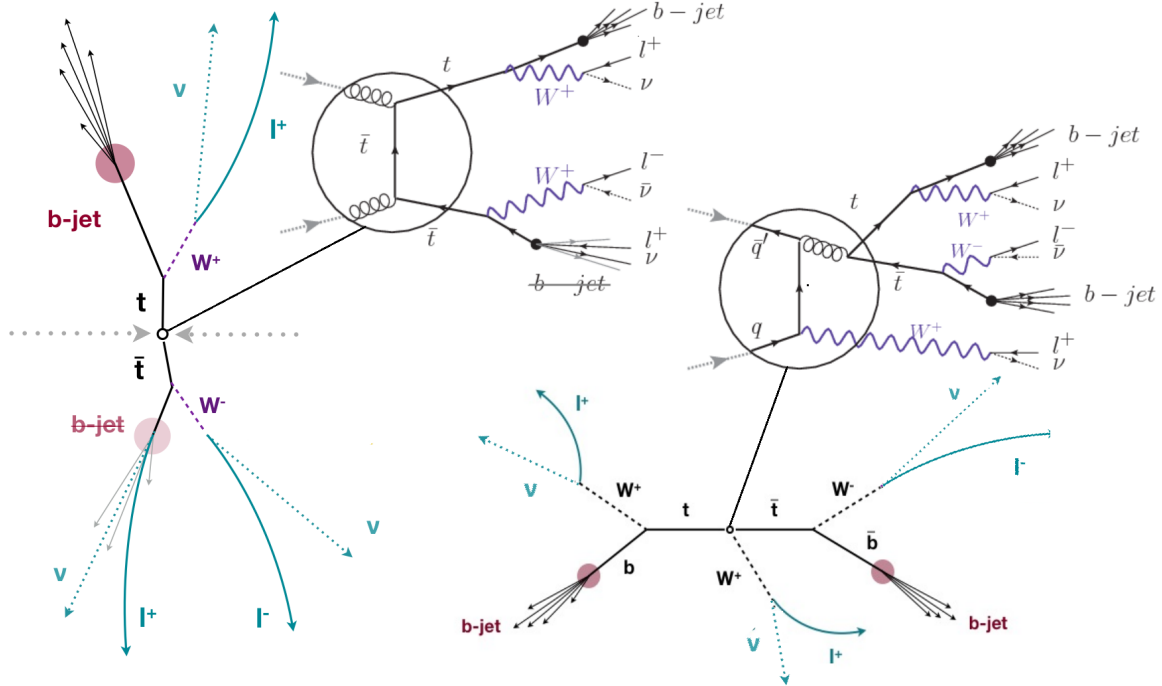


Figure 6.3: $t\bar{t}$ (left) and $t\bar{t}W$ (right) events signature as they would be seen in the detector; the Feynman diagrams including the whole evolution up to the final state are also showed. The $t\bar{t}$ process signature is very similar to that of the signal process with one fake lepton and no forward activity. The $t\bar{t}W$ process present a higher b -jet multiplicity compared to the signal process, a prompt lepton and no forward activity.

2356 leptons in processes like $t\bar{t} + \text{jets}$ or $Z + \text{jets}$ can be charge misidentified, leading to
 2357 backgrounds increments. An identification variable have been designed in order to
 2358 reject this type of background events.

2359 6.4 Data and MC Samples

2360 6.4.1 Full 2016 data set

2361 The data set used in this analysis was collected by the CMS experiment during 2016
 2362 at while running at $\sqrt{s} = 13\text{TeV}$ and corresponds to a total integrated luminosity
 2363 of 35.9fb^{-1} . Only periods when the CMS magnet was on were considered when

2364 selecting the data samples; that corresponds to the 23Sep2016 (Run B to G) and
 2365 PromptReco (Run H) versions of the datasets.

2366 Multilepton final states with either two same-sign leptons or three leptons tar-
 2367 get the case where the Higgs boson decays to a pair of W bosons, τ leptons, or Z
 2368 bosons, and where the top quark decays leptonically, hence, the SingleElectron,
 2369 SingleMuon, DoubleEG, MuonEG, DoubleMuon dataset (see Table A.1) compose the
 2370 full dataset. The certified luminosity sections are selected using the golden JSON file
 2371 defined by the CMS experiment [148].

2372 6.4.2 Triggers

2373 The events considered are those online-reconstructed events triggered by one, two, or
 2374 three leptons. Single-lepton triggers are included in order to boost the acceptance
 2375 of events where the p_T of the sub-leading lepton falls below the threshold of the
 2376 double-lepton triggers. The trigger efficiency is increased by including double-lepton
 2377 triggers in the $3l$ category, and single-lepton triggers in all categories; it is possible
 2378 given the logical “or” of the trigger decisions of all the individual triggers in a given
 2379 category. Table A.2 shows the lowest-threshold non-prescaled triggers present in the
 2380 High-Level Trigger (HLT) menus for both Monte-Carlo and data in 2016.

2381 Trigger efficiency scale factors

2382 Trigger efficiency describes the ability of events to pass the trigger requirements. It
 2383 is measured in simulated events using generator information given that there is no
 2384 trigger bias with the MC sample. Measuring the trigger efficiency in data requires a
 2385 more elaborated procedure; first, select a set of events collected by a trigger that is
 2386 uncorrelated with the lepton triggers such that the selected events form an unbiased

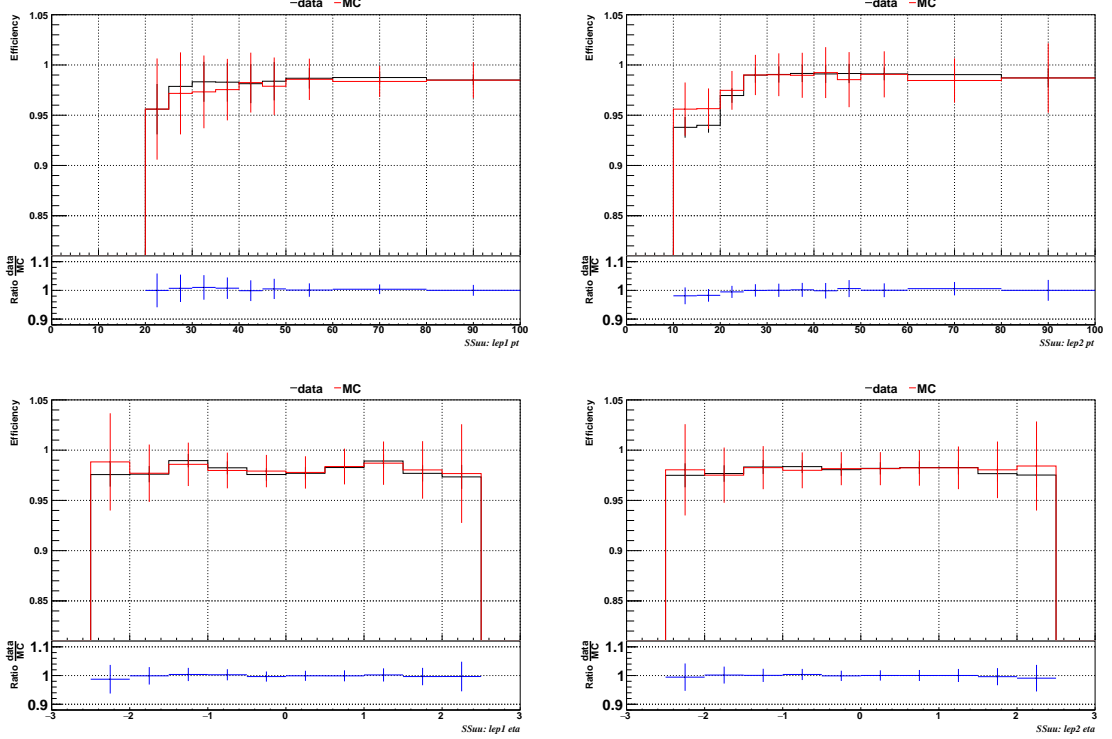


Figure 6.4: Comparison between data and MC trigger efficiencies in the same-sign $\mu\mu$ category, as a function of the p_T and η of the leading lepton (left) and the sub-leading lepton (right) [151].

sample. In this analysis, that uncorrelated trigger is a MET trigger. Second step is looking for candidate events with exactly two good leptons (exactly three good leptons for the $3l$ channel). Finally, measure the efficiency for the candidate events to pass the logical “or” of triggers being considered in a given event category as defined in Table A.2.

Comparisons between the data and MC efficiencies for each category, showed in Figures 6.4, 6.5, 6.6, and 6.7, reveal that they are in good agreement; the difference is corrected by applying scale factors derived from the ratio between both efficiencies. Applied flat scale factors in each category are shown in Tab. 6.1; they have been inherited from Reference [151].

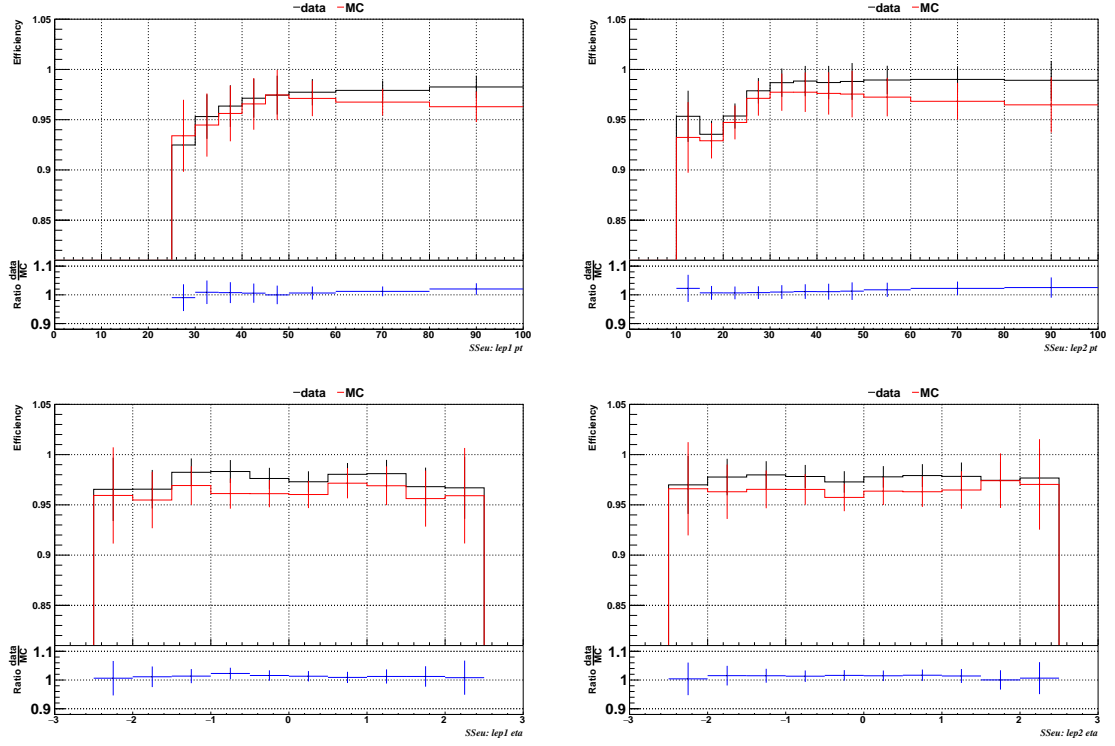


Figure 6.5: Comparison between data and MC trigger efficiencies in the same-sign $e\mu$ category, as a function of the p_T and η of the leading lepton (left) and the sub-leading lepton (right) [151].

Category	Scale Factor
ee	1.01 ± 0.02
$e\mu$	1.01 ± 0.01
$\mu\mu$	1.00 ± 0.01
3l	1.00 ± 0.03

Table 6.1: Trigger efficiency scale factors and associated uncertainties, shown here rounded to the nearest percent.

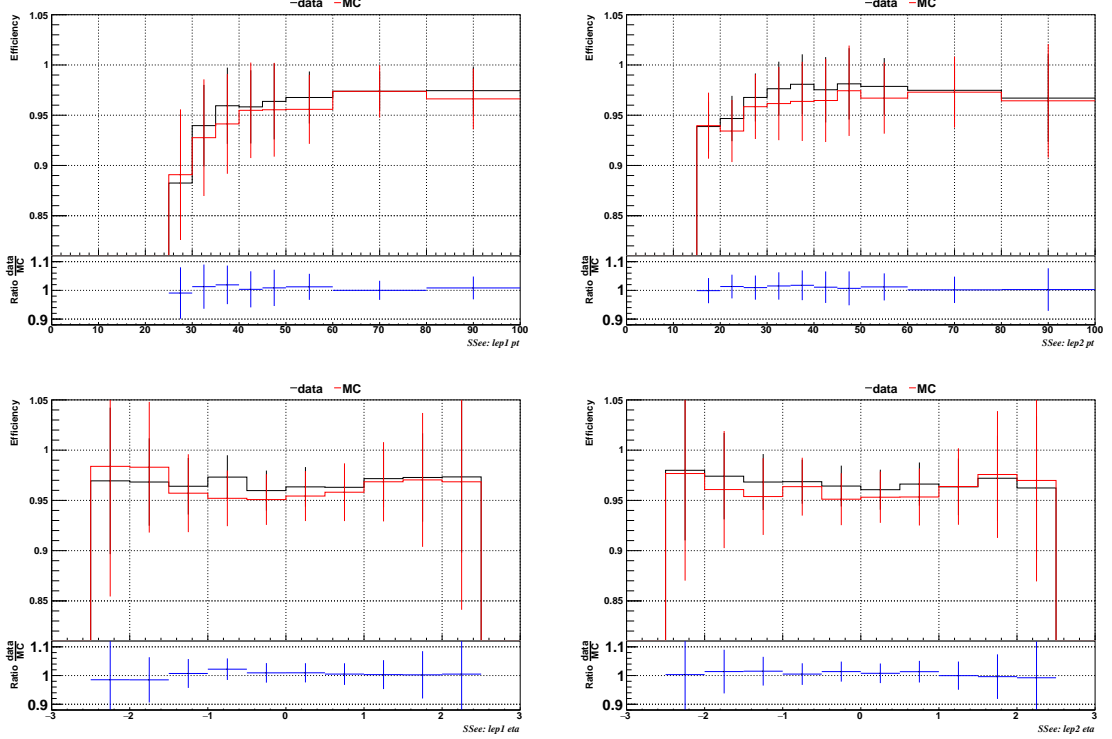


Figure 6.6: Comparison between data and MC trigger efficiencies in the same-sign ee category, as a function of the p_T and η of the leading lepton (left) and the sub-leading lepton (right) [151].

2397 6.4.3 Signal modeling and MC samples

2398 Technical developments on the event generator side allow for an event-wise reweighting
 2399 that can change the event kinematics based on specific generation parameters;
 2400 in this way, not only the case of $\kappa_t = -1$, but a whole range of κ_t and κ_V val-
 2401 ues may be investigated. The MC samples used in this analysis correspond to the
 2402 RunIISummer16MiniAODv2 campaign produced with CMSSW_80X. The two signal
 2403 samples, for tHq and tHW , were produced with MG5_aMC@NLO (version 5.222),
 2404 in leading-order order mode, and are normalized to next-to-leading-order cross sec-
 2405 tions (see Table A.3). Each sample is generated with a set of event weights corre-
 2406 sponding to different values of κ_t and κ_V couplings as shown in Table A.4.

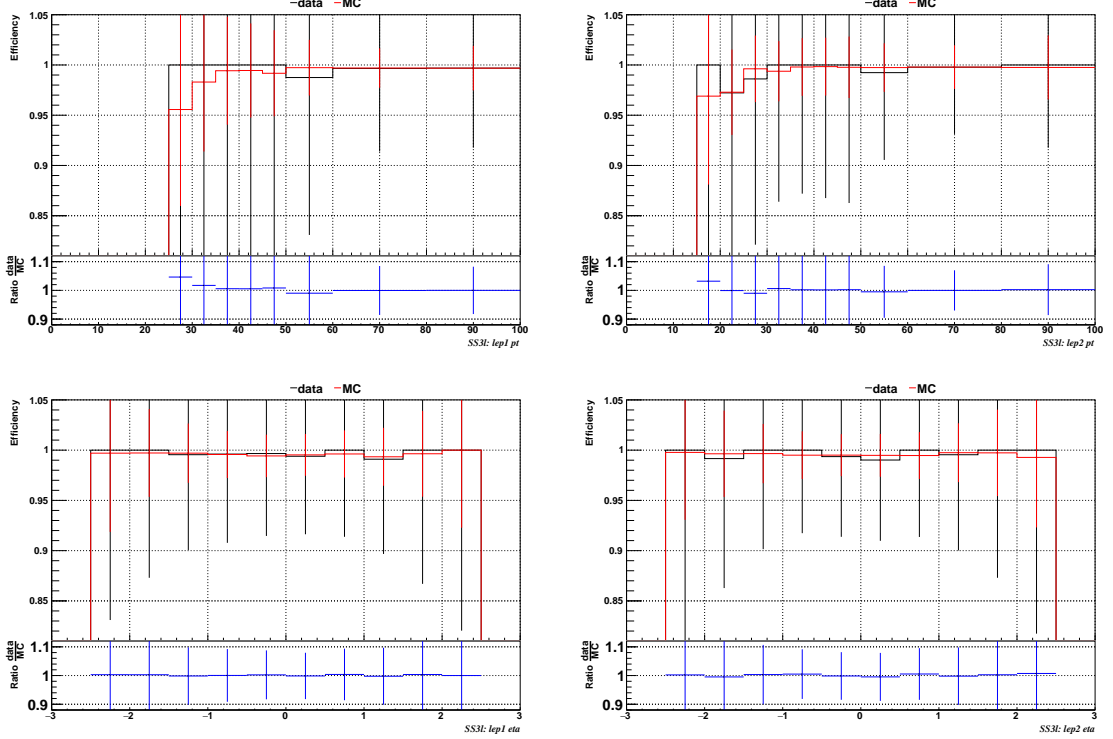


Figure 6.7: Comparison between data and MC trigger efficiencies in the $3l$ category, as a function of the p_T and η of the leading lepton (left) and the sub-leading lepton (right) [151].

Sample	σ [pb]	BF
/THQ_Hincl_13TeV-madgraph-pythia8_TuneCUETP8M1/	0.7927	0.324
/THW_Hincl_13TeV-madgraph-pythia8_TuneCUETP8M1/	0.1472	1.0

Table 6.2: MC signal samples used in this analysis; cross section and branching fraction are also listed. See Ref. [157] for more details.

Different MC generators were used to generate the background processes. The dominant sources ($t\bar{t}$, $t\bar{t}W$, $t\bar{t}Z$, $t\bar{t}H$) were produced using AMC@NLO interfaced to PYTHIA8, and are scaled to NLO cross sections. Other processes are simulated using POWHEG interfaced to PYTHIA, or bare PYTHIA (see table A.5 and [145] for more details).

Sample	σ [pb]
TTWJetsToLNu_TuneCUETP8M1_13TeV-amcatnloFXFX-madspin-pythia8	0.2043
TTZToLLNuNu_M-10_TuneCUETP8M1_13TeV-amcatnlo-pythia8	0.2529
ttHJetToNonbb_M125_13TeV_amcatnloFXFX_madspin_pythia8_mWCutfix /store/cmst3/group/susy/gpetrucc/13TeV/u/TTLL_m1to10_LO_NoMS_for76X/	0.2151 0.0283
WGToLNuG_TuneCUETP8M1_13TeV-madgraphMLM-pythia8	585.8
ZGTo2LG_TuneCUETP8M1_13TeV-amcatnloFXFX-pythia8	131.3
TGJets_TuneCUETP8M1_13TeV_amcatnlo_madspin_pythia8	2.967
TGJets_TuneCUETP8M1_13TeV_amcatnlo_madspin_pythia8	2.967
TTGJets_TuneCUETP8M1_13TeV-amcatnloFXFX-madspin-pythia8	3.697
WpWpJJ_EWK-QCD_TuneCUETP8M1_13TeV-madgraph-pythia8	0.03711
ZZZ_TuneCUETP8M1_13TeV-amcatnlo-pythia8	0.01398
WWZ_TuneCUETP8M1_13TeV-amcatnlo-pythia8	0.1651
WZZ_TuneCUETP8M1_13TeV-amcatnlo-pythia8	0.05565
WW_DoubleScattering_13TeV-pythia8	1.64
tZq_ll_4f_13TeV-amcatnlo-pythia8_TuneCUETP8M1	0.0758
ST_tWll_5f_LO_13TeV-MadGraph-pythia8	0.01123
TTTT_TuneCUETP8M1_13TeV-amcatnlo-pythia8	0.009103
WZTo3LNu_TuneCUETP8M1_13TeV-powheg-pythia8	4.4296
ZZTo4L_13TeV_powheg_pythia8	1.256
TTJets_SingleLeptFromTbar_TuneCUETP8M1_13TeV-madgraphMLM-pythia8	182.1754
TTJets_SingleLeptFromT_TuneCUETP8M1_13TeV-madgraphMLM-pythia8	182.1754
TTJets_DiLept_TuneCUETP8M1_13TeV-madgraphMLM-pythia8	87.3
DYJetsToLL_M-10to50_TuneCUETP8M1_13TeV-amcatnloFXFX-pythia8	18610
DYJetsToLL_M-50_TuneCUETP8M1_13TeV-madgraphMLM-pythia8	6024
WJetsToLNu_TuneCUETP8M1_13TeV-amcatnloFXFX-pythia8	61526.7
ST_tW_top_5f_inclusiveDecays_13TeV-powheg-pythia8_TuneCUETP8M1	35.6
ST_tW_antitop_5f_inclusiveDecays_13TeV-powheg-pythia8_TuneCUETP8M1	35.6
ST_t-channel_4f_leptonDecays_13TeV-amcatnlo-pythia8_TuneCUETP8M1	70.3144
ST_t-channel_antitop_4f_leptonDecays_13TeV-powheg-pythia8_TuneCUETP8M1	26.2278
ST_s-channel_4f_leptonDecays_13TeV-amcatnlo-pythia8_TuneCUETP8M1	3.68064
WWTo2L2Nu_13TeV-powheg	10.481

Table 6.3: List of background samples used in this analysis (CMSSW 80X). In the first section of the table are listed the samples of the processes for which we use the simulation to extract the final yields and shapes, in the second section the samples of the processes we will estimate from data. The MC simulation is used to design the data driven methods and derive the associated systematics.

Sample	σ [pb]
ttWJets_13TeV_madgraphMLM	0.6105
ttZJets_13TeV_madgraphMLM	0.5297/0.692

Table 6.4: Leading-order $t\bar{t}W$ and $t\bar{t}Z$ samples used in the signal BDT training.

2412 6.5 Object Identification

2413 In this section, the specific definitions of the physical objects in terms of the numerical
 2414 values assigned to the reconstruction parameters are presented; thus, the provided
 2415 details summarize and complement the descriptions presented in previous chapters.
 2416 The object reconstruction and selection strategy used in this thesis is inherited from
 2417 the analyses in References [145, 151], thus, the information in this section is extracted
 2418 from those documents unless other References are stated.

2419 6.5.1 Lepton reconstruction and identification

2420 Two types of leptons are defined in this analysis: *signal leptons* are those coming from
 2421 W, Z and τ decays which usually are isolated from other particles; *background leptons*
 2422 are defined as leptons produced in b -jet hadron decays, light-jets misidentification,
 2423 and photon conversions.

2424 The process of reconstruction and identification of electron and muon candidates
 2425 was described in chapter3, hence, the identification variables used in order to retain
 2426 the highest possible efficiency for signal leptons while maximizing the rejection of
 2427 background leptons are listed and described in the following sections ².

2428 The identification variables include not only observables related directly to the re-
 2429 constructed leptons themselves, but also to the clustered energy deposits and charged
 2430 particles in a cone around the lepton direction (jet-related variables); an initial loose
 2431 preselection of leptons candidates is performed and then an MVA discriminator, re-
 2432 fered to as *lepton MVA* discriminator, is used to distinguish signal leptons from
 2433 background leptons.

² the studies performed to optimize the identification are far from the scope of this thesis, therefore, only general descriptions are provided

2434 **Muons**

2435 The Physics Objects Groups (POG) at CMS, are in charge of studying and defining
 2436 the set of selection criteria applied on the course of reconstruction and identification
 2437 of particles. These selection criteria are implemented in the CMS framework in the
 2438 form of several object identification working points according to the strength of the
 2439 requirements.

2440 The muon candidates are reconstructed by combining information from the tracker
 2441 system and the muon detection system of CMS detector and the POG defined three
 2442 working points for muon identification *MuonID* [152];

2443 • *POG Loose Muon ID* is a particle identified as a muon by the PF event re-
 2444 construction and also reconstructed either as a global-muon or as an arbitrated
 2445 tracker-muon. This identification criteria is designed to be highly efficient for
 2446 prompt muons and for muons from heavy and light quark decays; it can be com-
 2447 plemented by applying impact parameter cuts in analyses with prompt muon
 2448 signals.

2449 • *POG Medium Muon ID* is a Loose muon with additional track-quality and
 2450 muon-quality (spatial matching between the individual measurements in the
 2451 tracker and the muon system) requirements. This identification criteria is de-
 2452 signed to be highly efficient in the separation of the muons coming from decay
 2453 in flight of heavy quarks and muons coming from B meson decays as well as
 2454 prompt muons. An additional category *MVA Prompt ID* is defined in this iden-
 2455 tification criteria directed to discriminated muons from B mesons and prompt
 2456 muons (from W,Z and τ decays). The Medium ID provides the same fake rate as
 2457 the Tight Muon ID but a higher efficiency on prompt and B-decays muons. [153]

2458 • *POG Tight Muon ID* is a global muon with additional muon-quality requirements
 2459 Tight Muon ID selects a subset of the PF muons.

2460 Only muons within the muon system acceptance $|\eta| < 2.4$ and minimum p_T of 5
 2461 GeV are considered.

2462 **Electrons**

2463 Electrons are reconstructed using information from the tracker and from the electro-
 2464 magnetic calorimeter and identified by an MVA algorithm (*MVA eID* discriminant)
 2465 using the shape of the calorimetric shower variables like the shape in η and ϕ , the clus-
 2466 ter circularity, widths along η and ϕ ; track-cluster matching variables like E_{tot}/p_{in} ,
 2467 E_{Ele}/p_{out} , $\Delta\eta_{in}$, $\Delta\eta_{out}$, $\Delta\phi_{in}$, $1/E - 1/p$; and track quality variables like χ^2 of the
 2468 GSF tracks, the number of hits used by the GSF filter [154].

2469 A loose selection based on η -dependent cuts on this discriminant is used to prese-
 2470 lect electron candidates, the full shape of the discriminant is used in the lepton MVA
 2471 selection to separate signal leptons from background leptons (described in Section
 2472 6.5.1).

2473 In order to reject electrons from photon conversions, electron candidates with
 2474 missing hits in the pixel tracker layers or matched to a conversion secondary vertex
 2475 are discarded. Electrons are selected for the analysis if they have $p_T > 7$ GeV and
 2476 are located within the tracker system acceptance region ($|\eta| < 2.5$).

2477 **Lepton vertexing and pile-up rejection**

2478 The impact parameter in the transverse plane d_0 , impact parameter along the z -
 2479 axis d_z , and the impact parameter significance in the detector space SIP_{3D} , are
 2480 considered to perform the identification and rejection of pile-up, misreconstructed

2481 tracks, and background leptons from b-hadron decays; pile-up and misreconstructed
 2482 track mitigation is achieved by imposing loose cuts on the impact parameter variables.
 2483 The full shape of the those variables is used in a lepton MVA classifier to achieve the
 2484 best separation between the signal and the background leptons.

2485 **Lepton isolation**

2486 PF is able to recognize leptons from two different sources: on one side, leptons from
 2487 the decays of heavy particles, such as W and Z bosons, which are normally isolated
 2488 in space from the hadronic activity in the event; on the other side, leptons from the
 2489 decays of hadrons and jets misidentified as leptons, which are not isolated as the
 2490 former. For highly boosted systems, like the lepton and the b -jet generated in the
 2491 semileptonic decay of a boosted top, the decay products tend to be more closer and
 2492 sometimes they even overlap; thus, the PF standard definition of isolation in terms of
 2493 the separation between the lepton candidates and other PF objects in the η - ϕ plane,

$$\Delta R = \sqrt{(\eta^l - \eta^i)^2 + (\phi^l - \phi^i)^2} < 0.3 \quad (6.1)$$

2494 which considers all the neutral, charged hadrons and photons in a cone around the
 2495 leptons, is refocused to the local isolation of the leptons through the mini-isolation
 2496 I_{mini} [155] defined as the sum of particle flow candidates p_T within a cone around
 2497 the lepton, corrected for the effects of pileup and divided by the lepton p_T

$$I_{mini} = \frac{\sum_R p_T(h^\pm) - \max \left(0, \sum_R p_T(h^0) + p_T(\gamma) - \rho \mathcal{A} \left(\frac{R}{0.3} \right)^2 \right)}{p_T(l)} \quad (6.2)$$

2498 where ρ is the pileup energy density, h^\pm, h^0, γ, l , represent the charged hadron, neutral
 2499 hadrons, photons, and the lepton, respectively. The radius R of the cone depends on

2500 the p_T of the lepton according to

$$R = \frac{10\text{GeV}}{\min(\max(p_T(l), 50\text{GeV}), 200\text{GeV})}, \quad (6.3)$$

2501 The p_T dependence of the cone size allows for greater signal efficiency. Setting a
 2502 cut on I_{mini} below a given threshold ensures that the lepton is locally isolated, even
 2503 in boosted systems. The effect of pileup is mitigated using the so-called effective area
 2504 correction \mathcal{A} listed in Table 6.6.

$ \eta $ range	$\mathcal{A}(e)$ neutral/charged	$A(\mu)$ neutral/charged
0.0 - 0.8	0.1607 / 0.0188	0.1322 / 0.0191
0.8 - 1.3	0.1579 / 0.0188	0.1137 / 0.0170
1.3 - 2.0	0.1120 / 0.0135	0.0883 / 0.0146
2.0 - 2.2	0.1228 / 0.0135	0.0865 / 0.0111
2.2 - 2.5	0.2156 / 0.0105	0.1214 / 0.0091

Table 6.5: Effective areas, for electrons and muons used to mitigate the effect of pileup by using the so-called effective area correction.

2505 A loose cut on I_{mini} is applied to pre-select the muon and electron candidates;
 2506 however, the full shape is used in the lepton MVA discriminator when performing the
 2507 signal lepton selection.

2508 Jet-related variables

2509 In order to reject misidentified leptons from b -jets, mostly coming from $t\bar{t}+jets$,
 2510 Drell-Yan+jets, and $W+jets$ events, the vertexing and isolation described in previous
 2511 sections are complemented with additional variables related to the closest recon-
 2512 structed jet to the lepton, i.e., the PF jets reconstructed³ around the leptons with
 2513 $\Delta R = \sqrt{(\eta^l - \eta^{jet})^2 + (\phi^l - \phi^{jet})^2} < 0.5$. The identification variables used in the lep-

³ charged hadrons from PU vertices are not removed prior to the jet clustering.

2514 ton MVA discriminator are the ratio p_T^l/p_T^{jet} , the CSV b-tagging discriminator value
 2515 of the jet, the number of charged tracks of the jet, and the relative p_T given by

$$p_T^{rel} = \frac{(\vec{p}_{jet} - \vec{p}_l) \cdot \vec{p}_l}{\|\vec{p}_{jet} - \vec{p}_l\|}. \quad (6.4)$$

2516 **LeptonMVA discriminator**

2517 Electrons and muons passing the basic selection process described above are referred
 2518 to as *loose leptons*. Additional discrimination between signal leptons and background
 2519 leptons is crucial considering that the rate of $t\bar{t}$ production is much larger than the
 2520 signal, hence, an overwhelming background from $t\bar{t}$ production. To maximally ex-
 2521 ploit the available information in each event to that end, the dedicated lepton MVA
 2522 discriminator, based on a boosted decision tree (BDT) algorithm, has been built so
 2523 that all the identification variables can be used together.

2524 The lepton MVA discriminator training is performed using simulated signal Loose
 2525 leptons from the $t\bar{t}H$ MC sample and fake leptons from the $t\bar{t}$ +jets MC sample,
 2526 separately for muons and electrons. The input variables used include vertexing, iso-
 2527 lation and jet-related variables, the p_T and η of the lepton, the electron MVA eID
 2528 discriminator and the muon segment-compatibility variables. An additional require-
 2529 ment known as *tight-charge* requirement, is imposed by comparing two independent
 2530 measurement of the charge, one from the ECAL supercluster and the other from the
 2531 tracker; thus, the consistency in the measurements of the electron charge is ensured
 2532 so that events with a wrong electron charge assignment are rejected; this variable is
 2533 particularly used in the $2lss$ channel to suppress opposite-sign events for which the
 2534 charge of one of the leptons has been mismeasured. The tight-charge requirement for
 2535 muons is represented by the requirement of a consistently well measured track trans-
 2536 verse momentum given by $\Delta p_T/p_T < 0.2$. Leptons are selected for the final analysis

2537 if they pass a given threshold of the BDT output, and are referred to as *tight leptons*
 2538 in the following.

2539 The validation of the lepton MVA algorithm and the lepton identification variables
 2540 is performed using data in various control regions; the details about that validation
 2541 are not discussed here but can be found in Reference [151].

2542 Selection definitions

2543 Electron and muon object identification is defined in three different sets of selections
 2544 criteria; the *Loose*, *Fakeable Object*, and *Tight* selection. These three levels of selection
 2545 are designed to serve for event level vetoes, the fake rate estimation application region,
 2546 and the final signal selection, respectively. The p_T of fakeable objects is defined as
 2547 $0.85 \times p_T(\text{jet})$, where the jet is the one associated to the lepton object. This mitigates
 2548 the dependence of the fake rate on the momentum of the fakeable object and thereby
 2549 improves the precision of the method.

2550 Tables 6.7 and 6.8 list the full criteria for the different selections of muons and
 2551 electrons.

Cut	Loose	Fakeable object	Tight
$ \eta < 2.4$	✓	✓	✓
p_T	$> 5\text{GeV}$	$> 15\text{GeV}$	$> 15\text{GeV}$
$ d_{xy} < 0.05$ (cm)	✓	✓	✓
$ d_z < 0.1$ (cm)	✓	✓	✓
$\text{SIP}_{3D} < 8$	✓	✓	✓
$I_{\text{mini}} < 0.4$	✓	✓	✓
is Loose Muon	✓	✓	✓
jet CSV	—	< 0.8484	< 0.8484
is Medium Muon	—	—	✓
tight-charge	—	—	✓
lepMVA > 0.90	—	—	✓

Table 6.6: Requirements on each of the three muon selections. In the cases where the cut values change between the selections, those values are listed in the table. Otherwise, whether the cut is applied is indicated.

Cut	Loose	Fakeable Object	Tight
$ \eta < 2.5$	✓	✓	✓
p_T	$> 7\text{GeV}$	$> 15\text{GeV}$	$> 15\text{GeV}$
$ d_{xy} < 0.05 \text{ (cm)}$	✓	✓	✓
$ d_z < 0.1 \text{ (cm)}$	✓	✓	✓
$\text{SIP}_{3D} < 8$	✓	✓	✓
$I_{\text{mini}} < 0.4$	✓	✓	✓
MVA eID $> (0.0, 0.0, 0.7)$	✓	✓	✓
$\sigma_{in\eta} < (0.011, 0.011, 0.030)$	—	✓	✓
$\text{H/E} < (0.10, 0.10, 0.07)$	—	✓	✓
$\Delta\eta_{in} < (0.01, 0.01, 0.008)$	—	✓	✓
$\Delta\phi_{in} < (0.04, 0.04, 0.07)$	—	✓	✓
$-0.05 < 1/E - 1/p < (0.010, 0.010, 0.005)$	—	✓	✓
p_T^{ratio}	—	$> 0.5^\dagger / -$	—
jet CSV	—	$< 0.3^\dagger / < 0.8484$	< 0.8484
tight-charge	—	—	✓
conversion rejection	—	—	✓
Number of missing hits	< 2	$== 0$	$== 0$
lepton MVA > 0.90	—	—	✓

Table 6.7: Criteria for each of the three electron selections. In cases where the cut values change between selections, those values are listed in the table. Otherwise, whether the cut is applied is indicated. In some cases, the cut values change for different η ranges. These ranges are $0 < |\eta| < 0.8$, $0.8 < |\eta| < 1.479$, and $1.479 < |\eta| < 2.5$ and the respective cut values are given in the form (value₁, value₂, value₃). For the two p_T^{ratio} and CSV rows, the cuts marked with a \dagger are applied to leptons that fail the lepton MVA cut, while the loose cut value is applied to those that pass the lepton MVA cut.

2552 In addition to the previously defined requirements for jets, they are required to
 2553 be separated from any lepton candidates passing the fakeable object selections by
 2554 $\Delta R > 0.4$.

2555 6.5.2 Lepton selection efficiency

2556 Efficiencies of reconstruction and selecting loose leptons are measured both for muons
 2557 and electrons using a tag and probe method on both data and MC, using $Z \rightarrow \ell^+ \ell^-$
 2558 [156]. The scale factors are derived from the ratio of efficiencies $\varepsilon_i(p_T, \eta)$ measured

for a given lepton in data/MC, according to

$$\rho(p_T, \eta) = \frac{\varepsilon_{data}(p_T, \eta)}{\varepsilon_{MC}(p_T, \eta)}. \quad (6.5)$$

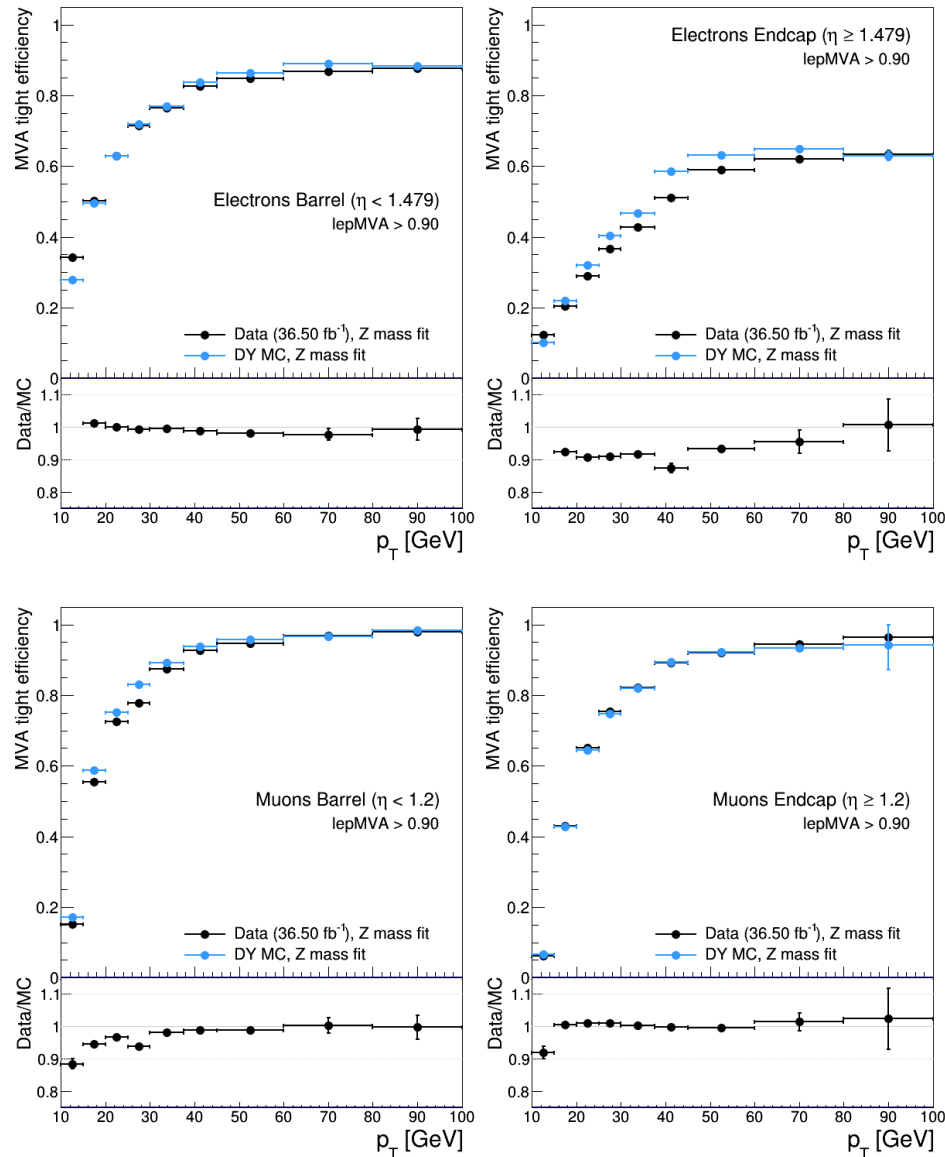


Figure 6.8: Tight vs loose selection efficiencies for electrons (top), and muons (bottom), for the $2lss$ definition, i.e., including the tight-charge requirement.

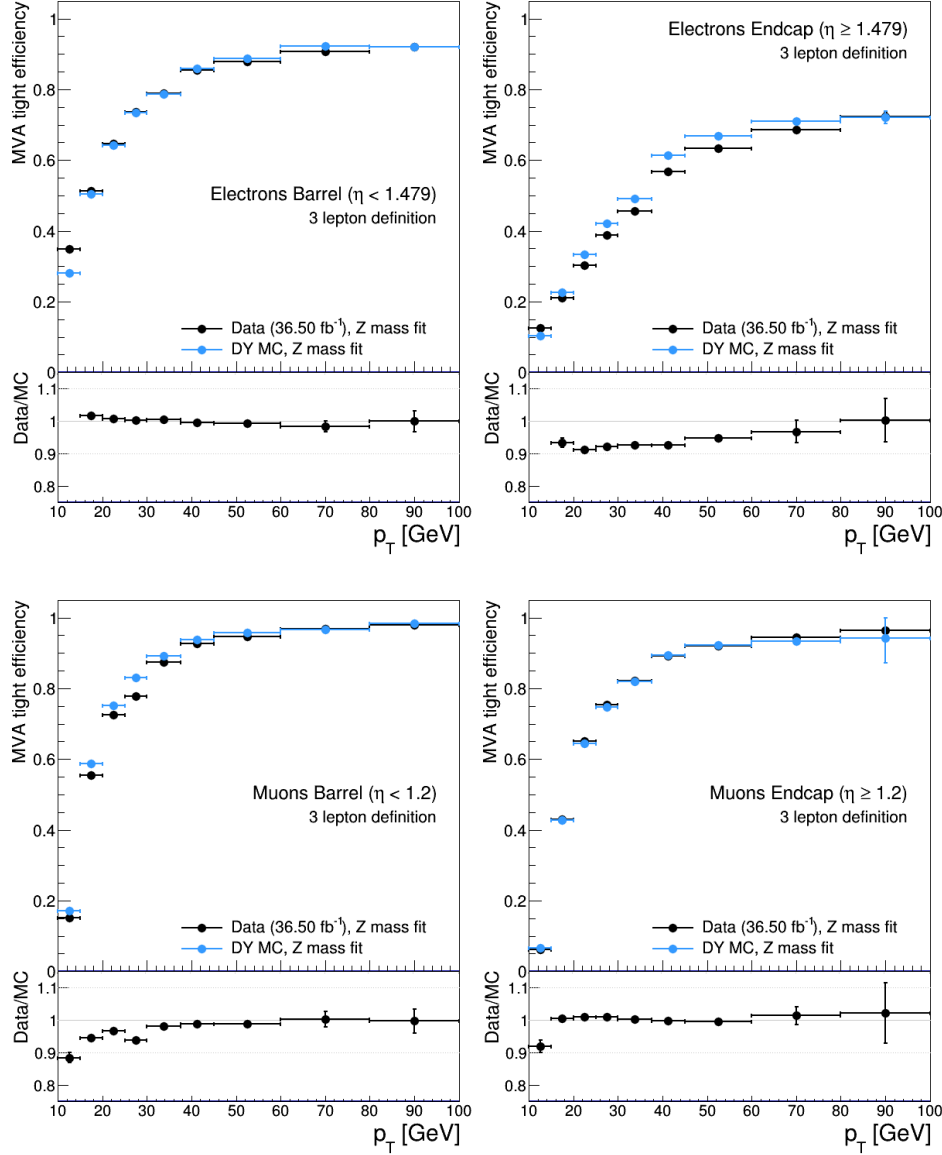


Figure 6.9: Tight vs loose selection efficiencies for electrons (top), and muons (bottom), for the $3l$ channel not including the tight-charge requirement.

2560 The scale factor for each event is used to correct the weight of the event in the
 2561 full sample; therefore, the full simulation correction is given by the product of all
 2562 the individual scale factors. The scale factors used in this thesis are inherited from
 2563 Reference [151] which in turns inherited them from leptonic SUSY analyses using
 2564 equivalent lepton selections.

2565 The efficiency of applying the tight selection as defined in Tables 6.7 and 6.8, on the
 2566 loose leptons are determined by using a tag and probe method on a sample of Drell-
 2567 Yan enriched events. Figures 6.8 and 6.9 show the efficiencies for the $2lss$ channel and
 2568 $3l$ channel respectively. Efficiencies in the $2lss$ channel have been produced including
 2569 the tight-charge requirement, while for the $3l$ channel it is not included. Number
 2570 of passed and failed probes are determined from a fit to the invariant mass of the
 2571 dilepton system. Simulation is corrected using these scale factors; note that they
 2572 depends on η and p_T .

2573 6.5.3 Jets and b -jet tagging

2574 In this analysis, jets are reconstructed by clustering PF candidates using the anti- k_t
 2575 algorithm with parameter distance $\Delta R = 0.4$; those charged hadrons that are not
 2576 consistent with the selected primary vertex are discarded from the clustering. The
 2577 jet energy is then corrected for the varying response of the detector as a function
 2578 of transverse momentum p_T and pseudorapidity η . Jets are selected for use in the
 2579 analysis only if they have $p_T > 25$ GeV and are separated from any selected leptons
 2580 by $\Delta R > 0.4$.

2581 Jets coming from the primary vertex and jets coming from pile-up vertices are
 2582 distinguished using a MVA discriminator based on the differences in the jet shapes,
 2583 in the relative multiplicity of charged and neutral components, and in the different
 2584 fraction of transverse momentum which is carried by the hardest components. Jet
 2585 tracks are also required to be compatible with the primary vertex.

2586 Jets originated from the hadronization of a b quark are selected using a MVA
 2587 likelihood discriminant which uses track-based lifetime information and reconstructed
 2588 secondary vertices (CSV algorithm). Only jets within the CMS tracker acceptance

2589 ($\eta < 2.4$) are identified with this tool. Data samples are used to measure the efficiency
 2590 of the b -jet tagging and the probability to misidentify jets from light quarks or gluons;
 2591 in both cases the measurements are parametrized as a function of the jet p_T and η
 2592 and later used to correct differences between the data and MC simulation in the b
 2593 tagging performance, by applying per-jet weights to the simulation, dependent on
 2594 the jet p_T , η , b tagging discriminator, and flavor (from simulation truth) [149]. The
 2595 per-event weight is taken as the product of the per-jet weights, including those of the
 2596 jets associated to the leptons. The weights are derived on $t\bar{t}$ and Z+jets events.

2597 Two working points are defined, based on the CSV algorithm output: *loose*' work-
 2598 ing point ($\text{CSV} > 0.46$) with a b signal tagging efficiency of about 83% and a mistagging
 2599 rate of about 8%; and *medium* working point ($\text{CSV} > 0.80$) with b -tagging efficiency of
 2600 about 69% and mistagging rate of order 1% [150]. Tagging of jets from charm quarks
 2601 have efficiencies of about 40% and 18% for loose and medium working points re-
 2602 spectively. Separate scale factors are applied to jets originating from bottom/charm
 2603 quarks and from light quarks in simulated events to match the tagging efficiencies
 2604 measured in the data.

2605 6.5.4 Missing Energy MET

2606 As stated in Section 3.4.1.1, the MET vector is calculated as the negative of the vector
 2607 sum of transverse momenta of all PF candidates in the event and its magnitude is
 2608 referred to as E_T^{miss} . Due to pile-up interactions, the performance in determining
 2609 MET is degraded; in order to correct for that, the energy from the selected jets and
 2610 leptons that compose the event is assigned to the variable H_T^{miss} . It is calculated in
 2611 the same way as E_T^{miss} and although it has worse resolution than E_T^{miss} , it is more
 2612 robust in the sense that it does not rely on the soft part of the event. The event

2613 selection uses a linear discriminator based on the two variables given by

$$E_T^{miss}LD = 0.00397 * E_T^{miss} + 0.00265 * H_T^{miss} \quad (6.6)$$

2614 taking advantage of the fact that the correlation between E_T^{miss} and H_T^{miss} is less
 2615 for events with instrumental missing energy than for events with real missing energy.
 2616 The working point $E_T^{miss}LD > 0.2$ was chosen to ensure a good signal efficiency while
 2617 keeping a good background rejection.

2618 6.6 Event selection

2619 .

2620 .

2621 .

2622 .

2623 .

2624 .

2625 .

2626 .

2627 .

2628 . . .

2629 . Multivariate techniques are used to discriminate the signal from the dominant
 2630 backgrounds. The analysis yields a 95% confidence level (C.L.) upper limit on the
 2631 combined tH + ttH production cross section times branching ratio of 0.64 pb, with
 2632 an expected limit of 0.32 pb, for a scenario with $kt = \sqrt{1.0}$ and $kV = 1.0$. Values
 2633 of kt outside the range of $\sqrt{1.25}$ to $\sqrt{1.60}$ are excluded at 95% C.L., assuming kV
 2634 = 1.0.

2635 Dont forget to mention previous constrains to ct check Reference ?? and Refer-
 2636 ences <https://link.springer.com/content/pdf/10.1007%2FJHEP01%282013%29088.pdf>
 2637 (paragraph after eq 2)

2638 **6.7 Background predictions**

2639 The modeling of reducible and irreducible backgrounds in this analysis uses the exact
 2640 methods, analysis code, and ROOT trees used for the $t\bar{t}H$ multilepton analysis. We
 2641 give a brief description of the methods and refer to the documentation of that analysis
 2642 in Refs. [145, 151] for any details.

2643 The backgrounds in three-lepton final states can be split in two broad categories:
 2644 irreducible backgrounds with genuine prompt leptons (i.e. from on-shell W and Z
 2645 boson decays); and reducible backgrounds where at least one of the leptons is “non-
 2646 prompt”, i.e. produced within a hadronic jet, either a genuine lepton from heavy
 2647 flavor decays, or simply mis-reconstructed jets.

2648 Irreducible backgrounds can be reliably estimated directly from Monte-Carlo sim-
 2649 ulated events, using higher-order cross sections or data control regions for the overall
 2650 normalization. This is done in this analysis for all backgrounds involving prompt lep-
 2651 tons: $t\bar{t}W$, $t\bar{t}Z$, $t\bar{t}H$, WZ , ZZ , $W^\pm W^\pm qq$, $t\bar{t}t\bar{t}$, tZq , tZW , WWW , WWZ , WZZ ,
 2652 ZZZ .

2653 Reducible backgrounds, on the other hand, are not well predicted by simulation,
 2654 and are estimated using data-driven methods. In the case of non-prompt leptons, a
 2655 fake rate method is used,

2656 Additional identification criteria are applied for electrons with p_T greater than 30
 2657 GeV to mimic the identification applied at trigger level in order to ensure consistency
 2658 between the measurement region and application region of the fake-rate.

2659 where the contribution to the final selection is estimated by extrapolating from
 2660 a sideband (or “application region”) with a looser lepton definition (the fakeable
 2661 object definitions in Tabs. 6.7 and 6.8) to the signal selection. The tight-to-loose
 2662 ratios (or “fake rates”) are measured in several background dominated data events
 2663 with dedicated triggers, subtracting the residual prompt lepton contribution using
 2664 MC. Non-prompt leptons in our signal regions are predominantly produced in $t\bar{t}$
 2665 events, with a much smaller contribution, from Drell–Yan production. The systematic
 2666 uncertainty on the normalization of the non-prompt background estimation is on the
 2667 order of 50%, and thereby one of the dominant limitations on the performance of
 2668 multilepton analyses in general and this analysis in particular. It consists of several
 2669 individual sources, such as the result of closure tests of the method using simulated
 2670 events, limited statistics in the data control regions due to necessary prescaling of
 2671 lepton triggers, and the uncertainty in the subtraction of residual prompt leptons
 2672 from the control region.

2673 The fake background where the leptons pass the looser selection are weighted
 2674 according to how many of them fail the tight criteria. Events with a single failing
 2675 lepton are weighted with the factor $f/(1-f)$ for the estimate to the tight selection
 2676 region, where f is the fake rate. Events with two failing leptons are given the negative
 2677 weight $-f_i f_j / (1-f_i)(1-f_j)$, and for three leptons the weight is positive and equal
 2678 to the product of $f/(1-f)$ factor evaluated for each failing lepton.

2679 Figures 6.10 show the distributions of some relevant kinematic variables, normal-
 2680 ized to the cross section of the respective processes and to the integrated luminosity.

2681

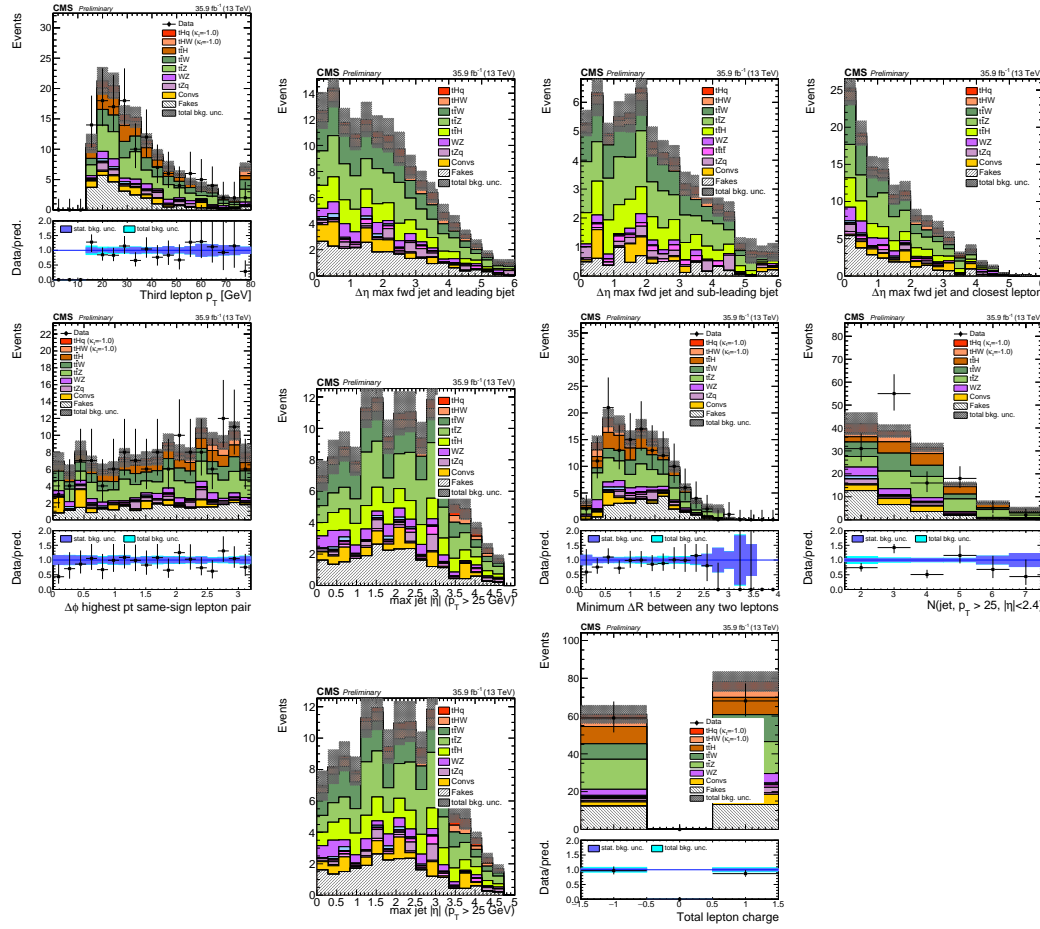


Figure 6.10: Distributions of input variables to the BDT for signal discrimination, three lepton channel, normalized to their cross section and to 35.9fb^{-1} .

2682 6.8 Signal discrimination

2683 The tHq signal is separated from the main backgrounds using a boosted decision
 2684 tree (BDT) classifier, trained on simulated signal and background events. A set of
 2685 discriminating variables are given as input to the BDT which produces a output
 2686 distribution maximizing the discrimination power. Table 6.9 lists the input variables
 2687 used while Figures 6.11 show their distributions for the relevant signal and background
 2688 samples, for the three lepton channel. Two BDT classifiers are trained for the two
 2689 main backgrounds expected in the analysis: events with prompt leptons from $t\bar{t}W$ and

2690 $t\bar{t}Z$ (also referred to as $t\bar{t}V$), and events with non-prompt leptons from $t\bar{t}$. The datasets
 2691 used in the training are the tHq signal (see Tab. A.3), and LO MADGRAPH samples
 2692 of $t\bar{t}W$ and $t\bar{t}Z$, in an admixture proportional to their respective cross sections (see
 2693 Tab. A.6).

Variable name	Description
nJet25	Number of jets with $p_T > 25$ GeV, $ \eta < 2.4$
MaxEtaJet25	Maximum $ \eta $ of any (non-CSV-loose) jet with $p_T > 25$ GeV
totCharge	Sum of lepton charges
nJetEta1	Number of jets with $ \eta > 1.0$, non-CSV-loose
detaFwdJetBJet	$\Delta\eta$ between forward light jet and hardest CSV loose jet
detaFwdJet2BJet	$\Delta\eta$ between forward light jet and second hardest CSV loose jet (defaults to -1 in events with only one CSV loose jet)
detaFwdJetClosestLep	$\Delta\eta$ between forward light jet and closest lepton
dphiHighestPtSSPair	$\Delta\phi$ of highest p_T same-sign lepton pair
minDRll	minimum ΔR between any two leptons
Lep3Pt/Lep2Pt	p_T of the 3 rd lepton (2 nd for ss2l)

Table 6.8: MVA input discriminating variables

2694 The MVA analysis consist of two stages: first a “training” where the MVA method
 2695 is trained to discriminate between simulated signal and background events, then a
 2696 “test” stage where the trained algorithm is used to classify different events from
 2697 the samples. The sample is obtained from a pre-selection (see Tab. ?? with pre-
 2698 selection cuts). Figures 6.12 show the input variables distributions as seen by the
 2699 MVA algorithm. Note that in contrast to the distributions in Fig. 6.11 only the main
 2700 backgrounds ($t\bar{t}$ from simulation, $t\bar{t}V$) are included.

2701 Note that splitting the training in two groups reveals that some variables show
 2702 opposite behavior for the two background sources; potentially screening the discrimi-
 2703 nation power if they were to be used in a single discriminant. For some other variables
 2704 the distributions are similar in both background cases.

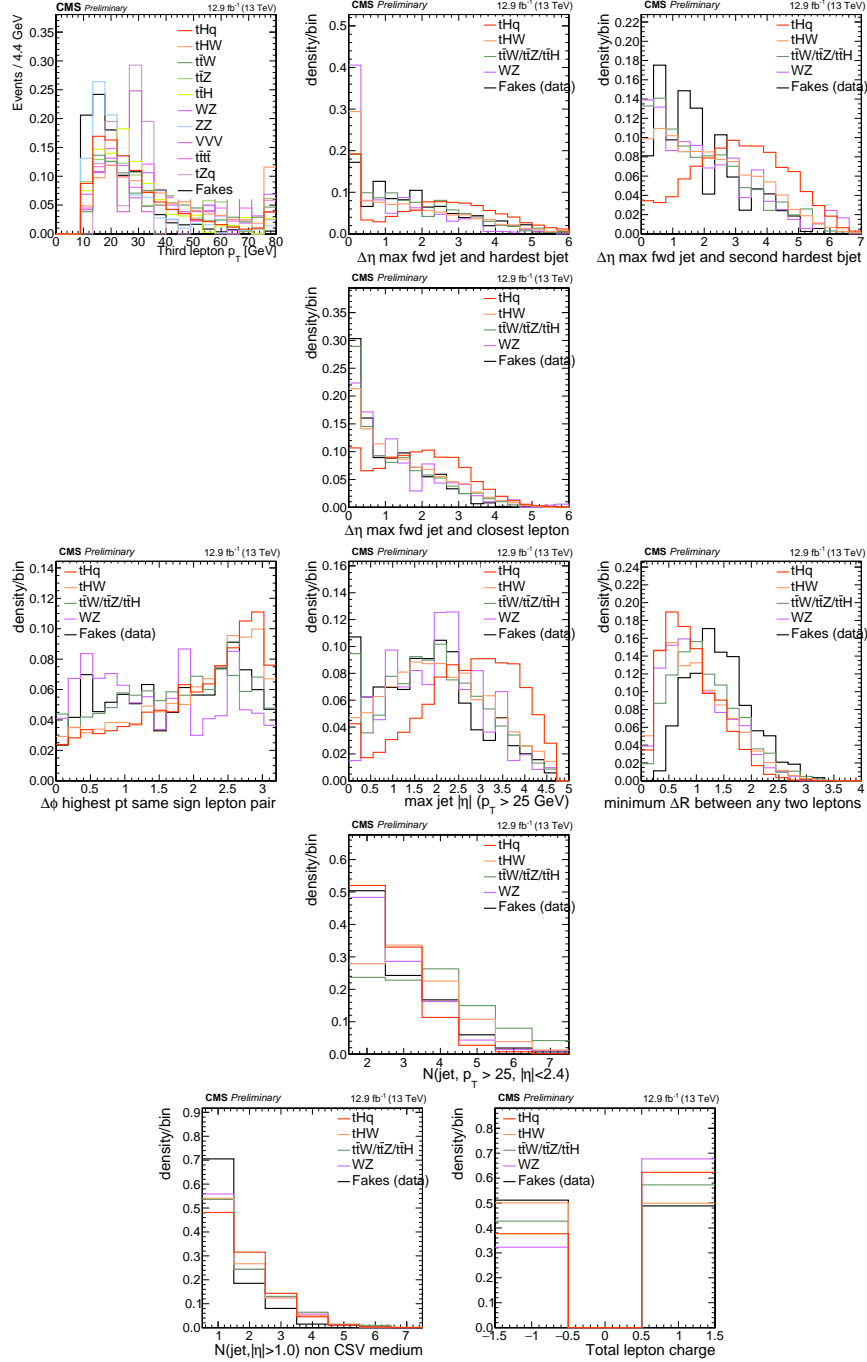


Figure 6.11: Distributions of input variables to the BDT for signal discrimination, three lepton channel.

2705 From table 6.9, it is clear that the input variables are correlated to some extend.

2706 These correlations play an important role for some MVA methods like the Fisher

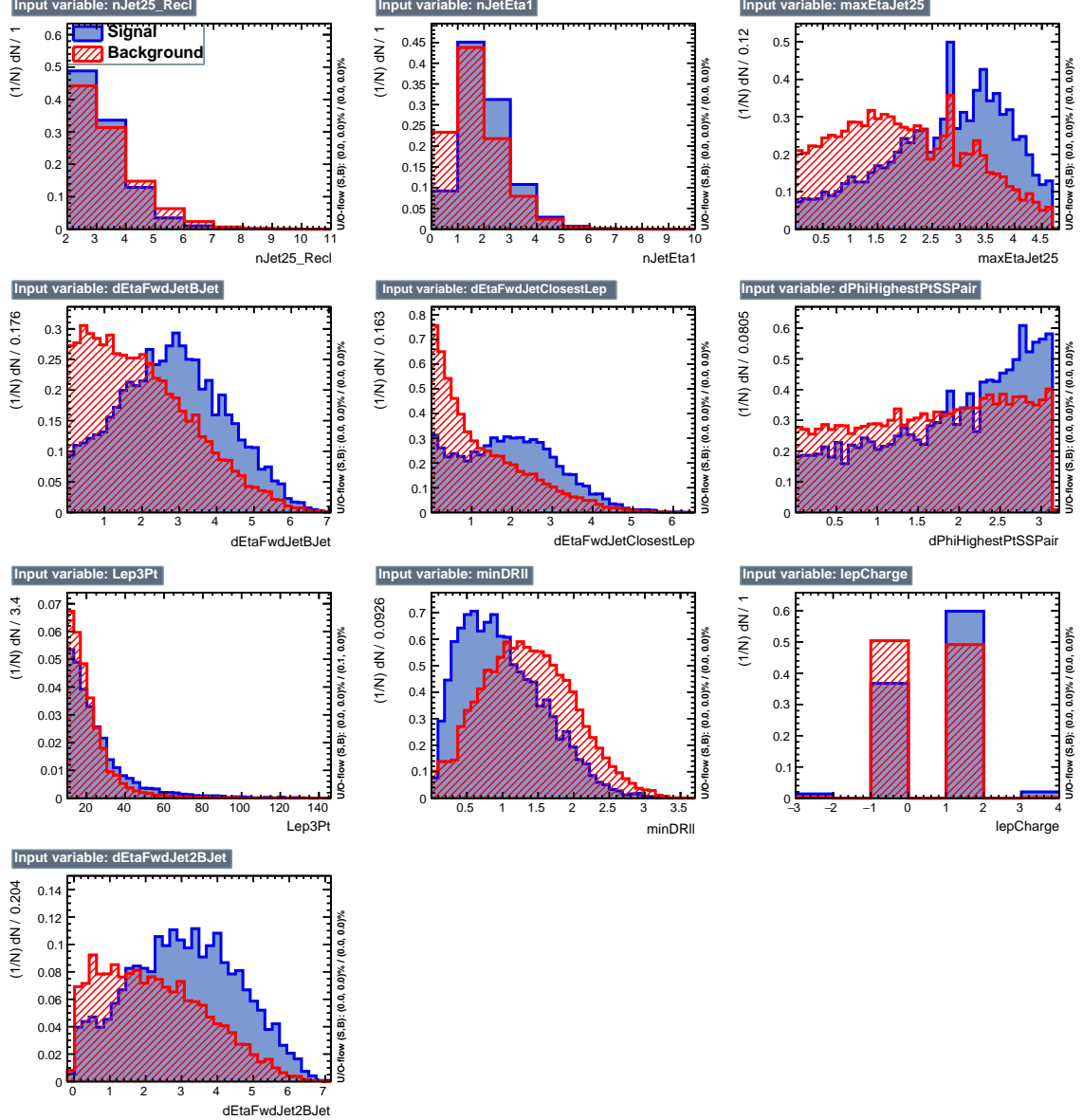


Figure 6.12: BDT inputs as seen by TMVA (signal, in blue, is tHq , background, in red, is $t\bar{t}$) for the three lepton channel, discriminated against $t\bar{t}$ (fakes) background.

discriminant method in which the first step consist of performing a linear transformation to an phase space where the correlations between variables are removed. In case a boosted decision tree (BDT) method however, correlations do not affect the performance. Figure 6.14 show the linear correlation coefficients for signal and background for the two training cases (the signal values are identical by construction). As

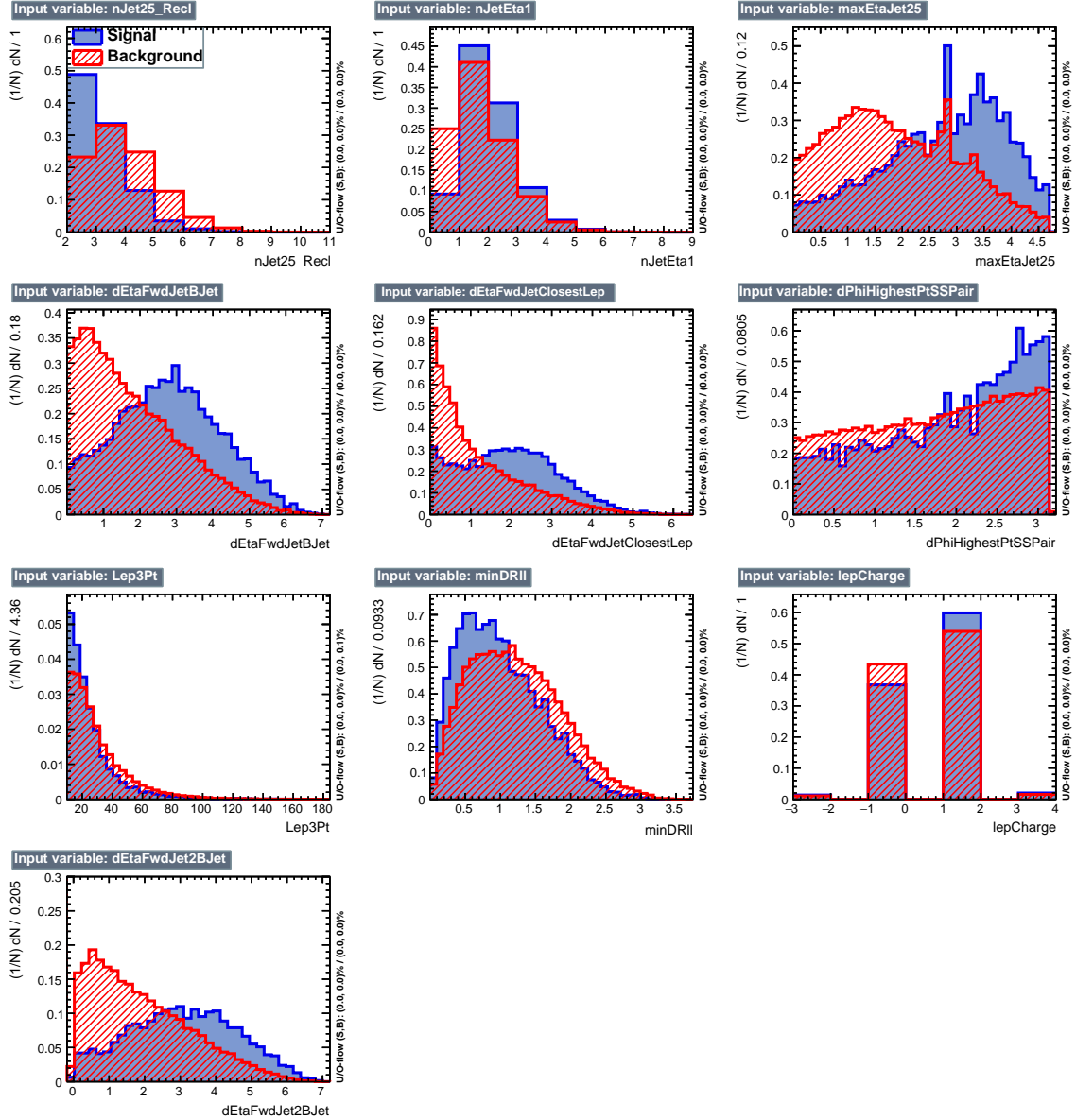


Figure 6.13: BDT inputs as seen by TMVA (signal, in blue, is tHq , background, in red, is $t\bar{t}W+t\bar{t}Z$) for the three lepton channel, discriminated against $t\bar{t}V$ background.

2712 expected, strong correlations appears for variables related to the forward jet activity.
 2713 Same trend is seen in case of the same sign dilepton channel in Figure ??.

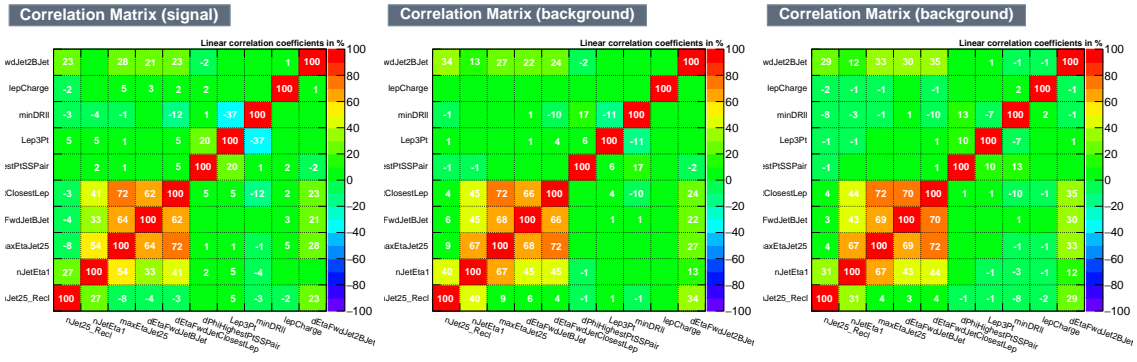


Figure 6.14: Signal (left), $t\bar{t}$ background (middle), and $t\bar{t}V$ background (right.) correlation matrices for the input variables in the TMVA analysis for the three lepton channel.

2714 6.8.1 Classifiers response

2715 Several MVA algorithms were evaluated to determine the most appropriate method
 2716 for this analysis. The plots in Fig. 6.15 (top) show the background rejection as a
 2717 function of the signal efficiency for $t\bar{t}$ and $t\bar{t}V$ trainings (ROC curves) for the different
 2718 algorithms that were evaluated.

2719 In both cases the gradient boosted decision tree (“BDTA_GRAD”) classifier offers
 2720 the best results, followed by an adaptive BDT classifier (“BDTA”). The BDTA_GRAD
 2721 classifier output distributions for signal and backgrounds are shown on the bottom of
 2722 Fig. 6.15. As expected, a good discrimination power is obtained using default discrim-
 2723 inator parameter values, with minimal overtraining. TMVA provides a ranking of the
 2724 input variables by their importance in the classification process, shown in Tab. 6.10.
 2725 The TMVA settings used in the BDT training are shown in Tab. 6.11.

2726 6.9 Additional discriminating variables

2727 Two additional discriminating variables were tested considering the fact that the
 2728 forward jet in the background could come from the pileup; since we have a real forward
 2729 jet in the signal, it could give some improvement in the discriminating power. The

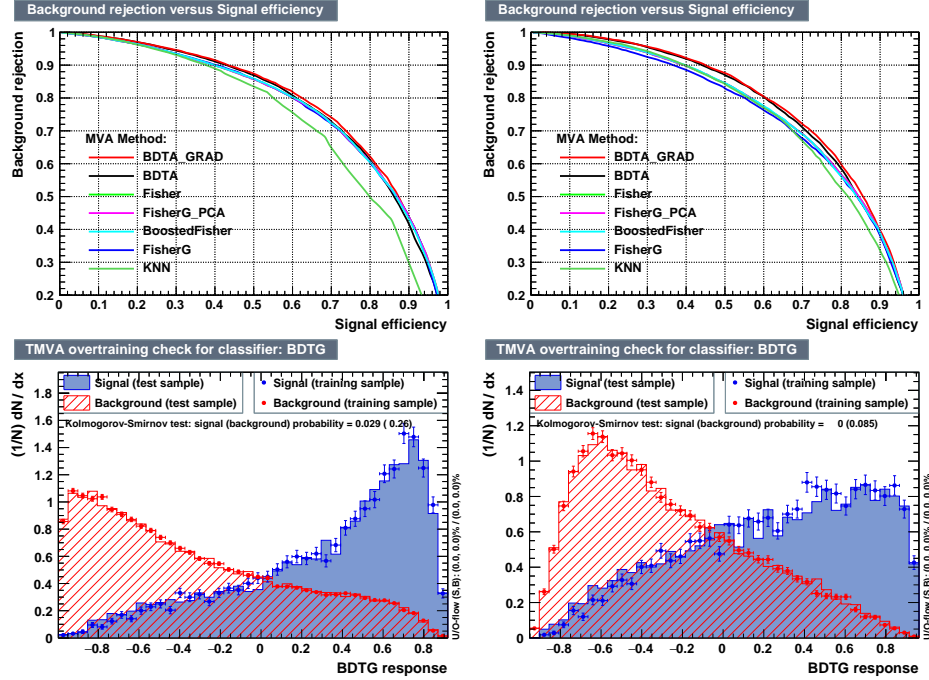


Figure 6.15: Top: background rejection vs signal efficiency (ROC curves) for various MVA classifiers (top) in the three lepton channel against $t\bar{t}V$ (left) and $t\bar{t}$ (right). Bottom: classifier output distributions for the gradient boosted decision trees, for training against $t\bar{t}V$ (left) and against $t\bar{t}$ (right).

ttbar training			ttV training		
Rank	Variable	Importance	Variable	Importance	
1	minDRll	1.329e-01	dEtaFwdJetBJet	1.264e-01	
2	dEtaFwdJetClosestLep	1.294e-01	Lep3Pt	1.224e-01	
3	dEtaFwdJetBJet	1.209e-01	maxEtaJet25	1.221e-01	
4	dPhiHighestPtSSPair	1.192e-01	dEtaFwdJet2BJet	1.204e-01	
5	Lep3Pt	1.158e-01	dEtaFwdJetClosestLep	1.177e-01	
6	maxEtaJet25	1.121e-01	minDRll	1.143e-01	
7	dEtaFwdJet2BJet	9.363e-02	dPhiHighestPtSSPair	9.777e-02	
8	nJetEta1	6.730e-02	nJet25_Recl	9.034e-02	
9	nJet25_Recl	6.178e-02	nJetEta1	4.749e-02	
10	lepCharge	4.701e-02	lepCharge	4.116e-02	

Table 6.9: TMVA input variables ranking for BDTA_GRAD method for the trainings in the three lepton channel. For both trainings the rankings show almost the same 5 variables in the first places.

2730 additional variables describe the forward jet momentum (fwdJetPt25) and the forward
 2731 jet identification(fwdJetPUID). Distributions for these variables in the three lepton
 2732 channel are shown in the Figure 6.16. The forward jet identification distribution

```

TMVA.Types.kBDT
NTrees=800
BoostType=Grad
Shrinkage=0.10
!UseBaggedGrad
nCuts=50
MaxDepth=3
NegWeightTreatment=PairNegWeightsGlobal
CreateMVApdfs

```

Table 6.10: TMVA configuration used in the BDT training.

2733 show that for both, signal and background, jets are mostly real jets.

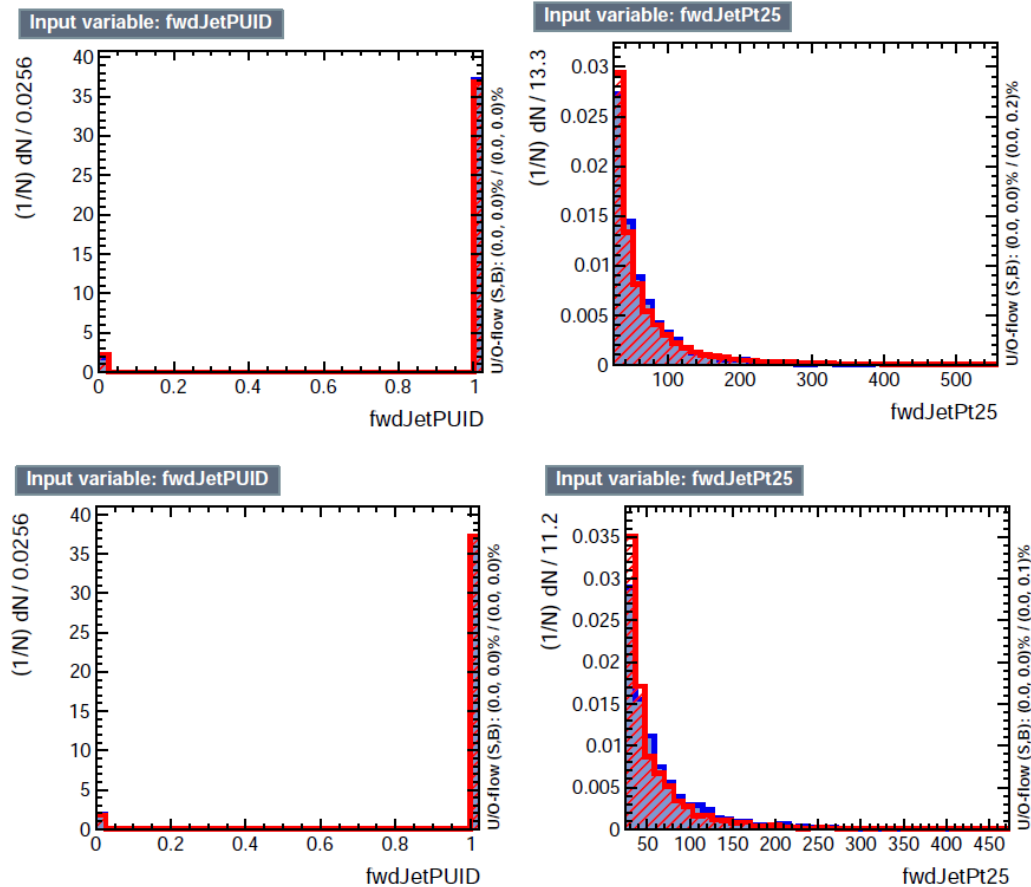


Figure 6.16: Additional discriminating variables distributions for `ttv` training (Top row) and `tt` training (bottom row) in the three lepton channel. The origin of the jets in the forward jet identification distribution is tagged as 0 for “pileup jets” while “real jets” are tagged as 1.

	ROC-integral
base 10 var ttv	0.848
+ fwdJetPUID ttv	0.849
+ fwdJetPt25 ttv	0.856
12 var ttv	0.856
base 10 var tt	0.777
+ fwdJetPUID tt	0.777
+ fwdJetPt25 tt	0.787
12 var	0.787

Table 6.11: ROC-integral for all the testing cases we made in the evaluation of the additional variables discriminating power. The improvement in the discrimination performance provided by the additional variables is about 1%

2734 The testing was made including in the MVA input one variable at a time, so we
 2735 can evaluate the dicrimination power of each variable, and then both simultaneously.
 2736 fwdJetPUID was ranked in the last place in importance (11) in both training (ttV
 2737 and tt) while fwdJetPt25 was ranked 3 in the ttV training and 7 in the tt training.
 2738 When training using 12 variables, fwdJetPt25 was ranked 5 and 7 in the ttV and tt
 2739 trainings respectively, while fwdJetPUID was ranked 12 in both cases.

2740 The improvement in the discrimination performance provided by the additional
 2741 variables is about 1%, so it was decided not to include them in the procedure. Table
 2742 6.12 show the ROC-integral for all the testing cases we made.

²⁷⁴³ **Appendix A**

²⁷⁴⁴ **Datasets and triggers**

Dataset name
/JetHT/Run2016X-23Sep2016-vY/MINIAOD
/HTMHT/Run2016X-23Sep2016-vY/MINIAOD
/MET/Run2016X-23Sep2016-vY/MINIAOD
/SingleElectron/Run2016X-23Sep2016-vY/MINIAOD
/SingleMuon/Run2016X-23Sep2016-vY/MINIAOD
/SinglePhoton/Run2016X-23Sep2016-vY/MINIAOD
/DoubleEG/Run2016X-23Sep2016-vY/MINIAOD
/MuonEG/Run2016X-23Sep2016-vY/MINIAOD
/DoubleMuon/Run2016X-23Sep2016-vY/MINIAOD
/Tau/Run2016B-23Sep2016-v3/MINIAOD
/JetHT/Run2016H-PromptReco-v3/MINIAOD
/HTMHT/Run2016H-PromptReco-v3/MINIAOD
/MET/Run2016H-PromptReco-v3/MINIAOD
/SingleElectron/Run2016H-PromptReco-v3/MINIAOD
/SingleMuon/Run2016H-PromptReco-v3/MINIAOD
/SinglePhoton/Run2016H-PromptReco-v3/MINIAOD
/DoubleEG/Run2016H-PromptReco-v3/MINIAOD
/MuonEG/Run2016H-PromptReco-v3/MINIAOD
/DoubleMuon/Run2016H-PromptReco-v3/MINIAOD

Table A.1: Full 2016 dataset used in the analysis. In the first section of the table are listed the 23Sep2016 samples; in the Run2016X-23Sep-vY label, X:B-G tag the run while Y:1,3 tag the version of the data sample. Second section list the PromptReco version of the dataset.

Same-sign dilepton (==2 muons)
HLT_Mu17_TrkIsoVVL_Mu8_TrkIsoVVL_DZ_v*
HLT_Mu17_TrkIsoVVL_TkMu8_TrkIsoVVL_DZ_v*
HLT_IsoMu22_v*
HLT_IsoTkMu22_v*
HLT_IsoMu22_eta2p1_v*
HLT_IsoTkMu22_eta2p1_v*
HLT_IsoMu24_v*
HLT_IsoTkMu24_v*
Same-sign dilepton (==2 electrons)
HLT_Ele23_Ele12_CaloIdL_TrackIdL_IsoVL_DZ_v*
HLT_Ele27_eta2p1_WP Loose_Gsf_v*
HLT_Ele27_WPTight_Gsf_v*
HLT_Ele25_eta2p1_WPTight_Gsf_v*
Same-sign dilepton (==1 muon, ==1 electron)
HLT_Mu23_TrkIsoVVL_Ele8_CaloIdL_TrackIdL_IsoVL_v*
HLT_Mu8_TrkIsoVVL_Ele23_CaloIdL_TrackIdL_IsoVL_v*
HLT_Mu23_TrkIsoVVL_Ele8_CaloIdL_TrackIdL_IsoVL_DZ_v*
HLT_Mu8_TrkIsoVVL_Ele23_CaloIdL_TrackIdL_IsoVL_DZ_v*
HLT_IsoMu22_v*
HLT_IsoTkMu22_v*
HLT_IsoMu22_eta2p1_v*
HLT_IsoTkMu22_eta2p1_v*
HLT_IsoMu24_v*
HLT_IsoTkMu24_v*
HLT_Ele27_WPTight_Gsf_v*
HLT_Ele25_eta2p1_WPTight_Gsf_v*
HLT_Ele27_eta2p1_WP Loose_Gsf_v*
Three lepton
HLT_DiMu9_Ele9_CaloIdL_TrackIdL_v*
HLT_Mu8_DiEle12_CaloIdL_TrackIdL_v*
HLT_TripleMu_12_10_5_v*
HLT_Ele16_Ele12_Ele8_CaloIdL_TrackIdL_v*
HLT_Mu23_TrkIsoVVL_Ele8_CaloIdL_TrackIdL_IsoVL_v*
HLT_Mu23_TrkIsoVVL_Ele8_CaloIdL_TrackIdL_IsoVL_DZ_v*
HLT_Mu8_TrkIsoVVL_Ele23_CaloIdL_TrackIdL_IsoVL_v*
HLT_Mu8_TrkIsoVVL_Ele23_CaloIdL_TrackIdL_IsoVL_DZ_v*
HLT_Ele23_Ele12_CaloIdL_TrackIdL_IsoVL_DZ_v*
HLT_Mu17_TrkIsoVVL_Mu8_TrkIsoVVL_DZ_v*
HLT_Mu17_TrkIsoVVL_TkMu8_TrkIsoVVL_DZ_v*
HLT_IsoMu22_v*
HLT_IsoTkMu22_v*
HLT_IsoMu22_eta2p1_v*
HLT_IsoTkMu22_eta2p1_v*
HLT_IsoMu24_v*
HLT_IsoTkMu24_v*
HLT_Ele27_WPTight_Gsf_v*
HLT_Ele25_eta2p1_WPTight_Gsf_v*
HLT_Ele27_eta2p1_WP Loose_Gsf_v*

Table A.2: Table of high-level triggers considered in the analysis.

Sample	σ [pb]	BF
/THQ_Hincl_13TeV-madgraph-pythia8_TuneCUETP8M1/	0.7927	0.324
/THW_Hincl_13TeV-madgraph-pythia8_TuneCUETP8M1/	0.1472	1.0

Table A.3: Signal samples and their cross section and branching fraction used in this analysis. See Ref. [157] for more details.

Different MC generators were used to generate the background processes. The dominant sources ($t\bar{t}$, $t\bar{t}W$, $t\bar{t}Z$, $t\bar{t}H$) were produced using AMC@NLO interfaced to PYTHIA8, and are scaled to NLO cross sections. Other processes are simulated using POWHEG interfaced to PYTHIA, or bare PYTHIA (see table A.5 and [145] for more details).

		<i>tHq</i>		<i>tHW</i>		
κ_V	κ_t	sum of weights	cross section [pb]	sum of weights	cross section [pb]	LHE weights
1.0	-3.0	35.700022	2.991	11.030445	0.6409	LHEweight_wgt[446]
1.0	-2.0	20.124298	1.706	5.967205	0.3458	LHEweight_wgt[447]
1.0	-1.5	14.043198	1.205	4.029093	0.2353	LHEweight_wgt[448]
1.0	-1.25	11.429338	0.9869	3.208415	0.1876	LHEweight_wgt[449]
1.0	-1.0		0.7927		0.1472	
1.0	-0.75	7.054998	0.6212	1.863811	0.1102	LHEweight_wgt[450]
1.0	-0.5	5.294518	0.4723	1.339886	0.07979	LHEweight_wgt[451]
1.0	-0.25	3.818499	0.3505	0.914880	0.05518	LHEweight_wgt[452]
1.0	0.0	2.627360	0.2482	0.588902	0.03881	LHEweight_wgt[453]
1.0	0.25	1.719841	0.1694	0.361621	0.02226	LHEweight_wgt[454]
1.0	0.5	1.097202	0.1133	0.233368	0.01444	LHEweight_wgt[455]
1.0	0.75	0.759024	0.08059	0.204034	0.01222	LHEweight_wgt[456]
1.0	1.0	0.705305	0.07096	0.273617	0.01561	LHEweight_wgt[457]
1.0	1.25	0.936047	0.0839	0.442119	0.02481	LHEweight_wgt[458]
1.0	1.5	1.451249	0.1199	0.709538	0.03935	LHEweight_wgt[459]
1.0	2.0	3.335034	0.2602	1.541132	0.08605	LHEweight_wgt[460]
1.0	3.0	10.516125	0.8210	4.391335	0.2465	LHEweight_wgt[461]
1.5	-3.0	45.281492	3.845	13.426212	0.7825	LHEweight_wgt[462]
1.5	-2.0	27.606715	2.371	7.809713	0.4574	LHEweight_wgt[463]
1.5	-1.5	20.476088	1.784	5.594971	0.3290	LHEweight_wgt[464]
1.5	-1.25	17.337465	1.518	4.635978	0.2749	LHEweight_wgt[465]
1.5	-1.0	14.483302	1.287	3.775902	0.2244	LHEweight_wgt[466]
1.5	-0.75	11.913599	1.067	3.014744	0.1799	LHEweight_wgt[467]
1.5	-0.5	9.628357	0.874	2.352505	0.1410	LHEweight_wgt[468]
1.5	-0.25	7.627574	0.702	1.789184	0.1081	LHEweight_wgt[469]
1.5	0.0	5.911882	0.5577	1.324946	0.08056	LHEweight_wgt[470]
1.5	0.25	4.479390	0.4365	0.959295	0.05893	LHEweight_wgt[471]
1.5	0.5	3.331988	0.3343	0.692727	0.04277	LHEweight_wgt[472]
1.5	0.75	2.469046	0.2558	0.525078	0.03263	LHEweight_wgt[473]
1.5	1.0	1.890565	0.2003	0.456347	0.02768	LHEweight_wgt[474]
1.5	1.25	1.596544	0.1689	0.486534	0.02864	LHEweight_wgt[475]
1.5	1.5	1.586983	0.1594	0.615638	0.03509	LHEweight_wgt[476]
1.5	2.0	2.421241	0.2105	1.170602	0.06515	LHEweight_wgt[477]
1.5	3.0	7.503280	0.5889	3.467546	0.1930	LHEweight_wgt[478]
0.5	-3.0	27.432685	2.260	8.929074	0.5136	LHEweight_wgt[479]
0.5	-2.0	13.956013	1.160	4.419093	0.2547	LHEweight_wgt[480]
0.5	-1.5	8.924438	0.7478	2.757611	0.1591	LHEweight_wgt[481]
0.5	-1.25	6.835341	0.5726	2.075247	0.1204	LHEweight_wgt[482]
0.5	-1.0	5.030704	0.4273	1.491801	0.08696	LHEweight_wgt[483]
0.5	-0.75	3.510528	0.2999	1.007273	0.05885	LHEweight_wgt[484]
0.5	-0.5	2.274811	0.1982	0.621663	0.03658	LHEweight_wgt[485]
0.5	-0.25	1.323555	0.1189	0.334972	0.01996	LHEweight_wgt[486]
0.5	0.0	0.656969	0.06223	0.147253	0.008986	LHEweight_wgt[487]
0.5	0.25	0.274423	0.02830	0.058342	0.003608	LHEweight_wgt[488]
0.5	0.5	0.176548	0.01778	0.068404	0.003902	LHEweight_wgt[489]
0.5	0.75	0.363132	0.03008	0.177385	0.009854	LHEweight_wgt[490]
0.5	1.0	0.834177	0.06550	0.385283	0.02145	LHEweight_wgt[491]
0.5	1.25	1.589682	0.1241	0.692099	0.03848	LHEweight_wgt[492]
0.5	1.5	2.629647	0.2047	1.097834	0.06136	LHEweight_wgt[493]
0.5	2.0	5.562958	0.4358	2.206057	0.1246	LHEweight_wgt[494]
0.5	3.0	14.843102	1.177	5.609519	0.3172	LHEweight_wgt[495]

Table A.4: κ_V and κ_t combinations generated for the two signal samples and their NLO cross sections. The *tHq* cross section is multiplied by the branching fraction of the enforced leptonic decay of the top quark (0.324). See also Ref. [157].

Sample	σ [pb]
TTWJetsToLNu_TuneCUETP8M1_13TeV-amcatnloFXFX-madspin-pythia8	0.2043
TTZToLLNuNu_M-10_TuneCUETP8M1_13TeV-amcatnlo-pythia8	0.2529
ttHJetToNonbb_M125_13TeV_amcatnloFXFX_madspin_pythia8_mWCutfix /store/cmst3/group/susy/gpetrucc/13TeV/u/TTLL_m1to10_LO_NoMS_for76X/	0.2151 0.0283
WGToLNuG_TuneCUETP8M1_13TeV-madgraphMLM-pythia8	585.8
ZGTo2LG_TuneCUETP8M1_13TeV-amcatnloFXFX-pythia8	131.3
TGJets_TuneCUETP8M1_13TeV_amcatnlo_madspin_pythia8	2.967
TGJets_TuneCUETP8M1_13TeV_amcatnlo_madspin_pythia8	2.967
TTGJets_TuneCUETP8M1_13TeV-amcatnloFXFX-madspin-pythia8	3.697
WpWpJJ_EWK-QCD_TuneCUETP8M1_13TeV-madgraph-pythia8	0.03711
ZZZ_TuneCUETP8M1_13TeV-amcatnlo-pythia8	0.01398
WWZ_TuneCUETP8M1_13TeV-amcatnlo-pythia8	0.1651
WZZ_TuneCUETP8M1_13TeV-amcatnlo-pythia8	0.05565
WW_DoubleScattering_13TeV-pythia8	1.64
tZq_ll_4f_13TeV-amcatnlo-pythia8_TuneCUETP8M1	0.0758
ST_tWll_5f_LO_13TeV-MadGraph-pythia8	0.01123
TTTT_TuneCUETP8M1_13TeV-amcatnlo-pythia8	0.009103
WZTo3LNu_TuneCUETP8M1_13TeV-powheg-pythia8	4.4296
ZZTo4L_13TeV_powheg_pythia8	1.256
TTJets_SingleLeptFromTbar_TuneCUETP8M1_13TeV-madgraphMLM-pythia8	182.1754
TTJets_SingleLeptFromT_TuneCUETP8M1_13TeV-madgraphMLM-pythia8	182.1754
TTJets_DiLept_TuneCUETP8M1_13TeV-madgraphMLM-pythia8	87.3
DYJetsToLL_M-10to50_TuneCUETP8M1_13TeV-amcatnloFXFX-pythia8	18610
DYJetsToLL_M-50_TuneCUETP8M1_13TeV-madgraphMLM-pythia8	6024
WJetsToLNu_TuneCUETP8M1_13TeV-amcatnloFXFX-pythia8	61526.7
ST_tW_top_5f_inclusiveDecays_13TeV-powheg-pythia8_TuneCUETP8M1	35.6
ST_tW_antitop_5f_inclusiveDecays_13TeV-powheg-pythia8_TuneCUETP8M1	35.6
ST_t-channel_4f_leptonDecays_13TeV-amcatnlo-pythia8_TuneCUETP8M1	70.3144
ST_t-channel_antitop_4f_leptonDecays_13TeV-powheg-pythia8_TuneCUETP8M1	26.2278
ST_s-channel_4f_leptonDecays_13TeV-amcatnlo-pythia8_TuneCUETP8M1	3.68064
WWTo2L2Nu_13TeV-powheg	10.481

Table A.5: List of background samples used in this analysis (CMSSW 80X). In the first section of the table are listed the samples of the processes for which we use the simulation to extract the final yields and shapes, in the second section the samples of the processes we will estimate from data. The MC simulation is used to design the data driven methods and derive the associated systematics.

Sample	σ [pb]
ttWJets_13TeV_madgraphMLM	0.6105
ttZJets_13TeV_madgraphMLM	0.5297/0.692

Table A.6: Leading-order $t\bar{t}W$ and $t\bar{t}Z$ samples used in the signal BDT training.

2750

References

- 2751 [1] J. Schwinger. "Quantum Electrodynamics. I. A Covariant Formulation". Phys-
2752 ical Review. 74 (10): 1439-61, (1948). <https://doi.org/10.1103/PhysRev.74.1439>
- 2754 [2] R. P. Feynman. "Space-Time Approach to Quantum Electrodynamics". Physical
2755 Review. 76 (6): 769-89, (1949). <https://doi.org/10.1103/PhysRev.76.769>
- 2756 [3] S. Tomonaga. "On a Relativistically Invariant Formulation of the Quantum
2757 Theory of Wave Fields". Progress of Theoretical Physics. 1 (2): 27-42, (1946).
2758 <https://doi.org/10.1143/PTP.1.27>
- 2759 [4] D.J. Griffiths, "Introduction to electrodynamics". 4th ed. Pearson, (2013).
- 2760 [5] F. Mandl, G. Shaw. "Quantum field theory." Chichester, Wiley (2009).
- 2761 [6] F. Halzen, and A.D. Martin, "Quarks and leptons: An introductory course in
2762 modern particle physics". New York: Wiley, (1984) .
- 2763 [7] File: Standard_Model_of_Elementary_Particle_dark.svg. (2017, June 12)
2764 Wikimedia Commons, the free media repository. Retrieved November 27, 2017
2765 from <https://www.collegiate-advanced-electricity.com/single-post/2017/04/10/The-Standard-Model-of-Particle-Physics>.

- 2767 [8] E. Noether, "Invariante Variationsprobleme", Nachrichten von der Gesellschaft
2768 der Wissenschaften zu Göttingen, mathematisch-physikalische Klasse, vol. 1918,
2769 pp. 235-257, (1918).
- 2770 [9] C. Patrignani et al. (Particle Data Group), Chin. Phys. C, 40, 100001 (2016)
2771 and 2017 update.
- 2772 [10] M. Goldhaber, L. Grodzins, A.W. Sunyar "Helicity of Neutrinos", Phys. Rev.
2773 109, 1015 (1958).
- 2774 [11] Palanque-Delabrouille N et al. "Neutrino masses and cosmology with Lyman-
2775 alpha forest power spectrum", JCAP 11 011 (2015).
- 2776 [12] M. Gell-Mann. "A Schematic Model of Baryons and Mesons". Physics Letters.
2777 8 (3): 214-215 (1964).
- 2778 [13] G. Zweig. "An SU(3) Model for Strong Interaction Symmetry and its Breaking"
2779 (PDF). CERN Report No.8182/TH.401 (1964).
- 2780 [14] G. Zweig. "An SU(3) Model for Strong Interaction Symmetry and its Breaking:
2781 II" (PDF). CERN Report No.8419/TH.412(1964).
- 2782 [15] M. Gell-Mann. "The Interpretation of the New Particles as Displaced Charged
2783 Multiplets". Il Nuovo Cimento 4: 848. (1956).
- 2784 [16] T. Nakano, K. Nishijima. "Charge Independence for V-particles". Progress of
2785 Theoretical Physics 10 (5): 581-582. (1953).
- 2786 [17] N. Cabibbo, "Unitary symmetry and leptonic decays" Physical Review Letters,
2787 vol. 10, no. 12, p. 531, (1963).

- 2788 [18] M.Kobayashi, T.Maskawa, “CP-violation in the renormalizable theory of weak
2789 interaction,” Progress of Theoretical Physics, vol. 49, no. 2, pp. 652-657, (1973).
- 2790 [19] File: Weak Decay (flipped).svg. (2017, June 12). Wikimedia Com-
2791 mons, the free media repository. Retrieved November 27, 2017
2792 from [https://commons.wikimedia.org/w/index.php?title=File:
2793 Weak_Decay_\(flipped\)\.svg&oldid=247498592](https://commons.wikimedia.org/w/index.php?title=File:Weak_Decay_(flipped)\.svg&oldid=247498592).
- 2794 [20] Georgia Tech University. Coupling Constants for the Fundamental Forces(2005).
2795 Retrieved January 10, 2018, from [http://hyperphysics.phy-astr.gsu.edu/
2796 hbase/Forces/couple.html#c2](http://hyperphysics.phy-astr.gsu.edu/hbase/Forces/couple.html#c2)
- 2797 [21] M. Strassler. (May 31, 2013).The Strengths of the Known Forces. Retrieved Jan-
2798 uary 10, 2018, from [https://profmattstrassler.com/articles-and-posts/
2799 particle-physics-basics/the-known-forces-of-nature/
2800 the-strength-of-the-known-forces/](https://profmattstrassler.com/articles-and-posts/particle-physics-basics/the-known-forces-of-nature/the-strength-of-the-known-forces/)
- 2801 [22] S.L. Glashow. “Partial symmetries of weak interactions”, Nucl. Phys. 22 579-
2802 588, (1961).
- 2803 [23] A. Salam, J.C. Ward. “Electromagnetic and weak interactions”, Physics Letters
2804 13 168-171, (1964).
- 2805 [24] S. Weinberg, “A model of leptons”, Physical Review Letters, vol. 19, no. 21, p.
2806 1264, (1967).
- 2807 [25] M. Peskin, D. Schroeder, “An introduction to quantum field theory”. Perseus
2808 Books Publishing L.L.C., (1995).
- 2809 [26] A. Pich. “The Standard Model of Electroweak Interactions” <https://arxiv.org/abs/1201.0537>
- 2810

- 2811 [27] G. Arnison et al. (UA1 Collaboration), Phys. Lett. B 122, 103 (1983).
- 2812 [28] M. Banner et al. (UA2 Collaboration), Phys. Lett. B 122, 476 (1983).
- 2813 [29] G. Arnison et al. (UA1 Collaboration), Phys. Lett. B 126, 398 (1983).
- 2814 [30] P. Bagnaia et al. (UA2 Collaboration), Phys. Lett. B 129, 130 (1983).
- 2815 [31] F.Bellaiche. (2012, 2 September). “What’s this Higgs boson anyway?”. Retrieved
2816 from: <https://www.quantum-bits.org/?p=233>
- 2817 [32] M. Endres et al. Nature 487, 454-458 (2012) doi:10.1038/nature11255
- 2818 [33] F. Englert, R. Brout. “Broken Symmetry and the Mass of Gauge
2819 Vector Mesons”. Physical Review Letters. 13 (9): 321-23.(1964)
2820 doi:10.1103/PhysRevLett.13.321
- 2821 [34] P.Higgs. “Broken Symmetries and the Masses of Gauge Bosons”. Physical Re-
2822 view Letters. 13 (16): 508-509,(1964). doi:10.1103/PhysRevLett.13.508.
- 2823 [35] G.Guralnik, C.R. Hagen and T.W.B. Kibble. “Global Conservation Laws
2824 and Massless Particles”. Physical Review Letters. 13 (20): 585-587, (1964).
2825 doi:10.1103/PhysRevLett.13.585.
- 2826 [36] CMS collaboration. “Observation of a new boson at a mass of 125 GeV with
2827 the CMS experiment at the LHC”. Physics Letters B. 716 (1): 30-61 (2012).
2828 arXiv:1207.7235. doi:10.1016/j.physletb.2012.08.021
- 2829 [37] ATLAS collaboration. “Observation of a New Particle in the Search for the Stan-
2830 dard Model Higgs Boson with the ATLAS Detector at the LHC”. Physics Letters
2831 B. 716 (1): 1-29 (2012). arXiv:1207.7214. doi:10.1016/j.physletb.2012.08.020.

- 2832 [38] ATLAS collaboration; CMS collaboration (26 March 2015). “Combined Mea-
 2833 surement of the Higgs Boson Mass in pp Collisions at $\sqrt{s}=7$ and 8 TeV with
 2834 the ATLAS and CMS Experiments”. Physical Review Letters. 114 (19): 191803.
 2835 arXiv:1503.07589. doi:10.1103/PhysRevLett.114.191803.
- 2836 [39] LHC InternationalMasterclasses“When protons collide”. Retrieved from http://atlas.physicsmasterclasses.org/en/zpath_protoncollisions.htm
- 2838 [40] CMS Collaboration, “SM Higgs Branching Ratios and Total Decay Widths (up-
 2839 date in CERN Report4 2016)”. <https://twiki.cern.ch/twiki/bin/view/LHCPhysics/CERNYellowReportPageBR> , last accessed on 17.12.2017.
- 2841 [41] R.Grant V. “Determination of Higgs branching ratios in $H \rightarrow W^+W^- \rightarrow l\nu jj$
 2842 and $H \rightarrow ZZ \rightarrow l^+l^-jj$ channels”. Physics Department, University of Ten-
 2843 nessee (Dated: October 31, 2012). Retrieved from <http://aesop.phys.utk.edu/ph611/2012/projects/Riley.pdf>
- 2845 [42] LHC Higgs Cross Section Working Group, Denner, A., Heinemeyer, S. et al.
 2846 “Standard model Higgs-boson branching ratios with uncertainties”. Eur. Phys.
 2847 J. C (2011) 71: 1753. <https://doi.org/10.1140/epjc/s10052-011-1753-8>
- 2848 [43] D. de Florian et al., LHC Higgs Cross Section Working Group,
 2849 CERNâš2017âš002-M, arXiv:1610.07922[hep-ph] (2016).
- 2850 [44] ATLAS and CMS Collaborations, “Measurements of the Higgs boson produc-
 2851 tion and decay rates and constraints on its couplings from a combined ATLAS
 2852 and CMS analysis of the LHC pp collision data at $\sqrt{s} = 7$ and 8 TeV,” (2016).
 2853 CERN-EP-2016-100, ATLAS-HIGG-2015-07, CMS-HIG-15-002.

- 2854 [45] J. A. Aguilar-Saavedra, R. Benbrik, S. Heinemeyer, and M. Perez-Victoria,
2855 “Handbook of vector-like quarks: Mixing and single production”, Phys. Rev. D
2856 88 (2013) 094010, doi:10.1103/PhysRevD.88.094010, arXiv:1306.0572.
- 2857 [46] A. Greljo, J. F. Kamenik, and J. Kopp, “Disentangling flavor vio-
2858 lation in the top-Higgs sector at the LHC”, JHEP 07 (2014) 046,
2859 doi:10.1007/JHEP07(2014)046, arXiv:1404.1278.
- 2860 [47] F. Demartin, F. Maltoni, K. Mawatari, and M. Zaro, “Higgs production in
2861 association with a single top quark at the LHC,” European Physical Journal C,
2862 vol. 75, p. 267, (2015). doi:10.1140/epjc/s10052-015-3475-9, arXiv:1504.00611.
- 2863 [48] F. Demartin, B. Maier, F. Maltoni, K. Mawatari, and M. Zaro, “tWH associated
2864 production at the LHC”, European Physical Journal C, vol. 77, p. 34, (2017).
2865 arXiv:1607.05862
- 2866 [49] F. Maltoni, K. Paul, T. Stelzer, and S. Willenbrock, “Associated production
2867 of Higgs and single top at hadron colliders”, Phys.Rev. D64 (2001) 094023,
2868 [hep-ph/0106293].
- 2869 [50] S. Biswas, E. Gabrielli, F. Margaroli, and B. Mele, “Direct constraints on the
2870 top-Higgs coupling from the 8 TeV LHC data,” Journal of High Energy Physics,
2871 vol. 07, p. 073, (2013).
- 2872 [51] M. Farina, C. Grojean, F. Maltoni, E. Salvioni, and A. Thamm, “Lifting de-
2873 generacies in Higgs couplings using single top production in association with a
2874 Higgs boson,” Journal of High Energy Physics, vol. 05, p. 022, (2013).
- 2875 [52] T.M. Tait and C.-P. Yuan, “Single top quark production as a window to physics
2876 beyond the standard model”, Phys. Rev. D 63 (2000) 014018 [hep-ph/0007298].

- 2877 [53] CMS Collaboration, “Modelling of the single top-quark production in associa-
2878 tion with the Higgs boson at 13 TeV.” <https://twiki.cern.ch/twiki/bin/viewauth/CMS/SingleTopHiggsGeneration13TeV>, last accessed on 16.01.2018.
- 2880 [54] CMS Collaboration, “SM Higgs production cross sections at $\sqrt{s} =$
2881 13 TeV.” <https://twiki.cern.ch/twiki/bin/view/LHCPhysics/CERNYellowReportPageAt13TeV>, last accessed on 16.01.2018.
- 2883 [55] S. Dawson, The effective W approximation, Nucl. Phys. B 249 (1985) 42.
- 2884 [56] S. Biswas, E. Gabrielli and B. Mele, JHEP 1301 (2013) 088 [arXiv:1211.0499
2885 [hep-ph]].
- 2886 [57] LHC Higgs Cross Section Working Group, “Handbook of LHC Higgs Cross
2887 Sections: 4.Deciphering the Nature of the Higgs Sector”, arXiv:1610.07922.
- 2888 [58] J. Ellis, D. S. Hwang, K. Sakurai, and M. Takeuchi.“Disentangling Higgs-Top
2889 Couplings in Associated Production”, JHEP 1404 (2014) 004, [arXiv:1312.5736].
- 2890 [59] CMS Collaboration, V. Khachatryan et al., “Precise determination of the mass
2891 of the Higgs boson and tests of compatibility of its couplings with the standard
2892 model predictions using proton collisions at 7 and 8 TeV,” arXiv:1412.8662.
- 2893 [60] ATLAS Collaboration, G. Aad et al., “Updated coupling measurements of the
2894 Higgs boson with the ATLAS detector using up to 25 fb^{-1} of proton-proton
2895 collision data”, ATLAS-CONF-2014-009.
- 2896 [61] File:Cern-accelerator-complex.svg. Wikimedia Commons, the free media repos-
2897 itory. Retrieved January, 2018 from <https://commons.wikimedia.org/wiki/File:Cern-accelerator-complex.svg>

- 2899 [62] J.L. Caron , “Layout of the LEP tunnel including future LHC infrastructures.”,
2900 (Nov, 1993). A C Collection. Legacy of AC. Pictures from 1992 to 2002. Re-
2901 trieved from <https://cds.cern.ch/record/841542>
- 2902 [63] M. Vretenar, “The radio-frequency quadrupole”. CERN Yellow Report CERN-
2903 2013-001, pp.207-223 DOI:10.5170/CERN-2013-001.207. arXiv:1303.6762
- 2904 [64] L.Evans. P. Bryant (editors). “LHC Machine”. JINST 3 S08001 (2008).
- 2905 [65] CERN Photographic Service.“Radio-frequency quadrupole, RFQ-1”, March
2906 1983, CERN-AC-8303511. Retrieved from <https://cds.cern.ch/record/615852>.
- 2908 [66] CERN Photographic Service “Animation of CERN’s accelerator network”, 14
2909 October 2013. DOI: 10.17181/cds.1610170 Retrieved from <https://videos.cern.ch/record/1610170>
- 2911 [67] C.Sutton. “Particle accelerator”.Encyclopedia Britannica. July 17,
2912 2013. Retrieved from <https://www.britannica.com/technology/particle-accelerator>.
- 2914 [68] L.Guiraud. “Installation of LHC cavity in vacuum tank.”. July 27 2000. CERN-
2915 AC-0007016. Retrieved from <https://cds.cern.ch/record/41567>.
- 2916 [69] J.L. Caron, “Magnetic field induced by the LHC dipole’s superconducting coils”.
2917 March 1998. AC Collection. Legacy of AC. Pictures from 1992 to 2002. LHC-
2918 PHO-1998-325. Retrieved from <https://cds.cern.ch/record/841511>.
- 2919 [70] AC Team. “Diagram of an LHC dipole magnet”. June 1999. CERN-DI-9906025
2920 retrieved from <https://cds.cern.ch/record/40524>.

- 2921 [71] CMS Collaboration “Public CMS Luminosity Information”. https://twiki.cern.ch/twiki/bin/view/CMSPublic/LumiPublicResults#2016__proton_proton_13_TeV_collis, last accessed 24.01.2018
- 2924 [72] J.L Caron. “LHC Layout” AC Collection. Legacy of AC. Pictures from 1992
2925 to 2002. September 1997, LHC-PHO-1997-060. Retrieved from <https://cds.cern.ch/record/841573>.
- 2927 [73] J.A. Coarasa. “The CMS Online Cluster:Setup, Operation and Maintenance
2928 of an Evolving Cluster”. ISGC 2012, 26 February - 2 March 2012, Academia
2929 Sinica, Taipei, Taiwan.
- 2930 [74] CMS Collaboration. “The CMS experiment at the CERN LHC” JINST 3 S08004
2931 (2008).
- 2932 [75] CMS Collaboration. “CMS detector drawings 2012” CMS-PHO-GEN-2012-002.
2933 Retrieved from <http://cds.cern.ch/record/1433717>.
- 2934 [76] Davis, Siona Ruth. “Interactive Slice of the CMS detector”, Aug. 2016,
2935 CMS-OUTREACH-2016-027, retrieved from <https://cds.cern.ch/record/2205172>
- 2937 [77] R. Breedon. “View through the CMS detector during the cooldown of the
2938 solenoid on February 2006. CMS Collection”, February 2006, CMS-PHO-
2939 OREACH-2005-004, Retrieved from <https://cds.cern.ch/record/930094>.
- 2940 [78] Halyo, V. and LeGresley, P. and Lujan, P. “Massively Parallel Computing and
2941 the Search for Jets and Black Holes at the LHC”, Nucl.Instrum.Meth. A744
2942 (2014) 54-60, DOI: 10.1016/j.nima.2014.01.038”

- 2943 [79] A. Dominguez et. al. “CMS Technical Design Report for the Pixel Detector
2944 Upgrade”, CERN-LHCC-2012-016. CMS-TDR-11.
- 2945 [80] CMS Collaboration. “Description and performance of track and primary-vertex
2946 reconstruction with the CMS tracker,” Journal of Instrumentation, vol. 9, no.
2947 10, p. P10009,(2014).
- 2948 [81] CMS Collaboration and M. Brice. “Images of the CMS Tracker Inner Bar-
2949 rel”, November 2008, CMS-PHO-TRACKER-2008-002. Retrieved from <https://cds.cern.ch/record/1431467>.
- 2951 [82] M. Weber. “The CMS tracker”. 6th international conference on hyperons, charm
2952 and beauty hadrons Chicago, June 28-July 3 2004.
- 2953 [83] CMS Collaboration. “Projected Performance of an Upgraded CMS Detector at
2954 the LHC and HL-LHC: Contribution to the Snowmass Process”. Jul 26, 2013.
2955 arXiv:1307.7135
- 2956 [84] L. Veillet. “End assembly of HB with EB rails and rotation inside SX ”,Jan-
2957 uary 2002. CMS-PHO-HCAL-2002-002. Retrieved from <https://cds.cern.ch/record/42594>.
- 2959 [85] J. Puerta-Pelayo.“First DT+RPC chambers installation round in the UX5 cav-
2960 ern.”. January 2007, CMS-PHO-OREACH-2007-001. Retrieved from <https://cds.cern.ch/record/1019185>
- 2962 [86] X. Cid Vidal and R. Cid Manzano. “CMS Global Muon Trigger” web site:
2963 Taking a closer look at LHC. Retrieved from https://www.lhc-closer.es/taking_a_closer_look_at_lhc/0.lhc_trigger

- 2965 [87] WLCG Project Office, “Documents & Reference - Tiers - Structure,”
 2966 (2014). <http://wlcg.web.cern.ch/documents-reference> , last accessed on
 2967 30.01.2018.
- 2968 [88] CMS Collaboration. “CMSSW Application Framework”, <https://twiki.cern.ch/twiki/bin/view/CMSPublic/WorkBookCMSSWFramework>,
 2969 last accesses 06.02.2018
- 2971 [89] A. Buckleya, J. Butterworthb, S. Giesekec, et. al. “General-purpose event gen-
 2972 erators for LHC physics”. arXiv:1101.2599v1 [hep-ph] 13 Jan 2011
- 2973 [90] A. Quadt. “Top Quark Physics at Hadron Colliders”. Advances in the Physics
 2974 of Particles and Nuclei. Springer-Verlag Berlin Heidelberg. DOI: 10.1007/978-
 2975 3-540-71060-8 (2007)
- 2976 [91] DurhamHep Data Project, “The Durham HepData Project - PDF Plotter.”
 2977 <http://hepdata.cedar.ac.uk/pdf/pdf3.html> , last accessed on 02.02.2018.
- 2978 [92] G. Altarelli and G. Parisi. “ASYMPTOTIC FREEDOM IN PARTON LAN-
 2979 GUAGE”, Nucl.Phys. B126:298 (1977).
- 2980 [93] Yu.L. Dokshitzer. Sov.Phys. JETP 46:641 (1977)
- 2981 [94] V.N. Gribov, L.N. Lipatov. “Deep inelastic e p scattering in perturbation the-
 2982 ory”, Sov.J.Nucl.Phys. 15:438 (1972)
- 2983 [95] F. Maltoni, G. Ridolfi, and M. Ubiali, “b-initiated processes at the LHC: a
 2984 reappraisal,” Journal of High Energy Physics, vol. 07, p. 022, (2012).
- 2985 [96] B. Andersson, G. Gustafson, G. Ingelman and T. Sjostrand, “Parton fragmen-
 2986 tation and string dynamics”, Physics Reports, Vol. 97, No. 2-3, pp. 31-145,
 2987 1983.

- 2988 [97] CMS Collaboration, “Event generator tunes obtained from underlying event
2989 and multiparton scattering measurements;” European Physical Journal C, vol.
2990 76, no. 3, p. 155, (2016).
- 2991 [98] J. Alwall et. al., “The automated computation of tree-level and next-to-leading
2992 order differential cross sections, and their matching to parton shower simula-
2993 tions,” Journal of High Energy Physics, vol. 07, p. 079, (2014).
- 2994 [99] T. Sjöstrand and P. Z. Skands, “Transverse-momentum-ordered showers and
2995 interleaved multiple interactions,” European Physical Journal C, vol. 39, pp.
2996 129–154, (2005).
- 2997 [100] S. Frixione, P. Nason, and C. Oleari, “Matching NLO QCD computations with
2998 Parton Shower simulations: the POWHEG method,” Journal of High Energy
2999 Physics, vol. 11, p. 070, (2007).
- 3000 [101] S. Agostinelli et al., “GEANT4: A Simulation toolkit,” Nuclear Instruments
3001 and Methods in Physics, vol. A506, pp. 250–303, (2003).
- 3002 [102] J. Allison et.al., “Recent developments in Geant4”, Nuclear Instruments and
3003 Methods in Physics Research A 835 (2016) 186-225.
- 3004 [103] CMS Collaboration “Full Simulation Offline Guide”, <https://twiki.cern.ch/twiki/bin/view/CMSPublic/SWGuideSimulation>, last accessed 04.02.2018
- 3006 [104] A. Giammanco. “The Fast Simulation of the CMS Experiment” J. Phys.: Conf.
3007 Ser. 513 022012 (2014)
- 3008 [105] A.M. Sirunyan et. al. “Particle-flow reconstruction and global event description
3009 with the CMS detector”, JINST 12 P10003 (2017) <https://doi.org/10.1088/1748-0221/12/10/P10003>.

- 3011 [106] The CMS Collaboration. “ Description and performance of track and pri-
 3012 mary vertex reconstruction with the CMS tracker”. JINST 9 P10009 (2014).
 3013 doi:10.1088/1748-0221/9/10/P10009
- 3014 [107] J. Incandela. “Status of the CMS SM Higgs Search” July 4, 2012. Pdf slides.
 3015 Retrieved from https://indico.cern.ch/event/197461/contributions/1478917/attachments/290954/406673/CMS_4July2012_Final.pdf
- 3017 [108] P. Billoir and S. Qian, “Simultaneous pattern recognition and track fitting by
 3018 the Kalman filtering method”, Nucl. Instrum. Meth. A 294 219. (1990).
- 3019 [109] W. Adam, R. Fruhwirth, A. Strandlie and T. Todorov, “Reconstruction of
 3020 electrons with the Gaussian sum filter in the CMS tracker at LHC”, eConf
 3021 C 0303241 (2003) TULT009 [physics/0306087].
- 3022 [110] K. Rose, “Deterministic Annealing for Clustering, Compression, Classification,
 3023 Regression and related Optimisation Problems”, Proc. IEEE 86 (1998) 2210.
- 3024 [111] R. Fruhwirth, W. Waltenberger and P. Vanlaer, “ Adaptive Vertex Fitting”,
 3025 CMS Note 2007-008 (2007).
- 3026 [112] CMS collaboration, “Performance of CMS muon reconstruction in pp collision
 3027 events at $\sqrt{s} = 7 \text{ TeV}$ ”, JINST 7 P10002 2012, [arXiv:1206.4071].
- 3028 [113] Coco, Victor and Delsart, Pierre-Antoine and Rojo-Chacon, Juan and Soyez,
 3029 Gregory and Sander, Christian, “Jets and jet algorithms”, Proceedings,
 3030 HERA and the LHC Workshop Series on the implications of HERA for LHC
 3031 physics: 2006-2008, pag. 182-204. <http://inspirehep.net/record/866539/files/access.pdf>, (2009), doi:10.3204/DESY-PROC-2009-02/54

- 3033 [114] M. Cacciari, G. P. Salam, and G. Soyez, “The anti- k_t jet clustering algorithm,”
3034 Journal of High Energy Physics, vol. 04, p. 063, (2008).
- 3035 [115] S. Catani, Y. L. Dokshitzer, M. H. Seymour, and B. R. Webber, “Longitudi-
3036 nally invariant K_t clustering algorithms for hadron hadron collisions”, Nuclear
3037 Physics B, vol. 406, pp. 187–224, (1993).
- 3038 [116] Y.L. Dokshitzer, G.D. Leder, S.Moretti, and B.R. Webber, “Better jet clustering
3039 algorithms,” Journal of High Energy Physics, vol. 08, p. 001, (1997).
- 3040 [117] B. Dorney. “Anatomy of a Jet in CMS”. Quantum Diaries. June
3041 1st, 2011. Retrieved from [https://www.quantumdiaries.org/2011/06/01/
3042 anatomy-of-a-jet-in-cms/](https://www.quantumdiaries.org/2011/06/01/anatomy-of-a-jet-in-cms/)
- 3043 [118] The CMS Collaboration.“Event Displays from the high-energy collisions at 7
3044 TeV”, May 2010, CMS-PHO-EVENTS-2010-007, Retrieved from [https://cds.
3045 cern.ch/record/1429614](https://cds.cern.ch/record/1429614).
- 3046 [119] The CMS collaboration. “Determination of jet energy calibration and transverse
3047 momentum resolution in CMS”. JINST 6 P11002 (2011). [http://dx.doi.org/
3048 10.1088/1748-0221/6/11/P11002](http://dx.doi.org/10.1088/1748-0221/6/11/P11002)
- 3049 [120] The CMS Collaboration, “Introduction to Jet Energy Corrections at
3050 CMS.”. <https://twiki.cern.ch/twiki/bin/view/CMS/IntroToJEC>, last ac-
3051 cessed 10.02.2018.
- 3052 [121] CMS Collaboration Collaboration. “Identification of b quark jets at the CMS
3053 Experiment in the LHC Run 2”. Tech. rep. CMS-PAS-BTV-15-001. Geneva:
3054 CERN, (2016). <https://cds.cern.ch/record/2138504>.

- 3055 [122] CMS Collaboration Collaboration. “Performance of missing energy reconstruction
3056 in 13 TeV pp collision data using the CMS detector”. Tech. rep. CMS-PAS-
3057 JME16-004. Geneva: CERN, 2016. <https://cds.cern.ch/record/2205284>.
- 3058 [123] CMS Collaboration, “New CMS results at Moriond (Electroweak) 2013”,
3059 Retrieved from http://cms.web.cern.ch/sites/cms.web.cern.ch/files/styles/large/public/field/image/HIG13004_Event01_0.png?itok=LAWZzPHR
- 3062 [124] CMS Collaboration, “New CMS results at Moriond (Electroweak) 2013”,
3063 Retrieved from http://cms.web.cern.ch/sites/cms.web.cern.ch/files/styles/large/public/field/image/TOP12035_Event01.png?itok=uMdnSqzC
- 3066 [125] K. Skovpen. “Event displays highlighting the main properties of heavy flavour
3067 jets in the CMS Experiment”, Aug 2017, CMS-PHO-EVENTS-2017-006. Re-
3068 trieval from <https://cds.cern.ch/record/2280025>.
- 3069 [126] G. Cowan. “Topics in statistical data analysis for high-energy physics”.
3070 arXiv:1012.3589v1
- 3071 [127] A. Hoecker et al., “TMVA-Toolkit for multivariate data analysis”
3072 arXiv:physics/0703039v5 (2009)
- 3073 [128] L. Lista. “Statistical Methods for Data Analysis in Particle Physics”, 2nd
3074 ed. Springer International Publishing. (2017) <https://dx.doi.org/10.1007/978-3-319-62840-0>

- 3076 [129] I. Antcheva et al., “ROOT-A C++ framework for petabyte data storage, sta-
 3077 tistical analysis and visualization ,” Computer Physics Communications, vol.
 3078 182, no. 6, pp. 1384â€¢1385, (2011).
- 3079 [130] Y. Coadou. “Boosted decision trees”, ESIPAP, Archamps, 9 Febru-
 3080 ary 2016. Lecture. Retrieved from https://indico.cern.ch/event/472305/contributions/1982360/attachments/1224979/1792797/ESIPAP_MVA160208-BDT.pdf
- 3083 [131] J.H. Friedman. “Greedy function approximation: A gradient boosting ma-
 3084 chine”. Ann. Statist. Volume 29, Number 5 (2001), 1189-1232. https://projecteuclid.org/download/pdf_1/euclid-aos/1013203451.
- 3086 [132] W. Verkerke and D. Kirkby, “The RooFit toolkit for data modeling,” arXiv
 3087 preprint physics, (2003).
- 3088 [133] CMS Collaboration, “Documentation of the RooStats-based statistics
 3089 tools for Higgs PAG”. <https://twiki.cern.ch/twiki/bin/view/CMS/SWGuideHiggsAnalysisCombinedLimit>, last accessed on 08.04.2018.
- 3091 [134] F. James, M. Roos, “MINUIT: Function minimization and error analysis”. Cern
 3092 Computer Centre Program Library, Geneve Long Write-up No. D506, 1989
- 3093 [135] J. Neyman and E. S. Pearson, “On the problem of the most efficient tests of
 3094 statistical hypotheses”. Springer-Verlag, (1992).
- 3095 [136] A.L. Read. “Modified frequentist analysis of search results (the CL_s method),”
 3096 (2000). CERN-OPEN-2000-205.
- 3097 [137] C. Palmer. “Searches for a Light Higgs with CMS”, CMS-CR-2012-215. <https://cds.cern.ch/record/1560435>.

- 3099 [138] A. Wald, “Tests of statistical hypotheses concerning several parameters when
 3100 the number of observations is large”, Transactions of the American Mathematical
 3101 society, vol. 54, no. 3, pp. 426–482, (1943).
- 3102 [139] G. Cowan, K. Cranmer, E. Gross, and O. Vitells, “Asymptotic formulae for
 3103 likelihood-based tests of new physics”, European Physical Journal C, vol. 71,
 3104 p. 1554, (2011).
- 3105 [140] S. S. Wilks, “The Large-Sample Distribution of the Likelihood Ratio for Testing
 3106 Composite Hypotheses”, Annals of Mathematical Statistics, vol. 9, pp. 60–62,
 3107 (03, 1938).
- 3108 [141] B. Hespel, F. Maltoni, and E. Vryonidou, “Higgs and Z boson associated pro-
 3109 duction via gluon fusion in the SM and the 2HDM”, JHEP 06 (2015) 065,
 3110 [https://dx.doi.org/10.1007/JHEP06\(2015\)065](https://dx.doi.org/10.1007/JHEP06(2015)065), arXiv:1503.01656.
- 3111 [142] ATLAS Collaboration, “Measurements of Higgs boson pro-
 3112 duction and couplings in diboson final states with the AT-
 3113 LAS detector at the LHC”, Phys. Lett. B726 (2013) 88–119,
 3114 doi:10.1016/j.physletb.2014.05.011, 10.1016/j.physletb.2013.08.010,
 3115 arXiv:1307.1427. [Erratum: Phys. Lett.B734,406(2014)].
- 3116 [143] CMS Collaboration, “Search for the associated production of a Higgs boson
 3117 with a single top quark in proton-proton collisions at $\sqrt{s} = 8$ TeV”, JHEP 06
 3118 (2016) 177, doi:10.1007/JHEP06(2016)177, arXiv:1509.08159.
- 3119 [144] B. Stieger, C. Jorda Lope et al., “Search for Associated Production of a Single
 3120 Top Quark and a Higgs Boson in Leptonic Channels”, CMS Analysis Note CMS
 3121 AN-14-140, 2014.

- 3122 [145] M. Peruzzi, C. Mueller, B. Stieger et al., “Search for ttH in multilepton final
3123 states at $\sqrt{s} = 13$ TeV”, CMS Analysis Note CMS AN-16-211, 2016.
- 3124 [146] CMS Collaboration, “Search for H to bbar in association with a single top quark
3125 as a test of Higgs boson couplings at $\sqrt{s} = 13$ TeV”, CMS Physics Analysis
3126 Summary CMS-PAS-HIG-16-019, 2016.
- 3127 [147] CMS Collaboration, “Search for production of a Higgs boson and a single top
3128 quark in multilepton final states in proton collisions at $\sqrt{s} = 13$ TeV”, CMS
3129 Physics Analysis Summary CMS-PAS-HIG-17-005, 2016.
- 3130 [148] CMS Collaboration, “PdmV2016Analysis,” (2016). <https://twiki.cern.ch/twiki/bin/viewauth/CMS/PdmV2016Analysis#DATA>, last accessed 11.04.2016.
- 3132 [149] B. WG, “BtagRecommendation80XReReco”, February, 2017. <https://twiki.cern.ch/twiki/bin/view/CMS/BtagRecommendation80XReReco>.
- 3134 [150] CMS Collaboration, “Identification of b quark jets at the CMS Experiment
3135 in the LHC Run 2”, CMS Physics Analysis Summary CMS-PAS-BTV-15-001,
3136 2016.
- 3137 [151] M. Peruzzi, F. Romeo, B. Stieger et al., “Search for ttH in multilepton final1
3138 states at $\sqrt{s} = 13$ TeV”, CMS Analysis Note CMS AN-17-029, 2017.
- 3139 [152] CMS Collaboration, “Baseline muon selections for Run-II.” <https://twiki.cern.ch/twiki/bin/view/CMS/CMSPublic/SWGuideMuonIdRun2>, last accessed on
3140 24.02.2018.
- 3142 [153] G. Petrucciani and C. Botta, “Two step prompt muon identification”, January,
3143 2015. <https://indico.cern.ch/event/368007/contribution/2/material/slides/0.pdf>.

- 3145 [154] H. Brun and C. Ochando, “Updated Results on MVA eID with 13 TeV samples”,
3146 October, 2014. [https://indico.cern.ch/event/298249/contribution/3/
3147 material/slides/0.pdf](https://indico.cern.ch/event/298249/contribution/3/material/slides/0.pdf).
- 3148 [155] K. Rehermann and B. Tweedie, “Efficient Identification of Boosted Semileptonic
3149 Top Quarks at the LHC”, JHEP 03 (2011) 059, [https://dx.doi:10.1007/
3150 JHEP03\(2011\)059](https://dx.doi.org/10.1007/JHEP03(2011)059), arXiv:1007.2221.
- 3151 [156] CMS Collaboration. “Tag and Probe”, [https://twiki.cern.ch/twiki/bin/
3152 view/CMS/TagAndProbe](https://twiki.cern.ch/twiki/bin/view/CMS/TagAndProbe), last accessed on 02.03.2018.
- 3153 [157] B. Maier, “SingleTopHiggProduction13TeV”, February, 2016. <https://twiki.cern.ch/twiki/bin/viewauth/CMS/SingleTopHiggsGeneration13TeV>.
3154